Optical time domain add-drop multiplexing employing fiber nonlinearities

Citation for published version (APA):
Verdurmen, E. J. M. (2006). *Optical time domain add-drop multiplexing employing fiber nonlinearities*. [Phd Thesis 1 (Research TU/e / Graduation TU/e), Electrical Engineering]. Technische Universiteit Eindhoven. https://doi.org/10.6100/IR615048

DOI:
10.6100/IR615048

Document status and date:
Published: 01/01/2006

Document Version:
Publisher's PDF, also known as Version of Record (includes final page, issue and volume numbers)

Please check the document version of this publication:

• A submitted manuscript is the version of the article upon submission and before peer-review. There can be important differences between the submitted version and the official published version of record. People interested in the research are advised to contact the author for the final version of the publication, or visit the DOI to the publisher's website.
• The final author version and the galley proof are versions of the publication after peer review.
• The final published version features the final layout of the paper including the volume, issue and page numbers.

Link to publication

General rights
Copyright and moral rights for the publications made accessible in the public portal are retained by the authors and/or other copyright owners and it is a condition of accessing publications that users recognise and abide by the legal requirements associated with these rights.

• Users may download and print one copy of any publication from the public portal for the purpose of private study or research.
• You may not further distribute the material or use it for any profit-making activity or commercial gain
• You may freely distribute the URL identifying the publication in the public portal.

If the publication is distributed under the terms of Article 25fa of the Dutch Copyright Act, indicated by the "Taverne" license above, please follow below link for the End User Agreement:

www.tue.nl/taverne

Take down policy
If you believe that this document breaches copyright please contact us at:

openaccess@tue.nl

providing details and we will investigate your claim.

Download date: 05. Oct. 2023

Optical Time Domain Add-Drop Multiplexing Employing Fiber Nonlinearities

PROEFSCHRIFT

ter verkrijging van de graad van doctor aan de
Technische Universiteit Eindhoven, op gezag van de
Rector Magnificus, prof.dr.ir. C.J. van Duijn, voor een
commissie aangewezen door het College voor
Promoties in het openbaar te verdedigen
op dinsdag 28 november 2006 om 16.00 uur

door

Erwin Josef Maria Verdurmen

geboren te Breda

Dit proefschrift is goedgekeurd door de promotoren:

prof.ir. A.M.J. Koonen
en
prof.ir. G.D. Khoe

Copromotor:
dr.ir. H. de Waardt

The research presented in this thesis was performed in the Electro-optical Communications systems group, department of Electrical Engineering of the Eindhoven University of Technology, the Netherlands.

CIP-DATA LIBRARY TECHNISCHE UNIVERSITEIT EINDHOVEN

Verdurmen, Erwin J.M.

Optical time domain add-drop multiplexing employing fiber nonlinearities / by
Erwin Josef Maria Verdurmen. -
Eindhoven : Technische Universiteit Eindhoven, 2006.
Proefschrift. - ISBN-10: 90-386-1923-5
ISBN-13: 978-90-386-1923-1
NUR 959
Trefw.: vezeloptica / nietlineaire optica / multiplexers / optische telecommunicatie / optische signaalverwerking.
Subject headings: high-speed optical techniques / nonlinear optics / time division multiplexing / optical fibre communication / optical information processing.

Samenstelling van de promotiecommissie:

Prof.dr.ir. A.C.P.M. Backx, Technische Universiteit Eindhoven, voorzitter
Prof.ir. A.M.J. Koonen, Technische Universiteit Eindhoven, eerste promotor
Prof.ir. G.D. Khoe, Technische Universiteit Eindhoven, tweede promotor
Dr.ir. H. de Waardt, Technische Universiteit Eindhoven, copromotor
Prof.dr.ir. P. Mégret, Faculté Polytechnique de Mons
Prof.dr. K.A.H. van Leeuwen, Technische Universiteit Eindhoven
Prof.dr. P.A. Andrekson, Chalmers University of Technology
Dr.ir. E. Tangdiongga, Technische Universiteit Eindhoven

The studies presented in this thesis were supported by the Towards Freeband Communication Impulse programme of the Ministry of Economic Affairs of the Netherlands

Abstract

Optical Time Domain Add-Drop Multiplexing Employing Fiber Nonlinearities

This thesis focuses on optical time division multiplexing (OTDM) technology at line data rates of 160 Gb/s and beyond. In particular time domain add-drop multiplexing has been addressed. Regarding the technology employed, add-drop multiplexers (ADMs) can be subdivided into two categories: semiconductor-based solutions and fiber-based solutions.

Regarding the semiconductor-based solutions, a study on the speed and power limits of an electroabsorption modulator (EAM) in an optically pumped configuration is carried out. In such a configuration, the cross-absorption modulation (XAM) in an EAM is utilized. A mathematical model based on propagation equations to simulate the XAM in the EAM has been developed. Good agreement is observed between the experimental results and the results obtained with the developed model of the EAM. Error-free demultiplexing from 80 to 10 Gb/s based on XAM in a commercially available EAM is presented. The concept of cross-polarization rotation (XPR) to increase the extinction ratio of the XAM based demultiplexer is introduced. Only a 1.2 dB sensitivity improvement by using XPR is observed. Feasibility of employing this device for 160 Gb/s demultiplexing, based on XAM and XPR, is studied. The performance of an EAM as all-optical demultiplexer strongly depends on the maximum non-destructive input power. With a higher clock power the saturation effect of the absorption will be stronger. The operation speed of the EAM as demultiplexer in an all-optical configuration is limited by the carrier recovery time. Increasing the reverse bias voltage shortens the recovery time. However this leads to an increase in absorption, which requires a higher input power to saturate the absorption, otherwise degradation of the signal-to-noise ratio (SNR) is unavoidable. All-optical demultiplexing with the available EAM and the limit of 13 dBm input power has limited us to demultiplexing from 160 to 10 Gb/s with an error floor of about 10^{-7}.

Several fiber-based ADM solutions have been studied. One of the most promising solutions is based on the nonlinear optical loop mirror (NOLM). An all-optical time domain ADM using highly nonlinear fiber (HNLF) in a NOLM, at bit rates higher than 80 Gb/s, is presented for the first time. Simulations and experiments at 160 Gb/s and 320 Gb/s have been performed. The performance limiting factors are crosstalk from neighboring channels for the drop function and incomplete removal of the dropped

channel due to the slopes of the switching window for the through function. The jitter between control and data and a non-optimized NOLM input coupling factor K further degrades the performance of the ADM. The results prove that ultra high speed OTDM add-drop multiplexing can be realized using nonlinear fiber, giving a prospect for 640 Gb/s operation.

The transmultiplexing of two 10 Gb/s NRZ WDM channels into one 20 Gb/s OTDM data stream, without the need of an extra conversion step from NRZ to RZ, is experimentally characterized. The conversion principle is based on the four-wave mixing (FWM) products of co-propagating control pulses and WDM channels in a HNLF. Another advantage of FWM transmultiplexing is the transparency towards alternative modulation formats, like for example phase modulated signals. Limitations of this technique have been studied. Conversion from 2×10 Gb/s WDM to 20 Gb/s OTDM is experimentally shown. Simulations predict that this technique is not suitable for conversion from 4×40 Gb/s WDM to 160 Gb/s OTDM, because the received optical power is too low due to insufficient efficiency of the FWM process.

An alternative technique that has been studied is based on cross-phase modulation (XPM) spectral broadening. This technique can be applied for time domain demultiplexing as well as for add-drop multiplexing. The advantage of this technique is the limited number of components required for construction of the ADM in comparison with the NOLM and the Kerr shutter, which is also extensively discussed in this work. Simulations and experimental results show the feasibility of this method at 160 Gb/s.

All previous presented work comprises all-optical time domain add-drop multiplexing for amplitude modulated (AM) signals. In this thesis an ADM for phase modulated signals is presented for the first time. Add-drop multiplexing of an 80 Gb/s RZ-DPSK OTDM signal based on a Kerr shutter, consisting of 375 m HNLF, has been proven experimentally. The phase information in the signal is preserved in the complete ADM, including a fiber, a polarization beam splitter and 2 EAMs. In the experiment, practical limitations limited our experiment to 80 Gb/s. An add-drop multiplexing experiment at 320 Gb/s with amplitude modulated signals shows the capability of the Kerr shutter as ultrafast gate.

All-optical signal processing using the Kerr effect in a HNLF and its potential applications for OTDM add-drop multiplexing are promising. Interferometric gates, based on fiber nonlinearities, are independent of the control pulse rate and can therefore operate at ultrafast speed, in the order of several femtoseconds. This makes them suitable as ADM and a good alternative to semiconductor-based solutions.

Contents

List of Acronyms

Each scientific field has its own jargon, and also a lot of acronyms. As a help to read this thesis, a list of acronyms is presented below.

ADM	Add-Drop Multiplexer
AM	Amplitude Modulator
ASE	Amplified Spontaneous Emission
B2B	Back-to-Back
BER	Bit Error Rate
QCSE	Quantum-Confined Stark Effect
CW	Continuous Wave
DCF	Dispersion Compensating Fiber
DDF	Dispersion Decreasing Fiber
DGD	Differential Group Delay
DPSK	Differential Phase Shift Keying
DQPSK	Differential Quadrature Phase Shift Keying
DSF	Dispersion Shifted Fiber
EAM	Electroabsorption Modulator
EDFA	Erbium-Doped Fiber Amplifier
ETDM	Electrical Time Division Multiplexing
FEC	Forward Error Correction
FOD	Fourth Order Dispersion
FWHM	Full Width Half Maximum
FWM	Four-Wave Mixing
GT-UNI	Gain Transparent Ultrafast Nonlinear Interferometer
GVD	Group Velocity Dispersion
HNLF	Highly Nonlinear Fiber
IFWM	Intra-channel Four-Wave Mixing
IM	Intensity Modulation
IXPM	Intra-channel Cross-Phase Mixing
MLL	Mode-Locked Laser
MQW	Multiple Quantum Well
MUX	Multiplexer
MZI	Mach-Zehnder Interferometer
NLSE	Nonlinear Schrödinger Equation

NOLM	Nonlinear Optical Loop Mirror
NRZ	Non-Return-to-Zero
OBPF	Optical Band Pass Filter
OOK	On-Off Keying
OSA	Optical Spectrum Analyzer
OSNR	Optical Signal-to-Noise Ratio
OTDM	Optical Time Division Multiplexing
PBS	Polarization Beam Splitter
PC	Polarization Controller
PD	Photo Diode
PM	Phase Modulator
PMD	Polarization Mode Dispersion
PRBS	Pseudo Random Bit Sequence
PSP	Principle States of Polarization
QCSE	Quantum-Confined Stark Effect
QW	Quantum Well
RF	Radio Frequency
RMS	Root Mean Square
RZ	Return-to-Zero
RZ-DPSK	Return-to-Zero Differential Phase Shift Keying
SBS	Stimulated Brillouin Scattering
SC	Super Continuum
SCG	Super Continuum Generation
SDH	Synchronous Digital Hierarchy
SDM	Spatial Division Multiplexing
SHB	Spectral-Hole Burning
SLALOM	Semiconductor Laser Amplifier in a Loop Mirror
SMF	Single Mode Fiber
SNR	Signal-to-Noise Ratio
SOA	Semiconductor Optical Amplifier
SOD	Second Order Dispersion
SPM	Self-Phase Modulation
SRS	Stimulated Raman Scattering
TDM	Time Division Multiplexing
TLS	Tuneable Laser Source
TOAD	Terahertz Optical Asymmetric Demultiplexer
TOD	Third Order Dispersion
TWRS	True Wave Reduced Slope
VA	Variable Attenuator
VPI	Virtual Photonics Incorporated™
WDM	Wavelength Division Multiplexing
XAM	Cross-Absorption modulation
XPM	Cross-Phase Modulation
XPR	Cross-Polarization Rotation

Chapter 1

Introduction

Today optical fiber technology plays an important role in the world of telecommunication. Telecommunication involves the transmission, switching and routing of signals over a long distance for the purpose of communication. This started out with people transmitting acoustical signals with drums or optical signals using smoke and fires, but nowadays it involves sending electromagnetic waves over optical fibers. Telecommunication is all around us with devices like the television, radio, telephone and of course internet. The demand for bandwidth is rapidly increasing and to cope with this the capacity of the network has to increase likewise. Fiber optic networks have the potential to deliver these high capacities, because of the inherent high bandwidth. For example, the total usable bandwidth in the window 1300-1625 nm is over 40 THz. The challenge in current communication networks is to employ the available bandwidth with the highest efficiency and the lowest cost.

1.1 Fiber Optic Network Infrastructure

In general, fiber optic networks can be divided into three layers. This is schematically shown in Figure 1.1. The long haul network, the metropolitan network and the access network. The "last mile" of the connection to the end-user is covered by the access network. Conventional access network infrastructures include twisted copper pair and coaxial cable, but optical fiber is also becoming increasingly more important in this area [1]. The access networks are connected to a metropolitan area network. This network connects several metro traffic aggregation points. A metropolitan area network usually covers a campus or a city. The long haul network links the various metro networks and forms the backbone of the global optical network. In the metro and long haul network single mode fiber plays an important role. An optical network can contain many nodes. In these nodes several processing functionalities might be required like amplification, routing, regeneration and/or switching between different signal formats, also known as transmultiplexing.

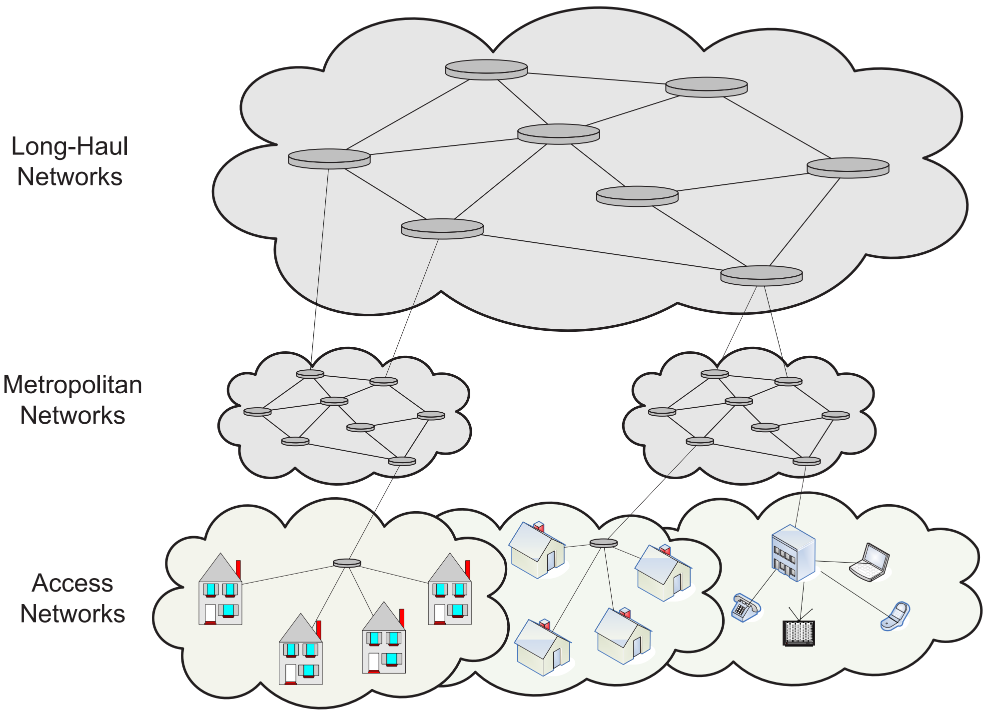

Figure 1.1: Optical network hierarchy: long-haul, metropolitan and access networks.

1.2 Optical Time Division Multiplexing

To increase the throughput of one single fiber, wavelength division multiplexing (WDM) and/or optical time division multiplexing (OTDM) can be employed. In WDM systems multiple optical carriers using different wavelengths transmit different data channels simultaneously over one fiber. WDM is schematically visualized in Figure 1.2. With WDM, a transmission capacity of over 10 Tbit/s over one single fiber has already been shown [2]. OTDM systems are similar to WDM systems because they also divide the fiber bandwidth into a large number of lower data rate channels. However, an OTDM system is generated by bit-interleaving the lower data rate channels in the time domain. An example of how to construct an OTDM signal is shown in Figure 1.3. Electrical signals at the base rate are converted into short optical pulses, which are delayed and combined into a high speed OTDM signal.

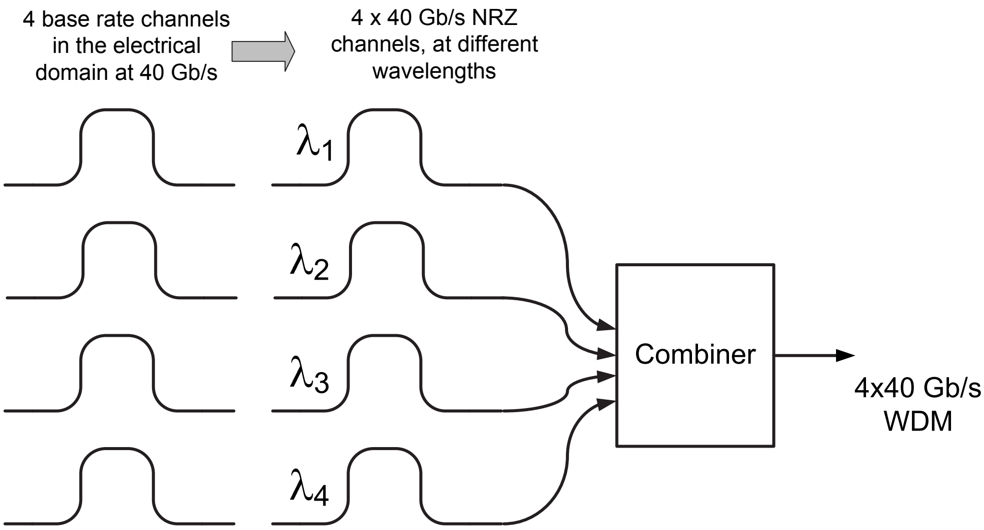

Figure 1.2: Four electrical base rate channels at 40 Gb/s are converted to four non-return-to-zero (NRZ) optical signals at $\lambda_1, \lambda_2, \lambda_3$ and λ_4 respectively, who are combined into a 4x40 Gb/s WDM signal.

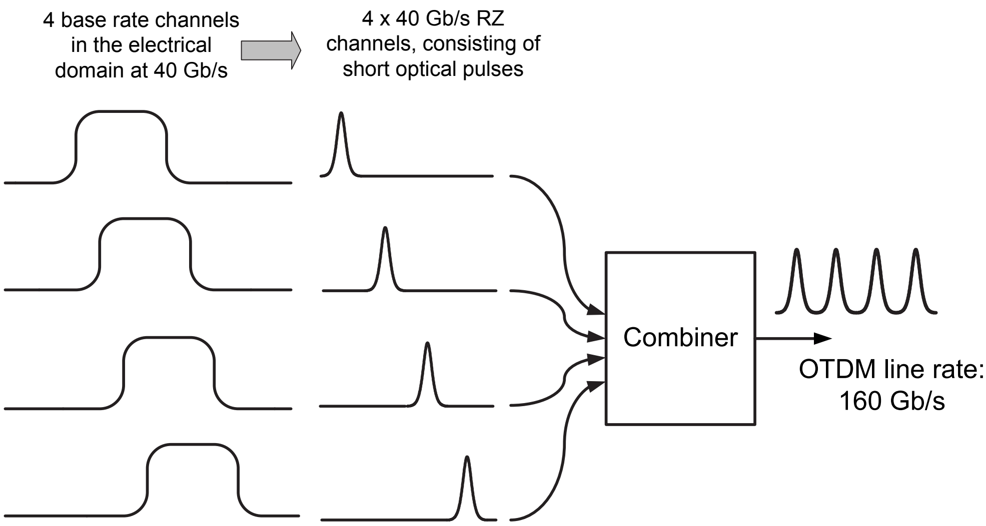

Figure 1.3: Four electrical base rate channels at 40 Gb/s are converted to short optical return-to-zero (RZ) pulses, who are time-interleaved to a 160 Gb/s line rate.

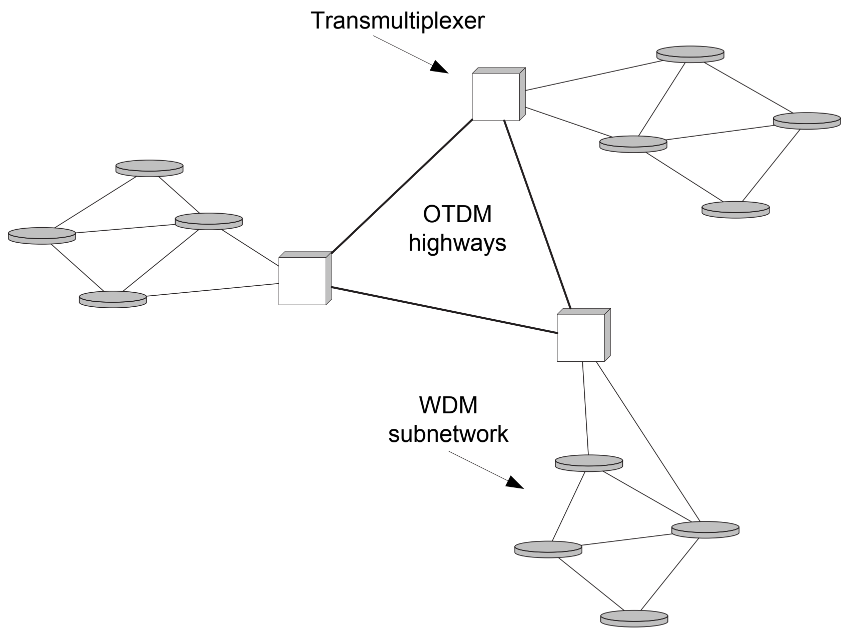

Figure 1.4: Possible network structure using OTDM highways and WDM subnetworks.

To enhance the throughput, a combination of WDM and OTDM can be considered [3, 4]. The total throughput of an OTDM, WDM or hybrid system is governed by the total bandwidth of the transmission medium rather than the bit rate of a channel. An example of a hybrid system is shown in Figure 1.4. In this example the network is subdivided into several smaller subnetworks operating with the WDM technique. An OTDM highway is used to interconnect the different subnetworks. At the interface points transmultiplexing between OTDM and WDM is necessary. The total capacity of the OTDM highway can be increased by expanding to a small number of wavelength multiplexed OTDM channels. This thesis focuses on key components in OTDM systems. A major issue in OTDM systems is the clear separation of the multiplexed pulses in the time domain to prevent channel crosstalk. It is necessary that the leading and trailing edge of the pulses do not overlap to avoid intra-channel interference. This means that the pulses should be shorter than the inverse aggregate bit rate. In the case of 160 Gb/s this results in pulses smaller than 6.25 ps, measured at the base of the pulse. The general requirement for the pulse width of a return-to-zero (RZ) OTDM signal to carry it over at least several kilometers of fiber is about 15-30% of the bit slot time [5]. For an alternating polarization multiplexed system a broader pulse can be tolerated, in general the pulse width requirement can be relaxed to 50-60% of the bit slot. To increase the bit rate of one single wavelength, shorter optical pulses are demanded. With the decrease of pulse width, the spectral width becomes broader as a logical consequence of the Fourier transform relation between pulse width and spectral width. For example, when the temporal shape of the pulse is Gaussian, the optical electric field can be written as:

$$E(t) = E_0 \exp\left[-(t/\tau)^2\right] \tag{1.1}$$

with E_0 the field amplitude and τ the $1/e^2$ width of the pulse in the time domain. If the pulse is transform-limited the corresponding spectrum can be found by taken the Fourier transform of equation (1.1). This is denoted by:

$$A(\omega) = A_0 \exp[-(\omega/\Delta\omega)^2] \tag{1.2}$$

with A_0 the spectral amplitude and $\Delta\omega = 2/\tau$ being the spectral width at the $1/e^2$ width of the optical pulse. A transform-limited pulse is a pulse, which is as short as its spectral bandwidth allows. In other words, its time-bandwidth product is as small as possible. For example, it is 0.315 for bandwidth-limited secant-shaped pulses or 0.44 for Gaussian-shaped pulses. In WDM systems, a broader spectral width requires an increase of the wavelength channel spacing. The ideal setting for the highest throughput is to create a WDM system with a channel allocation as dense as possible. The spacing of the channels is then determined by the spectral width of the optical pulses.

The guidelines for selecting the bit rate per wavelength channel depend on the choice of granularity, rather than the required total line rate. In a Tbit/s system fewer channels with a higher bit rate per channel are easier to handle than a large number of channels with a lower bit rate per channel. The maximum bit rate per WDM channel is limited by the maximum electronic data rate. At this moment the highest bit rate available with an electronic multiplexer/demultiplexer module is 100 Gb/s [6, 7]. When higher bit rates are desired, OTDM technology is required. The realization of OTDM networks demands the development of new technologies such as ultra-high-speed optical switches, sources, buffers, format transmultiplexers, as well as new network protocols. In [8] a next generation core network is presented, including a cost analysis with the assumption of a maturing of the OTDM technology. It is concluded that for a 100 Tb/s demand scenario the 160 Gb/s solution is the most cost effective.

Another advantage of OTDM technology is that the increase of the line rate to 160 Gb/s, or even higher, reduces the number of required light sources with respect to spatial division multiplexing (SDM) and WDM. This leads to a lower system complexity and simplification of the network management and thus reducing the costs. Therefore, it is possible that OTDM might not only be used on long-haul distances, but also might be attractive on shorter distances, such as metro or access networks.

Ultrashort optical pulses that come with high-speed OTDM technology have some unique properties over conventional optical waveforms at 10 or 40 Gb/s. One of the properties is a large optical electromagnetic field in a short timescale, which leads to the usage of nonlinear effects under modest average power conditions. These nonlinear effects are utilized in our all-optical time domain add-drop multiplexers (ADMs), which are described at a later stage in this thesis.

1.3 Optical Time Division Demultiplexing

Although new developments make it possible to create 100 Gb/s electrical time division multiplexed (ETDM) systems targeted for 100 Gb/s Ethernet applications, in general synchronous digital hierarchy (SDH) oriented channel rates of more than 40 Gb/s require OTDM. Fast optical demultiplexers are needed to extract one channel at a base rate of for example 10 or 40 Gb/s out of the high speed OTDM signal. Several demultiplexing techniques are based on the semiconductor laser amplifier in a loop mirror (SLALOM) [9], the gain-transparent SLALOM switch [10–12], the terahertz optical asymmetric demultiplexer (TOAD) [13], nonlinear optical loop mirror (NOLM) [14–16], gain-transparent Mach-Zehnder interferometer (MZI) switch [12, 17], ultrafast nonlinear interferometer [12, 18], electroabsorption modulator (EAM) [19, 20], monolithic integration of a photodiode and an EAM (PD-EAM) optical gate [21], polarization switching in an semiconductor optical amplifier (SOA) [22], four-wave mixing (FWM) in an SOA [23] or fiber [24], cascaded second-order nonlinear effect in quasi-phase matched $LiNbO_3$ waveguide device [25] and cross-phase modulation (XPM) induced spectral broadening and filtering in a highly nonlinear fiber (HNLF) [26, 27] or an SOA [28]. The demultiplexing is only one function of a complete OTDM add-drop multiplexing node. The concept of add-drop multiplexing is elaborated in the next section.

1.4 Optical Add-Drop Multiplexing

A time domain add-drop multiplexer (ADM) is a key component in a high speed OTDM network. For example, such an ADM could be applied at the cross-section of the OTDM highway and the WDM subnetwork depicted in Figure 1.4. In this section several methods to achieve add-drop multiplexing are discussed. Time domain add-drop multiplexing is schematically visualized in Figure 1.5. One (or more) channels can be dropped and one (or more) channels can be inserted in the empty time slot(s). A synchronized control signal simultaneously creates a drop and through function. The through operation is also called continue operation in the literature. To keep consistent with the publications the through term will be used. The performance of various ADMs are compared based on several important characteristics, namely robustness, complexity, polarization dependence, efficiency, number of tributaries and speed limitations.

Several ADMs presented in literature use two control signals instead of one control signal [29, 30]. The first control signal at the base rate is to provide the drop functionality and a second control signal that is a $(N-1)\times$ multiplexed clock signal to create the through function, where N is the total number of base rate channels. Although it requires a more complex clock pulse generation stage, it could relax the requirements on the functionalities of the optical switch. Separate switching mechanisms can be used to create the drop and through function. In such an ADM with two control pulses, for example with a 4×40 Gb/s OTDM signal, the incoming data signal would be split and one control signal at 40 GHz for wavelength conversion of the dropped channel would be applied to the first part of the OTDM signal, and one

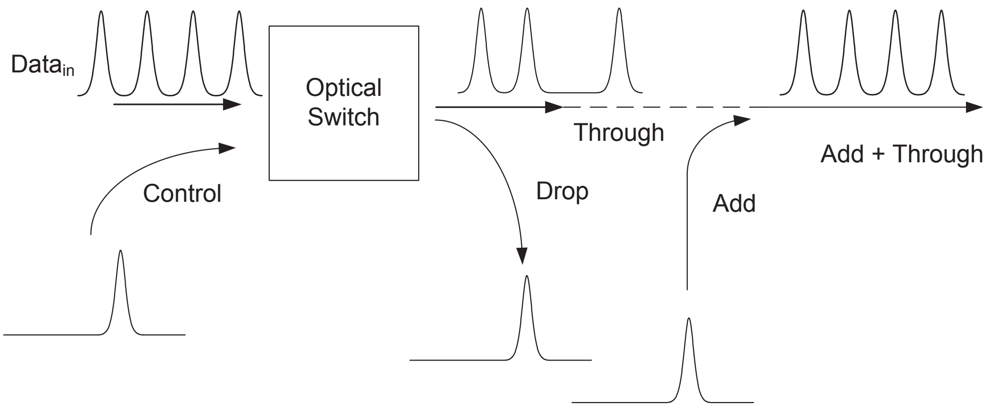

Figure 1.5: Schematic of the functionality of a time domain ADM with one control signal.

control signal at 3×40 GHz to convert the wavelength of the through channels would be applied to the second part of the OTDM signal.

This thesis focuses on ADMs based on one control signal, because of the less complex control pulse generation stage. In general such time domain ADMs can be subdivided into two categories. The first category is based on active semiconductor devices and the second category is based on passive switching employing fiber nonlinearities.

1.4.1 Semiconductor-Based Add-Drop Multiplexing

In this section an overview is given of the state-of-the-art on optical time domain ADMs based on semiconductor technology. The configurations based on gain-transparent semiconductor optical amplifiers (SOAs), electroabsorption modulators (EAMs), Mach-Zehnder structures and four-wave mixing (FWM) in an SOA are described in this section.

Gain-Transparent Semiconductor Optical Amplifier

A gain-transparent SOA has the advantage that the gain for a data signal in the C-band (1530-1565 nm) is hardly influenced by the saturation that is induced by a 1300 nm control pulse. The data signal is in fact far away from the gain and ASE-maximum of the SOA. Thus, the data experiences a negligible amplitude change. Moreover, a very small amount of noise is added. However a strong phase shift around 1550 nm is still observed. This effect is utilized in the gain-transparent ultrafast nonlinear interferometer (GT-UNI). A simplified schematic explaining the operation principle of the GT-UNI is shown in Figure 1.6. The GT-UNI is a good candidate for add-drop multiplexing at 160 Gb/s with a 10 Gb/s base rate [31–33]. A birefringent element, for example a polarization maintaining fiber, splits the incoming data pulses into two orthogonally polarized components, which are delayed in time with respect

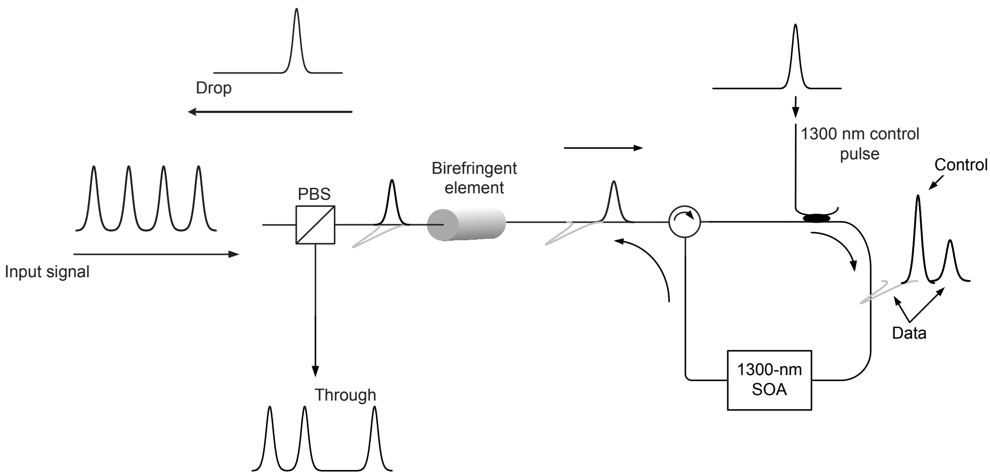

Figure 1.6: All-optical ADM using the GT-UNI. PBS: polarization beam splitter, SOA: semiconductor optical amplifier.

to each other. Those two polarized components are launched into a polarization insensitive 1300 nm SOA together with the control pulse at 1300 nm, which is precisely aimed to be located in between the two polarized components. The control pulse induces a change in the refractive index of the SOA. The phase of the data component that immediately follows the control pulse experiences a XPM induced phase shift, because of the control pulse induced refractive index change. The gain however is not influenced for the data signal that is located in the C-band. After traveling through the SOA, the signal is transmitted back through the birefringent element. As a result, the relative time delay between the both polarized components is canceled again. The state of polarization (SOP) of the recombined data pulse is then determined by the relative phase difference between the two polarized components. Without control pulse the two polarized components experience the same conditions in the loop and the phase difference between the two components is not altered, consequently the signal is sent to the through port. On the other hand, if the control pulse is introduced in between the two polarization components the phase difference between the two components is altered and the signal is sent to the drop port.

In [32] the average power of the input signal was 20 dBm, in order to compensate for the losses of the 1550 nm signal that occur because of propagation through the 1300 nm SOA. The average power of the control signal was 8 dBm. The complexity of this setup is quite large. High quality control pulses must be generated at the base rate and at the wavelength 1300 nm. Moreover, the control pulses should be synchronized with the data input pulses. The input data pulses have to be split in two orthogonally polarized components with equal powers, which makes this method strongly polarization dependent. The speed limitations of this method depend on the recovery time of the SOA, which is in the order of 100 ps. The SOA needs to be recovered, or at least partly, in the time between two control pulses. Apart from the GT-UNI, the gain-transparent SOA can also be placed inside a TOAD switch. Again, the 1300 nm SOA is used as nonlinear element to only modulate the refractive index and the phase of a C-band signal, while the gain for the C-band signal remains nearly unchanged [34].

Electroabsorption Modulator

An application with EAMs provides another promising method to create an ADM. The EAM has to be designed with traveling-wave electrodes to overcome the RC time limitation. 160 Gb/s add-drop operation at a 40 Gb/s base rate has been shown [35]. Two separate EAMs are required to implement the drop and through function. Both EAMs are operated at different bias voltages and the phase of the 40 GHz radio frequency (RF) driving signal is optimized separately for the drop and through operation. The 40 Gb/s base rate is favorable for the EAM, while on the other hand, it is more difficult to achieve for SOA-based switches. After all, an increase of the base rate from 10 Gb/s to 40 Gb/s reduces the maximum gain and phase change in an SOA, because the available time for the carrier density to recover is decreased from 100 ps to 25 ps. A schematic of this EAM-based ADM is shown in Figure 1.7. The advantage of this ADM configuration is that the switching window is generated

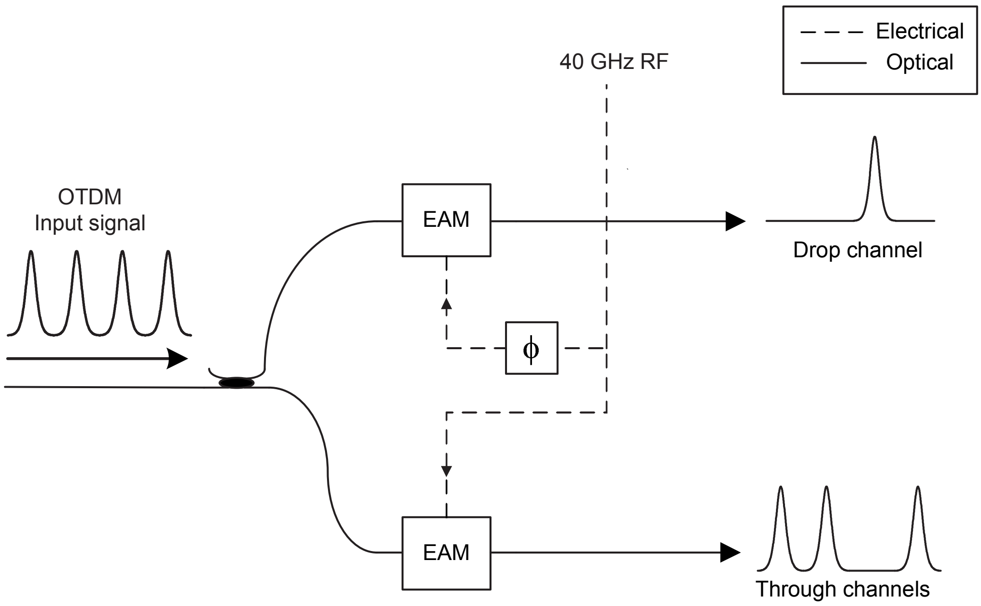

Figure 1.7: ADM using two EAMs, ϕ: phase shifter.

without an interferometer. Consequently, a lower number of components are required. Moreover, EAMs can be made nearly polarization insensitive and the complete ADM is suitable for integration on one single optical chip. A disadvantage is the required electrical control signal, making this an opto-electronic solution. In [35] the average optical input power is 5 dBm and the RF signal is a 6 V_{pp} sinusoidal microwave signal. The speed is limited by the electrical bandwidth of the EAM. The switching window is therefore dependent on the speed of current electronics. At this moment, the maximum bit rate that can be handled by an EAM-based ADM is 160 Gb/s with a 40 Gb/s base rate. The feasibility of an alternative add-drop multiplexing technique based on an optically controlled EAM is addressed in Chapter 2.

Mach-Zehnder Interferometer

A Mach-Zehnder interferometer (MZI) with integrated SOAs has been shown successfully in creating a 40 Gb/s OTDM ADM with a 10 Gb/s base rate [36, 37]. The operation principle of a MZI-SOA ADM is schematically shown in Figure 1.8. The

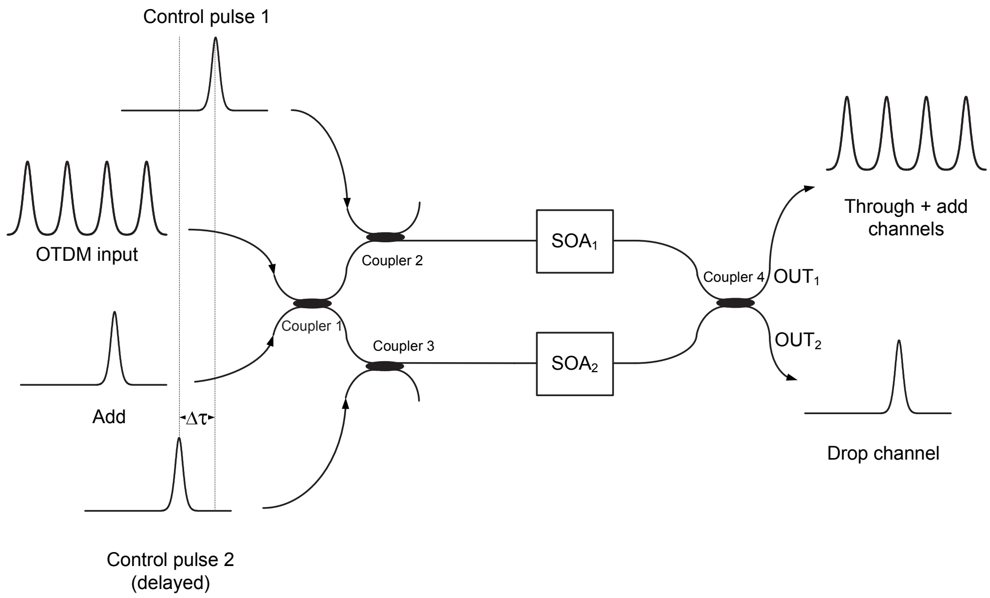

Figure 1.8: ADM using a MZI-SOA.

input OTDM data signal and the add channel are inserted into two arms of the MZI. Control pulse 1 is inserted in the upper arm of the MZI and control pulse 2 in the lower arm. Both pulses are $\Delta\tau$ delayed with respect to each other. Control pulse 1 induces a phase shift on the data signal in the upper arm through XPM in the SOA. When the signal from the lower and upper arm interfere at 3 dB coupler 4, the targeted demultiplexed channel will be sent to output port 2 (OUT_2), whereas the add channel is sent to output port 1 (OUT_1). Moreover, the add channel is located in the original time slot of the demultiplexed channel. An instance of time $\Delta\tau$ later, the delayed control pulse 2 in the lower arm of the MZI induces the same phase shift on the data signal as in the upper arm. The interference at 3 dB coupler 4 now results in transmitting the remaining OTDM channels (through channels) to OUT_1.

In [37] an alternative approach is presented to minimize the sensitivity penalty that arises between optimization for either add or drop operation. The idea is to simultaneously apply co-propagating operation for the drop-functionality and counter-propagating operation for the through-functionality. The disadvantage is that two optical clock signals are required to separately generate the drop and through function. The average optical input power at the SOAs required for good operation is approximately 3 dBm.

One advantage of an ADM based on a MZI-SOA solution is that it can be fully integrated on a photonic chip. No conversion to the electrical domain is needed, thus this represents an all-optical solution. Another advantage is the achievability of polarization independence of the SOAs. However, the speed of this operation principle is limited due to the limited recovery time of the SOA. The maximum speed of operation of this ADM configuration shown up to date is 40 Gb/s with a 10 Gb/s base rate, although higher operation speeds have been achieved for demultiplexing only. In [17] error-free demultiplexing from 336 Gb/s to 10.5 Gb/s is presented.

Bidirectional SOA FWM

In [29] bidirectional FWM in an SOA is reported as switching mechanism for a 40 Gb/s ADM with a 10 Gb/s base rate. The operation principle of this ADM is schematically shown in Figure 1.9. The incoming OTDM signal is split and launched into both sides of the SOA, visualized by arrow 1 and arrow 2. Wavelength conversion with a 10 GHz control signal (arrow 3) and filtering at the new wavelength provides the dropped channel (arrow 5). Simultaneously, in the opposite direction wavelength conversion based on FWM with a 3×10 GHz control signal (arrow 4) and filtering at the new wavelength provides the three converted through channels (arrow 6).

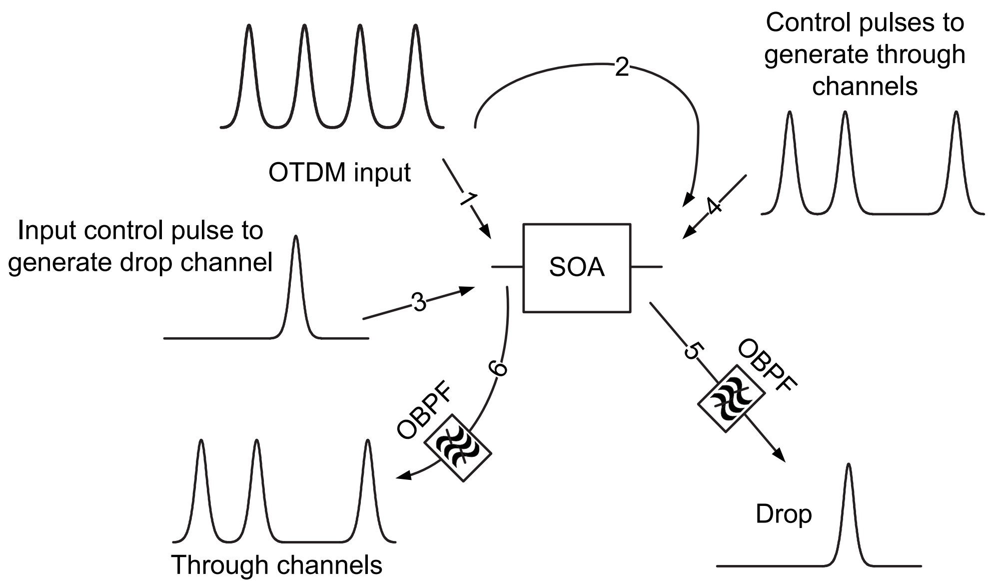

Figure 1.9: ADM using FWM in a bi-directional SOA.

Two disadvantages arise when FWM is adopted as switching mechanism. The first disadvantage is the inherent polarization dependence of FWM. Secondly, FWM exhibits a low conversion efficiency. When the bit rate is increased, in general smaller pulses with larger spectral widths are employed and lower efficiencies are obtained. The advantage of this concept is that the SOA can be integrated. In principle the concept of FWM in SOAs is a fast process, but the conversion efficiency limits the maximum obtainable speed. So far, the maximum ADM operation speed based on FWM in an SOA presented, is with a 40 Gb/s line rate and a 10 Gb/s base rate. The average power for the pump and input signal used in the experiment described in [29] is 4.36 and 0.53 dBm, respectively.

1.4.2 Fiber-Based Add-Drop Multiplexing

The second category of ADMs is based on switching in a highly nonlinear fiber (HNLF). HNLF is a special type of fiber with increased nonlinear coefficient γ. A γ-value as high as possible is preferred for all-optical switching in fiber. The nonlinear coefficient of a fiber is given by:

$$\gamma = \frac{n_2 \omega_0}{c A_{\text{eff}}} \tag{1.3}$$

γ can be increased by decreasing the effective cross sectional area (A_{eff}) of the fiber, or increasing the nonlinear refractive index (n_2). The nonlinear refractive index n_2 can be increased by doping (e.g. with Ge or Bi_2O_3). Several examples of ADMs that exploit the nonlinear effect in a HNLF are the NOLM, the XPM induced wavelength switch and the Kerr shutter. They are briefly discussed in this section.

Nonlinear Optical Loop Mirror

A NOLM is used in *[38]* to create a full add-drop node at 160 Gb/s with a 40 Gb/s base rate. A fiber-based NOLM exploits the nonlinear phase shift induced in a fiber placed in a loop mirror for optical switching. A schematic view of a NOLM is shown in Figure 1.10. In the NOLM the input signal is split into two parts: one clockwise and one counterclockwise propagating signal. By inserting an external control pulse in the loop in one of the directions the data channel that co-propagates with that control pulse receives a phase shift because of XPM between the high energy control pulse and the selected data channel. When the clockwise and counterclockwise signal interfere at the 3-dB coupler the phase shifted signal will be sent to the "demultiplexed data" output port, while the unchanged channels will be reflected back to the input port. Maximum add-drop multiplexing operation speed obtained with the NOLM is 320 Gb/s *[39]*. The average power for the input signal at 320 Gb/s and the control signal is 5 dBm and 13 dBm, respectively. The operation speed is limited due to chromatic dispersion, polarization mode dispersion (PMD) and untargeted nonlinear effects like FWM and self-phase modulation (SPM). An alternative ADM with a 40 Gb/s line rate and 10 Gb/s base rate channels is presented in [40, 41]. This OTDM add-drop multiplexing concept is based on OTDM-to-WDM conversion in a NOLM followed by a WDM ADM. In the end, the WDM signal is converted back to an OTDM signal in a second NOLM. In this concept the signal processing is employed in the frequency

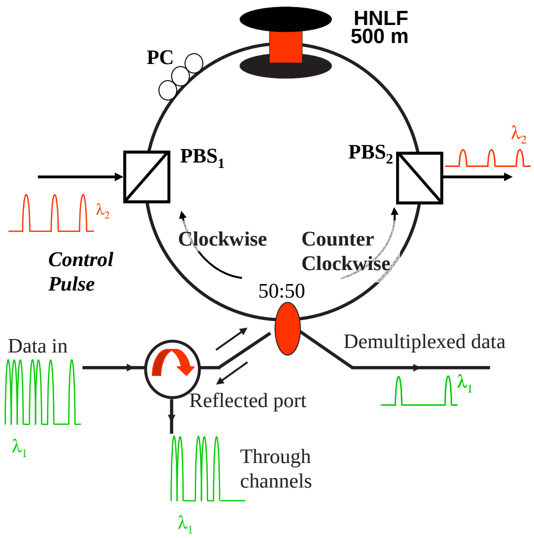

Figure 1.10: Schematic view of a fiber-based nonlinear optical loop mirror ADM.

domain by applying fiber Bragg grating technology. A high peak dropped channel timeslot suppression ratio of 35 dB can be obtained. A disadvantage of this scheme is the rather complex setup.

XPM Induced Wavelength Shifting

In [30] a wavelength converter based on a XPM induced wavelength shifting in HNLF is adopted to create an ADM. The concept is based on the two control pulses ADM. The first control signal to create the drop function and the second control signal to create the through function. On the other hand, in [42, 43] a 80 Gb/s ADM is created with only one control channel. The XPM induced wavelength shifting based ADM has a simple setup, which is shown in Figure 1.11. If the data channel overlaps with the rising edge of the control pulse, it experiences a red frequency shift, but if the data channel overlaps with the falling edge of the control pulse, it experiences a blue frequency shift. The frequency shift is caused by the time derivative of the control pulse intensity profile. To realize a full add-drop multiplexing scheme, the dropped channel needs to be completely removed at the through port. The drop channel needs therefore to be pushed out of the original wavelength band as far as possible. In order to achieve this, the data signal pulse width should be affected by only one of the slopes of the control pulse. In the case of a symmetric control pulse the data signal pulse width should be less than half of the control pulse width. On the other hand, the control pulse width should be less than half of the bit slot of the OTDM data, as the through-function should not affect the neighboring channels. This concept has been demonstrated at 80 Gb/s, but can be increased towards 160 Gb/s. The average power of the 80 Gb/s input signal employed in [30] was 13.5 dBm, while the average

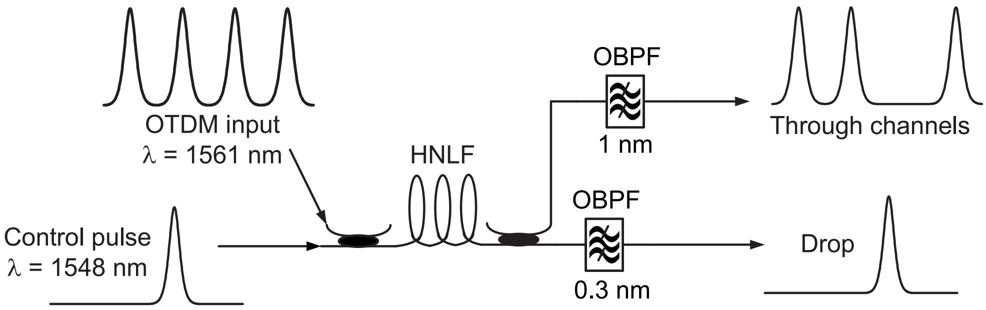

Figure 1.11: Schematic view of a XPM induced wavelength shifting based ADM.

power of the control signal 26.5 dBm was. The operation speed is limited due to the chromatic dispersion, PMD and untargeted nonlinear effects like SPM and FWM.

Kerr Shutter

The Kerr shutter employs the Kerr effect of the fiber. The Kerr effect is the intensity dependent change of the refractive index of the fiber. This effect will be more thoroughly explained in Chapter 3. By introducing an intense, high power control pulse co-propagating with an OTDM signal in the fiber the refractive index of the fiber is changed and a phase shift to the co-propagating data channel is introduced. The Kerr shutter uses the nonlinear phase shift induced by this control pulse to change the state of polarization (SOP) of one OTDM channel that is targeted to be switched in a HNLF [44–46], *[47]*. The power of the OTDM signal is low compared to the high energy control pulse.

The principle of the Kerr shutter is shown in Figure 1.12. The high power control pulse and the input signal are linearly polarized at the input of the nonlinear medium with a 45° angle between each other. A polarization beam splitter (PBS) blocks the transmission of the input signal in the direction of the drop port in case of no control signal. When the control signal is present, the parallel and perpendicular components of the input signal experience a different change in refractive index due to the control signal induced birefringence. This results in a different phase shift between the two components of the input signal. When the induced phase difference between the two polarization components of the data signal at the end of the fiber equals π, then the signal at the output is perpendicular in polarization compared to the data signal at the output that is not influenced by the external control pulse. In this case one single PBS can be used to extract the drop channel as well as the through channels. When the nonlinear phase shift is less than π, two separate PBSs are required to separately optimize for drop and for through operation. Speeds up to 320 Gb/s have been obtained using this method. In [46] the average power of the 320 Gb/s input signal was 9 dBm and the average power of the control signal was 15.9 dBm. The operation speed is limited due to chromatic dispersion, PMD and untargeted nonlinear effects like FWM and SPM.

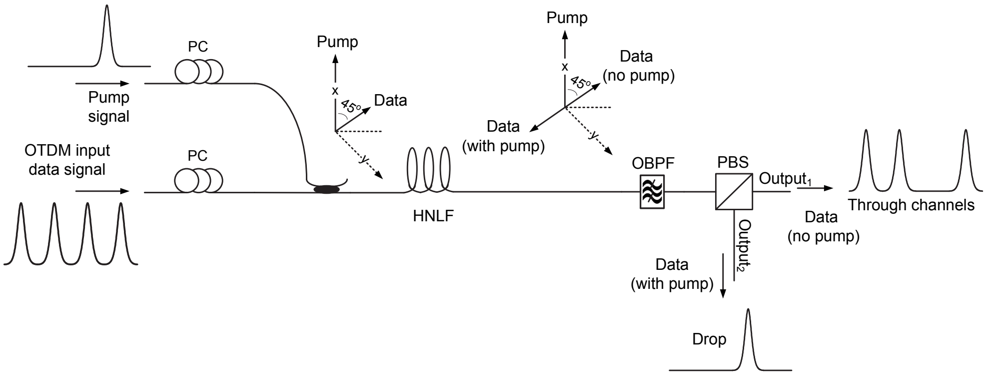

Figure 1.12: Schematic of an optical Kerr shutter in an ADM configuration.

1.4.3 Comparison Add-Drop Multiplexers

An overview of the existing add-drop multiplexing techniques is shown in Table 1.1. As the bit rates of the OTDM signals are increased, HNLF based ADMs receive more attention thanks to the ultrafast fiber nonlinearities.

Table 1.1: Comparison of current technology of time domain ADMs.

Time Domain Add-Drop Multiplexers				
Reference	Medium	Configuration	Result	year
[36, 37]	SOA	MZI	40 Gb/s	1998
[34]	SOA	GT-SOA in TOAD	40 Gb/s	1999
[29]	SOA	Bi-directional FWM	40 Gb/s	2000
[31–33]	SOA	GT-UNI	160 Gb/s	2003
[42, 43]	HNLF	XPM induced spectral broadening	80 Gb/s	2004
[35]	EAM	traveling wave EAMs	160 Gb/s	2004
[46]	HNLF	Kerr shutter	320 Gb/s	2005
[39]	HNLF	NOLM	320 Gb/s	2005

The EAM-based ADM looks like the most advantageous semiconductor-based solution for 160 Gb/s operation with a 40 Gb/s base rate. The setup is compact, has a low polarization sensitivity and no noise is added thanks to the absorptive behavior of the EAM. Up to now the speed in electronics limits the operation to 160 Gb/s. The optical power levels can be kept at moderate levels of 5 dBm. Two other methods based on semiconductor devices employ an SOA in gain-transparent mode. The gain-transparent SOA has lower gain changes (<1 dB), but also a lower maximum phase change. This is no problem if no π phase shift is required, like for example in the GT-UNI, where the output is split and separate optimization for the drop and through function is realized. On the other hand, this concept is more complex, because high quality control pulses have to be generated at the base rate at 1300 nm. Moreover, this method is strongly dependent on the polarization, because the input data pulses have to be split in two orthogonally polarized components with equal powers. The speed limitations of this method depend on the recovery time of the SOA. The SOA needs to be recovered, or at least partly, in the time between two control pulses. The SOA recovery time also limits the speed of operation of the MZI-SOA ADM. The concept based on bi-directional FWM in an SOA has the disadvantage of a low conversion efficiency and a polarization dependence. Moreover, one control signal at 10 GHz for wavelength conversion of the dropped channel and one counter-propagating control signal at 3×10 GHz to convert the through channels is required for a fully operational ADM. This seems to work fine, however, a complicated control pulse generation stage that simultaneously generates the drop and through control pulse streams has to be created.

On the other hand, fiber-based ADMs have wideband characteristics and over Tb/s operation speed due to the ultrafast fiber nonlinearities. Technologies based on the NOLM and the Kerr shutter have already proven the feasibility of 320 Gb/s ADMs, with average optical control pulse power levels in the order of 15 dBm. In the experiments with the NOLM and Kerr shutter ADMs, the speed is not limited by the response time of the fiber nonlinearities, but more by the dispersion and involvement of untargeted nonlinear effects like FWM and SPM.

The design of the fiber is of great importance for fiber-based ADMs. A high nonlinear coefficient is important because it relaxes the requirements of the control pulse peak power. It also reduces the required interaction length, which increases the robustness and relaxes the dispersion issue. The short pulses of the high bit rate OTDM signal require a careful design of the zero-dispersion point, group velocity dispersion (GVD), dispersion slope and ultimately even the fourth order dispersion (see section 3.2). The disadvantage of fiber-based solutions is that they cannot be integrated on a photonic chip, because the fibers are still too long (in the order of a few hundred meters). However, effort has been made to reduce the size of the bobbin for small HNLF modules [48]. It has been shown that a 500 m long fiber with a 60 μm core can be wound on a bobbin with an inner diameter of 12 mm. Also, effort has been made to increase the nonlinear coefficient fo the fiber such that 1 meter long fibers can be used in ADMs [44].

1.5 Framework of the Research

The work described in this thesis has been performed within the framework of the "Freeband Kennisimpuls programme". Freeband Kennisimpuls (Knowledge Impulse) is a joint initiative of the Dutch government, knowledge institutions and industry and, as a research programme, forms part of the government action plan "Competing with ICT Competencies". The programme's objective is to raise knowledge regarding modern telecommunications within Dutch knowledge institutions (universities and institutes) to an international top level. Our project "Key components for 160 to 640 Gb/s Optical Time Domain Multiplexed (OTDM) Networking" is subdivided into two parts. One part is devoted to the development of an optical chip with an integrated mode-locked laser (MLL) clock recovery, operating in the C-band (1530-1565 nm). The injection seeded 160 Gb/s input signal is used to lock the free running frequency

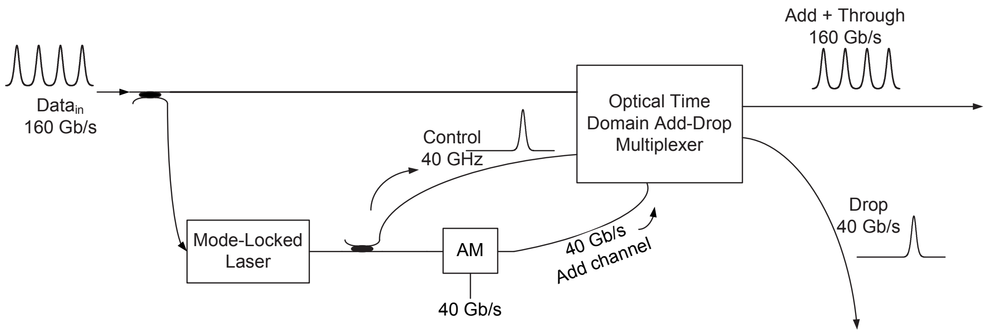

Figure 1.13: Schematic of a time domain add-drop multiplexer employing a mode-locked laser as clock recovery unit

of the MLL to the incoming signal at 160 GHz and is then divided to 40 GHz. My colleague Yohan Barbarin has been working on that topic [49, 50]. The second part, subject of this thesis, involves high-speed switching technologies at 160 Gb/s or faster for all-optical multiplexing, demultiplexing and add-drop multiplexing. Here it is assumed that an optical clock signal is available from an MLL clock recovery chip. A schematic diagram of the total ADM unit is shown in Figure 1.13.

1.6 Aim and Outline of this Thesis

The objective of the work presented in this thesis is to explore high-speed switching technologies at 160 Gb/s or at higher speeds. References to own work will be reflected in italic throughout this thesis, in order to better differentiate between general references and own work. The focus in this thesis lays on applications like all-optical time domain demultiplexing and add-drop multiplexing. In our project an optical clock signal, generated by an MLL is assumed to drive the ADM. A test-bed at 160 Gb/s, followed by a test-bed at 320 Gb/s towards 640 Gb/s has to be realized.

Firstly, the switching capabilities of an optically pumped EAM are investigated. A complete model of an EAM that includes the contribution of the electric field does not exist. Therefore, a model describing the behavior of an optically pumped EAM must be designed. Such a model can help us to find the maximum obtainable bit rate for demultiplexing one channel at the base rate out of a high-speed OTDM signal.

Secondly, fiber-based optical add-drop multiplexers (ADMs) are studied. Several ADM techniques employing passive HNLF are explored. The different fiber-based ADM technologies are compared based on complexity, robustness, efficiency, performance and speed limitation.

Compared to WDM, OTDM is a technique that needs to mature and therefore requires attention, which gives rise to several research questions. The research questions that this thesis tries to answer are:

- Is it possible to develop an add-drop multiplexer based on electroabsorption modulators in an optically pumped configuration? Moreover, is it possible to integrate this solution with an all-optical mode-locked laser clock recovery device?

- What is the most suitable add-drop multiplexing technique based on the Kerr effect in a highly nonlinear fiber?
- Can we combine transmultiplexing from OTDM-to-WDM and WDM-to-OTDM to make a more flexible network node?
- Despite the increased interest in differential phase shift keying (DPSK) systems, add-drop multiplexing has not been investigated for DPSK so far. Therefore, we want to know if it is possible to create an all-optical time domain add-drop multiplexer for phase modulated signals?

A study on the limits of all-optical time-domain demultiplexing using cross-absorption modulation (XAM) in an electroabsorption modulator is presented in Chapter 2. A model based on propagation equations to simulate the XAM effect in the EAM has been developed. Simulations and experimental results are presented for demultiplexing from a 160 Gb/s OTDM signal to a 10 Gb/s channel.

In Chapter 3 the basic theory of fiber nonlinearities and dispersion are addressed. The wave equation and the influence of the fiber nonlinearities as well as the dispersion effects on this wave equation are examined. It is crucial to have fundamental knowledge about the influence of the Kerr nonlinearity, pulse walk-off and polarization mode dispersion on OTDM systems. Especially, when the target is to design an OTDM ADM employing ultra-short pulses.

In Chapter 4, a concept to employ the NOLM as key component in an all-optical time domain ADM is presented. The NOLM incorporates a 500 m long HNLF. The tolerance of the coupler ratio and the timing jitter are addressed. Simulations and experimental work confirm operation up to 320 Gb/s OTDM.

Chapter 5 focuses on the FWM effect in a HNLF and its use to OTDM systems. FWM is transparent to both bit rate and modulation format. This makes it attractive for all-optical signal processing of phase modulated signals. Examples are wavelength conversion and/or transmultiplexing from OTDM-to-WDM and from WDM-to-OTDM. Demultiplexing from 160 Gb/s to a 10 Gb/s base rate and transmultiplexing from OTDM-to-WDM and WDM-to-OTDM is studied. The combination of both transmultiplexing schemes allows the construction of an ADM based on FWM in HNLF. Conversion from 2×10 Gb/s WDM to 20 Gb/s OTDM is experimentally shown. Simulations predict that this technique is not suitable for conversion from 4×40 Gb/s WDM to 160 Gb/s OTDM, because the received optical power is too low. Limitations of the transmultiplexing techniques are discussed.

The feasibility of creating an all-optical ADM based on XPM spectral broadening and based on the Kerr shutter are explored in Chapter 6 and 7, respectively. Also, the feasibility to realize an ADM for RZ-DPSK OTDM signals based on the Kerr shutter in HNLF is discussed, because of the recent interest in differential phase shift keying (DPSK) signals.

In Chapter 8, 640 Gb/s OTDM systems are looked upon. The influence of fourth order dispersion is studied and a first step towards add-drop multiplexing is taken.

Chapter 9 finalizes this thesis with the conclusions and recommendations.

Chapter 2

Electroabsorption Modulator as All-Optical Demultiplexer

The electroabsorption modulator (EAM) has already shown to be a key component in realizing high-speed OTDM systems [51]. The functionalities include pulse generation [52], data modulation [53], wavelength conversion [54–58], clock recovery [20, 59–62], 3R regeneration [63–65] and OTDM demultiplexing [20, 21, 66–69]. Recent efforts on the integration of mode-locked lasers (MLLs) have led to very interesting options to generate an all-optical clock recovery [70]. The next step would be to integrate an optically controlled gate together with an MLL to create an all-optical integrated OTDM demultiplexer. An EAM could serve as such an optically activated gate by exploiting the cross-absorption modulation (XAM) mechanism. In this chapter a detailed study on the potential of using a commercially available multiple quantum well-EAM (MQW-EAM) as a key element in an optically pumped drop configuration is presented. The XAM concept will be compared with a new concept that utilizes the cross-polarization rotation (XPR) in addition to the XAM in the EAM. The injected high-intensity pump signal saturates the EAM, which leads to XAM, but it also introduces additional birefringence in the EAM. This additional birefringence leads to a rotation of the polarization (XPR). The XPR+XAM can improve the extinction ratio compared to the use of XAM only.

The chapter starts with the basic absorption properties of an EAM in section 2.1. In section 2.2 the operation principles of different demultiplexing methods using an EAM are explained. A theoretical assessment of the XAM effect in the EAM has been investigated by modeling, the model is presented in section 2.3. The purpose of the presented model is to study the behavior of the EAM in a quantitative matter. In the following section 2.4, the simulation results of an optically pumped drop configuration are presented. After that, in section 2.5 the experimental results are discussed. Finally, the last section of this chapter (section 2.6) describes the limitations regarding the EAM as all-optical demultiplexer in an OTDM system. The results of the research described in this chapter are published in *[71, 72]*.

2.1 Basic Absorption Properties

An EAM is realized with a core waveguide (usually InGaAsP) sandwiched between two InP materials doped p^+ and n, respectively. The waveguide absorbs the light when it is reversely biased, but is transparent when no bias is applied. The absorbing coefficient α of the EAM varies with the wavelength of the incident light and with the electric field in the active region, which is imposed by the reverse bias voltage. In Figure 2.1 the relation between the absorption and the reverse bias voltage of our MQW-EAM (V_{EAM}) is depicted for two different wavelengths.

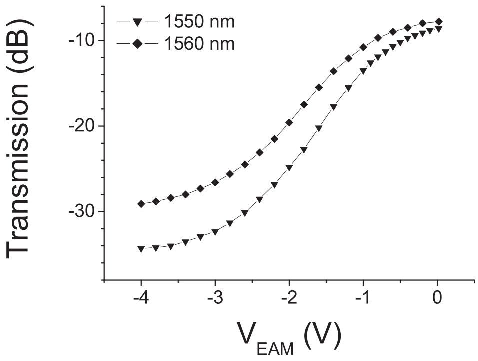

Figure 2.1: Transmission versus the reverse bias of the EAM.

A bulk semiconductor EAM is based on the Franz-Keldysh effect. Under an applied electric field, the probability of lateral carrier tunneling of an electron from the valence band to the conduction band via absorption of a photon with an energy below the material band gap energy is greater than zero. This effect, the Franz-Keldysh effect, red-shifts the absorption edge, as is visualized in Figure 2.2. The electron and hole states in a bulk semiconductor crystal are schematically shown under appliance of an electrical field.

The MQW-EAM utilizes the quantum-confined Stark effect (QCSE) [73]. When an external electric field perpendicular to the wells is applied, the energy of the well states is reduced, resulting in a lower effective band gap. Figure 2.3 shows how the transition energy in a QW is reduced from E_{e-h} to E'_{e-h} under the appliance of an external electric field. Compared with bulk material EAMs, the MQW-EAMs have higher modulation efficiencies and lower drive voltages, because the band gap in QW structures can change significantly faster than the absorption near the band gap in comparable bulk structures.

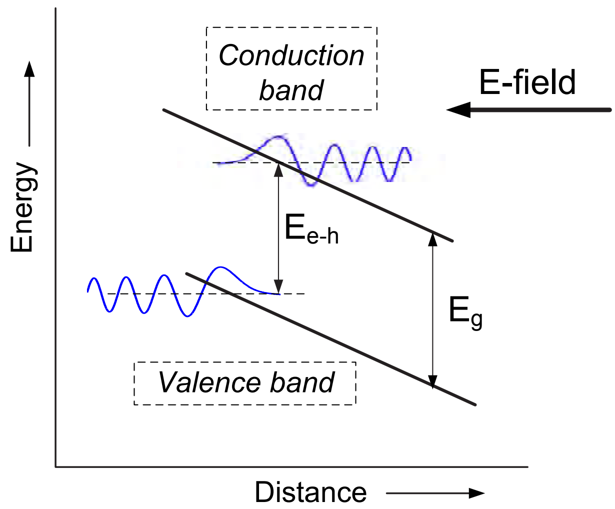

Figure 2.2: Schematic of the Franz-Keldysh effect in an EAM. Under appliance of an electrical field, the energy separation between electrons and holes E_{e-h} is lower than the band gap energy E_g.

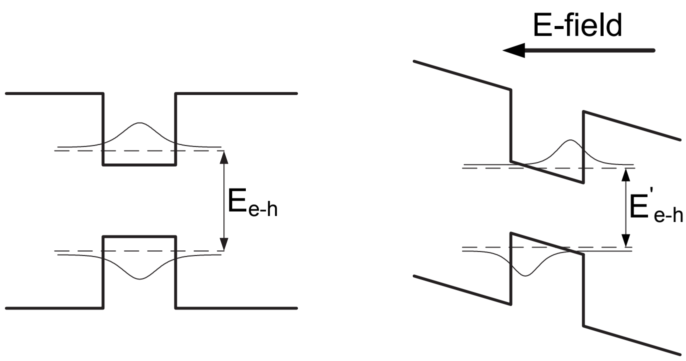

Figure 2.3: Schematic of the quantum-confined Stark effect in an EAM. The electron and hole wave functions are shown without (left) and with (right) electric field.

2.2 Operation Principle

In this section, the different operation principles of the EAM as demultiplexer are discussed. Besides all-optical fiber-based demultiplexing techniques that have been demonstrated by using cross-phase modulation (XPM) and four-wave mixing (FWM) in a highly nonlinear fiber (HNLF) [24, 27], another attractive option for demultiplexing is with active components, i.e. semiconductor optical amplifiers (SOAs). Demultiplexing with SOAs can be based on FWM [23], or SOAs can also be placed in an interferometric structure such as the semiconductor laser amplifier in a loop mirror [12], the terahertz optical asymmetric demultiplexer [13] or the gain transparent ultrafast non-linear interferometer [18, 31]. However, these schemes require complex configurations. Using only a single EAM is promising due to the possibility of monolithic integration, with a simple waveguide structure [68] or a traveling wave design as in [35] and [66].

2.2.1 Electrically Driven

By driving the EAM with a radio frequency (RF) signal, an optical time window for the OTDM signal is created. In such a way a time domain add-drop multiplexer (ADM) can be realized [19, 35]. The disadvantage of this method is that an RF clock signal is required. With an optical clock signal in an optically pumped demultiplexing configuration, no optical to electrical (O-E) or electrical to optical (E-O) converter is required.

2.2.2 Cross-Absorption Modulation

Cross-absorption modulation (XAM) occurs when two beams are launched into an EAM. One of these two beams has a high power, the pump signal. The other lower power signal is called the probe signal. Electron-hole pairs are generated inside the EAM because of the absorption of the high power optical pump signal. The absorption coefficient is reduced, due to the increase in photon-generated number of carriers. Also, the electric field across the active region is screened (lowered) because of the increased number of carriers inside the EAM, thereby lowering the absorption for the probe signal. This results in a higher output of the probe in the presence of a logical "1" in the stronger pump signal. This effect can be used for non-inverting wavelength conversion [74], but also for all-optical demultiplexing [20].

2.2.3 Cross-Polarization Rotation

The concept of cross-polarization rotation (XPR) in an EAM is used to enforce the already operating XAM-effect by utilizing the rotation of the polarization. The concept of XPR is schematically shown in Figure 2.4. The OTDM data input is fed into the EAM, in counter-propagating direction to the clock signal. Injecting a high-intensity clock signal reduces the absorption coefficient of the EAM. A change in the absorption coefficient means a change in the refractive index, since they are related through the Kramers-Krönig equation. The injected clock signal also induces additional birefringence in the EAM, which causes the TE and the TM mode of the OTDM signal to experience a different refractive index change, resulting in a rotation of the polarization *[75]*. The first polarization controller (PC_1) is used to adjust the polarization of the input signal to be approximately 45° to the orientation of the EAM layers. The polarization of the clock signal is controlled by PC_3. The high-intensity clock signal at a different (or same) wavelength as the OTDM signal saturates the EAM. The output of the EAM is sent to the polarization beam splitter (PBS) via the circulator. The polarization controller PC_2 is used to adjust the polarization in such a way that the

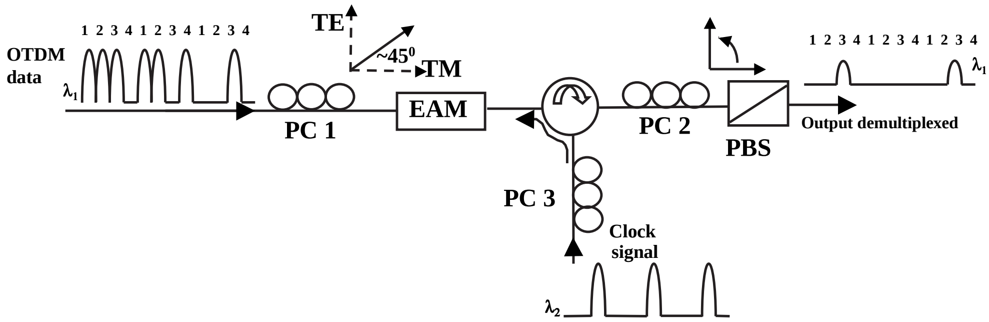

Figure 2.4: Principle of demultiplexing using XPR in a polarization sensitive EAM, PC: Polarization Controller, PBS: Polarization Beam Splitter.

PBS blocks the OTDM signal in case where no clock signal is present in the EAM. On the other hand part of the signal is allowed to pass through the PBS in the presence of a clock-generated control pulse inside the EAM, as the polarization is rotated. The high-intensity clock signal inside the EAM also induces XAM. XPR and XAM both work in the same direction and thus the extinction ratio at the output is improved.

2.3 Electroabsorption Modulator Model

Theoretical assessment of the XAM effect in the EAM has been studied through modeling. The purpose of the model presented in this section is to investigate the behavior of the EAM in a quantitative manner. This model is experimentally verified and the limitations of the commercially available EAM are assessed. To model the absorption dynamics of the EAM we compute the well carrier densities, well carrier temperatures as well as the photon density at every point inside the EAM, similar to the model presented in [76]. The parameters used in the simulations are listed in appendix Table C.1. The Fermi levels and temperatures of the carriers in the valence and conduction band are given by the balance equations for carriers and their energy in the absorbing region. The absorption coefficient also takes into account both spectral-hole burning (SHB) and carrier heating/cooling. Instead of using a field dependency in the Fermi distribution and the energy density, a simple carrier-density sweep-out model [77] is employed that assumes a reverse bias voltage to put the EAM in the absorption regime. This sweep-out model describes the increase of the sweep-out time at high carrier densities. This is not a real physical model but it is used to describe the behavior of the sweep-out time in a phenomenological way. We have implemented this simplified relation for the sweep-out time in which the variation is dependent on the carrier density. The sweep-out time (τ_{so}) is varying from $\tau_o = 8$ ps ($N = 0$) at low densities to $\tau_{tr} = 25$ ps ($N = N_{tr}$) at transparency, based on the results in [77]:

$$\tau_{so}(N) = \frac{\tau_o \tau_{tr}}{\tau_{tr}\left(1 - \frac{N}{N_{tr}}\right) + \tau_0 \frac{N}{N_{tr}}} \tag{2.1}$$

The pulse propagation is modeled by the propagation equation of the complex pulse amplitude $A(z,t)$. $A(z,t)$ is a slowly varying function of z and t, and satisfies:

$$\left(\frac{\partial}{\partial z}+\frac{1}{v_g}\cdot\frac{\partial}{\partial t}\right)A(z,t)=-\frac{1}{2}\Big(\Gamma(1+i\alpha_H)\cdot\alpha(z,t)+\alpha_{int}\Big)\cdot A(z,t) \tag{2.2}$$

where α_H is the linewidth enhancement factor, v_g is the group velocity, Γ is the confinement factor, α_{int} represents the internal loss coefficient and $\alpha(z,t)$ is the absorption coefficient, averaged over the thickness of the active region. The pulse amplitude is expressed by:

$$A(z,t)=\sqrt{S(z,t)}e^{i\phi(z,t)} \tag{2.3}$$

where $S(z,t)$ is the photon density and $\phi(z,t)$ is the phase of the light. Equation (2.2) leads to the following expressions for the photon density and the phase in the active region:

$$\frac{\partial S(z,t)}{\partial z}+\frac{1}{v_g}\frac{\partial S(z,t)}{\partial t} = -\Big(\Gamma\cdot\alpha(z,t)+\alpha_{int}\Big)\cdot S(z,t) \tag{2.4}$$

$$\frac{\partial\phi(z,t)}{\partial z}+\frac{1}{v_g}\cdot\frac{\partial\phi(z,t)}{\partial t} = -\frac{1}{2}\cdot\Gamma\cdot\alpha_H\cdot\alpha(z,t) \tag{2.5}$$

This equation is simplified by a transformation to a shifted time frame $t'=t-\frac{z}{v_g}$. Doing so leads to the following differential equations for the photon density and phase in the active region:

$$\frac{\partial S(z,t')}{\partial z} = -\Big(\Gamma\cdot\alpha(z,t)+\alpha_{int}\Big)\cdot S(z,t') \tag{2.6}$$

$$\frac{\partial\phi(z,t')}{\partial z} = -\frac{1}{2}\cdot\Gamma\cdot\alpha_H\cdot\alpha(z,t) \tag{2.7}$$

The absorption coefficient $\alpha(z,t)$ is calculated as a function of the well carrier densities, and takes both SHB and carrier heating/cooling into account. Electroabsorption effects are not included, because the field is not described. Therefore, band-filling only induces the absorption changes. The absorption coefficient is expressed as:

$$\alpha(z,t)=\frac{\alpha_0}{1+\epsilon_{sup}\cdot S(z,t)}\cdot\Big(1-f_c(\epsilon_{Fc},\epsilon_c^0,T_c)-f_v(\epsilon_{Fv},\epsilon_v^0,T_v)\Big) \tag{2.8}$$

where α_0 is the unsaturated absorption coefficient, and f_c and f_v are the Fermi distributions of the conduction and valence band, respectively. They are characterized by the Fermi levels ϵ_{Fi}, temperatures T_i and kinetic energy of the generated carriers ϵ_i^0 (i=c,v refers to the conduction and valence band, respectively) [76]. The term ϵ_{sup} is the absorption suppression factor due to SHB. The kinetic energy of the generated carriers in conduction and valence band are in resonance with the photons energy $\hbar\omega_0$. This is shown by:

$$\epsilon_c^0=(\hbar\omega_0-E_{gap})\frac{m_v}{m_c+m_v} \tag{2.9}$$

$$\epsilon_v^0=(\hbar\omega_0-E_{gap})\frac{m_c}{m_c+m_v} \tag{2.10}$$

where m_c and m_v are the mass of the electrons in the conduction band and the holes in the valence band, respectively. E_{gap} is the band gap energy of InGaAsP-material and $\hbar = h/2\pi$ is the reduced Planck's constant. The Fermi distributions f_i can be written as:

$$f_i = \left(1 + \exp\left[\frac{\epsilon - \epsilon_{Fi}}{k_B T_i}\right]\right)^{-1}, \qquad i = c, v \tag{2.11}$$

where k_B is the Boltzmann constant, and ϵ is the kinetic energy of the carrier. The equations that describe the dynamics of the Fermi levels and the temperatures are given by the balance equations for carriers and their energy in the absorbing region:

$$\frac{\partial n(z,t)}{\partial t} = \alpha(z,t) \cdot v_g \cdot \Gamma \cdot S(z,t) - \frac{n(z,t) - n_{eq}}{\tau_{so}(n)} \tag{2.12}$$

$$\frac{\partial p(z,t)}{\partial t} = \alpha(z,t) \cdot v_g \cdot \Gamma \cdot S(z,t) - \frac{p(z,t) - p_{eq}}{\tau_{so}(p)} \tag{2.13}$$

The balance equation for the energy density in the absorbing region is:

$$\frac{\partial u_i(z,t)}{\partial t} = S(z,t) \cdot v_g \cdot \alpha(z,t) \cdot \epsilon_i^0 - \frac{u_i - u_{Li}}{\tau_{ui}} - \frac{u_i}{\tau_{so}} \tag{2.14}$$

The variables n and p represent the local electron and hole densities, n_{eq} and p_{eq} are the local electron and hole densities in equilibrium, ϵ_i^0 is the energy of the generated electrons (i=c, equation (2.9)) or holes (i=v, equation (2.10)) and τ_{ui} represents the energy relaxation time. The energy relaxes to the energy at lattice temperature: u_{Li}. The change in number of carriers in the valence and conduction band, which is indicated in equation (2.12) and (2.13), is given by the absorption of photons that leads to the generation of an electron and a hole minus the number of carriers that are swept out of the active region, characterized by the sweep-out time τ_{so}. The first term in equation (2.14) are the number of generated carriers multiplied by the kinetic energy of the generated carrier. The second and third term of equation (2.14) are relaxation terms to the energy in the lattice and due to the sweep-out of the carriers.

In quantum well (QW) absorbers the photo-generated carriers are confined in the QW in the direction of the external field, so the field will not heat the carriers in the QW. Therefore, we may neglect the influence of the field on carrier temperature dynamics. The carrier density ($n_i, i = c, v$) and the energy density ($u_i, i = c, v$) are described by:

$$n_i = N_i \cdot F_{1/2}\left[\frac{\epsilon_{Fi}}{k_B T_i}\right] \tag{2.15}$$

$$u_i = \frac{3}{2} \cdot k_B \cdot T_i \cdot N_i \cdot F_{3/2}\left[\frac{\epsilon_{Fi}}{k_B T_i}\right] \tag{2.16}$$

where $F_{1/2}$, $F_{3/2}$ are the Fermi-Dirac integral of the order 1/2 respectively 3/2. N_i ($i = c, v$) is the effective density of states:

$$N_i = 2 \cdot \left(\frac{m_i k_B T_i}{2\pi\hbar^2}\right)^{3/2} \tag{2.17}$$

The above mentioned equations are solved to model the propagation of an optical pulse through the active region of an EAM. The intensity of the optical pulse is introduced into the set of equations via the photon density $S(z,t)$. The propagation of the optical pulse through the active region of the EAM is governed by the propagation equation (equation (2.2)) of the slowly varying amplitude $A(z,t)$. The slowly varying amplitude is related to the photon density via equation (2.3). The propagation equation for the photon density and the phase of the light wave, equation (2.4) and (2.5) are solved for each step in the length of the device (the device is divided into a number of sections with length: dz) and each instance of time (spaced by the sample time: dt). Crucial in the model is the calculation of the absorption coefficient α (equation (2.8)). To calculate the absorption coefficient, it is required that the values of the Fermi distributions f_c and f_v are known. To obtain f_c and f_v, we have to determine the energy of the generated carriers (ϵ_c^0, ϵ_v^0), the Fermi levels (ϵ_{Fv}, ϵ_{Fc}) and the temperatures (T_v, T_c) of the carriers. ϵ_c^0 and ϵ_v^0 are given by equations (2.9) and (2.10). ϵ_{Fv}, ϵ_{Fc}, T_v and T_c are deduced from equation (2.15) and (2.16). To solve these two coupled equations, the carrier density ($n_c = n$,$n_v = p$), the energy density (u_c, u_v) and the effective density of states (N_i, equation (2.17)) are substituted into equation (2.15) and (2.16). The carrier density (n_c,n_v) and the energy density (u_c, u_v) are given by their balance equations (2.12)-(2.14). The differential equations of n, p, u_c and u_v are coupled, via $S(z,t)$ to equation (2.3). We conclude that the propagation of the optical pulse through the active region of the EAM is governed by a set of five coupled differential equations that can be solved numerically.

The linewidth enhancement factor α_H is proportional to the ratio of the wavelength-shift to the net gain change. The net gain (or net absorption) change is a nonlinear process for the EAM. Therefore, it can be concluded that α_H is strongly dependent on the absorption loss change that is directly related with the applied reverse bias voltage and the wavelength [78]. α_H decreases with increasing reverse bias and can even become negative [79, 80]. We can therefore conclude that the low α_H under normal operation conditions increases with an increasing optical pump power that bleaches the absorption. The increased linewidth enhancement factor can be utilized to create optically induced phase shifts that can be exploited in interferometric configurations [54, 55, 81].

2.4 Simulation Results

The model, described in the previous section, is used to simulate the demultiplexing of a 10 or 40 Gb/s channel out of a 160 Gb/s OTDM signal. An incoming 160 Gb/s signal at $\lambda_1 = 1550$ nm and a 10 or 40 GHz optical clock signal at $\lambda_2 = 1540$ nm are injected into the EAM. First the switching window is investigated by analyzing the static operation. A continuous wave (CW) at $\lambda_1 = 1550$ nm signal is co-propagating with a $\lambda_2 = 1540$ nm clock signal. The incremental step in the length of the EAM in the simulations is $dz = 5\mu$m. Figure 2.5 shows the switching windows for three different clock pulses. The power of the CW signal is 0 dBm. The energy of the clock-pulses is 1.1 pJ, corresponding to a 10.5 dBm average power for the 10 GHz and 16.5 dBm average power for a 40 GHz clock signal. The clock pulses are secant-

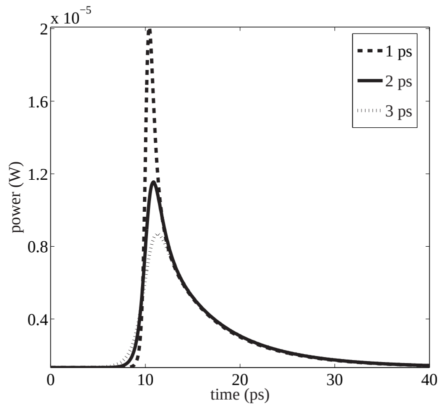

Figure 2.5: The switching window created with a 1, 2 and 3 ps clock pulse. $P_{CW} = 0$ dBm, co-propagating signal and the average power of the clock signal is 10.5 dBm. Length of the active region of the EAM is 150 μm.

shaped and their widths are respectively 1, 2 and 3 ps at full width half maximum (FWHM). The corresponding switching windows are 1.8 ps, 4.6 ps and 7 ps FWHM. We can deduce from Figure 2.5 that the switching window becomes smaller when using shorter clock pulses. The disadvantage of the switching windows from Figure 2.5 is the large tail, which complicates the suppression of the adjacent channel. The tail originates from the carrier sweep-out time, which limits the recovery speed of the absorption. An example of an eye-diagram of a demultiplexed signal is shown in Figure 2.6. The clock signal is at 40 GHz and the power of the pulse is 1.6 pJ. This power is not high enough to create a high contrast gate for the targeted channel. An increased saturation of the absorption is required for an increased contrast ratio between the targeted channel and the adjacent channels. By increasing the power of the clock signal, the saturation of the absorption is increased and the targeted channel is less absorbed, resulting in a higher contrast of the switching gate leading to a higher suppression ratio of the non-targeted channels. The relation between the channel suppression ratio and the power of the clock signal is shown in Figure 2.7(a) for co- and counter-propagating operation.

The length of the active region in this simulation is chosen to be 150 μm and the pulse width of the clock signal is 1.7 ps, corresponding to the actual pulse width in the experiments. The input power of the OTDM data signal is 3 dBm and the pulse width is 2 ps. The channel suppression ratio is the ratio between the minimum of the targeted drop channel and the maximum non-targeted drop channel. The optimum clock power for both operation modes is around 17 dBm for a 10 Gb/s base rate and 23 dBm for a 40 Gb/s base rate. This corresponds to an energy per clock pulse of 5 pJ. This high power is required to bleach the absorption. The channel suppression ratio increases with increasing clock power until a certain optimum value. The decrease of the suppression ratio for a further increase of the input power is caused by

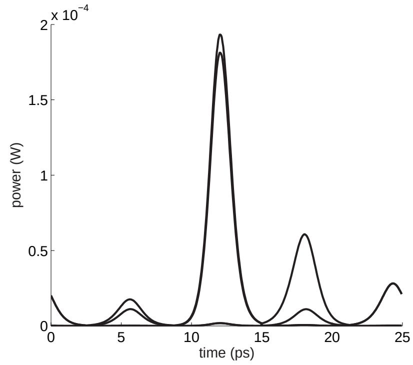

Figure 2.6: Eye diagram of the demultiplexed 40 Gb/s channel. Clock pulses are 1.6 pJ, which corresponds to a 18 dBm average power.

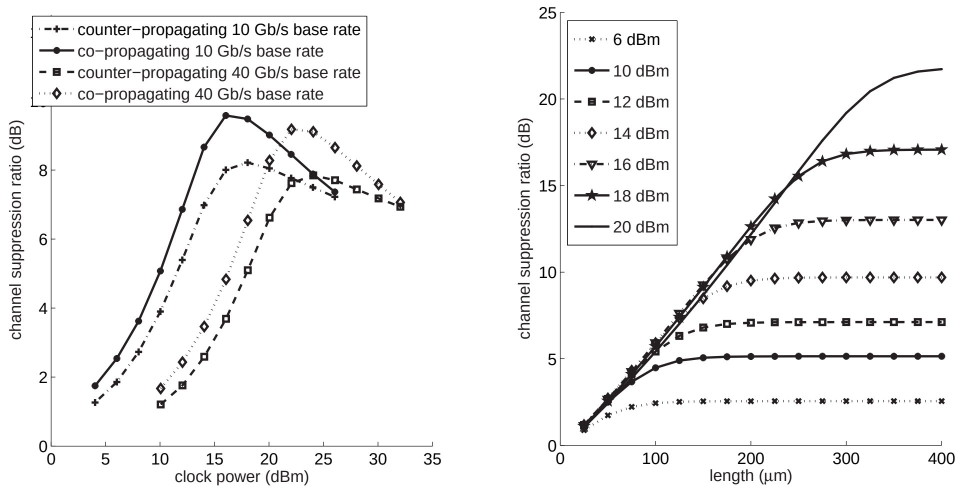

(a) Clock power versus channel suppression ratio (b) Length active region versus channel suppression ratio

Figure 2.7: Average clock power versus the channel suppression ratio (a), where the length of the active region of the EAM is 150 μm. The channel suppression ratio versus the length of the active region of the EAM, for co-propagating operation is shown in (b) for several different average clock powers.

the longer recovery time due to a stronger saturation of the absorption. A comparison between co- and counter-propagating operation shows the best performance for co-propagating operation, because of the longer interaction time between signal and clock pulses. Figure 2.7(b) shows the channel suppression ratio for several values of the average clock power as a function of the length of the active region of the EAM for co-propagating operation. Similar results are obtained for counter-propagating operation. As expected, the improvement of suppression ratio levels out after a particular length of the active region, when the power of the clock pulse decreases to a level where the absorption is no longer influenced. To obtain suppression ratios of 20 dB or higher for co-propagating operation the optimal length of the EAM is larger than 300 μm and the average clock power is 20 dBm or higher.

2.5 Experimental Results

The experimental setup is shown in Figure 2.8. The transmitter consists of a commercial mode-locked laser (MLL), which generates 2 ps FWHM pulses. A Mach-Zehnder modulator operated at 9.9853 Gb/s with a 2^7-1 pseudo random bit sequence (PRBS) and a passive delay line multiplexer (MUX) to 80 or 160 Gb/s follows the MLL. A low PRBS word length is used out of practical perspective. The multiplexer is constructed out of couplers, where the signal is first split in two arms and one part is delayed with respect to the other before they are combined into one signal again. To guarantee a phase decorrelated signal at the output, the delay in one arm needs to be at least half the word length. Longer PRBS word lengths would therefore require longer delay lines inside the multiplexers, resulting in more costly and more unstable equipment. The signal is amplified by an Erbium-doped fiber amplifier (EDFA) to compensate for the losses in the MZI modulator and the multiplexing stages. A 5 nm optical band-pass filter (OBPF) is used to filter out part of the amplified spontaneous emission (ASE) noise of the EDFA. The clock signal enters the EAM in a counter-propagating direction via the circulator. Counter-propagating operation has been chosen to minimize the chances of damaging the EAM by injecting too much optical power at one of the facets. The gated OTDM channel at the base rate is then amplified by another EDFA and filtered with a 3 nm OBPF, before it is sent to the receiver and bit error rate (BER) test set.

The clock signal is derived from the same MLL source as the OTDM signal. However, to avoid interference between clock and data the wavelength is converted from 1550 nm to 1540 nm based on super continuum generation (SCG) in a 500 m long highly nonlinear fiber (HNLF). The experimental setup for this wavelength conversion is shown in Figure 2.9. The parameters of the HNLF are listed in Table A.1 in Appendix A. The average power at the input of the HNLF is 17 dBm. The spectrum of the input pulse is broadened and this so-called super continuum generated spectrum is sliced with a 5 nm OBPF with center frequency λ_c=1540 nm. The FWHM pulse width of 1.7 ps of the converted clock pulse is measured on an Agilent terascope with a bandwidth of 750 GHz. The measured pulse is shown in Figure 2.10. More information on SCG can be found in Appendix B.

The EAM used in the experiments is a commercially available device acquired from OKI (type OM5754C-30B). It allows a maximum injected optical peak power of 13 dBm power, which is a limiting factor for the performance of the EAM as an all-optical demultiplexer. Counter-propagating operation is used to minimize the chances of damaging the device due to a high input power. The clock power is step-by-step

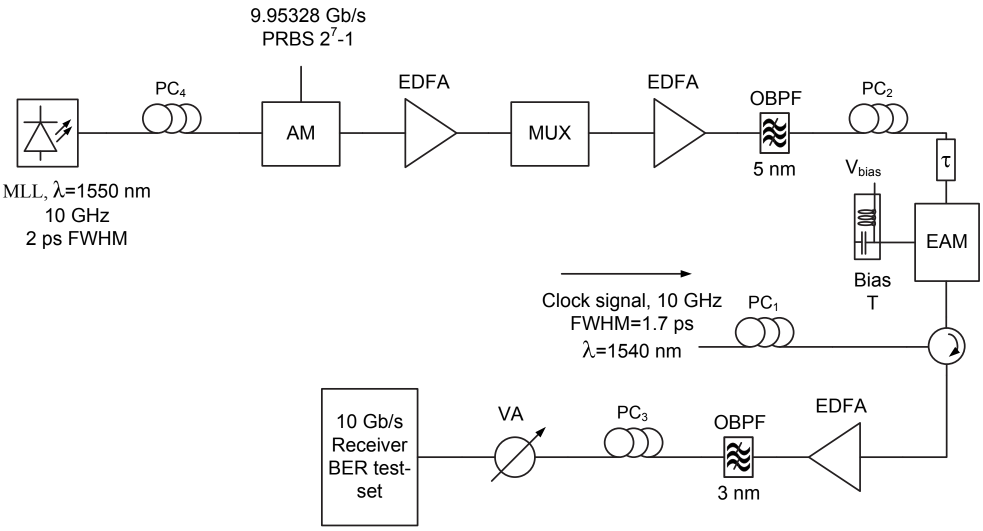

Figure 2.8: Experimental setup of the BER-measurement of the all-optical demultiplexing based on XAM in an EAM. AM: amplitude modulator, PC: polarization controller, VA: variable attenuator and τ: optical tuneable delay line

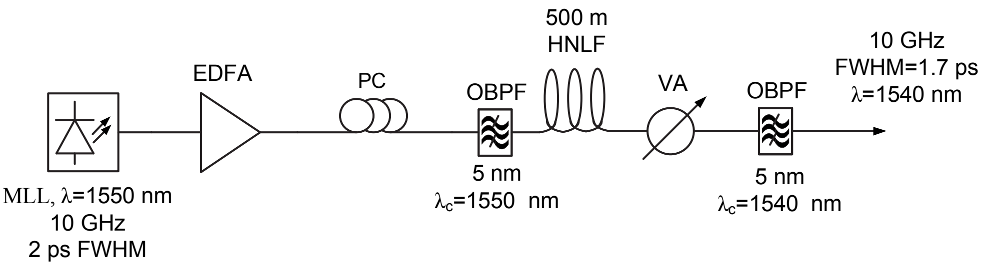

Figure 2.9: Wavelength conversion of the 10 GHz clock signal.

increased to a maximum value of 12 dBm average power, whereas we would have preferred a higher average input power considering the results of the simulations.

2.5.1 Switching Window

First the static characteristics of the EAM are considered before looking at the switching window. The output power versus the reverse bias for several wavelengths with 0 dBm input power is shown in Figure 2.11. This figure indicates that the longer wavelengths, close to the band edge have a relatively small absorption change, due to the relatively low density of states there. On the other hand, shorter wavelengths require more energetic pulses to bleach the absorption and a considerable amount

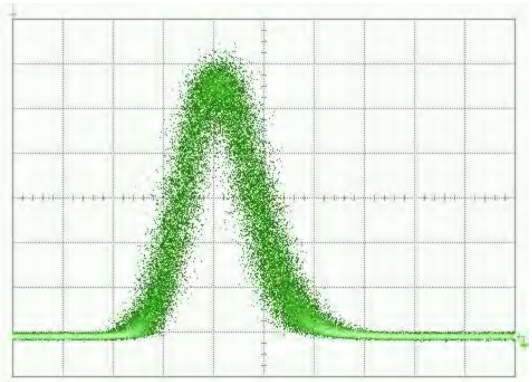

Figure 2.10: Super continuum generated pulse at 1540 nm, 1.7 ps FWHM, x-scale: 1 ps/div, y-scale: a.u.

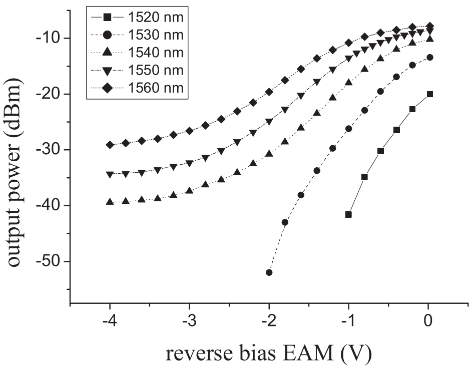

Figure 2.11: Static measurement of CW output power in [dBm] versus reverse bias voltage of the EAM in [V] for $P_{CW_{in}} = 0$ dBm and $\lambda_{CW} = 1520 - 1560$ nm.

of absorption is already observed at $V_{EAM} = 0$ V. Therefore, a trade-off has to be made between extinction ratio and a reasonable output power. A good extinction ratio and a reasonable output power are important for our OTDM signal, thus we chose 1550 nm. The clock signal is set to 1540 nm. The clock signal is required to be highly absorbed to have a large influence on the carrier density, creating a gate for the OTDM signal. The switching windows are analyzed by injection of a CW at 1550 nm and 2 dBm average power and an optical clock signal at 1540 nm and 10 dBm average power into the EAM. The acquired switching windows have been analyzed on the Agilent terascope. The width, rise times and fall times have been measured. The relation between the FWHM of the switching window and the reverse bias voltage of

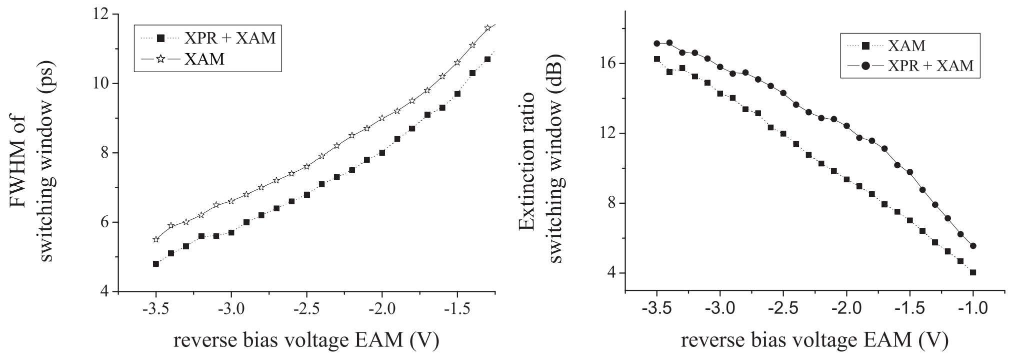

(a) Switching window versus channel reverse bias voltage

(b) Extinction ratio versus reverse bias voltage

Figure 2.12: Switching window (ps) (a) and the extinction ratio (dB) (b) of the switching window versus the reverse bias voltage of the EAM (V) for XAM and XPR+XAM.

the EAM is shown in Figure 2.12(a). A higher reverse bias voltage leads to a faster sweep-out of the photo-generated carriers in the active region of the EAM, because the electrical field working on the carriers is stronger. Therefore, increasing the reverse bias voltage reduces the width of the switching window. The switching window created by XPR+XAM in the EAM is compared with the switching window created by XAM only. The difference in switching window width is circa 1 ps and does not depend on the reverse bias voltage of the EAM. The extinction ratio of the switching window as a function of the reverse bias voltage of the EAM is shown in Figure 2.12(b). The extinction ratio of the switching window created by XPR+XAM has a 1 to 2 dB advantage compared to the switching window created by XAM only. A larger reverse bias voltage leads to a higher extinction ratio of the switching window, which results in a larger channel suppression ratio of the non-targeted channels. The simulations reveal a suppression ratio of 5 dB at a 10 dBm clock power for the length of the active region: $L \geq 150\mu$m. The extinction ratio of the switching window is not exactly the same as the channel suppression ratio. A large tail in the switching window would decrease the channel suppression ratio, but not the extinction ratio of the switching window. Therefore, we have also investigated the tail in the switching window. The total recovery time of the carriers, which corresponds to a tail in the switching window, is equal for the XAM method and the XPR+XAM method. To analyze the tail of the switching window we measured the fall and rise times. The results are shown in Figure 2.13. The fall time is defined as the time to go from the 90%-point on the transition to the 10%-point, and the rise time is defined as the time to go from the 10%-point on the transition to the 90%-point. The minimum fall time for XAM and XPR+XAM is respectively 3.2 and 2.5 ps at V_{EAM} = -3.5 V. The rise time, however, does not strongly depend on the reverse bias voltage of the EAM, as can be seen in Figure 2.13. Increasing the speed of operation of the EAM as all-optical switch requires an increase in reverse bias voltage of the EAM. However, the

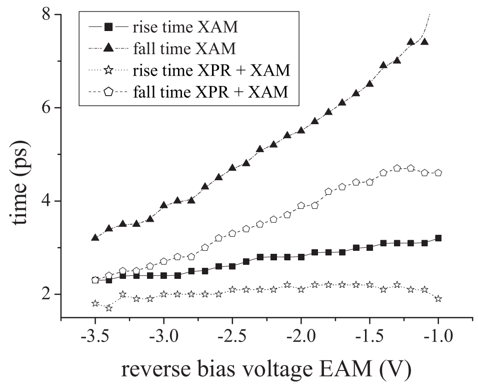

Figure 2.13: Fall and rise times of the switching windows versus the reverse bias voltage of the EAM, P_{CLOCK}=12 dBm and λ_{CLOCK} = 1540 nm, P_{CW} = 2 dBm and λ_{CW} = 1550 nm.

disadvantage is that the absorption in the EAM is also increased and higher optical power is required to saturate the absorption. Therefore, a careful trade-off has to be made for the optimum reverse bias voltage. A specific optimum reverse bias voltage is given in the sections 2.5.2 and 2.5.3 that describe the experimental demultiplexing results.

2.5.2 80 to 10 Gb/s Demultiplexing

For demultiplexing from 80 to 10 Gb/s we compared the demultiplexed channel with the original 10 Gb/s signal, the back-to-back (B2B) signal. Both demultiplexing methods, XAM and XPR+XAM are considered. The average input powers coupled into the EAM were P_{CLOCK} = 12 dBm and P_{OTDM}= 2 dBm. After passing through the EAM the signal is first amplified by an EDFA. This is necessary because the EAM is operating in the absorption regime and the received signal power is around -20 dBm. The amplified signal is filtered and attenuated in order not to overload the receiver. During the optimization of the BER, a careful tuning of the reverse bias voltage of the EAM led to best performance at V_{EAM}= -1.9 V. In Figure 2.14 the eye-diagrams of the demultiplexed channels for both XAM and XPR+XAM are shown. The difference observed between the two methods can be seen by looking at the suppression ratio of the remaining non-targeted channels. Another difference is a much lower received optical power for the XPR+XAM method. As the rotation of the polarization is about 10° to 15°, a large part of the signal power is blocked at the PBS. The experimental results are compared with the developed simulation model, with input parameters L = 150 μm, P_{CLOCK} = 12 dBm, pulse width T_{CLOCK}=1.7 ps and in counter-propagating operation. The result of this simulation is visualized in Figure 2.15. A suppression ratio of about 8.3 dB of the adjacent channel is obtained in the simulations. This

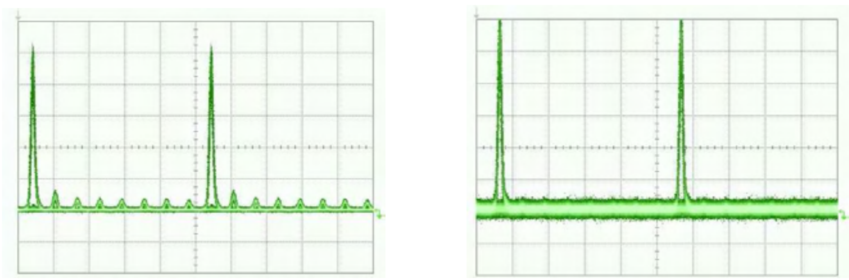

(a) The XAM (b) The XPR+XAM

Figure 2.14: The demultiplexed channel from 80 to 10 Gb/s for XAM and for XPR+XAM in the EAM. x-scale: 20 ps/div, y-scale: a.u.

simulation result is very close to the experimentally measured value of 10 dB. A BER measurement assessed the performance of the all-optical demultiplexer. We used the 10 Gb/s return-to-zero (RZ) signal in a B2B BER measurement, as a reference for the dropped channels. Figure 2.16 summarizes the measured BER performances for all eight channels. The average sensitivity penalty for BER of 10^{-9} is 6.7 dB for XPR+XAM and 7.9 dB for XAM. The penalty is due to the ASE noise of the EDFAs and foremost the incomplete removal of the non-targeted channels. Although ASE can be filtered, filtering can never remove the ASE noise that occupies the same spectral region as the signal. If we could increase the clock input power beyond the limit of 13 dBm damage level of the EAM, an improvement of the suppression ratio of the non-targeted channels and a reduction of the sensitivity penalty is expected.

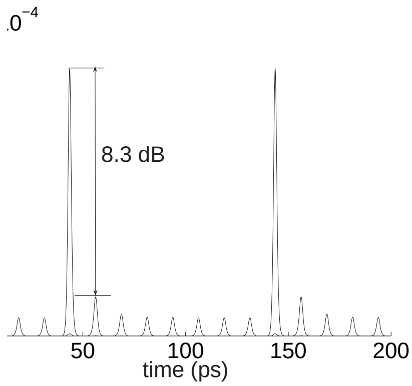

Figure 2.15: Simulation result of demultiplexing 80 to 10 Gb/s based on XAM.

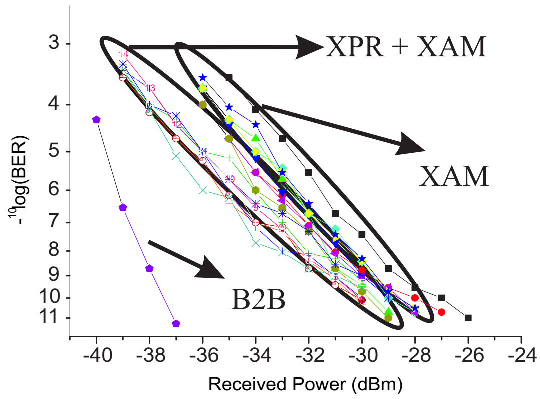

Figure 2.16: The BER performance of demultiplexing from 80 to 10 Gb/s for all the eight channels based on XPR+XAM and XAM compared to the B2B measurement

2.5.3 160 to 10 Gb/s Demultiplexing

As demultiplexing from 80 to 10 Gb/s was demonstrated to be error free, the next step is to examine demultiplexing from 160 to 10 Gb/s. The input powers to the EAM were P_{CLOCK}= 12 dBm and P_{OTDM}= 6 dBm. After passing through the EAM the signal is first amplified by an EDFA. This signal is filtered and attenuated in order not to overload the receiver. During the optimization of the BER, careful tuning of the bias voltage of the EAM led to best performance at V_{EAM}= -2.8 V. The change in V_{EAM} to a higher reverse bias voltages leads to a faster response time resulting in a smaller switching window. The power of the OTDM input signal injected into the EAM is increased from 2 to 6 dBm to obtain a reasonable signal-to-noise ratio (SNR) at the output, as the absorption at V_{EAM}= -2.8 V is larger than at -1.9 V. The demultiplexed eye-diagrams for XAM and XPR+XAM are shown in Figure 2.17. We

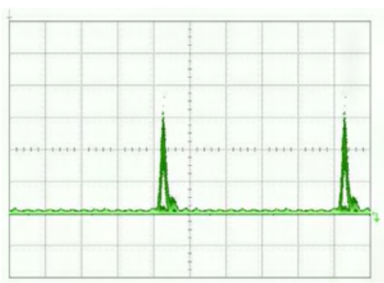

(a) The XAM

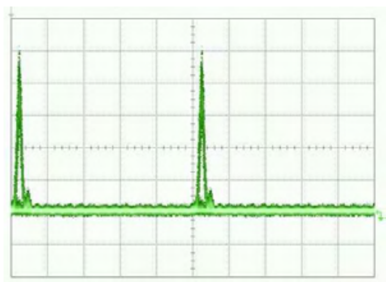

(b) The XPR+XAM

Figure 2.17: The demultiplexed channel from 160 to 10 Gb/s for XAM and for XPR+XAM in the EAM. X-scale: 20 ps/div, y-scale: a.u.

observed an error floor of 10^{-7}, mainly caused by the insufficiently small switching window. This is indicated by the small suppression ratio of the adjacent channel. The experimental results are compared with the simulation results from the model described in section 2.3. The simulation result is visualized in Figure 2.18. The

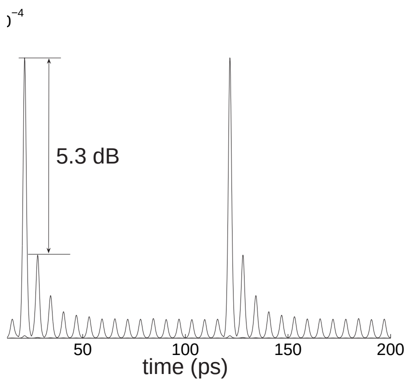

Figure 2.18: Simulation result of demultiplexing from 160 to 10 Gb/s based on XAM.

suppression of the adjacent channel in the simulations is 5.3 dB. The simulations are in good agreement with the experimental results. If we could increase the input power beyond the 13 dBm damage level to about 17 dBm higher suppression ratios of non-targeted channels can be expected. We expect based on the results obtained from our simulation model that an increase of the input power will lead to error free demultiplexing. Although a small penalty for the insufficiently small switching window is still expected.

2.6 Conclusion

A comprehensive study on cross-absorption modulation (XAM) in an electroabsorption modulator (EAM) has been performed. A model has been developed based on propagation equations to simulate the XAM effect in the EAM. The model includes an absorption coefficient, which is determined via a function of carrier distributions in the active region. The effects of spectral-hole burning (SHB) and carrier cooling are also taken into account. Good agreement between the experimental results and the theoretical model of the EAM has been shown. We have demonstrated error-free demultiplexing from 80 to 10 Gb/s based on XAM in a commercially available EAM. We also introduced the concept of cross-polarization rotation (XPR) to increase the extinction ratio of the XAM-based demultiplexer. However, we did not observe a significant improvement by using XPR, only a 1.2 dB sensitivity improvement is observed. In addition, it introduces polarization sensitivity to the demultiplexing configuration. Furthermore, we have studied the feasibility of using this method at 160 Gb/s.

The performance of the EAM as all-optical demultiplexer is strongly dependent on the maximum non-destructive input power. With a higher clock power the saturation effect of the absorption will be stronger. Stronger absorption saturation leads also to an increased induced birefringence change resulting in a larger rotation of the polarization. The operation speed of the EAM as demultiplexer in an all-optical configuration is limited by the carrier recovery time. Increasing the reverse bias voltage shortens the recovery time. However, this leads to an increase in absorption, which requires a higher input power to saturate the absorption, otherwise degradation of the SNR is unavoidable. In [68] demultiplexing from 160 to 10 Gb/s in co-propagating operation has been shown using a 2.3 ps pulse with 16.3 dBm average power, in a XAM optimized EAM structure. The requirement for high input power is also expected from our simulation model; however, we were severely limited by the maximum non-destructible input power of the commercially available EAM, besides our EAM is optimized for external modulation and not for XAM. All-optical demultiplexing with the available EAM and the limit of 13 dBm input power has limited us to demultiplexing from 160 to 10 Gb/s with an error floor of about 10^{-7}. When there is a 40 GHz RF signal available a suitable 160 to 40 Gb/s add-drop multiplexing [35] with traveling wave EAMs has been shown feasible.

An optically pumped EAM can also be used in a MZI structure [81]. The advantage of using EAMs in a MZI structure instead of the conventional SOA-based MZI is the passive nature of this switch, eliminating the SOA induced noise. Moreover, the recovery time of a reverse biased EAM in the order of tens of picoseconds is much faster than the 100 ps recovery time of the SOA, making the EAM-based MZI attractive for ultrafast optical switching.

Chapter 3

Fiber Characteristics

An essential component in an optical communication system is the fiber. The fiber is mainly used as optical waveguide for low loss transmission of optical signals. Besides as a transmission medium the fiber can also be employed as nonlinear medium in an all-optical switch. It takes advantage of the ultrafast response time of the Kerr nonlinearity that lies in the order of a few femtoseconds. This ensures a fiber to be a good candidate as nonlinear medium in a time domain all-optical add-drop multiplexer (ADM). The disadvantage of using a fiber as nonlinear element is the relatively long interaction length that is required compared to semiconductor materials. However, advances in production technology of highly nonlinear fiber (HNLF) made it possible to construct fiber-based switches with fibers of only 1 meter [44, 82], which reduces the size of the switch considerably. In our all-optical ADM configurations a HNLF of several hundreds of meters is employed.

In this chapter the fundamentals of fiber nonlinearities are addressed. A complete theoretical study of the nonlinear effects is beyond the scope of this work. Therefore, only the pulse propagation through a fiber and the different nonlinear phenomena that influence the optical waves are shortly described. We start with describing the wave equation and the pulse propagation inside an optical fiber. Moreover, the influence of the nonlinearities on this wave equation is examined in section 3.1. In section 3.2 the effects of dispersion are described. The origin of chromatic dispersion and the effect of pulse walk-off and polarization mode dispersion (PMD) are discussed. There are two categories of nonlinearities in the fiber.

In the first category of nonlinearities, no energy is transferred between the electromagnetic field and the dielectric medium, as would occur if frequencies were tuned near the resonance frequency of the fiber. Nonlinear interactions in this category (involving electron oscillations) are extremely fast by nature, therefore enabling the assumption of a medium response that is essentially instantaneous with the applied electromagnetic field. These processes are called nonresonant. Nonresonant processes can be described as an intensity dependent variation in the refractive index of silica fiber, commonly described as the Kerr effect, described in section 3.3. Examples of phenomena associated with the Kerr effect discussed in this chapter are self-phase modulation (SPM) in section 3.3.1, cross-phase modulation (XPM) in section 3.3.2

and four-wave mixing (FWM) in section 3.3.3.

The second category are the resonant processes, also referred to as the nonlinear inelastic scattering processes. In inelastic scattering processes the optical field transfers part of its energy to the nonlinear medium. Two examples of inelastic scattering processes are stimulated Raman scattering (SRS) and stimulated Brillouin scattering (SBS). As these nonlinear inelastic scattering processes do not play an important role in the all-optical ADMs employed in this work, the theory of these nonlinearities is refrained from this chapter. More information on inelastic scattering processes can be found in [83, 84].

3.1 Pulse Propagation

To understand the propagation of light in a fiber it is necessary to have fundamental knowledge of the way the electromagnetic fields of a light wave propagate in such a medium. Dispersion and nonlinearities influence the propagation. In this section, we include the dispersion and nonlinearities in the wave equation and derive an expression for the propagation of pulses through a fiber. Moreover, a description of the nonlinear coefficient γ is given and the relation between γ, the nonlinear refractive index n_2, the dielectric constant ϵ_r and the third order susceptibility $\chi^{(3)}$ is shown. The wave equation, which describes the phenomenon of light propagation through a fiber is given by [83]:

$$\nabla \times \nabla \times \underline{E}(\underline{r}, t) = -\frac{1}{c^2}\frac{\partial^2 \underline{E}(\underline{r}, t)}{\partial t^2} - \mu_0 \frac{\partial^2 \underline{P}(\underline{r}, t)}{\partial t^2} \tag{3.1}$$

where $\underline{E}(\underline{r}, t)$ is the electric field vector, $\underline{P}(\underline{r}, t)$ is the dielectric polarization vector, $c = 1/\sqrt{\mu_0 \epsilon_0}$ is the speed of light in vacuum, ϵ_0 is the vacuum permittivity and μ_0 is the vacuum permeability. This equation is often simplified by $\nabla \times \nabla \times \underline{E} = \nabla(\nabla \cdot \underline{E}) - \nabla^2 \underline{E} = -\nabla^2 \underline{E}$, under the assumption that the fiber medium is homogeneous and that ϵ and μ ($\mu_r \approx 1$ in an optical fiber) do not depend on the spatial coordinates. In general the evaluation of $\underline{P}(\underline{r}, t)$ requires a quantum mechanical approach. However when the optical frequency is far away from the resonance frequency of the medium, the dielectric polarization vector $\underline{P}(\underline{r}, t)$ can be described in a phenomenological way as a power series of the electric field vector $\underline{E}(\underline{r}, t)$ by:

$$\begin{aligned} \underline{P}(\underline{r}, t) &= \epsilon_0 \left(\chi^{(1)} \underline{E}(\underline{r}, t) + \chi^{(2)} \underline{E}^2(\underline{r}, t) + \chi^{(3)} \underline{E}^3(\underline{r}, t) + ... \right) \\ &= \underline{P}_L(\underline{r}, t) + \underline{P}_{NL}(\underline{r}, t) \end{aligned} \tag{3.2}$$

where $\chi^{(n)}$ is the n^{th}-order susceptibility tensor, a tensor of rank $n+1$, which is a material coefficient that is independent of the electric field $\underline{E}(\underline{r}, t)$. The coefficient $\chi^{(1)}$ is a second-rank tensor. It determines the linear part of the polarization P_L. The second and higher terms in equation (3.2) are referred to as the nonlinear polarization P_{NL}. Most work in nonlinear optics involves $\chi^{(2)}$ or $\chi^{(3)}$. Higher order processes are in general extremely weak and will therefore not be considered in this work. The susceptibilities $\chi^{(2)}$ and $\chi^{(3)}$ are third and fourth rank tensors and contain therefore respectively 27 and 81 different terms. The nonlinear polarization induced by $\chi^{(2)}$, also called quadratic nonlinear response, becomes zero in a medium with inversion symmetry such as an optical fiber. The nonlinear polarization induced by $\chi^{(3)}$, also called the cubic nonlinear response, in optical fiber can be reduced to one independent term [83, 84]. Now the linear and nonlinear polarization can be expressed as:

$$\underline{P}_L(\underline{r}, t) = \epsilon_0 \chi^{(1)} \underline{E}(\underline{r}, t) \tag{3.3}$$

$$\underline{P}_{NL}(\underline{r}, t) = \epsilon_0 \chi^{(3)} \underline{E}(\underline{r}, t)\underline{E}(\underline{r}, t)\underline{E}(\underline{r}, t) \tag{3.4}$$

By inserting equation (3.2) and (3.3) into equation (3.1), the wave equation is described as a partial differential equation dependent on $\underline{P}_{NL}(\underline{r}, t)$:

$$\nabla^2 \underline{E}(\underline{r}, t) - \frac{1}{c^2}\frac{\partial^2 \underline{E}(\underline{r}, t)}{\partial t^2} - \mu_0 \epsilon_0 \chi^{(1)} \frac{\partial^2 \underline{E}(\underline{r}, t)}{\partial t^2} = \mu_0 \frac{\partial^2 \underline{P}_{NL}(\underline{r}, t)}{\partial t^2} \tag{3.5}$$

By substituting the linear part of the dielectric constant $\epsilon_L = 1 + \chi^{(1)}$ into equation (3.5), it transforms into:

$$\nabla^2 \underline{E}(r, t) - \mu_0 \epsilon_L \epsilon_0 \frac{\partial^2 \underline{E}(r, t)}{\partial t^2} = \mu_0 \frac{\partial^2 \underline{P}_{NL}(r, t)}{\partial t^2} \tag{3.6}$$

When equation (3.4) is substituted into equation (3.6) a term oscillating at ω_0 and a term oscillating at $3\omega_0$ is found (ω_0 is the central frequency of the pulse spectrum). This third-harmonic frequency requires phase matching and is generally negligible in optical fibers. Therefore, the nonlinear polarization can be written as:

$$\underline{P}_{NL}(\underline{r}, t) \approx \epsilon_0 \epsilon_{NL} \underline{E}(\underline{r}, t) \tag{3.7}$$

with the nonlinear part of the dielectric constant given by:

$$\epsilon_{NL} = \frac{3}{4}\chi^{(3)} |\underline{E}(\underline{r}, t)|^2 \tag{3.8}$$

The wave equation can now be written as:

$$\nabla^2 \underline{E}(\underline{r}, t) - \mu_0 \epsilon_r \epsilon_0 \frac{\partial^2 \underline{E}(\underline{r}, t)}{\partial t^2} = 0 \tag{3.9}$$

with the dielectric constant (ϵ_r) given by: $\epsilon_r = \epsilon_L + \epsilon_{NL}$. In the slowly varying envelope approximation it is useful to separate the rapidly varying part of the electric field from the slowly varying part. Assuming x polarization, the electric field is written in the form:

$$\underline{E}(\underline{r}, t) = \frac{1}{2} E_{SV}(\underline{r}, t) \exp(-i\omega_0 t) \underline{a}_x + c.c. \tag{3.10}$$

where $E_{SV}(\underline{r}, t)$ is the slowly varying part of the electric field and $\underline{a}_x$ is the unity vector in the x-direction. The complex conjugate terms are included because the fields are real and otherwise important nonlinear terms would be missing without them [84]. To analyze the wave equation for the slowly varying field $E_{SV}(\underline{r}, t)$ it is more convenient to work in the frequency domain.

$$\tilde{E}_{SV}(\underline{r}, \omega - \omega_0) = \int_{\infty}^{\infty} E_{SV}(\underline{r}, t) \exp\left(i(\omega - \omega_0)t\right) dt \tag{3.11}$$

The wave equation can now be written in the frequency domain as:

$$\nabla^2 \tilde{E}_{SV} + \epsilon_r(\omega) k_0^2 \tilde{E}_{SV} = 0 \tag{3.12}$$

where $k_0 = \omega/c$ is the propagation constant and $\epsilon_r(\omega)$ is the frequency dependent dielectric constant. In an optical fiber the relation between the refractive index and the dielectric constant can be written as:

$$n = \sqrt{\epsilon_r} \tag{3.13}$$

The refractive index n is intensity dependent because of the dependence on ϵ_{NL}:

$$n(I) = n_0 + n_2 \cdot I \tag{3.14}$$

with I the intensity of the optical field in [W/m^2], and the linear refractive index n_0 given by:

$$n_0 = \sqrt{1 + Re(\chi^{(1)})} \tag{3.15}$$

and n_2 is the nonlinear refractive index, defined as:

$$n_2 = \frac{3}{8n_0} Re(\chi^{(3)}) \tag{3.16}$$

For the slowly varying field a solution is assumed of the form:

$$\tilde{E}_{SV}(\underline{r}, \omega - \omega_0) = F(x, y)\tilde{A}(z, \omega - \omega_0) \exp(i\beta_0 z) \tag{3.17}$$

where $\tilde{A}(z, \omega - \omega_0)$ is a slowly varying amplitude function in the z direction, $F(x, y)$ is the transverse distribution of the fundamental fiber mode and β_0 is the dispersion free part of the propagation coefficient. By using the inverse Fourier transform on equation (3.17) and substituting this into equation (3.10) the electric field can now be written as:

$$\underline{E}(\underline{r}, t) = \frac{1}{2} F(x, y) A(z, t) \exp(i(\beta_0 z - \omega_0 t)) + c.c. \tag{3.18}$$

where $A(z, t)$ is the slowly varying pulse envelope. In [83] is described how with the method of separation of variables an expression is found for the nonlinear Schrödinger equation (NLSE) that describes the propagation of optical signals in a fiber:

$$\frac{\partial A}{\partial z} + \frac{i\beta_2}{2}\frac{\partial^2 A}{\partial T^2} - \frac{\beta_3}{6}\frac{\partial^3 A}{\partial T^3} - i\frac{\beta_4}{24}\frac{\partial^4 A}{\partial T^4} + \frac{\alpha}{2} A = i\gamma|A|^2 A \tag{3.19}$$

where the retarded time frame $T = t - z/\nu_g$ is introduced to be able to describe the pulse peak as it propagates at group velocity ν_g, α is the attenuation constant and β_2, β_3 and β_4 are related to the second, third and fourth order dispersion coefficient, respectively. The group velocity if given by:

$$\nu_g = \left(\frac{d\beta}{d\omega}\right)^{-1} = \frac{1}{\beta_1} \tag{3.20}$$

The nonlinearity in the fiber is usually described by the nonlinear coefficient γ:

$$\gamma = \frac{n_2 \omega_0}{c A_{\text{eff}}} \tag{3.21}$$

where n_2 is the nonlinear refractive index given by equation (3.16) and A_{eff} is the effective cross-sectional area of the fiber.

3.2 Chromatic Dispersion

The refractive index of an optical fiber is dependent on the frequency of the light propagating through the fiber. This implies that different frequency components of a light pulse travel at different velocities. This effect is referred to as chromatic dispersion. The dispersion effects induced by the propagation through fiber can be given by the Taylor expansion of the phase constant β by:

$$\beta = \beta_0 + \beta_1(\omega - \omega_0) + \frac{\beta_2}{2}(\omega - \omega_0)^2 + \frac{\beta_3}{6}(\omega - \omega_0)^3 + \frac{\beta_4}{24}(\omega - \omega_0)^4 + ... \qquad (3.22)$$

with

$$\beta_m = \left(\frac{d^m \beta}{d\omega^m}\right)_{\omega=\omega_0} \qquad (m = 0, 1, 2, 3, ...) \qquad (3.23)$$

where ω_0 is the center frequency of the optical pulse. Second-, third-, and fourth-order dispersion arise from the terms including β_2, β_3 and β_4, respectively. The dispersion parameter most commonly used is D, expressed in [ps·nm^{-1}·km^{-1}]. The dispersion parameter D can be seen as the amount of broadening in picoseconds that would occur in a pulse with a bandwidth of 1 nm while propagating through 1 km of fiber. The dispersion coefficient D is given by:

$$D = \frac{d\beta_1}{d\lambda} = -\frac{2\pi c}{\lambda^2}\beta_2 \qquad [\mathrm{ps \cdot nm^{-1} \cdot km^{-1}}] \qquad (3.24)$$

For pulses shorter than 1 ps, it is necessary to include the contribution of β_3 to the dispersion effects even when $\beta_2 \neq 0$. The third order dispersion (TOD) is normally described by the dispersion slope parameter S:

$$S = \frac{4\pi c}{\lambda^3}\beta_2 + \left(\frac{2\pi c}{\lambda^2}\right)^2 \beta_3 \qquad [\mathrm{ps \cdot nm^{-2} \cdot km^{-1}}] \qquad (3.25)$$

In very high speed OTDM systems, the pulse width is very short ($<$ 1ps) and under certain circumstances the fourth order dispersion (FOD) becomes important as well [85]. The FOD is covered by β_4. The second order dispersion (SOD), TOD and FOD are included in the NLSE given in equation (3.19).

3.2.1 Pulse Walk-Off

An important feature of chromatic dispersion is the walk-off between pulses at two wavelengths λ_1 and λ_2. Due to a mismatch in group velocity the pulses propagate at different speeds inside the fiber. Walk-off between two signals is expressed by the walk-off parameter d_{12}:

$$d_{12} = \beta_{11} - \beta_{12} = \frac{1}{\nu_{g1}} - \frac{1}{\nu_{g2}} \qquad [\mathrm{s/m}] \qquad (3.26)$$

where ν_{g1} and ν_{g2} are the group velocities of the two signals. The walk-off length L_W is often used to clarify the distance when the two pulses separate totally and is defined by:

$$L_W = \frac{T_0}{|d_{12}|} \qquad (3.27)$$

where T_0 is the pulse width. For our fiber-based ADM configurations it is important to know the difference in propagation time between control and data pulses at the end of the fiber. This is referred to as the walk-off time: t_w. The walk-off time between the two wavelengths λ_1 and λ_2 is given by the length of the fiber and the difference in group velocities at the given wavelengths:

$$t_w = L \cdot |d_{12}| \tag{3.28}$$

In the normal dispersion region ($\beta_2 > 0$), a longer wavelength pulse travels faster, while the opposite occurs in the anomalous dispersion region. The parameters of our HNLF indicate a value for the dispersion and dispersion slope at 1550 nm (see appendix A). When a constant dispersion slope is assumed over the whole C-band (1530-1565 nm), the dispersion parameter is given by:

$$D(\lambda) = D_{1550} - S_{1550} \cdot (1550 \cdot 10^{-9} - \lambda) \tag{3.29}$$

The first order dispersion parameter $\beta_1 = \frac{1}{\nu_g}$ is deduced by substituting equation (3.29) into equation (3.24):

$$\beta_1(\lambda) = \left(D_{1550} - S_{1550} \cdot 1550 \cdot 10^{-9} + \frac{1}{2} S_{1550} \cdot \lambda \right) \lambda + c \tag{3.30}$$

where c is a constant. Substituting equation (3.29) and (3.30) into equation (3.28) gives us the following equation for the walk-off time between two pulses at two different wavelengths:

$$\begin{aligned} t_w = L\Big(& D_{1550}(\lambda_2 - \lambda_1) - S_{1550} \cdot 1550 \cdot 10^{-9} \cdot \\ & (\lambda_2 - \lambda_1) + \frac{1}{2} S_{1550} \cdot (\lambda_2^2 - \lambda_1^2)\Big) \end{aligned} \tag{3.31}$$

For example, two signals, $\lambda_1 = 1545$ nm and $\lambda_2 = 1565$ nm, co-propagating through HNLF$_1$, whose parameters are listed in Table A.1. The zero dispersion wavelength of HNLF$_1$ is $\lambda_0 = 1545$ nm, the length is $L = 0.5$ km and the value of the dispersion and dispersion slope at 1550 nm are $D_{1550} = 0.13$ ps·nm^{-1}·km^{-1} and $S_{1550} = 0.03$ ps·nm^{-2}·km^{-1}. Substituting these values into equation (3.31) results in a walk-off time of 2.8 ps.

3.2.2 Polarization Mode Dispersion

A single mode fiber (SMF) supports the propagation of two polarized modes in orthogonal directions. When the core of the fiber shows slight asymmetry in geometry and/or refractive index (birefringence), the light traveling along one polarization axis travels faster (fast axis), while it travels slower along the other axis (slow axis). This effect is called polarization mode dispersion (PMD) and results in pulse broadening and eventually in pulse break up. PMD has been extensively studied for long-haul systems, but is increasingly important for high bit rate OTDM systems, because the OTDM signal itself consists of short pulses that will be easily broadened by PMD [86]. The difference in propagation time between the slow and fast axis at the end

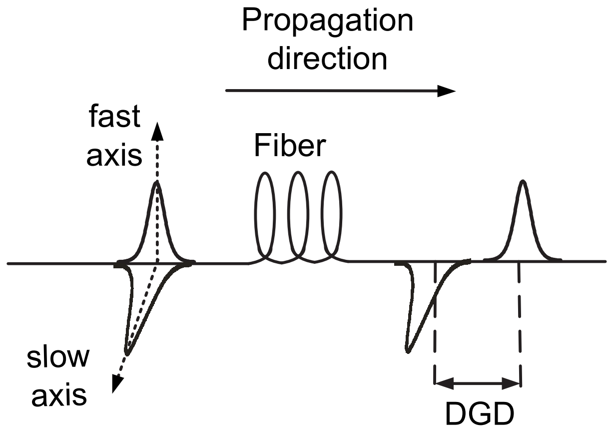

Figure 3.1: The polarization mode along the fast axis travels faster than the polarization mode along the slow axis. The difference in propagation time is given by the differential group delay (DGD).

of the fiber is given by $\Delta\tau$, which is more commonly referred to as the differential group delay (DGD). This effect is schematically shown in Figure 3.1. This effect can be understood if we assume that an incoming pulse is subdivided into two principle states of polarization (PSP) that do not change due to PMD. Both principle states of polarization experience a different refractive index due to birefringence and will therefore travel at a different speed. The difference in arrival time for the so called slow and fast axis after traveling through a fiber of length L is given by [83]:

$$\Delta\tau = \left| \frac{L}{\nu_{gx}} - \frac{L}{\nu_{gy}} \right| = L|\beta_{1x} - \beta_{1y}| \tag{3.32}$$

where $\nu_{gx} = 1/\beta_{1x}$ and $\nu_{gy} = 1/\beta_{1y}$ are the group velocities of both polarization modes. Random changes over the fiber make it more useful to describe the PMD by the root-mean-square (RMS) value of $\Delta\tau$ after averaging over these random perturbations. Usually, not the root-mean-square (RMS) value of $\Delta\tau$ is given, but the PMD parameter D_p. The relation between the root-mean-square (RMS) value of $\Delta\tau$ and D_p is:

$$D_p = \sqrt{\frac{\langle(\Delta\tau)^2\rangle}{L}} \qquad [\mathrm{ps}/\sqrt{\mathrm{km}}] \tag{3.33}$$

The PMD values of the fibers used in our all-optical time domain ADMs are listed in Appendix A. For uniformly birefringent fibers the DGD can be assumed constant and is defined as the first order PMD. In practise, the DGD as well as the PSPs both randomly vary with the wavelength. This is the origin of higher order PMD. Besides wavelength changes, also environmental changes like temperature changes, vibrations, bending and twisting make the DGD and PSP drift randomly in time. The best way to treat PMD is therefore by means of statistics. For sufficiently long

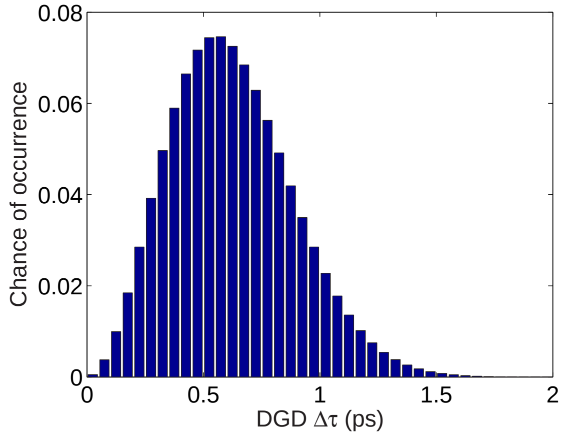

Figure 3.2: The chance of occurrence of a certain DGD value for an interval for $\langle\Delta\tau\rangle$=0.625 ps.

fibers, the statistical nature can be described by a Maxwellian distribution [87]:

$$p(\Delta\tau) = \frac{2\Delta\tau^2}{\sqrt{2\pi}q^3}\exp[-(\frac{\Delta\tau^2}{2q^2})] \tag{3.34}$$

where q^2 is the variance given by:

$$q^2 = \frac{\pi}{8}\langle\Delta\tau\rangle^2 \tag{3.35}$$

The variance of the PMD over the wavelength is commonly known as the second-order PMD. The bandwidth of the signal in combination with the wavelength dependence of the DGD determines the total impact of the second-order PMD. An example of the statistical distribution of the DGD is depicted in Figure 3.2.2. The chance that the actual DGD falls within an interval of 0.05 ps is indicated. In this example, the RMS value of $\Delta\tau$ is chosen to be $\langle\Delta\tau\rangle = 0.625$ ps, which corresponds to 10% of the bit slot time at 160 Gb/s.

The tolerance towards PMD has a direct relation with the employed modulation format. It has been shown that the PMD induced optical signal-to-noise ratio (OSNR) penalty tends to increase with the increase of the data signal duty cycle, because larger duty cycles lead to a larger PMD-induced intersymbol interference [88]. In the situation of similar duty cycles, systems employing the differential phase shift keying (DPSK) modulation format have an increased tolerance towards PMD compared to on-off keying (OOK) systems. Moreover, the balanced detector receiver for DPSK systems can cancel signal distortion to some extent [89]. The introduction of differential quadrature phase shift keying (DQPSK) increases the PMD tolerance even further. The increased PMD tolerance of DQPSK opens the possibilities to perform a 151x43 Gb/s WDM transmission experiment over 4,080 km [90], as well as a 2.56 Tb/s polarization multiplexed DQPSK-OTDM transmission experiment over 160 km [91].

Outage

It is common to quantify the impact of the PMD on the performance of an optical system by looking at the outage. The outage is defined as the probability that a system reaches an unacceptable penalty level, which can be measured by looking at the eye-opening, Q-factor or bit error rate (BER). Bearing in mind the dependence on the employed modulation format, on average it is stated that a PMD value equal to $15 \sim 22\%$ of the bit slot time is tolerable, measured at an outage probability of 10^{-4} with a 1 dB OSNR margin [92]. To be on the safe side, usually 10% of the bit slot time is taken as a rule of thumb for the PMD tolerance. Regarding a 160 Gb/s system with a 6.25 ps bit slot time this would imply a total PMD tolerance of 0.625 ps. Systems encompassing larger PMD values require some form of mitigation. A transmission system at 160 Gb/s system over a fiber with PMD parameter $D_p = 0.1\mathrm{ps}/\sqrt{\mathrm{km}}$ requires mitigation if the transmission distance is more than 39 km.

PMD mitigation

PMD mitigation techniques can be subdivided into three categories [92]. The first category includes passive mitigation techniques. Passive mitigation includes the usage of different modulation formats that are more robust against PMD, soliton transmission, forward error correction (FEC) and polarization scrambling. The second category includes electrical mitigation techniques like transversal filters and decision feedback equalizers. Electrical mitigation has been shown suitable for 10 Gb/s systems [93], but it is more difficult to realize for high speed OTDM signals. The third and last category comprises the optical PMD mitigation techniques. Optical mitigation techniques are designed to reverse the effects of PMD in a transmission link. The random nature of PMD requires adaptive compensation techniques. In general, the employment of adaptive compensation techniques demands for performance monitoring and a feedback signal in order to automatically track and compensate for the PMD. These monitoring/feedback signals can for example be based on the degree of polarization, or on the received RF spectrum. More information on the influence of PMD and mitigation techniques on high-speed optical fiber transmission can be found in [94].

3.3 Kerr Effect

The change of the refractive index of glass (n) in response to an optical field which travels through the glass is known as the Kerr effect. The Kerr effect is named after John Kerr, a Scottish physicist, who first discovered the effect in 1875. The dependence of the refractive index on the intensity of the optical signal is described by equation (3.14). The presence of the Kerr effect gives rise to a number of different nonlinear effects, depending on the optical field at the input of the fiber.

The nonlinear refractive index of a standard SMF is low. High switching power and long interaction lengths are usually required to obtain a sufficient nonlinear phase shift for all-optical switching. The typical value of the nonlinear refractive index coefficient for silica is $n_2 = 2.2 \cdot 10^{-20}$ m^2/W [83], which corresponds to $\gamma \approx 1.3$ W^{-1}km^{-1}. To decrease the required switching power and reduce the required interaction length an increase of the nonlinear coefficient of the fiber, given by equation (3.21), is required. A combination of the proper doping of the fiber core to increase n_2 and reducing the core size to decrease the size of the effective cross-sectional area A_{eff}, leads to an increase of the nonlinear coefficient γ. Various phenomena associated with the Kerr effect will be addressed here: SPM in section 3.3.1, XPM in section 3.3.2 and FWM in section 3.3.3.

3.3.1 Self-Phase Modulation

Self-phase modulation (SPM) is one of the nonlinear optical effects, which are induced by the Kerr effect. An intense light pulse that travels inside the fiber induces an intensity dependent change in the refractive index of the fiber. This results in an intensity dependent phase shift, as the optical pulse travels through the fiber. As a result, the frequency spectrum of the pulse is changed. SPM becomes an increasingly important effect in optical communication systems where short, intense pulses are employed, like in our experimental work on ADMs. The total phase shift imposed on an optical signal in a fiber varies with the distance z and is given by:

$$\phi(z,t) = n_0 z k_0 + n_2 \cdot I(t) k_0 z \tag{3.36}$$

The first term of equation (3.36) represents the linear phase shift and the second term represents the nonlinear phase shift. When the optical signal is intensity modulated, a phase modulation occurs due to the nonlinear phase shift. This effect is called SPM. The intensity of the optical field $I(t)$ is considered to be uniformly distributed across an effective cross-sectional area A_{eff}. The optical power is related to the intensity by:

$$P(t) = I(t) \cdot A_{\text{eff}} \tag{3.37}$$

To accurately describe the SPM induced phase shift, it is necessary to take the reduction of the optical power with the transmission length into account. The impact of the nonlinearity reduces with reduced optical power. To include transmission losses α in the description of SPM, it is common to introduce the effective length:

$$L_{\text{eff}} = \frac{1 - e^{-\alpha L}}{\alpha} \tag{3.38}$$

The SPM induced phase shift can now be described by:

$$\phi_{\text{SPM}} = \gamma P(t) L_{\text{eff}} \tag{3.39}$$

After propagation through a fiber the SPM induced phase shift caused a chirp on the transmitted field. The instant frequency of the optical field after transmission is given by:

$$\omega(t) = \omega_0 - \frac{d\phi(t)}{dt} = \omega_0 - \gamma L_{\text{eff}} \frac{dP(t)}{dt} \tag{3.40}$$

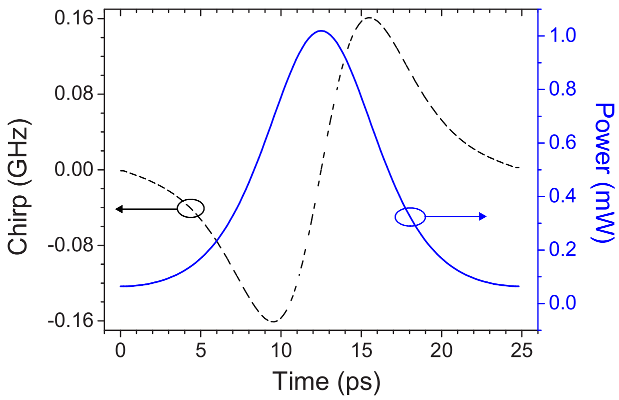

Figure 3.3: Chirp on a 2-ps pulse induced by SPM.

An example of the instant frequency change (=chirp) of a 2-ps secant-shaped pulse is shown in Figure 3.3 for transmission through 100 meter fiber with $\gamma = 15$ $\mathrm{W^{-1}km^{-1}}$, while neglecting the dispersion. The presence of a chirp causes a nonlinear broadening of the spectrum, which depends on the bandwidth and on the shape of the injected signal. SPM spectral broadening can enhance pulse broadening due to chromatic dispersion. But when the pulse propagates in the anomalous dispersion region ($\beta_2 < 0$) the combined effects of dispersion and SPM can be used for pulse compression or soliton propagation [95].

3.3.2 Cross-Phase Modulation

Cross-phase modulation (XPM) is the change of the phase of a light signal caused by the interaction with another light signal at a different wavelength. Compared to SPM the induced phase shift by XPM is two times as strong for co-polarized beams and 2/3 times as strong for orthogonal polarized beams. Therefore, the total nonlinear phase shift at the end of a fiber with length L can be written as:

$$\phi = n_2(I_s + bI_p)k_0 L_{\text{eff}} \tag{3.41}$$

where I_s and I_p are the intensities of the input signal and the pump signal. n_2 is the nonlinear refractive index, k_0 is the propagation constant and L_{eff} is the effective length. It is more common to express the phase shift in terms of optical power instead of intensity and to use the fiber nonlinear coefficient γ, which is related to the nonlinear refractive index n_2 (see equation (3.21)). Equation (3.41) then transforms into:

$$\phi = \gamma L_{\text{eff}}(P_s + bP_p) \tag{3.42}$$

The parameter b equals to 2 when the two light waves have different wavelengths but the same polarizations, and 2/3 when they have orthogonal polarizations. The first part in equation (3.42) refers to SPM and the second part refers to XPM. In equation (3.42) the dispersion effects, which would result in walk-off between control and data, are neglected.

When two pulse trains at different wavelengths are present in a fiber, the two pulses trains will walk-off and separate from each other due to dispersion (see section 3.2.1). The distance it takes two pulses to separate completely is given by the walk-off length L_W in equation (3.27). Therefore it can be concluded that XPM is only effective within a certain distance of the fiber: $L \leq L_W$. If two Gaussian pulses (with a width of T_0) co-propagate together, the maximum spectral broadening induced by XPM and taking the walk-off into account can be expressed by [83]:

$$\Delta\nu_{max} = \frac{\gamma P_p L_W}{\pi T_0} = \frac{\gamma P_p}{\pi |d_{12}|} \tag{3.43}$$

Here P_p is the peak power of the much stronger pump signal. The chirp is inversely proportional to the walk-off parameter ($d_{12} = \beta_{11} - \beta_{12}$). A small walk-off parameter relates to a long walk-off length, resulting in a long interaction time between the two pulse trains. To enhance the XPM induced phase change given by the second part of equation (3.42), this needs to be maximized. Because the nonlinear coefficient of the fiber is a parameter that cannot be changed, the only parameters that can be influenced are the effective length L_{eff} and the pump power P_p. One way to increase the effective length is to use Raman amplification. It has been shown that Raman amplification in fiber increases the effective length and therefore enhances the nonlinear processes that are dependent on L_{eff}, like e.g. XPM, SPM and FWM in fibers. By combining Raman amplification with EDFA amplification, the optical signal-to-noise ratio (OSNR) and extinction ratio of an XPM based wavelength converter in a fiber can be optimized [96].

3.3.3 Four-Wave Mixing

Four-wave mixing (FWM) is a parametric interaction among four waves satisfying a particular phase relationship, named phase matching. There are two distinct FWM processes. In one process, three photons are annihilated and a new photon is created at the sum frequency of the three photons.

$$\omega_4 = \omega_1 + \omega_2 + \omega_3 \tag{3.44}$$

Where ω_j (j=1,2,3,4) is the frequency of the optical wave j. In this case, the phase matching condition is:

$$k_1 + k_2 + k_3 - k_4 = 0 \tag{3.45}$$

where $k_j = n_j \omega_j / c$ is the propagation constant of wave j. In practice, the phase matching condition for this process is hard to satisfy in fiber. In the other process, two photons at ω_1 and ω_2 are absorbed and two photons are created at the Stokes and anti-Stokes bands:

$$\omega_3 + \omega_4 = \omega_1 + \omega_2 \tag{3.46}$$

The phase matching condition is now relatively easy to satisfy when $\omega_1 = \omega_2$, also referred to as degenerate FWM. In this case, the FWM process can be explained as an intense pump wave at ω_1 that excites two spectral sidebands symmetrically at frequencies $\omega_3 = \omega_1 - \Omega$ and $\omega_4 = \omega_1 + \Omega$. The two sidebands, in the case $\omega_3 < \omega_4$ are often called Stokes band (ω_3) and anti-Stokes band (ω_4). In this case, FWM transfers the energy from an intense pump wave to the frequency shifted waves. When one weak signal at frequency ω_3 is launched into the fiber together with an intense pump wave, the weak wave will be amplified and a new wave at frequency ω_4 will be generated. This is often called the parametric gain amplification process. If the phase matching condition is satisfied, the new generated waves can also serve as pump wave to generate more new waves.

The FWM process employed in our experimental work, described in Chapter 5, is the degenerate case. The FWM product is then given by $\omega_{\text{FWM}} = \omega_4 = 2\omega_1 - \omega_3$. Here a mathematical derivation of the growth of the FWM product will be given. The incoming field $\underline{E}(\underline{r}, t)$ is defined as a superposition of the pump signal $\underline{E}_1$ and the incoming data signal $\underline{E}_3$:

$$\underline{E}(\underline{r}, t) = \underline{E}_1(\underline{r}, t) + \underline{E}_3(\underline{r}, t) \tag{3.47}$$

with the electric field that we assume to be a wave propagating in the z-direction and being linearly polarized along the x-axis:

$$\underline{E}_j(\underline{r}, t) = \frac{1}{2} E_j e^{-i\beta_{\omega_j} z} e^{i(\omega_j t + \phi_j)} + c.c., \qquad j = 1, 3 \tag{3.48}$$

where β_{ω_j} is the phase constant of the j^{th} propagating field. Furthermore, it is assumed that the power of the pump signals E_1 and E_3 remain undepleted. By substituting equation (3.47) into equation (3.4) and only looking at the terms that produce a product at $\omega_4 = 2\omega_1 - \omega_3$, the following value for the nonlinear polarization is obtained:

$$P_{NL}^{\omega_4}(z, t) = \frac{3}{4} \epsilon_0 \chi^{(3)} E_1^2 E_3^* \exp[-i(2\beta_{\omega_1} - \beta_{\omega_3})z] e^{-i\omega_4 t + i(2\phi_1 - \phi_3)} + c.c. \tag{3.49}$$

Under the assumption that the pump field at ω_1 remains undepleted the growth of the FWM product can be described as [84]:

$$\frac{dE_4(z, t)}{dz} = \frac{-i3\omega_4}{8n_{\omega 4} c} \chi^{(3)} E_1^2 E_3^* e^{-i\Delta\beta(\omega_4)z} \tag{3.50}$$

where $n_{\omega 4}$ is the refractive index at ω_4 and $\Delta\beta(\omega_4)$ represents the phase mismatch parameter associated with the generation of the FWM product at ω_4

$$\Delta\beta(\omega_4) = 2\beta_{\omega_1} - \beta_{\omega_3} - \beta_{\omega_4} \tag{3.51}$$

The strength of the FWM product at ω_4 generated at the output of a fiber of length L can be found by integrating equation (3.50) from $z = 0$ to $z = L$:

$$\begin{aligned} E_4(L, t) = \frac{-i3\omega_4}{8n_{\omega_4} c} \chi^{(3)} E_1^2 E_3^* L \frac{\sin[\Delta\beta(\omega_4)L/2]}{\Delta\beta(\omega_4)L/2} \cdot \\ \exp(-i\Delta\beta(\omega_4)L/2) e^{-i\omega_4 t + i(2\phi_1 - \phi_3)} \end{aligned} \tag{3.52}$$

Including the walk-off, fiber losses and pulsed operation is not straightforward. In [97] an expression for a time dependent conversion efficiency $\eta(t)$ is derived for the small signal theory. Deriving an exact analysis involves a number of difficult processes that influence the nonlinear interaction, like pump depletion, SPM, XPM and dispersion that eventually leads to walk-off and pulse broadening. The work in this thesis therefore encompasses simulations that solve the NLSE to determine the growth of the FWM components with the purpose to comprehend the outcome of the experimental work.

3.4 Conclusion

In this chapter, the dispersion and the relevant nonlinear effects occurring in an optical fiber have been discussed. In this thesis a highly nonlinear fiber (HNLF) is employed as key element in several time domain optical add-drop multiplexers (ADMs). The nonlinearity of a fiber and the dispersion are included in the wave equation that describes the propagation of the light in the fiber. The nonlinear Schrödinger equation (NLSE) evolves from the wave equation. The NLSE includes the effects of fiber losses, chromatic dispersion and fiber nonlinearity. The NLSE is a powerful tool to numerically solve the propagation of an optical wave through a fiber.

The dispersion effect causes the different frequency components of a light pulse to travel at different velocities. The dispersion is expressed by the dispersion parameter D and is the amount of broadening in picoseconds that would occur in a pulse with a bandwidth of 1 nm while propagating through 1 km of fiber. The walk-off time between two pulses determines the time that the two pulses can interact and is important for all-optical switching in fiber. Polarization mode dispersion (PMD) occurs when the core of the fiber shows a slight asymmetry and the light in one of the polarization directions travels faster than the other.

The Kerr effect originates from the intensity dependence of the refractive index of the fiber. The presence of the Kerr effect gives rise to several nonlinear effects. The Kerr effects self-phase modulation (SPM), cross-phase modulation (XPM) and four-wave mixing (FWM) have been surveyed in this chapter. To improve all-optical switching in HNLF it is important to employ a fiber with the highest possible nonlinear coefficient γ, to decrease the required switching power and interaction length. To increase the nonlinearity of the fiber, the nonlinear refractive index n_2 should be increased and/or the size of the fiber core should be reduced.

Chapter 4

Nonlinear Optical Loop Mirror

One of the most well-known nonlinear fiber-based switches is the nonlinear optical loop mirror (NOLM) [14]. A NOLM can be utilized for wavelength conversion [98], demultiplexing [15, 99–105] and signal regeneration [100, 106, 107]. In this chapter we propose to use the NOLM as an all-optical time domain add-drop multiplexer. Section 4.1 describes the operation principle of the NOLM. Simulations on the NOLM as all-optical time domain add-drop multiplexer are shown in section 4.2. Section 4.3.2 and 4.3.3 describe the 160 Gb/s and 320 Gb/s add-drop multiplexing experiments, respectively. Finally, in section 4.4 the conclusions are stated. The results of the research described in this chapter have been published in *[38, 39, 108, 109]*.

4.1 Operation Principle

A fiber-based NOLM exploits the nonlinear phase shift induced in a fiber placed in a loop mirror for optical switching. A schematic view of a NOLM is shown in Figure 4.1. In the NOLM, the incoming data signal is split into two equal parts by a 3-dB coupler; a clockwise and a counterclockwise part. For both signals the optical path length is exactly the same since they follow the same path but in opposite direction. This means that the same phase change is experienced for both paths and the signal will be reflected back to the input port. When the NOLM is used for demultiplexing, a control signal is inserted in the loop in the clockwise direction via a polarization beam splitter (PBS_1), as indicated in Figure 4.1. The polarization controller (PC) in the loop is adjusted in such a way that the control signal leaves the loop at PBS_2. Alternatively, a coupler and an optical bandpass filter (OBPF) at the output port can be used instead of PBS_1 and PBS_2 for the injection and extraction of the control signal. The advantage of using PBSs is that no OBPF is required at the output to reject the control signal and select the drop and through channels. Therefore, the detrimental effect of spectral broadening and spectral overlap between control and data is minimized.

In the case of time-domain demultiplexing, the control signal is a short pulse with repetition rate equal to the OTDM base rate and a maximum full width at half

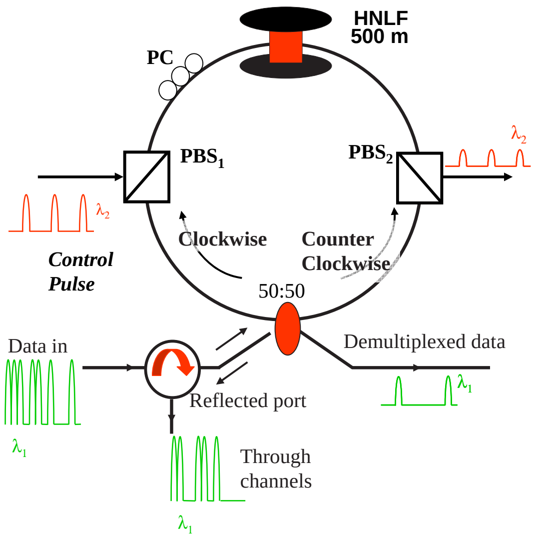

Figure 4.1: Schematic view of a fiber-based nonlinear optical loop mirror.

maximum (FWHM) pulse width equal to the OTDM signal time slot (6.25 ps for 160 Gb/s). The clockwise signal that co-propagates with the control pulse experiences a XPM induced phase shift that equals π, while propagating through the HNLF. When the clockwise and counterclockwise signal meet again at the 3-dB coupler, both contributions interfere positively and the signal is sent to the "demultiplexed data" output port. In the absence of the control pulse, interference at the 3-dB coupler leads to the output of the through channels back to the "reflected port", where they can be transmitted into the optical network via a circulator.

When the switching window, generated by the control pulse, of the NOLM is broad enough to completely switch the targeted drop channel of the OTDM signal, a new channel at the base rate can be added in the empty time slot through the use of an additional 3-dB coupler

The reflectivity and transmissivity of the NOLM can be described as a function of the coupler ratio K and the XPM induced phase shift, by the use of the transfer matrices. The electric field of the optical signals inside the NOLM are given by:

$$\begin{pmatrix} E_{cw} \\ E_{ccw} \end{pmatrix} = \begin{pmatrix} \sqrt{1-K} & -i\sqrt{K} \\ -i\sqrt{K} & \sqrt{1-K} \end{pmatrix} \begin{pmatrix} E_{\mathrm{in}} \\ 0 \end{pmatrix} \tag{4.1}$$

The signals E_{cw} and E_{ccw} travel clockwise and counter-clockwise through the loop, respectively. When the signals meet back again at the 3-dB coupler, the phase of the clockwise signal is shifted by $\Delta\phi$, because of the pump signal induced XPM. The fields at the reflected and transmitted port of the coupler can therefore be written as:

$$\begin{pmatrix} E_R \\ E_T \end{pmatrix} = \begin{pmatrix} \sqrt{1-K} & -i\sqrt{K} \\ -i\sqrt{K} & \sqrt{1-K} \end{pmatrix} \begin{pmatrix} E_{ccw} \\ E_{cw}e^{-i\Delta\phi} \end{pmatrix} \tag{4.2}$$

The reflectivity and the transmissivity can be derived from

$$|E_R|^2 = R|E_{\text{in}}|^2 \tag{4.3}$$
$$|E_T|^2 = T|E_{\text{in}}|^2 \tag{4.4}$$

By solving equations (4.1)-(4.4) the following expressions for R and T are obtained:

$$R = 2K(1-K)(1+\cos\Delta\phi) \tag{4.5}$$
$$T = (1-K)^2 + K^2 - 2K(1-K)\cos\Delta\phi \tag{4.6}$$

A theoretical derivation of transmission through a loop mirror, including polarization dependence, excess loss of the coupler, loss through propagation inside the loop and influence of birefringence inside the loop is given in [110].

4.2 System Simulations

The performance of the NOLM as an all-optical time domain add-drop multiplexer (ADM) is simulated with the VPI TransmissionMaker software tool. Several of the mostly frequently used simulation blocks are described in Appendix D. The simulations take into account fiber nonlinear effects like SPM, XPM, FWM and second and third order dispersion effects. The fiber model used in the simulations solves the nonlinear Schrödinger equation (NLSE) of linearly-polarized optical waves by using the split-step Fourier method. This method is described in more detail in Appendix D.1.1. The parameters for the HNLF used in the simulations (and experiments) are listed in Table A.1 in Appendix A.

4.2.1 Switching Window Characterization

To analyze the switching characteristics of the NOLM a static simulation has been made with a short control pulse (=pump signal) and a continuous wave (CW) signal (=probe signal). For this static pump-probe simulation the wavelengths of pump and probe are chosen symmetrically around the zero-dispersion wavelength of the fiber to minimize the walk-off time. A large wavelength spacing between control and data wavelength is required to avoid overlap in the spectral domain. Therefore, a large spectral spacing of 20 nm between control and data signal is applied. The wavelength of the data signal is 1555 nm and the wavelength of the control signal is 1535 nm. The pump signal is a 2 ps FWHM secant-shaped pulse at a 40 GHz repetition rate. The peak power of the pump signal is optimized to obtain the maximum contrast ratio for the switching window.

The CW signal that co-propagates with the pump signal experiences a nonlinear phase shift of π radians. The static characteristic of the switching windows at the through and drop port are shown in Figure 4.2 and 4.3, respectively. The shape of the switching window is similar to the shape of the control pulse for the drop port and to the inverse of the control pulse for the through port. Best ADM results would therefore be obtained with a rectangular shaped control pulse. The evolution of the XPM induced phase change on the probe signal is shown in Figure 4.4. A 180°

phase change in the clockwise direction is observed, while the phase of the counter-propagating probe signal remains constant.

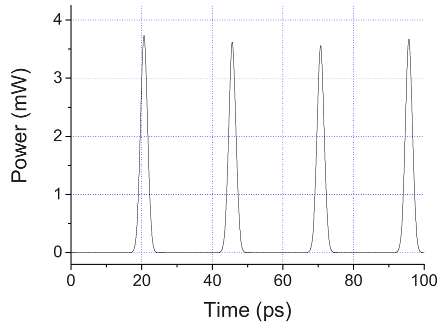

Figure 4.2: Static switching characteristic of the drop port of the NOLM, $\tau_{control} = 2$ ps.

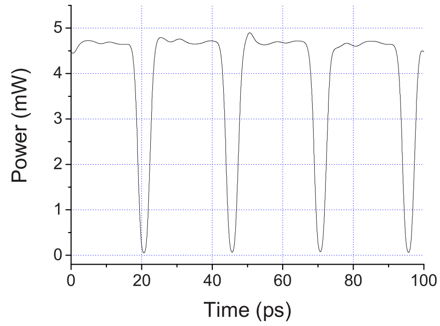

Figure 4.3: Static switching characteristic of the through port of the NOLM, $\tau_{control} = 2$ ps.

In our experimental results described in section 4.3.2 and 4.3.3 an orthogonal relation between the polarization of the pump signal and the polarization of the data signal is achieved by coupling the pump signal inside the loop with a PBS.

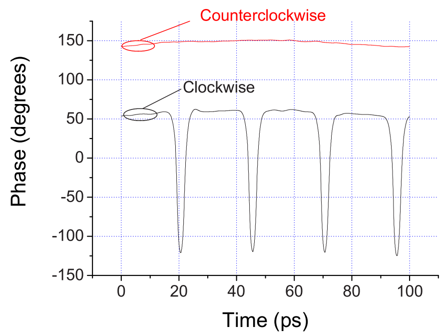

Figure 4.4: The XPM induced phase change on the 1555 nm CW signal co-propagating with the 40 GHz control signal in the clockwise direction.

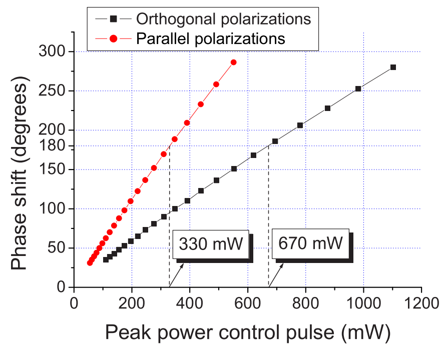

Figure 4.5: XPM induced phase change (degrees) of the 1555 nm signal, versus the control pulse peak power (mW) for orthogonal polarizations and parallel polarizations.

The state of polarization of the data signal and pump signal evolve in a complicated and unpredictable manner; however if the two signals have a sufficiently close optical frequency they will remain orthogonally polarized [111]. We did not investigate in how far the control and data signal remained orthogonally polarized in our ADM, but according to [112], the PC in the NOLM (see Figure 4.1) can be optimized in such a way that the control pulse is changed to a linearly polarized state and can be removed from the loop by PBS_2. To investigate the influence of the orthogonal polarization of the control pulses on the data pulses, a simulation has been performed for parallel and orthogonal polarization between pump and CW signal. The acquired phase shift versus the peak power of the pump signal is shown in Figure 4.5, for a 2 ps FWHM pump pulse. The relation between the phase shift and the peak power of the pump signal has a different slope for a parallel pump-probe polarization state compared to the orthogonal pump-probe polarization state. The difference can be explained by the theory described in chapter 3. The nonlinear phase shift induced by XPM can be estimated by equation (3.42). The effective length of our HNLF is $L_{\text{eff}} = 484$ m, the nonlinear index is $\gamma = 15\ \text{W}^{-1}\text{km}^{-1}$, b=2 for parallel polarizations and b=$\frac{2}{3}$ for orthogonal polarizations. For a targeted π nonlinear phase shift, the estimated values of the required pump signal peak power are $P_{po} = 649$ mW for orthogonal polarizations and $P_{pp} = 216$ mW for parallel polarizations according to equation (3.42). The required values for the peak power of the 2 ps FWHM pump pulse obtained from the simulations can be deducted from Figure 4.5, and are $P_{po} = 670$ mW for orthogonal polarizations and $P_{pp} = 330$ mW for parallel polarizations. The theoretical approach to estimate the required switching power was expected to yield a lower value than the simulated value because equation (4.5) does not include any dispersion effects. Also, the influence of other nonlinear effects, like e.g. SPM that changes the shape of the pump signal in the time domain and indirectly also the peak power of the pump signal, are not included in equation (3.42).

4.2.2 Add-Drop Multiplexing Performance

To employ the fiber-based NOLM as a key element in an ADM it is important to study the optimum settings of the NOLM. In general, the performance of a NOLM is degraded by channel crosstalk originating from the leakage of non-targeted channels and by intensity fluctuations on the demultiplexed signals due to a relative timing jitter between incoming data and control pulses. In previous theoretical/analytical work on demultiplexing with a NOLM, a signal-to-noise (SNR) analysis has been performed [113]. In [114] the effect of timing jitter has been topic of research and also the influence of the dispersion slope [115] has been studied. We have extended the theoretical work towards time domain ADM with a NOLM. In this section, a performance assessment of an ADM based on a NOLM is carried out by simulations.

The limit of the NOLM as an all-optical demultiplexer and add-drop multiplexer strongly depends on the parameters of the nonlinear element in the loop and on the quality of the control signal. There are two effects that have to be taken into account that degrade the performance of the NOLM. The first is channel crosstalk originating from the leakage of non-targeted channels. This can occur because of the XPM induced phase shift on the counter-propagating data signal. Leakage of non-targeted channels can also be caused by a coupler with a value slightly deviating from the optimum $K = 0.5$. To minimize the effect of the XPM induced phase shift of the control signal time-averaged power on the counter-propagating signal, an optical bias controller can be implemented [116]. In our simulation and experimental work, the pump signal has a low duty cycle ratio compared to the duty cycle of the base rate. Therefore, the counter-propagating phase shift is neglected.

The second detrimental effect that causes intensity fluctuations on demultiplexed signals is caused by the combined effects of timing jitter and the corresponding profile of the switching window. The two above mentioned detrimental effects are investigated in detail in section 4.2.3 and 4.2.4, respectively. The simulations have been performed for 160 and 320 Gb/s OTDM line rates with a 40 Gb/s base rate.

For the simulation of an ADM based on HNLF inside a NOLM, a 160 Gb/s OTDM signal with 1.5 ps FWHM pulses and a 40 Gb/s base rate is used. The wavelength of the OTDM signal is $\lambda_s = 1555$ nm. The control signal is a 40 GHz pulse train of 1.5 ps FWHM pulses at the wavelength $\lambda_c = 1535$ nm. The average power of the 160 Gb/s OTDM data signal power inserted into the HNLF is 0 dBm. The output of the drop and through port of the NOLM are shown in Figure 4.6 and 4.7, respectively. The peak power of the control pulse in the simulations is 350 mW. In the through channel, there is some residual of the dropped channel clearly visible, because of the too narrow switching window. Similar results are obtained in an experimental setup under similar conditions. An example of a non-optimized through window obtained in the experiments is shown in Figure 4.8.

To obtain a good cleaned bit time slot in between the through channels, the control pulse needs to be broader. Therefore, the width of the control pulse has been changed to 5 ps, see Figure 4.9. The output of the drop and through port are now shown in Figure 4.10 and 4.11, respectively. The empty time slot in the through channel is now better cleaned and the eye diagram of the drop channel still remains clear and open. The peak power of the control pulse is 240 mW. The difference in peak power between the control pulses with 1.5 ps and 5 ps FWHM widths proves that there is a dependence of the optimum peak power of the control signal on the pulse width. To study this dependence, an optimization of the peak power versus the receiver sensitivity of the dropped and added channel is performed. The sensitivity is the minimum required power to obtain BER of 10^{-9}. The details of the BER analysis carried out in the simulation of the fiber-based NOLM ADM can be found in Appendix D. The sensitivity of the demultiplexed channel is shown in Figure 4.12 for several control pulse widths. The sensitivity of the drop channel is stable for small pulse widths, i.e. 1 and 1.5 ps. For broader control pulses of 6.5 ps, the peak power should be limited to 300 mW in order to prevent degradation of the sensitivity due to demultiplexing of the neighboring channels. In Figure 4.13, the sensitivity of the added channel is shown versus the control pulse peak power for several values of the control pulse width. The optimum peak power for a 1.3 ps control pulse is 350 mW, while for a 6.5 ps control pulse the optimum pulse peak power is about 225 mW. The difference can be explained by the combination of SPM and dispersion on the control pulse during propagation through the HNLF. The spectrum of the 1.3 ps control pulse is broader and is therefore stronger influenced by SPM under equal peak power conditions. Moreover, dispersion effects on the 1.3 ps pulse broaden the pulse and reduce the peak power. According to our simulations, the optimum pulse width for

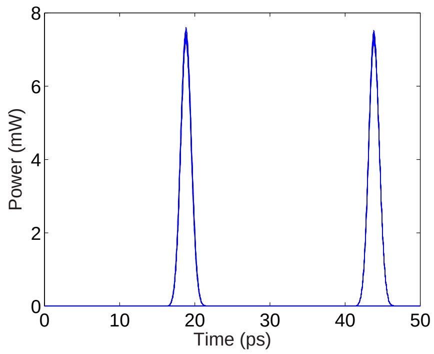

Figure 4.6: Drop channel output (1555nm) of the loop mirror with 1.5 ps control pulse at 1535 nm

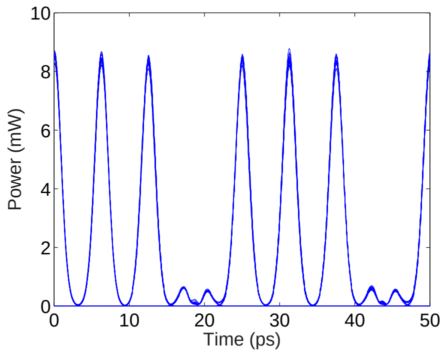

Figure 4.7: Through channel output (1555nm) of the loop mirror with 1.5 ps control pulse at 1535 nm

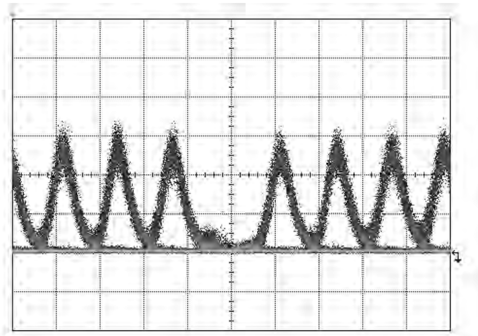

Figure 4.8: Experimental measurement of the through channels with a 2 ps control pulse. X-sale: 5ps/div, y-scale: a.u.

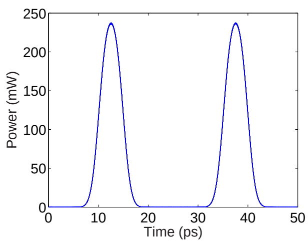

Figure 4.9: Broadened control signal, $\tau_{\text{control}} = 5.0$ ps.

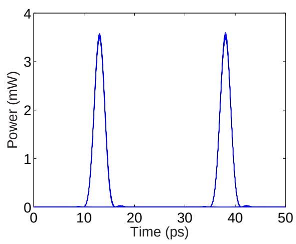

Figure 4.10: Simulation drop port, $\tau_{\text{control}} = 5.0$ ps.

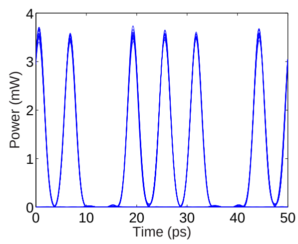

Figure 4.11: Simulation through port, $\tau_{\text{control}} = 5.0$ ps.

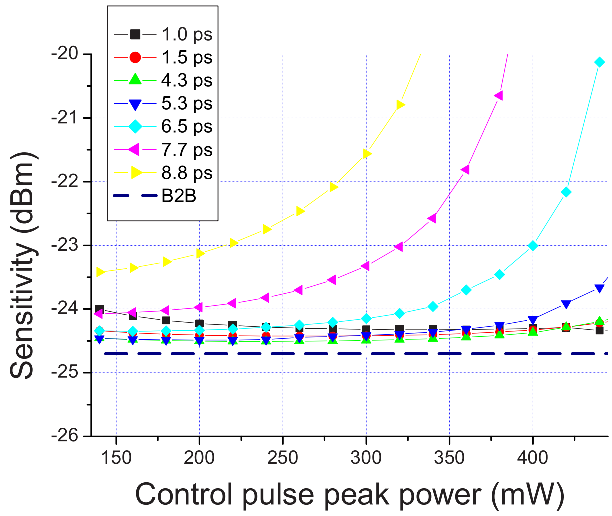

Figure 4.12: Receiver sensitivity of the dropped channel at 40 Gb/s after the 160 Gb/s ADM versus the peak power of the control signal for several values of the control pulse width.

160 Gb/s add-drop operation is 5.3 ps FWHM and the optimum peak power is 250 mW. This assumption is valid for a secant-shaped control pulse.

4.2.3 Jitter Effects

As indicated in the previous section the ADM performance can be degraded due to timing jitter between control and data. To investigate this, the influence of the timing jitter between control and data is analyzed by applying a variable RMS jitter value on the control signal. Simulations have been performed for a 160 and 320 Gb/s line rate with a 40 Gb/s base rate. The timing jitter in combination with the switching profile induces intensity fluctuations on the demultiplexed channel and imperfect cleaning of the empty time slot at the through port. The detrimental effect of the timing jitter is assessed in our simulations in term of the receiver sensitivity power penalty.

A schematic of the simulation setup is shown in Figure 4.14. The timing jitter block introduced this effect in the control pulse. Examples of a 5.1 ps FWHM control pulse with and without 650 fs RMS jitter are shown in the insets of Figure 4.14. The control and data carrier wavelengths are chosen symmetrically around the zero dispersion wavelength of the fiber in order to minimize the walk-off between control and data signals. The peak power of the control pulse is optimized for add-drop operation by tuning to the optimized values deduced from Figure 4.12 and 4.13. In the simulation scheme, the counter-propagating signal is simulated by going through a second HNLF with exactly the same parameters. The pulse peak power of the 160

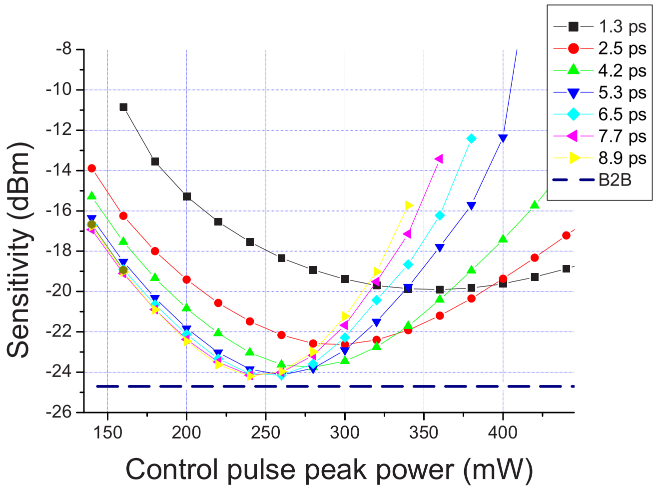

Figure 4.13: Receiver sensitivity of the added channel at 40 Gb/s after the 160 Gb/s ADM versus the peak power of the control signal for several values of the control pulse width.

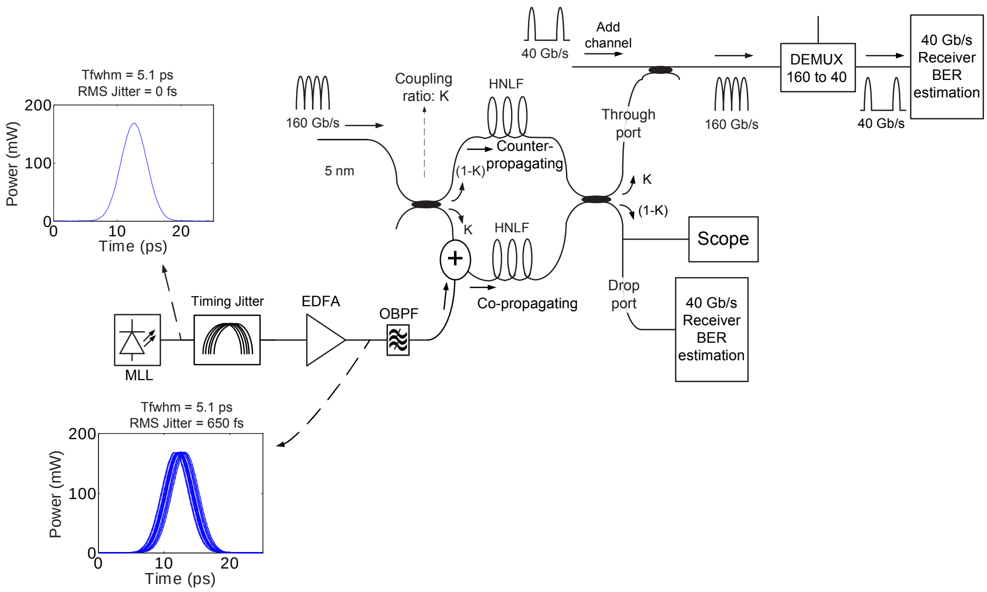

Figure 4.14: Schematic of the simulation setup used in VPI to study the NOLM and its dependence on the control signal jitter.

Gb/s OTDM signal entering the HNLF is 25 mW, corresponding to 6 dBm average power. Four return-to-zero (RZ) 40 Gb/s transmitters with 1.9 ps FWHM secant-shaped pulses are combined into an OTDM 160 Gb/s line rate. The output of the OTDM multiplexer is amplified from -15 dBm to +10 dBm average power with an EDFA with a noise figure of 4. The output of this amplifier is filtered with a 300 GHz OBPF. The control signal is inserted only in the lower arm of the NOLM. The control pulse is Gaussian shaped and the width is varied, as well as the RMS value of the timing jitter. The ideal value of 0.5 is taken for the coupler ratio K.

The sensitivities of the dropped and added channel versus the RMS timing jitter of the control pulse and the control pulse width are shown in Figure 4.15(a) and 4.15(b), respectively. The sensitivity of the add and drop channels are compared with a RZ back-to-back (B2B) signal at 40 Gb/s, with the same receiver parameters as used for the add and drop simulations. The B2B channel is visualized as a plane under the graphs depicted in Figure 4.15(a) and 4.15(b). The sensitivity of the B2B signal is -24.7 dBm. The sensitivity penalty for the dropped channel at optimized control pulse width and no jitter is 0.3 dB. The switching window can be broader than the pulse width of the targeted channel. No large power-penalty is expected as long as the neighboring pulses remain "un-switched" and the targeted channel still falls within the switching window. This relatively broad switching window relaxes the jitter requirements between data and control signal.

From Figure 4.15(a), we can deduce that a small control pulse of 630 fs has a sensitivity penalty of 0.9 dB when no jitter is included. Increasing the RMS value of the jitter leads to an increased penalty. The tolerance towards the jitter becomes larger for broader control pulses. However, when the control pulse becomes larger than the bit time slot of 6.25 ps a sensitivity penalty due to switching of neighboring channels is observed. The optimum value of the control pulse width is when there is no penalty due to switching of non-targeted channels and the targeted channel falls completely within the switching window. For the drop operation a control pulse width between 2.5 ps and 6.3 ps minimizes the penalty. The RMS timing jitter must remain below 900 fs to ensure a sensitivity penalty < 1 dB at BER$=10^{-9}$.

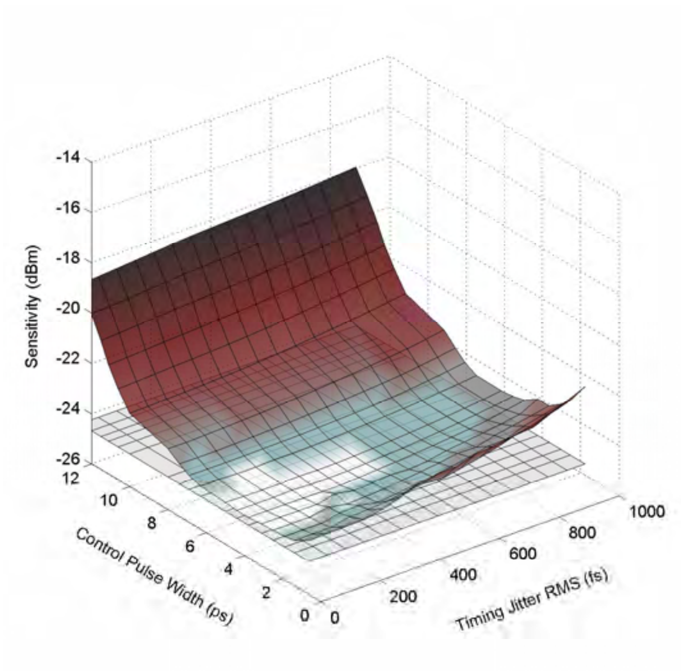

(a) Receiver sensitivity of the dropped channel at 40 Gb/s.

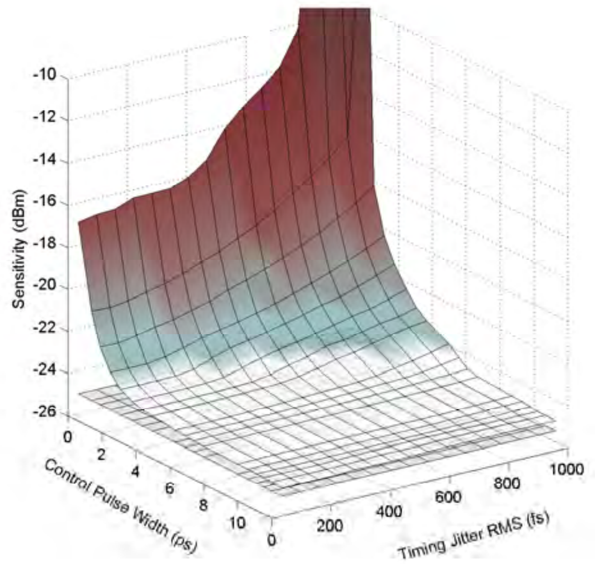

(b) Receiver sensitivity of the added channel at 40 Gb/s.

Figure 4.15: Sensitivity of the dropped (a) and the added (b) channel of the 160 Gb/s ADM versus the timing jitter and the width of the control pulse.

The jitter tolerance of the added channel is improved when going from a pulse width of 630 fs to a pulse width of 12 ps, see Figure 4.15(b). The targeted drop channel has a larger chance to completely fall inside the switching window. As a result the time slot is better cleaned and better performance of the added channel can be observed. Therefore, the outcome of the simulations show a smaller increase in sensitivity penalty for larger control pulses. The sensitivity penalty for the added channel at optimized control pulse width and no jitter is 0.5 dB.

Optimal operation of the add-drop multiplexer is achieved with the broadest control pulse, that still minimizes the penalty in drop operation. From our simulation results, the optimum width is $\approx$ 6 ps.

Regarding the control pulse shape, it is important to minimize the tail of the pulse in order to minimize the switching of the non-targetted channels. It is advisable to reduce the pulse width of the control signal when the tail is large.

A similar series of simulations was carried out to study the ADM performance for a a 320 Gb/s OTDM line rate with a 40 Gb/s base rate. The wavelengths of the control and data signal remain unchanged at 1535 and 1555 nm respectively. The pulse width of the OTDM data signal is 800 fs. The bandwidth of the OBPFs has been changed to 800 GHz. The sensitivity of the dropped channel versus the RMS timing jitter of the control pulse and the control pulse width is shown in Figure 4.16(a). The sensitivity penalty for the dropped channel at optimized control pulse width and no jitter is 0.5 dB. The sensitivity penalty of the dropped channel is reduced with increasing control pulse width, with an optimum pulse width between 2.1 and 2.7 ps FWHM. Increasing the width of the control pulse further leads to an increase of the sensitivity penalty because of crosstalk from the neighboring channels. The sensitivity of the added channel versus the RMS timing jitter and width of the control pulse is shown in Figure 4.16(b). The sensitivity penalty for the added channel at optimized control pulse width and no jitter is 0.7 dB. The optimum pulse width for the best add operation is in the range 2.5 to 3.1 ps. Larger or smaller pulse widths lead to an uncleaned time bit slot in the through channel. The RMS timing jitter should be below 150 fs RMS timing jitter to ensure a sensitivity penalty < 1 dB at BER$=10^{-9}$.

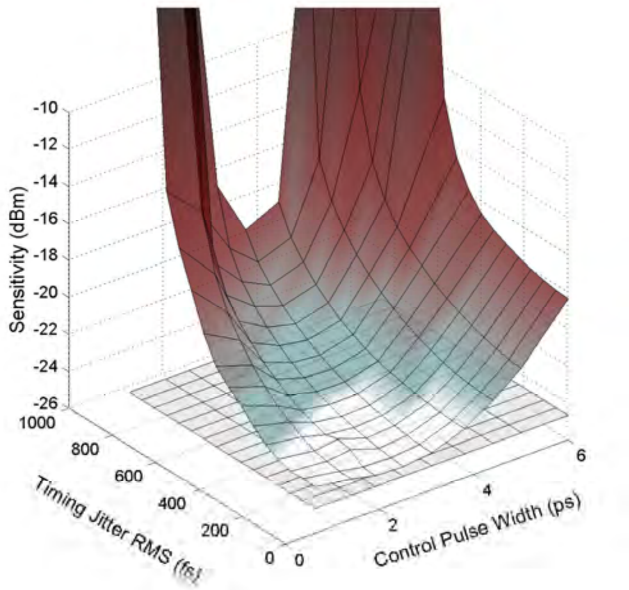

(a) Receiver sensitivity of the dropped channel at 40 Gb/s.

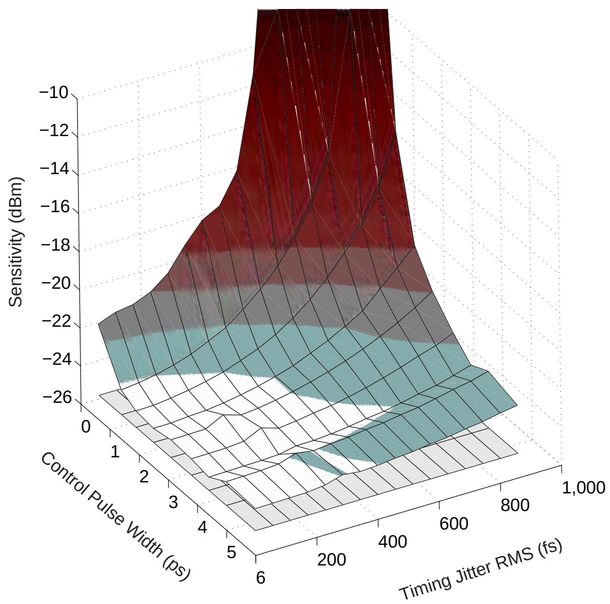

(b) Receiver sensitivity of the added channel at 40 Gb/s.

Figure 4.16: Sensitivity of the dropped (a) and the added (b) channel of the 320 Gb/s ADM versus the timing jitter and the width of the control pulse.

4.2.4 Coupler Ratio Effects

The coupler ratio of the 3-dB coupler in the NOLM is assumed to be exactly 50-50 in most theoretically approaches. In this ideal approach, all signal power that is not influenced by an external control pulse will be reflected back to the input port. When $|K-0.5| > 0$, part of the input signal is transmitted to the demultiplexed output port without presence of a control pulse. We have carried out simulations to determine the tolerance of the ADM on the coupler ratio K.

The input signal is a 160 Gb/s (4×40 Gb/s) OTDM signal with 1.9 ps FWHM secant-shaped pulses at the wavelength $\lambda_{in} = 1555$ nm. The detrimental effect of a non-ideal coupler on the ADM is assessed in our simulations in terms of the receiver sensitivity power penalty at BER=10^{-9}. The receiver sensitivity performance of the drop and add channels versus the coupler ratio K and the control pulse width is shown in Figure 4.17(a) and 4.17(b), respectively. As can be seen, the optimum coupler factor is around the ideal value of $K = 0.5$. The tolerance of the coupler ratio to keep the sensitivity penalty at BER=10^{-9} within 1 dB from the optimum value is $|K-0.5| < 0.12$. Noticeable is the indifference of the performance of the add channel, regarding the coupler ratio K (see Figure 4.17(b)). This is in accordance with the theory of a NOLM. According to equation (4.5), the reflectivity is always zero when a π phase shift is obtained. It is concluded that only the drop channel is influenced by a non-optimized coupler ratio.

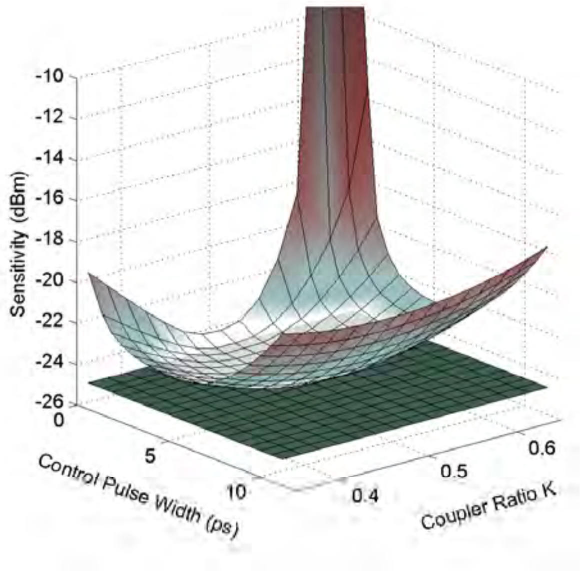

(a) Sensitivity of the 40 Gb/s dropped channel.

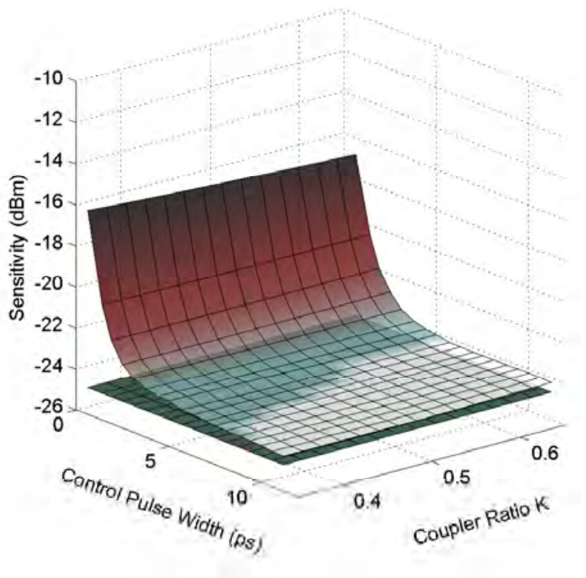

(b) Sensitivity of the 40 Gb/s added channel.

Figure 4.17: Sensitivity of the dropped (a) and the added (b) channel versus the coupler ratio of the NOLM input coupler and the control pulse width.

4.2.5 Optimum Settings

The optimum settings of the NOLM as ADM and the tolerances towards jitter and coupler ratio that follow from the simulations are summarized in Table 4.1. The tolerance towards jitter is increased, if broader switching windows are applied. However, when the control pulse becomes larger than the bit time slot of the OTDM signal a sensitivity penalty, due to switching of neighboring channels, is observed. The coupler ratio effects the performance of the dropped channel, but the added channel is not influenced. Finally, we conclude that an imbalanced coupler has a larger effect on ADMs with shorter control pulses.

Table 4.1: Summary of the optimum settings for the NOLM as time domain ADM.

Parameter	Value
Pulse width control at 160 Gb/s	5 ps
Peak power control pulse	225 mW
RMS jitter for <1 dB sensitivity penalty at BER=10^{-9} for 160 Gb/s ADM	<900 fs
RMS jitter for <1 dB sensitivity penalty at BER=10^{-9} for 320 Gb/s ADM	<150 fs
Coupler ratio K (<1 dB sensitivity penalty at BER=10^{-9}) for 160 Gb/s ADM	$\lvert K-0.5\rvert < 0.12$

4.3 Experimental Results

In this section the performance of the NOLM as key component in an OTDM ADM is experimentally assessed.

4.3.1 Experimental Setup

The schematic of the transmitter is shown in Figure 4.18. The MLL produces 39.813 GHz, 1.5 ps FWHM pulses at 1549 nm. Calmar kindly provided us the MLL PSL-40 for temporary use. This MLL pulse train is modulated at 40 Gb/s with PRBS 2^7-1 data with a Ti:LiNbO$_3$ Mach-Zehnder modulator. Afterwards the signal is amplified, filtered and pre-compensated in 6 meter dispersion compensating fiber (DCF) with $D = -100$ ps·nm^{-1}·km^{-1}. A low PRBS word length is used out of practical perspective. The multiplexer is constructed out of couplers, where the signal is first split in two arms and one part is delayed with respect to the other before they are combined into one signal again. To guarantee a phase decorrelated signal at the output, the delay in one arm needs to be at least half the word length. Longer PRBS word lengths would therefore require longer delay lines inside the multiplexers, resulting in more costly and more unstable equipment. The control signal and the 160 Gb/s OTDM signal are obtained from the same MLL. To avoid crosstalk between the control and OTDM signal the wavelength of the 39.813 GHz control signal is converted to 1555.78 nm. The conversion is based on super continuum generation (SCG) in 2.25 km dispersion shifted fiber (DSF). The parameters of the DSF are given in Table A.3 in Appendix A. The control signal is acquired by slicing the generated SC spectrum with a multilayer dielectric thin-film filter with -3 dB bandwidth $\Delta\lambda = 0.92$ nm. The generated control pulse width is 6 ps. The SCG is more thoroughly described in Appendix B.

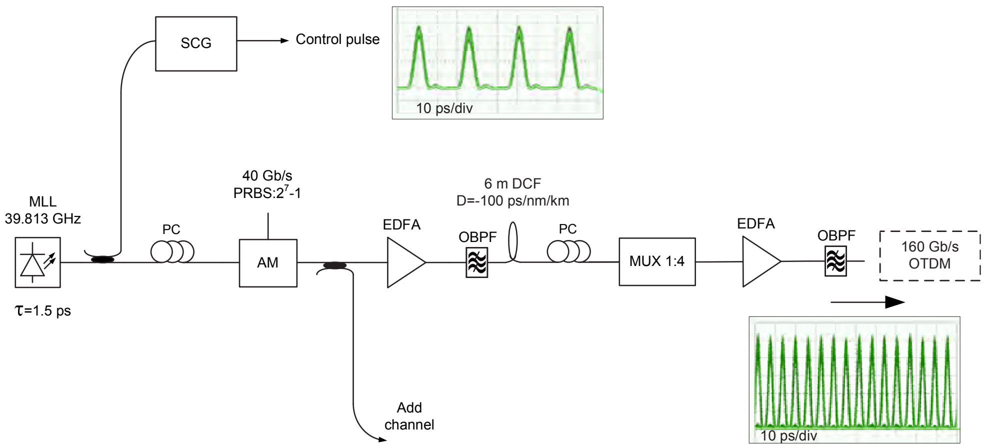

Figure 4.18: Schematic of the experimental setup of the transmitter of the 160 Gb/s OTDM signal with a 40 Gb/s base rate.

Figure 4.19 shows the setup of the ADM based on a fiber-based NOLM configuration. Both the 3-dB coupler and the 500 m long HNLF in the NOLM are non-polarization maintaining fibers. Orthogonally polarized signal and control pulse streams are used in the experiments. The parameters of the HNLF used in the experiment are listed in Table A.1. The 40 GHz control signal at 1555.78 nm is coupled into the loop through PBS_1 and travels in clockwise direction. The walk-off between the signal and control pulse is only 0.95 ps, according to equation (3.31), because the HNLF has a small dispersion slope of $S = 0.03$ ps·nm^{-2}·km^{-1}. The OTDM channel coinciding with the control signal experiences an extra phase shift induced by the XPM effect. The control signal, which is orthogonally polarized, is removed from the loop through PBS_2 by proper adjustment of polarization controller 3 (PC_3). Thus, when the clockwise and counterclockwise signal interfere at the coupler one OTDM channel will be sent to the drop port, whereas the through port contains the 3 remaining channels. A 40 Gb/s add channel, deduced from the same source as the input signal and controlled by a delay line, is inserted after the through port by a passive fiber combiner. For the remaining 40 Gb/s channels and the added channel, time domain demultiplexing with a single EAM has been employed to retrieve the 40 Gb/s tributaries. The switching window is about 7 ps FWHM, which is slightly wider than the 160 Gb/s time slot, resulting in a small excess penalty.

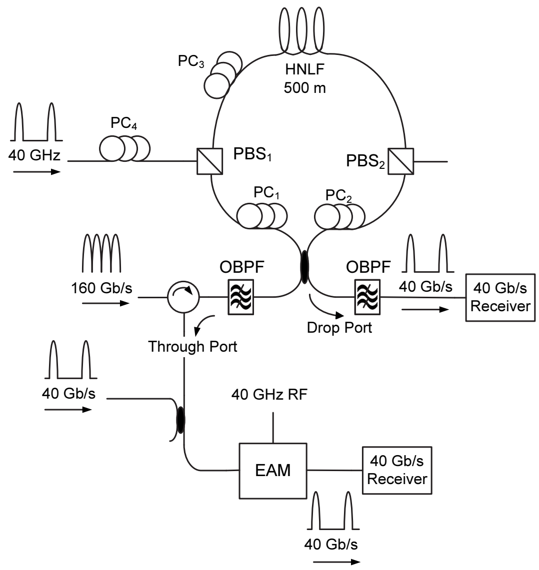

Figure 4.19: Schematic of the experimental setup of the 160 Gb/s ADM, with 40 Gb/s base rate, based on using HNLF in a NOLM.

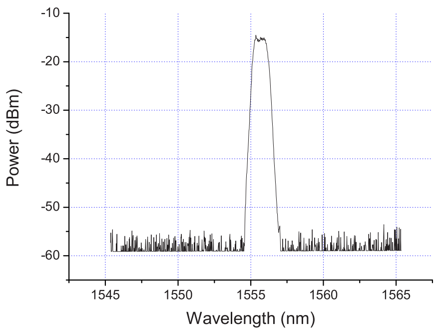

Figure 4.20: Control signal at 1555.78 nm before entering the NOLM (res. bw. = 0.06 nm).

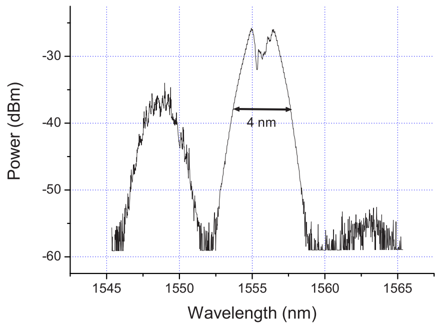

Figure 4.21: OTDM signal at 1549 nm and control pulse at 1555.78 nm after the transmission through 0.5 km of HNLF. (res. bw. = 0.06 nm).

4.3.2 Add-Drop Multiplexing at 160 Gb/s

The results on the 160 Gb/s ADM described in this section have been published in *[38]*. In the experiments, the average power of the 160 Gb/s OTDM signal coupled into the HNLF is 5 dBm and the average power of the 40 GHz control pulse is 22 dBm. The corresponding control pulse peak power is 660 mW, which induces a π phase shift on one of the OTDM channels that needs to be dropped. The spectrum of the control pulse before entering the NOLM is shown in Figure 4.20 and the spectrum of the control pulse and OTDM signal inside the loop after passing through the HNLF is shown in Figure 4.21. A broadening of the spectrum of the control pulse is observed to 4 nm as indicated in Figure 4.21, because of SPM. Figure 4.22 shows the eye diagram of the original 160 Gb/s OTDM signal. The small signal in the zero level is due to the extinction ratio of the 40 Gb/s modulator. Figure 4.23 and 4.24 display the eye diagrams of the dropped channel and through channels, respectively. The eye diagram of the added channel is shown in Figure 4.25. From the eye diagrams we see that excellent dropping and good removal of one channel at the through port are achieved simultaneously.

The performance of the OTDM ADM was assessed by measuring BER values. As a reference for the dropped channels we used the 40 Gb/s RZ signal in a B2B BER measurement. Figure 4.26 summarizes the measured BER performances. Figure 4.26(a) shows the BER performance of the four dropped channels, and Figure 4.26(b) shows the BER of the through channels and one added channel. The average sensitivity penalty for the dropped channels is 3 dB. As a reference for the through channel we used the original 160 Gb/s signal as the input signal to the demultiplexer based on a single EAM. The average penalty of the dropped through channels is 1.4 dB, and an extra 3 dB penalty for the dropped added-channel is observed. The sensitivity penalties are due to the optical signal-to-noise ratio (SNR) reduction by ASE

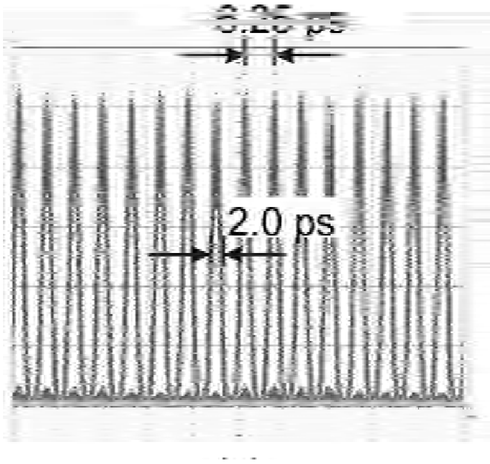

Figure 4.22: 160 (4 × 40) Gb/s OTDM input signal to the NOLM.

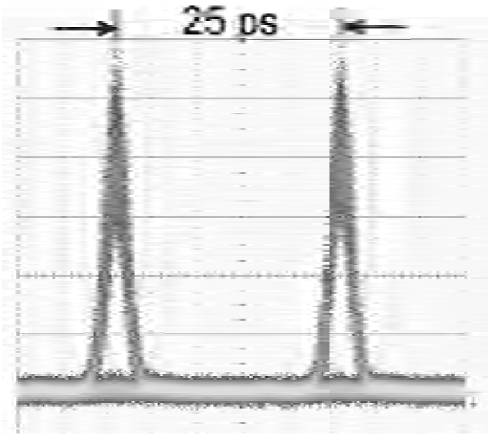

Figure 4.23: 40 Gb/s dropped signal at the drop output port of the NOLM.

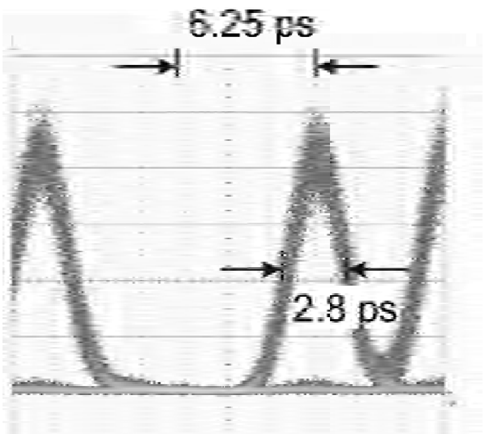

Figure 4.24: Empty time slot and the 3 × 40 Gb/s through channels.

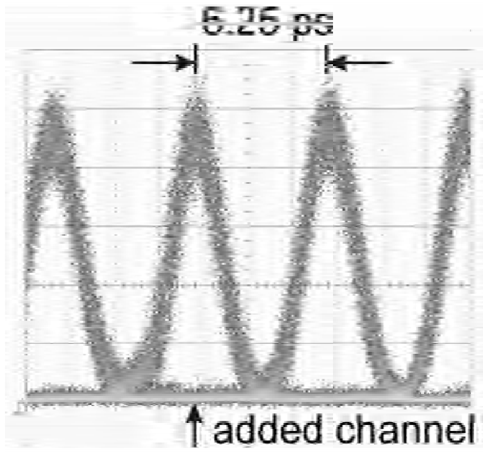

Figure 4.25: Through channels with inserted 40 Gb/s added channel.

noise of the EDFAs in the system and the interferometric crosstalk between the added channel and the remaining signal due to incomplete removal of the dropped channel at the through port. Also, pulse broadening in the through channels is observed from 2 ps to 2.8 ps, leading to more crosstalk in the demultiplexer with a single EAM because the EAM switching window is too wide and fractional parts of neighboring pulses are switched to the dropped channel.

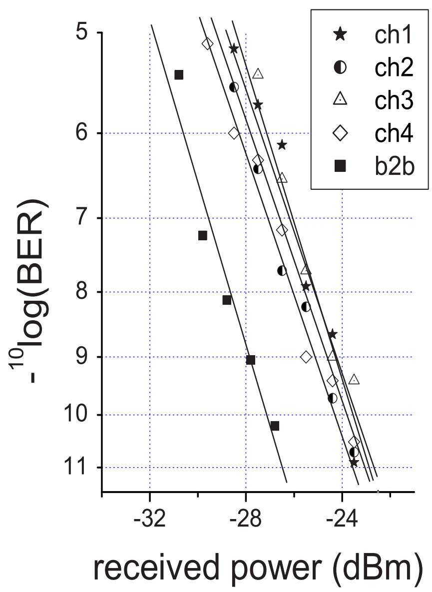

(a) Dropped channels.

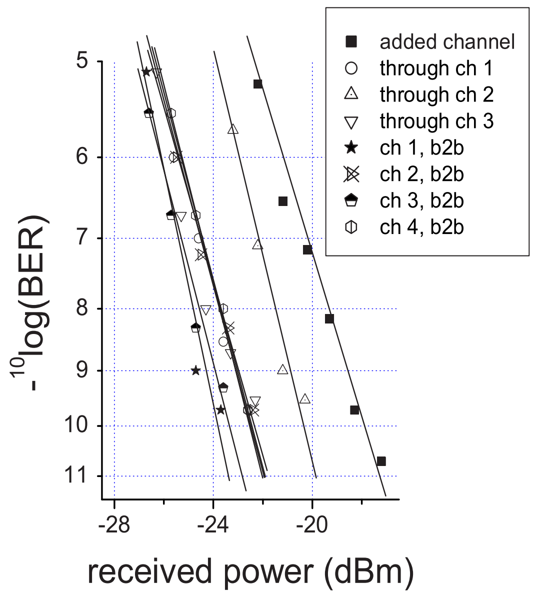

(b) Through channels and added channel.

Figure 4.26: BER performance of the 160 Gb/s ADM.

4.3.3 Add-Drop Multiplexing at 320 Gb/s

The results on the 320 Gb/s ADM described in this section have been published in *[39]*. For the generation of the 320 (32 × 10) Gb/s an MLL that produces pulses at 9.9538 GHz, 2.1 ps FWHM at $\lambda_d = 1552$ nm is used. This is a commercial available MLL from Pritel. The narrow pulse required for the generation of a 320 Gb/s OTDM signal is generated by compressing the pulse in 1 km dispersion decreasing fiber to 850 fs. The narrowed pulse is then modulated with $2^7 - 1$ PRBS data and time multiplexed with passive delay line multiplexers to a 320 Gb/s OTDM signal. The spectrum of the 320 Gb/s signal is shown in Figure 4.27. The control pulse for add-drop operation at 320 Gb/s was 2.8 ps FWHM, with a square top shape, as can be seen in Figure 4.32. The control pulse is generated by SCG and filtering (Appendix B.1.2). The wavelength of the control pulse is $\lambda_c = 1540$ nm and the spectrum is visualized in Figure 4.28.

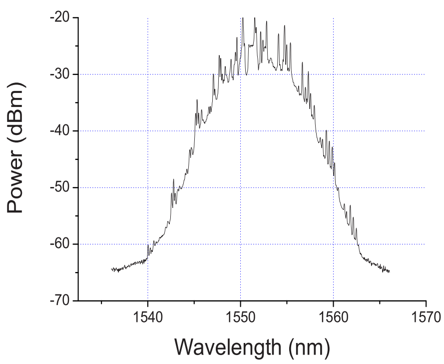

Figure 4.27: Spectrum of the 320 Gb/s OTDM signal (res. bw. = 0.06 nm).

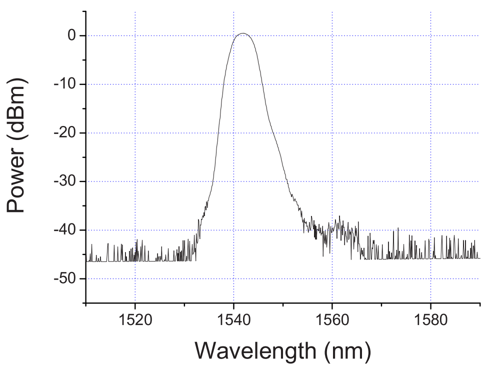

Figure 4.28: Spectrum of the 10 GHz control pulse (res. bw. = 0.06 nm).

The control pulse is amplified to an average power coupled into the HNLF of 13 dBm, and the OTDM signal power coupled into the HNLF was 5 dBm. The square shape and relatively large width of the control pulse makes it possible to simultaneous demultiplex and create a through channel. The walk off between control and data was negligible because both signals are placed around the zero dispersion point ($\lambda_0 = 1545$ nm) of the HNLF and moreover the dispersion slope (S = 0.03 ps·nm^{-2}·km^{-1}) of the HNLF is small. The eye diagrams of the 320 Gb/s ADM are shown in Figure 4.29, 4.30 and 4.31. The eye diagram of the dropped channel is clear and open. As a result, error-free BER performance was achieved (see Figure 4.33), although a 6 dB power penalty for the drop operation was measured. The penalty was caused by crosstalk from the neighboring channels due to the too broad switching window of 2.8 ps. Noteworthy is that this switching window of 2.8 ps is required to obtain good performance of the through operation. Also, spectral broadening of the control signal causes spectral overlap between control and data signals. The output of the through

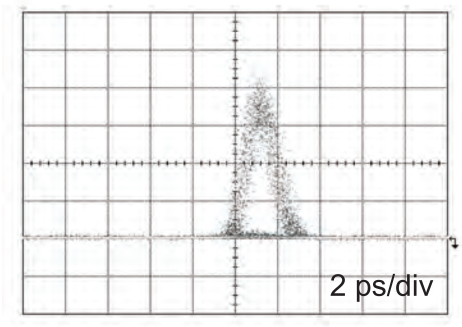

Figure 4.29: Dropped channel, 320 to 10 Gb/s demultiplexing.

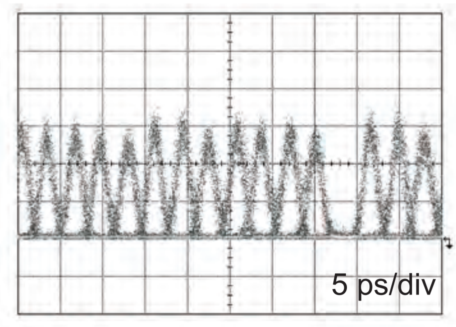

Figure 4.30: Through channels (31 × 10 Gb/s)

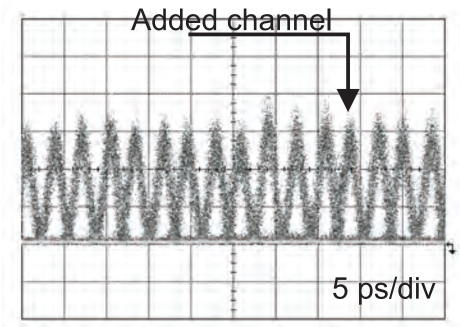

Figure 4.31: Through + added channel

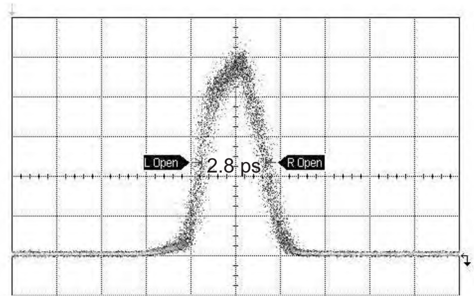

Figure 4.32: Control pulse at 10 GHz for the 320 (32 × 10) Gb/s ADM.

port showed good cleaning of the dropped channel. After adding a new channel at 10 Gb/s in the empty time slot, no large distortions were observed in the eye diagram of the added channel.

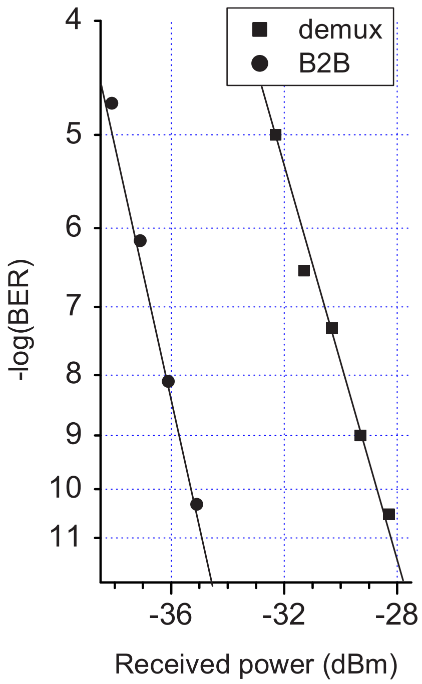

Figure 4.33: BER measurements of the dropped channel at 10 Gb/s, compared with a 10 Gb/s B2B signal.

4.4 Conclusion

A study on fiber-based NOLM configurations for add-drop multiplexing has been performed. Simulations for optimization of the power and width of the control pulse provide an optimum pulse width of 5 ps and a peak power of 225 mW for a 160 Gb/s add-drop multiplexer (ADM). A study on the influence of timing jitter between control and data signal on the NOLM based ADM has been performed. For a 160 Gb/s ADM the results of the jitter tolerance simulations show a reduced jitter-related receiver sensitivity penalty for broader control pulses. Optimal operation of the add-drop multiplexer is achieved with the broadest control pulse that is still acceptable for drop operation. The optimum control pulse is found to be approximately 6 ps wide. The RMS timing jitter should be below 900 fs RMS timing jitter to ensure a sensitivity penalty < 1 dB at BER=10^{-9}. The optimum pulse width for best ADM operation at 320 Gb/s is in the range 2.5 to 3.1 ps. Broader or narrower pulse widths lead to an uncleaned time bit slot in the through channel. The RMS timing jitter should be below 150 fs RMS timing jitter to ensure a sensitivity penalty smaller than 1 dB at BER=10^{-9}. A coupler ratio $|K - 0.5| < 0.12$ keeps the BER of the 40 Gb/s channel demultiplexed out of the 160 Gb/s OTDM signal within a 1-dB sensitivity penalty at BER=10^{-9}.

The feasibility of an all-optical OTDM ADM at 160 Gb/s with a 40 Gb/s base rate and at 320 Gb/s with a 10 Gb/s base rate has been experimentally proven. The performance limiting factors are crosstalk from neighboring channels for the drop function and incomplete removal of the dropped channel due to the slopes of the switching window for the through function. The jitter between control and data and an non-optimized K factor further degrades the performance of the ADM.

The results prove that ultra high speed OTDM add-drop multiplexing can be realized using nonlinear fiber, giving a prospect for 640 Gb/s operation. Add-drop multiplexing at 640 Gb/s however requires stricter requirements on dispersion and dispersion slope. Higher bit rates require shorter pulses which means a broader spectrum and an increased influence of the dispersion and the dispersion slope, resulting in a walk-off between control and data signals.

Chapter 5

Four-Wave Mixing

Four-Wave Mixing (FWM) in optical fiber systems can be either useful or harmful, depending on the application. It can induce crosstalk in wavelength division multiplexing (WDM) systems and thus reduce the system performance. On the other hand, in applications like wavelength conversion [117], time demultiplexing [97], parametric amplification [97], phase conjugation, squeezing [118], dispersion monitoring [119] and super continuum generation FWM can play an important positive role. The theory of FWM is more extensively described in paragraph 3.3.3.

In this chapter, an extensive study on FWM in highly nonlinear fiber (HNLF) and its applications for optical time division multiplexing (OTDM) systems are presented. All-optical demultiplexing based on FWM in HNLF is covered in section 5.1. The transmultiplexing from OTDM-to-WDM and from WDM-to-OTDM is described in section 5.2. The results of the research on demultiplexing are published in *[108]* and the results on transmultiplexing in *[120]*. In section 5.3 wavelength conversion for phase modulated signals is discussed. Finally, in section 5.4 some conclusions are drawn.

5.1 Demultiplexing

FWM is an inherently fast process, which makes it suitable for ultra high bit rate signal processing. In [24] demultiplexing from a 500 Gb/s OTDM rate to a 10 Gb/s base rate has been presented based on FWM in a polarization maintaining dispersion shifted fiber (DSF). An intense signal (pump) together with a weaker signal (probe) are required for demultiplexing based on degenerate FWM in a HNLF. The pump signal is a pulse train at a repetition rate equal to the base rate of the OTDM signal. The nonlinear interaction creates a new signal f_{demux} at two times the pump frequency minus the probe frequency according to:

$$f_{demux} = 2 \cdot f_{pump} - f_{probe} \tag{5.1}$$

The FWM mechanism is more extensively explained in section 3.3.3. The frequency f_{demux}, which contains the information of the targeted channel, can be filtered using a common optical band pass filter (OBPF). The FWM-product is only generated when control and OTDM signal overlap in the time domain. When a channel contains a logical zero no FWM-product will be generated. In this way the targeted channel is converted to the new frequency. In a FWM demultiplexer with no walk-off ($t_w = 0$) the switching window has the profile of the square of the control pulse. However, when the control pulse is placed at the zero-dispersion wavelength (λ_0) there is always a walk-off, because the spectral components at the zero-dispersion wavelength travel the fastest. Therefore the width of the switching window is equal to the square of the control pulse plus the walk-off time. The walk-off time can be calculated using equation (3.31). Apart from FWM in fiber, FWM can also be performed in an semiconductor optical amplifier (SOA). In [23] 160 Gb/s to 40 Gb/s demultiplexing has been shown. An SOA can be integrated together with a mode-locked laser (MLL) clock recovery that recovers the clock from the incoming signal and generates short optical pulses at the base rate. In such a way an ADM could be created, for example with a structure as proposed in Figure 5.1.

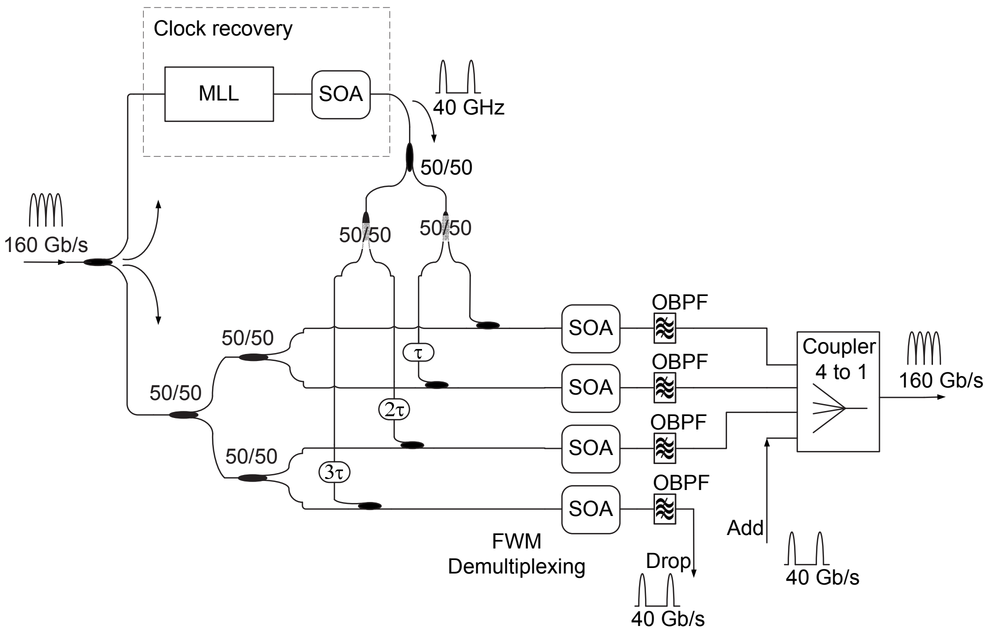

Figure 5.1: A possible add-drop configuration based on FWM in semiconductor optical amplifiers (SOAs). MLL: Mode-locked laser, τ=6.25 ps delay.

5.1.1 160 Gb/s to 10 Gb/s

An experimental setup has been built to test the performance of our HNLF as nonlinear element in a FWM demultiplexer. The demultiplexing in HNLF is more efficient than in normal fiber, therefore shorter lengths of fibers can be used, which increases the robustness. Moreover, it reduces the required optical power levels. The experimental results have been compared with a simulation model that is built in the VPI simulation tool (see Appendix D).

Experimental Results

We have experimentally assessed the feasibility of demultiplexing one 10 Gb/s channel out of a 160 Gb/s OTDM data signal based on FWM in HNLF. The schematic of the setup is shown in Figure 5.2.

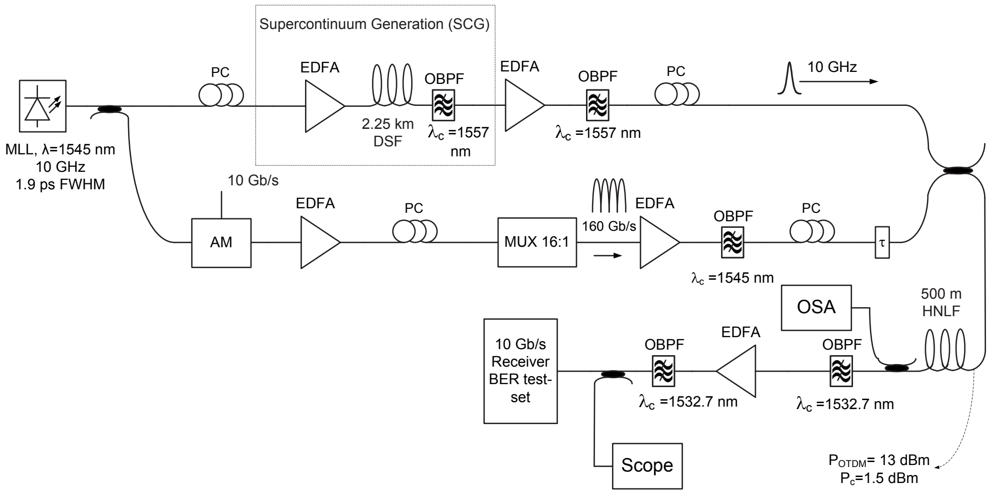

Figure 5.2: Schematic of the experimental setup for demultiplexing one 10 Gb/s channel out of a 160 Gb/s OTDM signal.

The control and OTDM signal are obtained from the same MLL source, by passively splitting the output of the MLL. The pulse train is generated by the MLL at a 10 GHz repetition rate and on a wavelength of 1545 nm. The pulses are converted to 1557 nm to create the control signal at a different wavelength. The wavelength conversion is based on super continuum generation (SCG) in a 2.25 km long DSF, the parameters of this fiber are listed in Table A.3 of Appendix A. The 160 Gb/s OTDM signal is generated by modulating the 10 GHz return-to-zero (RZ) pulse train with a 10 Gb/s pseudo random bit sequence (PRBS) of length $2^7 - 1$ and passively multiplexing this channel up to 160 Gb/s. The OTDM and control signals are amplified and coupled into a 500 m long HNLF. The parameters of this fiber are listed in Table A.1 of Appendix A. A large unwanted spectral broadening of the control pulse spectrum is observed when a high power optical control pulse is used, because the control pulse is in the anomalous dispersion region of the HNLF. Optimal operation is achieved when the pump signal is at the zero-dispersion wavelength (λ_0 = 1545 nm) of the fiber. Therefore an intense OTDM signal is employed as pump signal, combined with a weaker control pulse as probe signal. The FWM mechanism will transfer energy from the strong input signal to the demultiplexing frequency as described in equation (5.1). The average optical power of the OTDM signal at the input of the HNLF is 13 dBm and the average power of the control signal at the input of the HNLF is 1.5 dBm. The resulting FWM product is generated at $f_{demux} = 1532.7$ nm, as is visible in the measured spectrum at the output of the HNLF, depicted in Figure 5.3. The measured spectrum is in good agreement with the results obtained from the simulations, also shown in Figure 5.3. A slightly broader input spectrum in

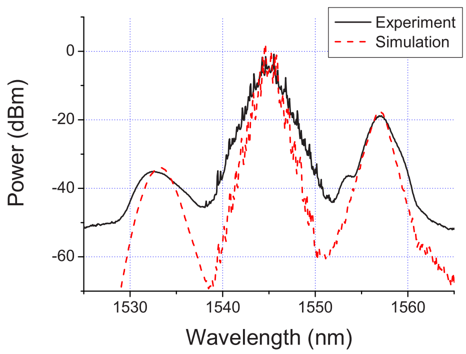

Figure 5.3: Spectrum at the output of the HNLF. The OTDM signal at $\lambda = 1545$ nm and the control pulse at $\lambda = 1557$ nm and the generated FWM product is at $\lambda = 1532.7$ nm (res. bw. =0.06 nm)

the experimental measurement is observed. This is because the actual data pulse is not truly transform-limited as is assumed in our simulations. The eye diagram of the demultiplexed channel is shown in Figure 5.4. The BER of the demultiplexed channel at 10 Gb/s is shown in Figure 5.5, compared with a B2B signal at 10 Gb/s. The BER curve of the demultiplexed channel is the average of all 16 channels. The sensitivity penalty at BER=10^{-9} is 2 dB. Upgrading to a 40 Gb/s base rate would not require an increase in power, because in this case the OTDM signal is employed as pump signal. A comparison of the above described demultiplexing experiment with similar experiments using a NOLM and/or employing XPM spectral broadening is presented in *[108]*.

5.2 Transmultiplexing

An extension of the network capacity by increasing the number of wavelengths also enlarges the complexity of optical cross-connects. Hybrid WDM/OTDM networks will reduce the management complexity of WDM networks. In these hybrid networks the conversion between WDM and OTDM signal formats plays an important role. In all of the previously presented research activities on conversion from WDM-to-OTDM [121–126], conversion from a NRZ WDM signal to a RZ WDM signal has

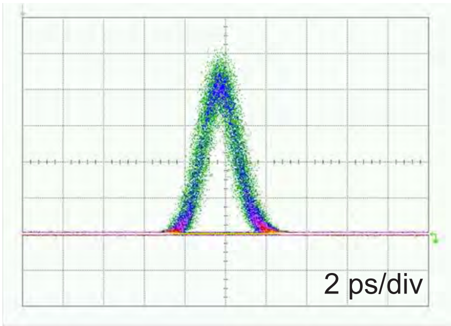

Figure 5.4: Eye diagram of the demultiplexed channel from 160 Gb/s to 10 Gb/s based on FWM in HNLF. Pulse width demultiplexed channel: $T_{fwhm} = 2$ ps.

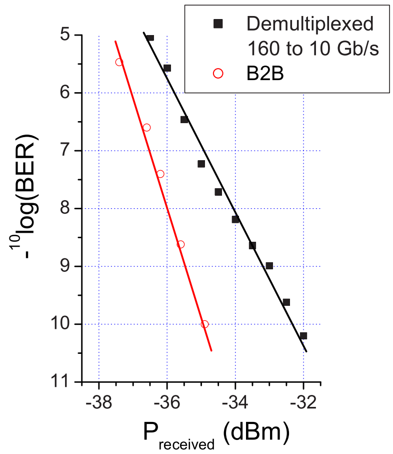

Figure 5.5: BER performance of demultiplexing from 160 Gb/s to 10 Gb/s.

to be performed at first, or a RZ WDM signal is assumed [127–129]. A diversity of conversion processes have been proven to be successful to convert from WDM-to-OTDM, such as in a saturable absorber (SA) [125], semiconductor optical amplifier (SOA) [122, 130], an electroabsorption modulator (EAM) [128], a nonlinear optical loop mirror (NOLM) [41, 127, 129] or in a highly nonlinear fiber (HNLF) based on cross-phase modulation (XPM) [123]. Conversion from OTDM-to-WDM and from WDM-to-OTDM has recently received renewed interest because of the feasibility to develop all optical add-drop multiplexers [40, 41, 125]. In [131] conversion from an OTDM signal to a WDM signal has been shown based on FWM in a HNLF, but no conversion from WDM-to-OTDM. However, to really improve the network flexibility by switching between OTDM and WDM networks, both the conversion from OTDM-to-WDM and from WDM-to-OTDM should be studied. In section 5.2.1 the OTDM-to-WDM conversion concept is shown by simulations and in section 5.2.2 we take a deeper look at the WDM-to-OTDM conversion.

5.2.1 OTDM-to-WDM Conversion

In [131] OTDM-to-WDM conversion is demonstrated by demultiplexing from 160 Gb/s to 4×40 Gb/s with 200 GHz spacing by using FWM in a 400 m long HNLF. The HNLF used in their experiment had a nonlinear coefficient $\gamma = 10.8$ $W^{-1}km^{-1}$ and a zero dispersion wavelength $\lambda_0 = 1546.05$ nm. To minimize the crosstalk in the demultiplexed channels, a 0.6 nm band pass filter was applied. This leads to a large increase in pulse width, but this is tolerable when we bear in mind that the demultiplexed channels are further processed at the 40 Gb/s base rate instead of the

160 Gb/s OTDM line rate. However, to return back from WDM-to-OTDM the pulse width needs to be compressed again. In this section the feasibility of the OTDM-to-WDM conversion based on FWM in our HNLF (see Table A.1) is shown for a 160 Gb/s OTDM signal with a 40 Gb/s base rate by simulations in VPI.

Simulations have been performed to simultaneously demultiplex the 160 Gb/s OTDM signal to 4 × 40 Gb/s base rate channels at four different wavelengths by applying FWM in HNLF. The demultiplexed channels can be selected by using four OBPFs with center frequencies at the FWM products. A schematic of the simulation setup is shown in Figure 5.6. Four clock signals at 40 GHz are required. The clock pulses can be generated with an MLL clock recovery in combination with SCG and spectral slicing *[132]*, or by four independent MLLs operating at the required wavelengths. The four clock pulses are combined and timing was adjusted for each clock signal so that they were separated from each other by approximately 6.25 ps.

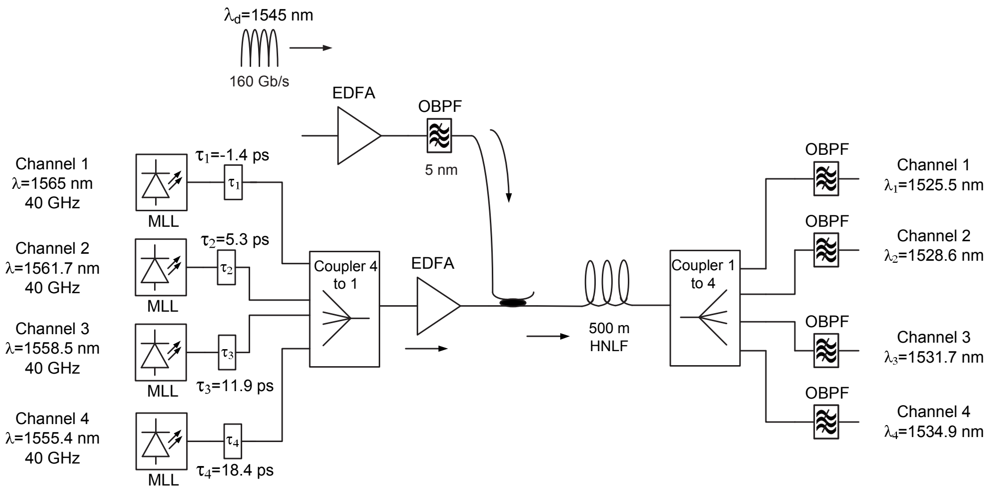

Figure 5.6: Setup of the simulation for simultaneous demultiplexing 4 × 40 Gb/s out of a 160 Gb/s OTDM signal by FWM with 4 × 40 GHz control signals.

The wavelength of the input OTDM signal at 160 Gb/s OTDM is $\lambda_d = 1545$ nm, such that it coincides with the zero-dispersion wavelength of our HNLF, to achieve phase-matching. The pulse width of the OTDM signal is 2 ps. The wavelengths of the control pulses are spaced by 400 GHz and are at 1565, 1561.7, 1558.5 and 1555.4 nm respectively, and the pulse width is 3 ps FWHM. The spectrum at the input of HNLF is shown in Figure 5.7. The four-wave mixing products are generated at the wavelengths: 1525.5, 1528.6, 1531.7 and 1534.9 nm. The spectrum at the output of $HNLF_1$ can be seen in Figure 5.8.

The average input power of the 160 Gb/s OTDM signal was 12 dBm, and the input power of the 4 × 40 GHz control signal was 10 dBm. To optimize the interaction between data and control pulse we have to consider the walk-off time between the OTDM signal and the control pulses. The walk-off time between control pulses and

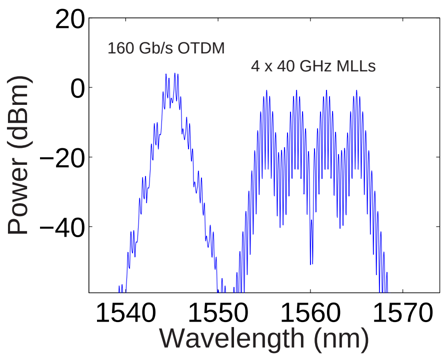

Figure 5.7: Spectrum at the input of the HNLF.

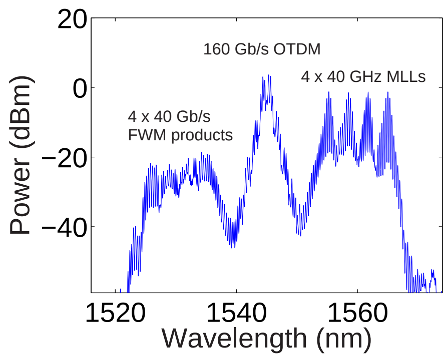

Figure 5.8: Spectrum after transmission through the HNLF.

data signal can be calculated by equation (3.31). The walk-off times for the control pulses 1 to 4 are respectively: $t_{w_1} = 2.8$ ps, $t_{w_2} = 1.9$ ps, $t_{w_3} = 1.2$ ps and $t_{w_4} = 0.7$ ps. The control pulses travel slower through the HNLF, so they are given a time-offset that is equal to half of the walk-off time plus the offset for the bit position. The time-offset can be seen in Figure 5.6. The time-offset for the first channel equals $t_{w_1}/2$ and the time-offset for channels 2,3 and 4 are $6.25 + t_{w_2}/2 = 5.3$ ps, $2 * 6.25 + t_{w_3}/2 = 11.9$ ps and $3 * 6.25 + t_{w_3}/2 = 18.4$ ps, respectively. The four simultaneously demultiplexed channels are visualized in Figures 5.9-5.12. The filter that is used for the selection of the FWM products is a trapezium-shaped OBPF. The bandwidth of the filter is 200 GHz (≈ 1.6 nm). The eyes are clear and open, which confirms good operation. The influence of the walk-off on the demultiplexed channels can be explained as a reduction of the conversion efficiency. The demultiplexed channel that is the farthest away from the zero-dispersion wavelength contains the lowest optical power.

5.2.2 WDM-to-OTDM Conversion

A logical next step after conversion from OTDM-to-WDM based on FWM in HNLF is to consider the opposite case, WDM-to-OTDM. The same nonlinear medium (HNLF) and nonlinear phenomenon (FWM) can be used to perform the conversion from WDM-to-OTDM. This technique has the ability to convert at high data rates due to the ultrafast fiber nonlinearities. Furthermore, FWM preserves both the amplitude and phase information. This is advantageous because of recent interest in advanced modulation formats such as RZ differential phase shift keying (RZ-DPSK) systems [133]. Moreover, the conversion process does not require conversion of the WDM channel from NRZ to RZ before the WDM-OTDM transmultiplexing. A conceptual diagram of our operation principle for WDM-to-OTDM conversion is shown in Figure 5.13. Two WDM channels ($f_1 + f_2$) operating at 10 Gb/s NRZ are overlapped in time with two control signals ($\text{control}_1 + \text{control}_2$). The control signals are the high power pumping signals and the WDM signals are the probe signals. The non-

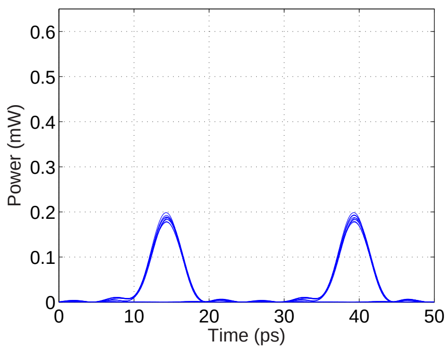

Figure 5.9: Demultiplexed channel 1 at wavelength $\lambda_1 = 1525.5$ nm.

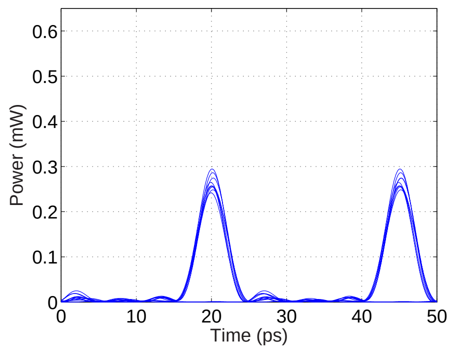

Figure 5.10: Demultiplexed channel 2 at wavelength $\lambda_2 = 1528.6$ nm.

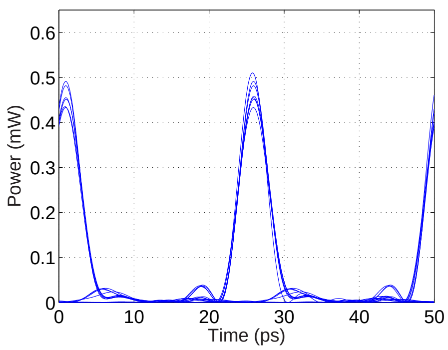

Figure 5.11: Demultiplexed channel 3 at wavelength $\lambda_3 = 1531.7$ nm.

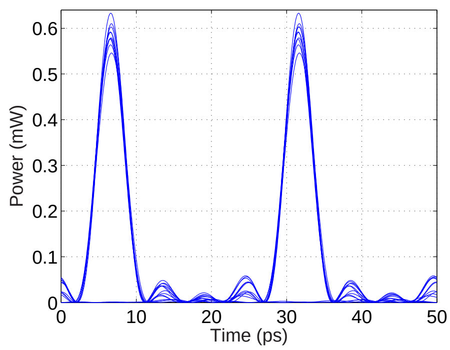

Figure 5.12: Demultiplexed channel 4 at wavelength $\lambda_4 = 1534.9$ nm.

linear interaction between WDM f_1, f_2 and control$_1$ and control$_2$ respectively in the HNLF creates a FWM product at a new frequency (f_{FWM}). The FWM product of WDM f_1 and control$_1$ is the same as the FWM product of WDM f_2 and control$_2$. The FWM products that arise because of interaction between f_1 and control$_2$ and between f_2 and control$_1$ are undesired rest products. The FWM efficiency is close to 1 for wavelengths close to the zero-dispersion point and the generated FWM product can therefore contain considerable power.

Simulations

Simulations have been performed for the 2×10 Gb/s WDM conversion to a 20 Gb/s OTDM signal. Simulations have been performed in VPI. The two WDM channels are at the wavelengths 1555.74 nm and 1558.92 nm, respectively. The wavelengths of the WDM channels correspond to the center frequencies of a WDM demultiplexer, also used in the experiments. The control signals are 6 ps FWHM secant-shaped

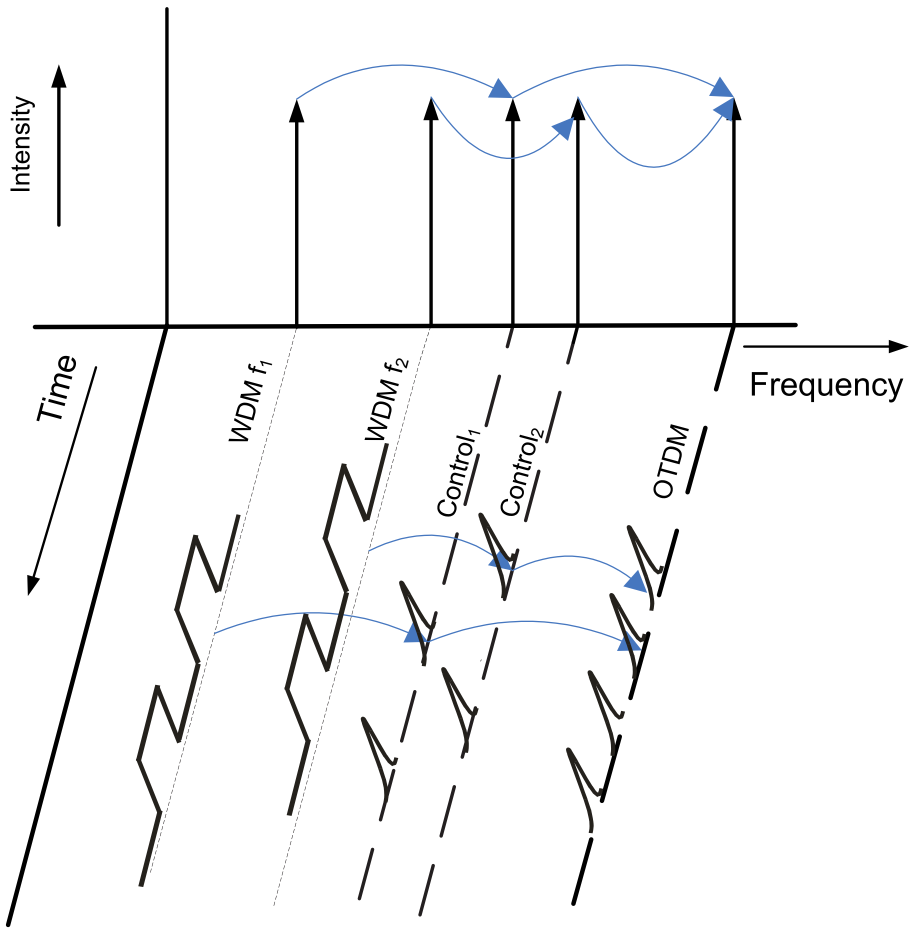

Figure 5.13: Schematic of the operation principle of WDM to OTDM conversion based on FWM.

pulse trains. The wavelengths of the control signals are 1549.15 nm and 1550.78 nm, respectively. The WDM signal and the control pulses are combined and inserted into a 500 m long HNLF. The parameters of this HNLF are listed in Table A.1. The FWM product generated at $\mathrm{f_{OTDM}}=2\cdot\mathrm{f_{control_1}}-\mathrm{f_{WDM_1}}$ = 1543 nm contains the 20 Gb/s OTDM signal. The power at the input of the HNLF is 9 dBm for both 10 GHz control signals and -1.1 dBm and 0.7 dBm for $\mathrm{WDM_1}$ and $\mathrm{WDM_2}$, respectively. The spectrum of the signal at the input and at the output of the HNLF is shown in Figure 5.14. The FWM product at λ = 1543 nm is clearly visible in the output spectrum. However unwanted FWM products are also created. For example the mixing of the 1558.92 and 1549.15 nm creates a FWM product at λ = 1539.4 nm. The output signal is filtered at 1543 nm with a 300 GHz OBPF. The eye diagram of the converted OTDM signal is depicted in Figure 5.15.

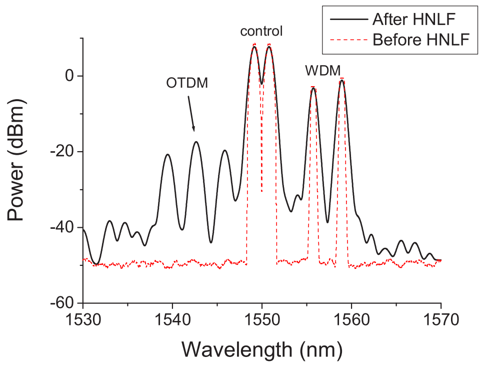

Figure 5.14: Spectrum at the input and at the output of the HNLF.

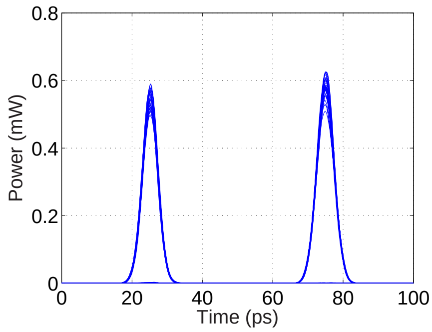

Figure 5.15: OTDM signal at 1543 nm at the output of the HNLF filtered with a 300 GHz OBPF.

Experiments

Figure 5.16 shows the experimental setup. The two 10 Gb/s WDM channels, tributaries of the resulting 20 Gb/s OTDM signal, are operated at the wavelengths 1555.74 and 1558.92 nm. The two control signals, operating at 1549.32 and 1550.92 nm, consist of a train of pulses at a 10 GHz repetition rate with a full width half maximum (FWHM) of 5.5 ps and are generated by spectral slicing of a super continuum (SC) spectrum. The SC generation takes place in 2.25 km long dispersion shifted fiber (γ=2.6 $W^{-1}km^{-1}$). The parameters of this fiber are listed in Table A.3. The output of the DSF is spectrally sliced by a 0.9 nm dielectric thin film band pass filter that is incorporated in a WDM demultiplexer. Both control signals are automatically synchronized with each other, because they are extracted from the same SC source. The synchronization between the WDM channels and the control signals is accomplished via tunable delay lines. The WDM signals are manually tuned such that the middle of the NRZ bit frame overlaps with the appropriate control pulse. The timing between WDM signal and the control pulse is correct as long as the control pulse does not overlap with the crossover point of the WDM signal. Both control signals are used as pumping wavelengths to generate the FWM product. The control signals and the WDM channels are combined in a WDM-multiplexer, before they are launched into the 500 m long HNLF. The average optical power of the control signals, WDM f_1 and WDM f_2 was 12.5, 10.8 and 7.8 dBm, respectively. The parameters of the HNLF used in our experiments are listed in Table A.1. At the output of the HNLF an OBPF is used to select the targeted FWM product. To assess the quality of the created OTDM signal, the 20 Gb/s OTDM signal was demultiplexed to one of the 10 Gb/s tributaries by gating an EAM with a 10 GHz RF signal. Using an optical tunable delay line, we can choose the targeted 10 Gb/s tributary for demultiplexing. The switching window of the EAM demultiplexer is 30 ps. The demultiplexed signal was then inserted into a receiver consisting of an optical preamplifier, a 3 nm OBPF and a photodiode with data and clock recovery to evaluate the BER.

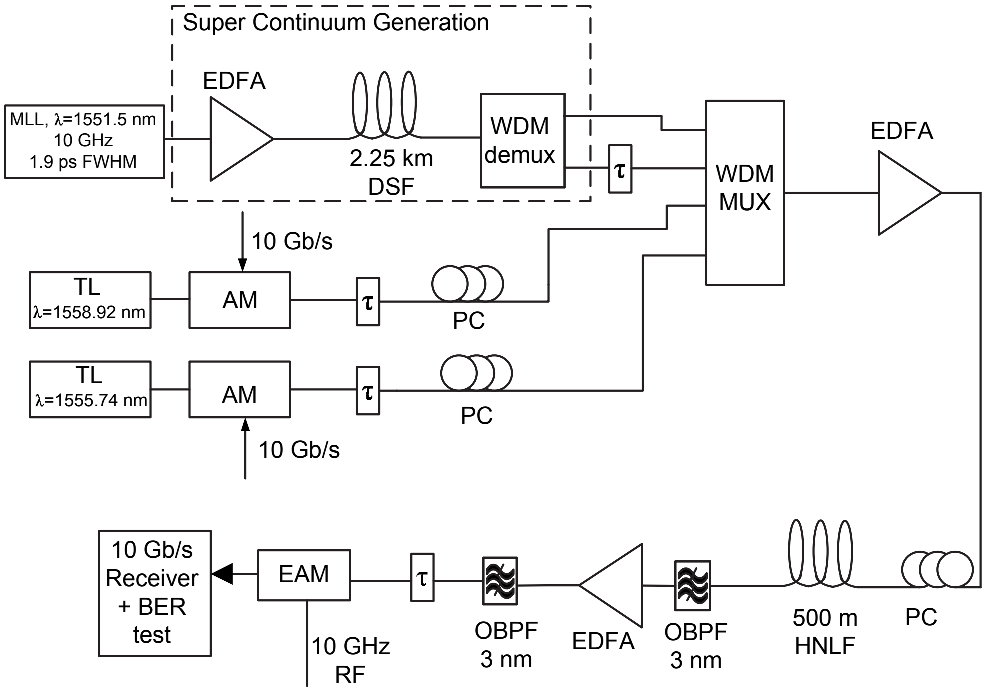

Figure 5.16: Experimental setup of transmultiplexing 2×10 Gb/s WDM to 20 Gb/s OTDM based on FWM in HNLF, τ: optical tunable delay line.

Figure 5.17(a) shows the eye diagrams of the two time interleaved control pulses. The power of both control pulses is 1.7 pJ (12.5 dBm) per pulse. The WDM signals were generated with two separate 10 Gb/s external modulators. Figure 5.17(b) shows the eye diagrams of the two WDM input signals. The wavelengths of the 10 Gb/s NRZ signals are 1555.74 nm and 1558.92 nm. The extinction ratio of the WDM channels are 18.7 and 17.5 dB respectively. The spectrum at the output of the HNLF is shown in Figure 5.18. Besides the FWM product at 1542.92 nm, the undesired mixing products of WDM f_1 and $control_2$ at 1539.7 nm, and WDM f_2 and $control_1$ at 1546.1 nm, also appear. Polarizations of the input signals were optimized to maximize the targeted FWM product at 1542.92 nm. Nevertheless, the scheme could be made polarization independent by applying a polarization-diversity configuration as in [134]. The eye diagram of the converted 20 Gb/s OTDM signal is depicted in Figure 5.19(a). The power of the received 20 Gb/s OTDM signal was -4.8 dBm and the pulse width was 4.2 ps. The conversion efficiency G_c is defined as the ratio between the received signal power and the signal power at the input of the HNLF. We measured this factor to be $G_c = -17.4$ dB for both wavelength channels. The main reason for this low efficiency is because of the conversion from NRZ (100 ps) to RZ (4.2 ps) signals. Also, part of the signal power is leaking to the unwanted FWM products, which reduces the conversion efficiency. The eye diagrams of both 10 Gb/s demultiplexed OTDM

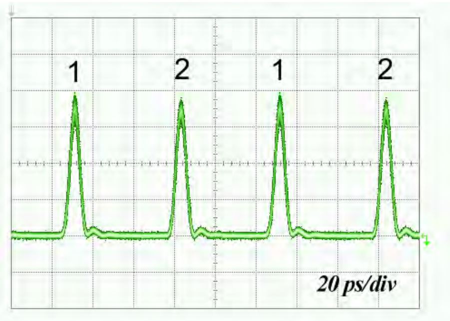

(a) Two time interleaved 10 GHz control signals at 1549.32 and 1550.92 nm.

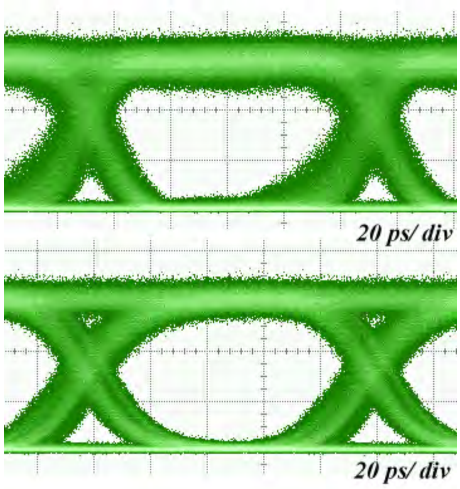

(b) 1555.74 nm (upper) and 1558.92 nm (lower) NRZ 10 Gb/s.

Figure 5.17: Eye diagrams of the 20 GHz control signal (a) and the input WDM signals (b).

channels are shown in Figures 5.19(b) and 5.19(c). The BER curves of the two OTDM channels are compared with those of the WDM back-to-back (B2B) signals and a 10 Gb/s RZ B2B signal (see Figure 5.20). A significant improvement of the BER is observed, because the receiver sensitivity for RZ signals is higher. Comparing the converted signals with the 10 Gb/s RZ B2B signal, a small penalty of 1 dB at BER $= 10^{-9}$ is observed. Our WDM-to-OTDM conversion concept has been published in *[120]*.

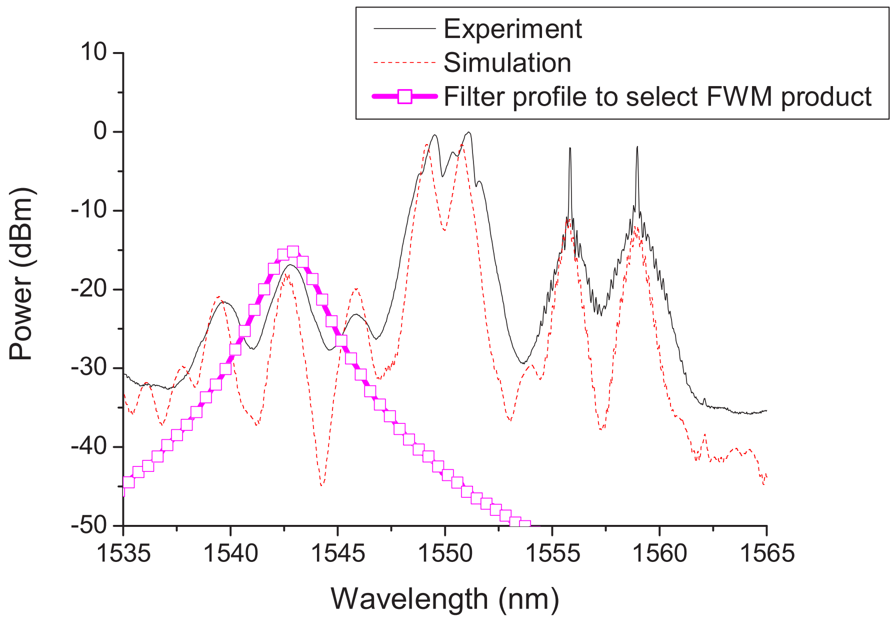

Figure 5.18: Spectrum at the output of the HNLF, simulation (dashed) and experimental (solid) (res. bw= 0.06 nm). The profile of the filter to select the FWM product is also depicted (squares).

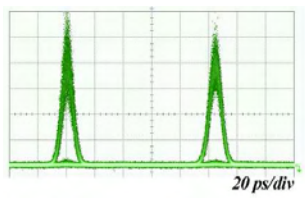

(a) 20 Gb/s OTDM signal

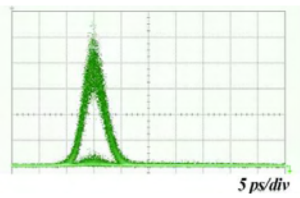

(b) 10 Gb/s signal originating from the 1555.74 nm WDM signal.

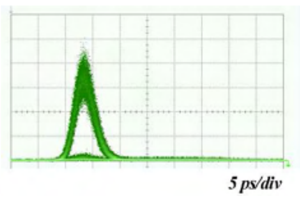

(c) 10 Gb/s signal originating from the 1558.92 nm WDM signal.

Figure 5.19: Eye diagram of the 20 Gb/s OTDM (a), demultiplexed signal from 20 Gb/s to 10 Gb/s originating from the 1555.74 nm (b) and 1558.92 nm WDM signal (c).

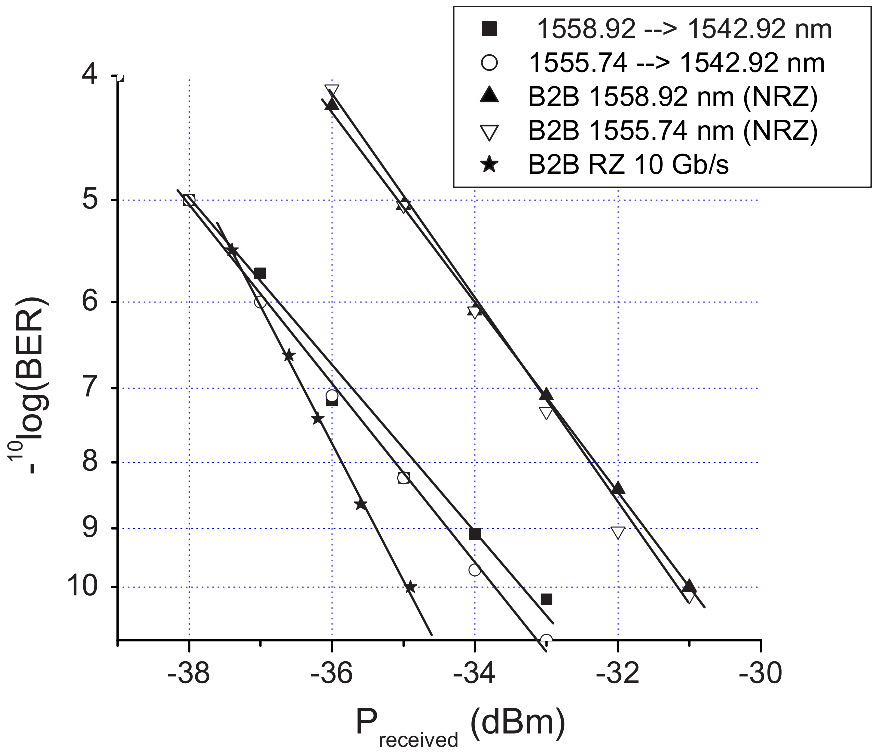

Figure 5.20: BER of the two 10 Gb/s channels, after WDM-to-OTDM transmultiplexing compared to B2B.

4 × 40 Gb/s WDM to 160 Gb/s OTDM

To investigate the possibility of upgrading the WDM-to-OTDM conversion based on FWM in HNLF towards a 160 Gb/s system, simulations of transmultiplexing a 4×40 Gb/s WDM signal to a 160 Gb/s OTDM signal have been performed. The four 40 GHz control pulses are placed close to the zero-dispersion wavelength of the fiber, in order to achieve nearly phase matched FWM. A MLL clock recovery can be used to generate a control pulse train at one wavelength. The control pulses at the other wavelengths can be generated by applying SCG and spectral slicing *[132]*. A second option for the generation of the four control signals is to use four MLL clock recovery devices. The setup of the simulation is shown in Figure 5.21. The width of the control

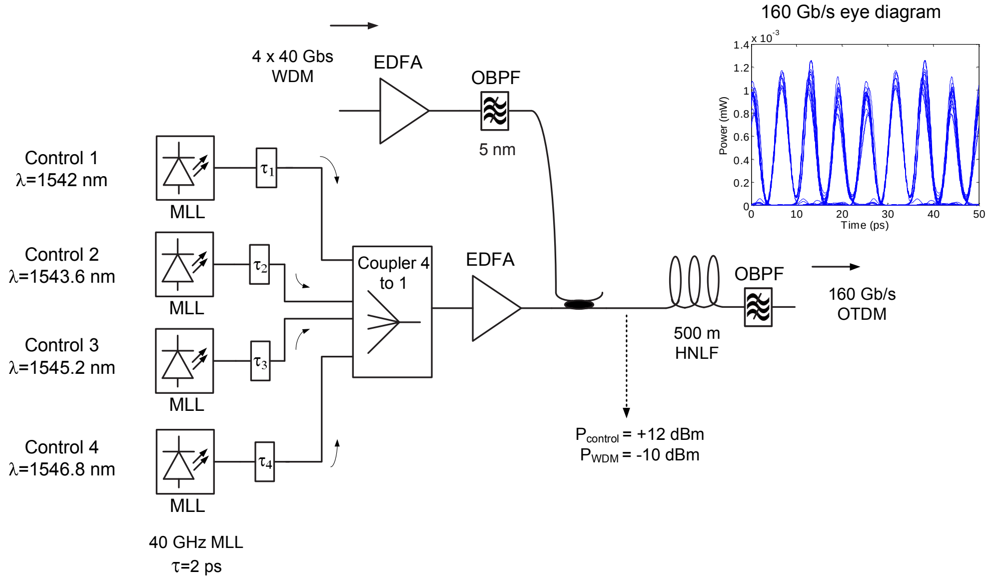

Figure 5.21: Schematic of the simulation setup for transmultiplexing a 4×40 Gb/s NRZ WDM signal to a 160 Gb/s OTDM signal.

pulse is 2 ps FWHM. The 4×40 GHz control pulses are used as pumping signal. The transmultiplexing would not work if the WDM channels are used as the pumping signal because the WDM channels will create strong FWM products by interaction with the other WDM channels. The spectrum at the input of the HNLF is shown in Figure 5.22 and the spectrum after transmission through the HNLF is shown in Figure 5.23. The four 40 GHz control signals were emitted at a 200 GHz spaced wavelength grid. The wavelengths of the control pulses are at 1542, 1543.6, 1545.2 and 1546.8 nm, respectively. The WDM signals are placed at a 400 GHz grid, and are located at the wavelengths: 1550, 1553.2, 1556.4 and 1559.6 nm. The control signals are amplified to 12 dBm average power and the average power of the WDM signals is -10 dBm. The resulting 160 Gb/s OTDM signal at $\lambda = 1534$ nm is shown in the inset in Figure 5.21. A trapezium shaped 300 GHz bandwidth OBPF is used to select the

160 Gb/s OTDM signal. The received power of the OTDM signal is -36 dBm. The received power is very low and a very sensitive amplifier with a very low noise figure is required to amplify this signal.

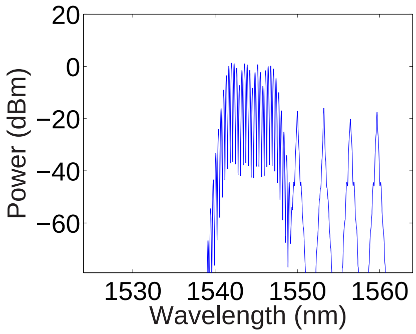

Figure 5.22: Spectrum at the input of the HNLF.

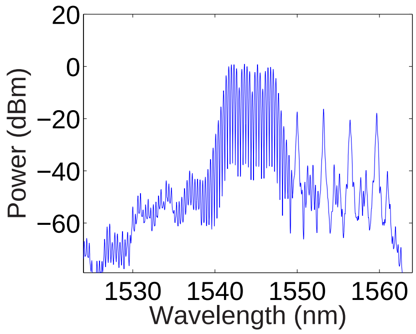

Figure 5.23: Spectrum after propagating through the HNLF.

Several problems appear when the WDM-to-OTDM transmultiplexing scheme is upgraded to 160 Gb/s:

- Higher bit rates require narrower control pulses. Narrower control pulses have a larger spectral bandwidth and a higher peak power making them more sensitive to XPM and SCG.
- The WDM channels produce FWM products with the other WDM channels. These unwanted mixing products can be clearly seen in the spectrum at the output of the HNLF (Figure 5.23). These unwanted FWM products can overlap with the original data and control signals. Crosstalk from the unwanted FWM products leads to signal-to-noise ratio (SNR) reduction. Careful optimization of the wavelength grid and/or unequal spacing of the channels can reduce the influence of this noise source.
- A narrow control pulse has a large spectral width, which requires that the control channels are spaced further apart than in the case of a broader control pulse. Otherwise FWM products arising from control pulses with un-targeted WDM channels will arise within the bandwidth of the transmultiplexed OTDM signal.
- An increased number of WDM channels leads to an increased number of control signals. Applying more WDM channels and control signals reduces the conversion efficiency, because the power is divided among more un-targeted FWM products. This resulted in a low output power (-36 dBm) of the OTDM signal.

All these disadvantages eventually lead to an error floor for transmultiplexing to 160 Gb/s as can be seen in Figure 5.24. The received average optical power versus the BER is shown for transmultiplexing from 4×40 Gb/s WDM to 160 Gb/s OTDM and is compared with transmultiplexing from 2×40 to 80 Gb/s and with a 40 Gb/s NRZ-B2B and RZ-B2B signal.

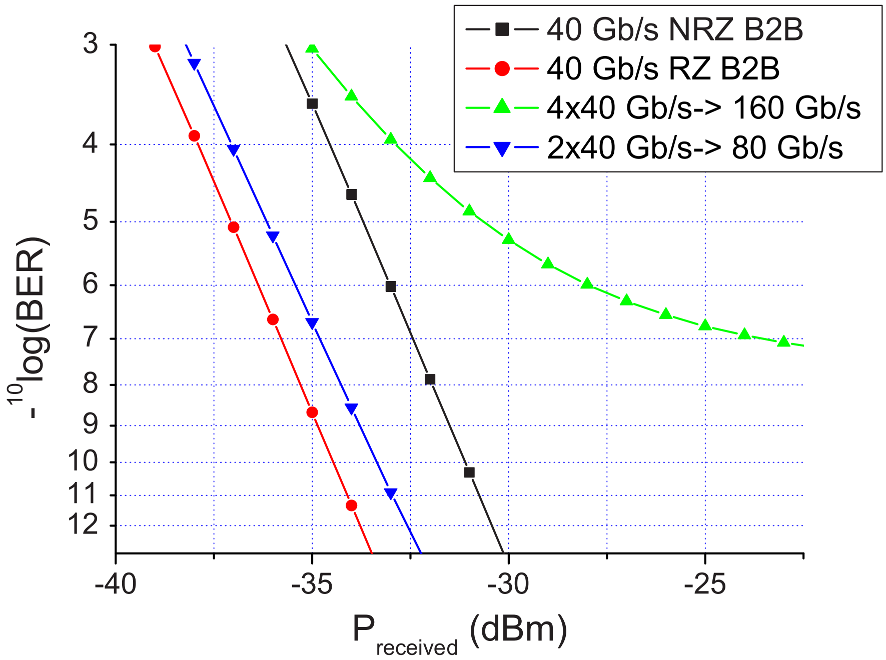

Figure 5.24: Received optical power versus the BER for transmultiplexing from 2 × 40 Gb/s to 80 Gb/s and 4 × 40 to 160 Gb/s, compared to a RZ and NRZ B2B signal.

5.3 RZ-DPSK Wavelength Conversion

FWM preserves both amplitude and phase information, which makes the process format independent. To provide validation of the format independence of our WDM-to-OTDM conversion concept, a proof-of-principle experiment for a RZ-DPSK wavelength converter based on FWM in HNLF is conducted. The wavelength converter converts a 10 Gb/s RZ-DPSK signal at the wavelength $\lambda = 1540.6$ nm to a new wavelength: $\lambda = 1549.6$ nm.

5.3.1 Transmitter

Our mode-locked lasers do not have phase stability from pulse to pulse, which is required for DPSK modulation. To be able to still work with RZ-DPSK signal formats, at first a conversion to a phase stable signal has to be performed. Any wavelength conversion process that copies only the envelope of the pulse and not the phase information to a phase stable continuous wave (CW) pump signal can be used for this purpose. In the experiments presented here the wavelength conversion to a phase

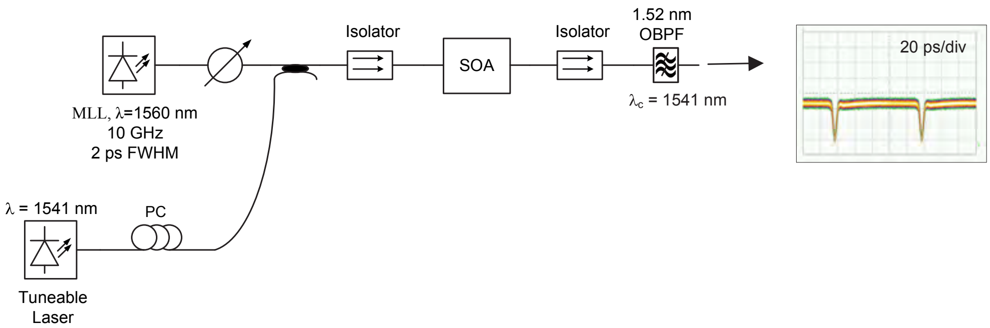

Figure 5.25: Schematic of the phase stable RZ-transmitter based on wavelength conversion in a single SOA plus OBPF.

stable 10 GHz RZ signal is performed in a single SOA [135]. The schematic of the transmitter is shown in Figure 5.25. In the SOA the inserted 10 GHz signal modulates the SOA carriers and thus the SOA gain. As a result, the CW probe light is modulated via cross-gain modulation, causing a pulse-inverted wavelength conversion. Furthermore, the injected 10 GHz signal also modulates the refractive index of the SOA. This results in a red frequency shift on the leading edge of the pulse and a blue shift on the trailing edge. As a consequence the spectrum of the probe light is broadened. The slow recovery of the gain of the SOA has been avoided by using the ultrafast component of the wavelength chirp ($\Delta\lambda \sim dg/dt$) that occurs during gain saturation. An OBPF at the blue-shifted sideband of the probe light selects this transient chirp component, which contains only the envelop of the original 10 GHz signal. The -3 dB bandwidth of the OBPF is 1.52 nm. By careful tuning the shape of the filter the system can be optimized in such a way that the slow gain recovery tail is completely compensated. A delayed interferometer is used to convert the inverted signal to a non-inverted signal. The schematic of the polarization delayed interferometer is shown in Figure 5.26. The interferometer used in this setup consists

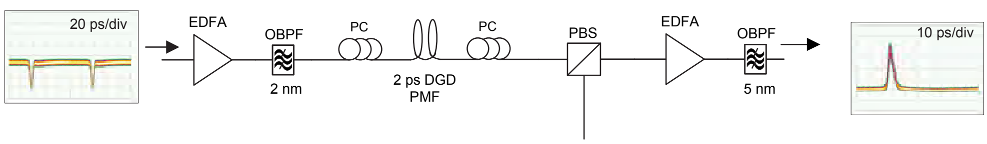

Figure 5.26: Schematic of the polarization delayed interferometer.

of a polarization controller (PC), a 2 ps differential group delay (DGD) polarization maintaining fiber (PMF) followed by another PC and a polarization beam splitter (PBS). The 2 ps DGD acts as a delay between the two principle state of polarizations (SOPs).

5.3.2 Receiver

The experimental setup of the RZ-DPSK receiver is shown in Figure 5.27. The receiver consists of an optical preamplifier, a 1 nm OBPF followed by a PC and a polarization dependent home-made Mach-Zehnder interferometer (MZI). After the MZI the phase information is converted to amplitude information and the signal is sent to a photodiode with data and clock recovery to evaluate the BER. The MZI is a 1-bit delay (100 ps) interferometer. The delay in one arm of the interferometer with respect to the other arm is 98.8 ps, which corresponds to $f = 10.122$ GHz. As a result the repetition frequency of our pulse source is changed to this value. We measured a 1 dB insertion loss and a 10 dB extinction ratio for the MZI. A schematic of an MZI is shown in Figure 5.28. After the MZI the signal is split and the power sent to the photodiode is controlled by a power monitoring unit and is kept constant at -5 dBm.

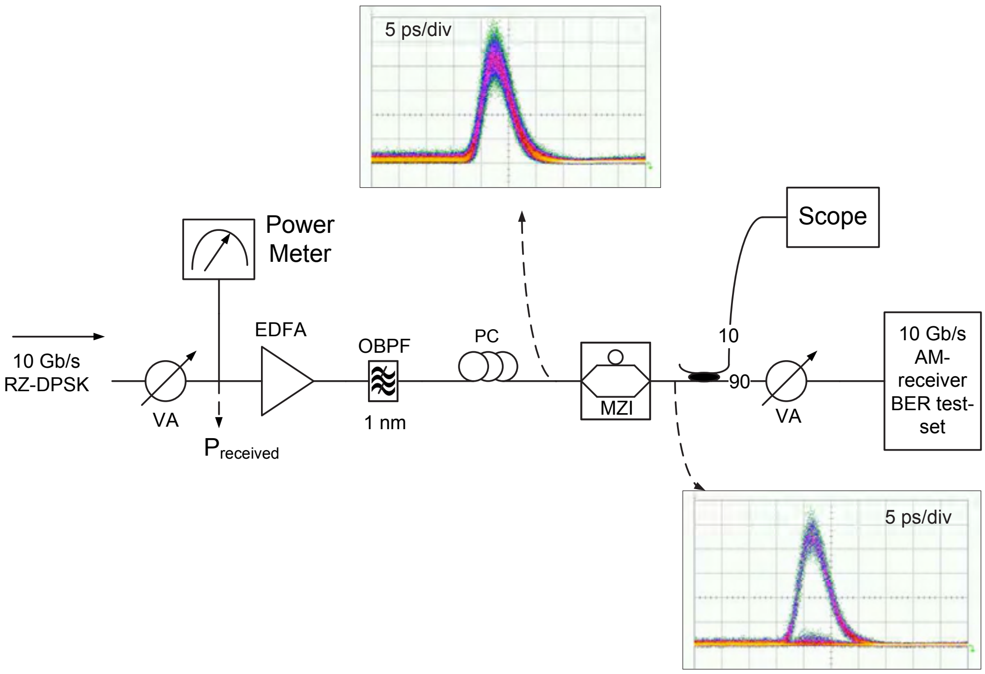

Figure 5.27: Schematic of the experimental setup for the DPSK receiver

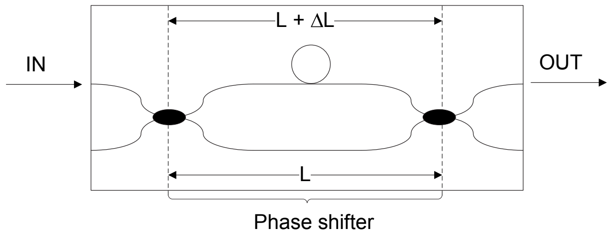

Figure 5.28: Schematic of the MZI used for a 10 Gb/s DPSK receiver. ΔL is the extra distance in the upper arm that corresponds to a delay of the optical signal of 100 ps.

The phase-to-amplitude conversion in a MZI can be understood by looking at the propagation matrix of this interferometer. The propagation matrix for a 3 dB coupler describing the relation between the input and output electrical fields can be described as [136]:

$$\underline{M}_{coupler} = \frac{1}{\sqrt{2}} \begin{pmatrix} 1 & -i \\ -i & 1 \end{pmatrix} \tag{5.2}$$

The matrix for the propagation in the two arms of the MZI contains the delay in one of the arms and can be described as:

$$\underline{M}_{\Delta\phi} = \begin{pmatrix} \exp(i\omega\tau) & 0 \\ 0 & 1 \end{pmatrix} \tag{5.3}$$

where τ is the delay in the upper arm caused by ΔL, see Figure 5.28. For the total transmission through the MZI we can write:

$$\begin{aligned} \underline{M} &= \underline{M}_{coupler} \cdot \underline{M}_{\Delta\phi} \cdot \underline{M}_{coupler} \\ &= \frac{1}{2} \begin{pmatrix} \exp(i\omega\tau) - 1 & -i\exp(i\omega\tau) - i \\ -i\exp(i\omega\tau) - i & -\exp(i\omega\tau) + 1 \end{pmatrix} \end{aligned} \tag{5.4}$$

The field at the output of the MZI can be written as $\underline{E}_{out} = M \cdot \underline{E}_{in}$. In this particular setup only one arm of the MZI input and output are used. The input field $\underline{E}_{in}$ can thus be written as:

$$\underline{E}_{in} = \begin{pmatrix} E_{in,1} \\ E_{in,2} = 0 \end{pmatrix} \tag{5.5}$$

which leads to the following equation for $E_{out,1}$:

$$E_{out,1} = \frac{1}{2} \left(\exp(i\omega\tau) - 1 \right) E_{in,1} \tag{5.6}$$

From equation (5.6) it can be seen that if $E_{in,1} \cdot \exp(i\omega\tau)$ and $E_{in,1}$ have equal phases they cancel each other out. On the other hand the output will be maximized when the phase difference between $E_{in,1} \cdot \exp(i\omega\tau)$ and $E_{in,1}$ equals π.

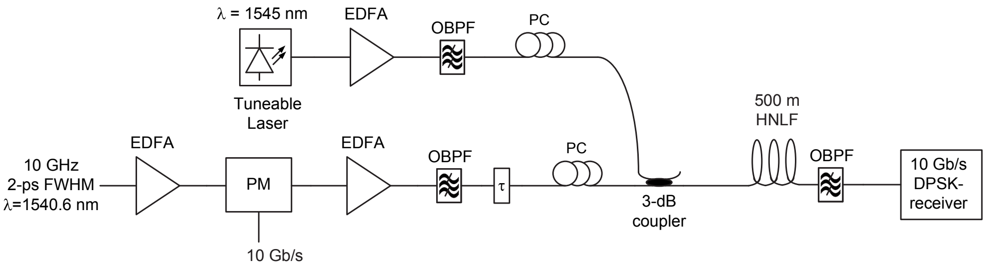

Figure 5.29: Schematic of the experimental setup for wavelength conversion of a 10 Gb/s RZ-DPSK signal based on FWM in a HNLF.

5.3.3 Results

The schematic of the experimental setup is shown in Figure 5.29. The phase stable RZ pulses at $\lambda = 1540.6$ nm are modulated by our $LiNbO_3$ 10 Gb/s phase modulator (PM). The 1540.6 nm 10 Gb/s RZ-DPSK signal is combined with a $\lambda = 1545$ nm CW signal. This CW signal acts as the pump signal for the FWM process in the HNLF. The targeted FWM product is generated at the wavelength $\lambda_{FWM} = 2 \cdot \lambda_{CW} - \lambda_{RZ-DPSK} = 1549.6$ nm. At the output of the HNLF the FWM product is selected by filtering the subsequent wavelength with an OBPF. In the experiments a cascade of three OBPFs is required to suppress the much stronger CW and input signal. The spectrum at the output of the HNLF is shown in Figure 5.30. Besides the FWM product at $\lambda_{FWM} = 1549.6$ nm also a FWM product at the wavelength $\lambda = 2 \cdot \lambda_{RZ-DPSK} - \lambda_{CW} = 1536.2$ nm appears. The FWM product at $\lambda = 1536.2$ nm is even stronger than at $\lambda_{FWM} = 1549.6$ nm. This is due to the high peak power in the RZ-DPSK signal, making this a pumping signal. Although the FWM product at $\lambda = 1536.2$ nm is stronger, it does not contain the phase information of the input RZ-DPSK signal. The strength of the FWM product at $\lambda = 1536.2$ nm can be approximated by equation (3.52). The phase of the product is given by $\phi = 2\phi_{RZ-DPSK} - \phi_{CW}$. The data information of the RZ-DPSK input signal is incorporated into the phase of this signal: $\phi_{RZ-DPSK} = 0$ or π. As a result, the phase of $\lambda = 1536.2$ nm includes $2 \cdot \phi_{RZ-DPSK} = 0$ or 2π and as a consequence the phase information is lost. After the wavelength conversion the converted RZ-DPSK signal is sent to the RZ-DPSK receiver. The power of the received FWM product is measured on the optical spectrum analyzer (OSA) with a 2 nm resolution. The power at $\lambda_{FWM} = 1549.6$ nm at the output of the HNLF is -25 dBm, and the power of the RZ-DPSK signal at the input of the HNLF is 6.6 dBm. The conversion efficiency of this FWM wavelength conversion process is thus measured to be -31.6 dB. To improve the conversion efficiency, the power of the RZ-DPSK signal should be reduced and the power of the pumping CW signal should be increased. In theory conversion efficiencies larger than 1 can be obtained [97].

The quality of the wavelength converted signal is assessed by a BER measurement. The point of received power is defined at point $P_{received}$, as depicted in Figure 5.27. The same receiver configuration is employed for the measurement of the B2B 10 Gb/s

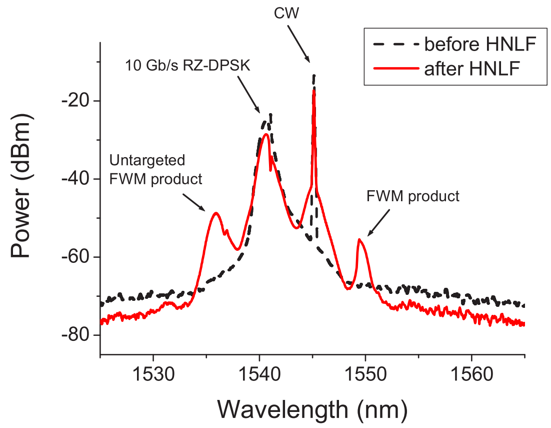

Figure 5.30: Spectrum at the input and output of the HNLF (res. bw.= 0.06 nm).

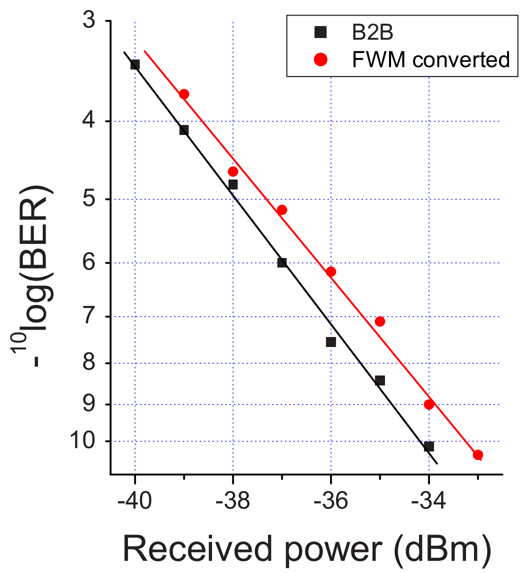

Figure 5.31: BER of the FWM converted 10 Gb/s RZ-DPSK signal at 1549.6 nm compared to the B2B 10 Gb/s RZ-DPSK.

RZ-DPSK signal as well as for the FWM wavelength converted RZ-DPSK signal. The results of the BER measurements are shown in Figure 5.31. A penalty at BER = 10^{-9} smaller than 1 dB is observed for the wavelength conversion process. Improvement in the sensitivity can be obtained by applying a balanced receiver.

5.4 Conclusion

FWM is a process that enables λ-conversion at terabit per second speed due to the ultrafast fiber response. FWM is transparent to both bit rate and modulation format. This makes it attractable for all-optical signal processing of phase modulated signals, for example wavelength conversion and/or transmultiplexing from OTDM-to-WDM and from WDM-to-OTDM. Practical limitations to the use of FWM as transmultiplexing technique are the limited control input power that can be employed, because higher control powers lead to an increase of unwanted effects like SPM, XPM and SCG in the HNLF. A Raman amplifier can be employed to enhance the FWM effect and improve the conversion efficiency [137]. We have shown demultiplexing from 160 Gb/s to a 10 Gb/s base rate. Furthermore transmultiplexing from OTDM-to-WDM and WDM-to-OTDM has been presented, which allows the possibility to create an ADM based on FWM in HNLF. Conversion from OTDM-to-WDM has been shown with a 160 Gb/s OTDM signal transmultiplexed to 4×40 Gb/s WDM signals [131]. Conversion from 2×10 Gb/s WDM to 20 Gb/s OTDM has been experimentally shown. Simulations predict that this technique is not suitable for conversion from 4×40 Gb/s WDM to 160 Gb/s OTDM, because the received optical power is too low. The received optical power is so low, because the conversion efficiency is low. The conversion efficiency is reduced with an increasing number of channels and a larger spectral width per channel. The increasing number of channels draws too much energy into the unwanted FWM products. The WDM-to-OTDM conversion technique based on FWM in HNLF is limited to two WDM channels of 40 or 80 Gb/s. Increasing the number of channels requires a different transmultiplexing technique with an extra NRZ-to-RZ conversion step.

Chapter 6

XPM Spectral Broadening in Highly Nonlinear Fiber

Cross-phase modulation (XPM) spectral broadening employs the XPM effect induced by a high power control pulse that coincides with a data signal inside a fiber. The broadening of the optical spectrum of the data signal combined with an optical band pass filter (OBPF) to select one of the created sidebands makes all-optical demultiplexing possible [26, 27]. The incoming data signal and the high energy control pulse are at different wavelengths. The control pulse induces a phase shift on the incoming data signal. This phase modulation is observed as a spectral broadening of the data signal. The XPM induced broadened part of the spectrum is filtered to convert the phase modulation to amplitude modulation. The same concept has also been used for 3R-regeneration experiments at 80 Gb/s [138] and 160 Gb/s [139, 140]. Moreover, this concept can be used to realize all-optical time domain add-drop multiplexing when the dropped channel is pushed as much as possible out of the original signal wavelength band, such that an optical band pass filter at the signal wavelength can be employed to select the through channels. Simultaneously a band pass filter centered at the new frequency of the demultiplexed channel selects the demultiplexed channel. In [42, 43] the authors present an 80 Gb/s add-drop multiplexer (ADM) based on the above mentioned principle. In this chapter we will extend the concept by assessing the ADM at 160 Gb/s. The outline of this chapter is as follows. In section 6.1 the theory of the XPM spectral broadening ADM is explained. In section 6.2 the simulations on demultiplexing from 160 Gb/s to 10 Gb/s and the simulations on a 160 Gb/s ADM are described. The experimental work on demultiplexing and add-drop multiplexing is covered in section 6.3. Finally, in section 6.4 conclusions are drawn.

6.1 Operation Principle

When two optical pulses at different wavelengths propagate in a single mode fiber (SMF), the slowly varying temporal amplitudes of the two pulses are governed by a set of two coupled nonlinear Schrödinger equations (NLSEs). Using the slowly varying wave envelope on the NLSE, the following expressions are derived [83]:

$$\frac{\partial A_1}{\partial z} + \frac{1}{\nu_{g1}}\frac{\partial A_1}{\partial t} + \frac{i\beta_{21}}{2}\frac{\partial^2 A_1}{\partial t^2} + \frac{\alpha_1}{2}A_1 = i\gamma_1(|A_1|^2 + 2|A_2|^2)A_1 \tag{6.1}$$

$$\frac{\partial A_2}{\partial z} + \frac{1}{\nu_{g2}}\frac{\partial A_2}{\partial t} + \frac{i\beta_{22}}{2}\frac{\partial^2 A_2}{\partial t^2} + \frac{\alpha_2}{2}A_2 = i\gamma_2(|A_2|^2 + 2|A_1|^2)A_2 \tag{6.2}$$

where A_1 represents the slowly varying amplitude of the data signal and A_2 represents the slowly varying amplitude of the control signal, ν_{gj} $(j = 1, 2)$ is the group velocity of the data (j=1) and control (j=2) signal, β_{2j} $(j = 1, 2)$ is the group velocity dispersion (GVD) coefficient for data and control signal and γ is the nonlinear coefficient of the fiber. The control pulse has to contain a much higher intensity than the data pulse, if XPM spectral broadening is to be used as time domain add-drop multiplexing technique. In a very simplified theoretical approach the dispersion, the losses and the difference in group velocity are neglected [43]. Moreover, we also assume that the control signal is much stronger than the data signal. If the control and data polarizations are parallel, the data signal will experience a XPM induced phase shift at the end of the fiber, by an interaction with the strong control pulse according to equation (3.42):

$$\phi_{NL} = 2\gamma L|A_2|^2 \tag{6.3}$$

where L is the length of the fiber. When we now introduce a frame of reference moving with the group velocity of the data pulse: $T = t - z/\nu_g$. Furthermore, we define the timing offset between the intensity peak of the control and the intensity peak of the data signal as ΔT. When we assume that the control pulse maintains its original shape during propagation through the fiber, the time-dependent nonlinear phase shift on the data pulse can be described by the XPM between data signal and the time-shifted control pulse:

$$\phi_{NL}(L, T) = 2\gamma L|A_2(T - \Delta T)|^2 \tag{6.4}$$

The corresponding frequency shift of the data pulse is then given by the derivative of the corresponding phase change, and is denoted by:

$$\Delta\omega(T) = -\frac{\partial \phi}{\partial T} = -2\gamma L\frac{\partial |A_2(T - \Delta T)|^2}{\partial t} \tag{6.5}$$

From equation (6.5) we can see that the frequency shift depends on the time derivative of the control pulse intensity profile, the length of the fiber and the fiber nonlinear coefficient γ. When the data pulse overlaps with the rising edge of the control pulse, the data signal receives a red frequency shift, because the derivative of the rising edge is positive. On the other hand, if the data pulse overlaps with the falling edge of the control pulse then the data signal will receive a blue frequency shift.

Although dispersion can be neglected, like e.g. in [43] where only a 50 meter long HNLF is used, dispersion becomes a more and more important factor when longer fibers or shorter pulses are used. Dispersion causes a broadening of control and data pulses, but also a walk-off between control and data. The influence of the walk-off on the switching of neighboring non-targeted channels can then no longer be neglected, if we use a 500 m long fiber. The walk-off length L_W is given in equation (3.27). The walk-off time t_w is defined as the difference in propagation time between control and data pulses at the end of the fiber. The walk-off time between two wavelengths λ_1 and λ_2 is a relation between the length of the fiber and the difference in group velocities at the given wavelengths. The formula for the walk-off time is given in equation (3.28). In the normal dispersion region where $\beta_2 > 0$, a pulse at a longer wavelength travels faster, while the opposite occurs in the anomalous dispersion region. Two different samples of HNLF are available for our experiments. These fibers will be referred to as $HNLF_1$ (parameters in Table A.1) and $HNLF_2$ (parameters in Table A.2) throughout the remaining of this chapter. The walk-off time has been calculated for these two different samples of HNLF.

When we assume a constant dispersion slope in the C-band (1530-1565 nm), the walk-off time is given by equation (3.31). In Figure 6.1 the walk-off between a control pulse and a 1555 nm data signal in 500 m $HNLF_1$ is depicted. The negative walk-

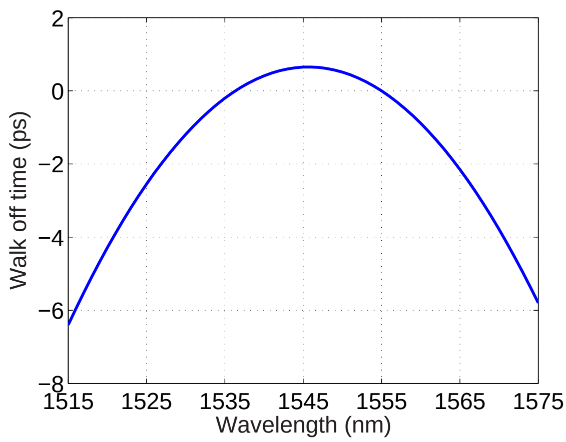

Figure 6.1: Walk-off time between a 1555 nm data signal and a control signal in 500 m $HNLF_1$ versus the wavelength of the control signal.

off time refers to slower traveling wavelength components, whereas the wavelengths around the zero-dispersion point ($\lambda_0 = 1545$ nm) are the fastest traveling wavelength components. A control wavelength of 1535 nm leads to no walk-off between data and control. However the strong peak power of the control pulse generates a super continuum (SC), where the spectrum of the control pulse is spread out over a large wavelength range. These new wavelength components will have a different GVD that introduces a walk-off between the new wavelength components and the data signal.

To prevent large broadening of the control pulse spectrum, it is preferable to keep the wavelength of the control pulse in the normal dispersion region. An optimum position of the control and data wavelengths is symmetrically around the zero dispersion point of the fiber. In that situation there is no walk-off. Only a spectral broadening of the pulses can result in changes of the wavelength, which in its turn results in some residual walk-off. To conclude, when the control pulse is at $\lambda_2 = 1540$ nm and the data pulse is at $\lambda_1 = 1550$ nm the walk-off is minimized.

The second nonlinear fiber, HNLF_2 (see Table A.2) is available in three lengths (2×125 m and 1×250 m) and has a zero dispersion point at $\lambda_0 = 1590$ nm. This indicates that we have to work in the normal dispersion region for control and data pulses, where spectral broadening is not as strong as in the anomalous dispersion region. When a pulse propagates through a normally dispersive medium, the higher frequency components travel slower than the lower frequency components. This means that a control pulse at $\lambda_c = 1540$ nm travels slower than a data pulse at $\lambda_s = 1550$ nm. By substituting L=125 m, $D_{1550} = -1.1 \cdot 10^{-6}$ s/m^2 and $S_{1550} = 0.029 \cdot 10^3$ s/m^3 into equation (3.31), the resulting walk-off time equals 1.5 ps. For add-drop multiplexing at 160 Gb/s and higher, a 1.5 ps walk-off time is too large. Therefore, in our experimental work on XPM spectral broadening add-drop multiplexing we will employ HNLF_1.

6.2 Simulations

Firstly, demultiplexing of a 10 Gb/s channel out of a 160 Gb/s OTDM signal has been studied. Secondly, a 160 Gb/s ADM with a 10 Gb/s base rate has been simulated. The time derivative of the control pulse induced phase shift equals to a broadening of the spectrum of the data according to equation (6.5). In the simulations, the parameters of HNLF_1 are used, similar to our experiments (parameters are listed in Table A.1). The simulations were carried out by solving the NLSE with the split-step Fourier method for the signal and control pulses, see appendix D.1.1. Both dispersion and nonlinear effects have been included. The polarization has been assumed to be linear and in the x-direction. This significantly simplifies and speeds up the simulation. Higher peak powers are required to achieve the same frequency shift, if the polarizations are not both in the x-direction, due to the reduced XPM effect between orthogonal polarizations.

6.2.1 Demultiplexing from 160 to 10 Gb/s

The 160 Gb/s OTDM signal with 10 Gb/s base rate consists of 2 ps FWHM pulses. The control pulse width is also 2 ps FWHM. Both the control and data signal are secant-shaped pulses. The wavelength of the control signal is 1540 nm and the wavelength of the OTDM signal is 1550 nm. The power of the control signal is 15 dBm (1.4 W peak power). The combined spectrum of the 10 GHz control signal and the 160 Gb/s OTDM signal at the input of HNLF_1 is shown in Figure 6.2. After the transmission through the 500 m long HNLF_1 the spectrum of the OTDM signal and the control pulse are broadened. The spectrum at the output of HNLF_1 is shown in Figure 6.3.

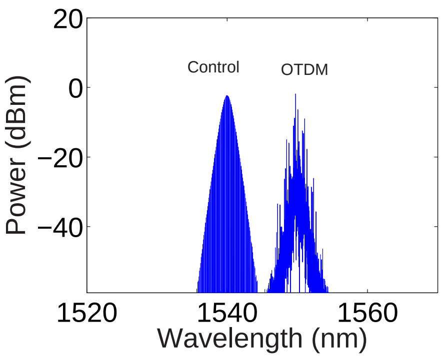

Figure 6.2: Spectrum of the combined control and OTDM signal before $HNLF_1$.

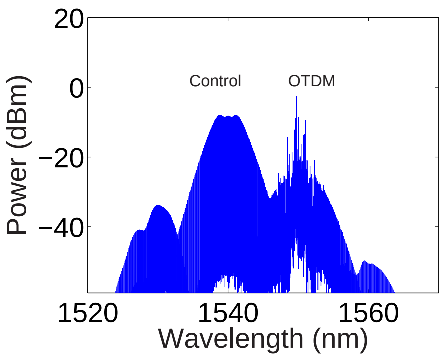

Figure 6.3: Spectrum of the combined control and OTDM signal after $HNLF_1$.

When $\Delta T = 0$ (the peak of the control pulse overlaps exactly with the peak of the data pulse), the leading edge of the control pulse introduces a red shift on the leading edge of the data pulse. Meanwhile the trailing edge of the control pulse induces a blue shift on the trailing edge of the data pulse. As the slope of the derivative is zero ($\frac{\partial |A_2|^2}{\partial T} = 0$) in the peak of the control pulse, the wavelength is not shifted at that point. Therefore, the signal spectrum after the nonlinear process is a symmetrically broadened spectrum, with a significant amount of energy still remaining inside the input signal wavelength band. A band pass filter is then employed to select one of the sidebands and to convert spectral broadening of the targeted channel into an intensity modulated demultiplexed channel.

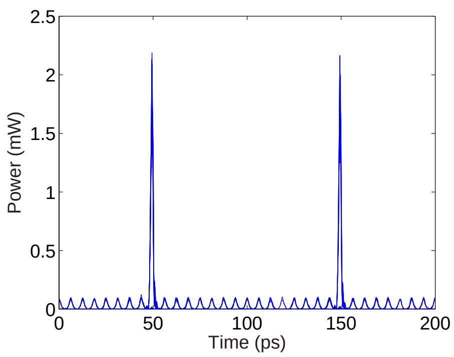

Figure 6.4: 5 nm second order Gaussian OBPF with center frequency: λ_c= 1556.6 nm

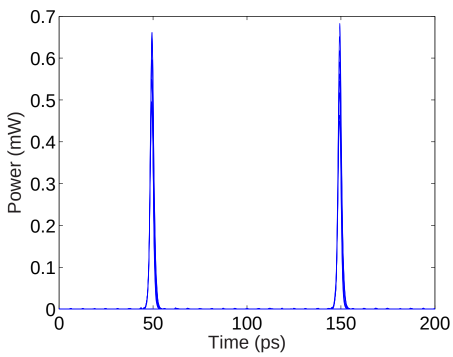

Figure 6.5: 5 nm fourth order Gaussian OBPF with center frequency: λ_c= 1556.6 nm

At the output of the fiber a band pass filter with center wavelength 1556.6 nm is placed to select the demultiplexed channel. The center wavelength of this filter is chosen at the longer wavelength side (red shift). In principle it is also possible to select the blue shifted component, however more crosstalk from the control signal will be experienced when the spectrum of the control pulse broadens. It is important to use an OBPF with a sharp edge to select the demultiplexed channel in order to minimize the crosstalk from the original 160 Gb/s data signal. The importance of the filter shape can be easily explained by looking at the selected wavelength shifted component filtered with a 5 nm 2^{nd} order OBPF with center frequency λ_c= 1556.6 nm in Figure 6.4 and compare it with using a 4^{th} order OBPF in Figure 6.5. The difference in suppression of the original 160 Gb/s signal at λ = 1550 nm is clearly visible.

6.2.2 Add-Drop Multiplexing at 160 Gb/s

Simulations have been performed for a 160 Gb/s ADM based on XPM spectral broadening in $HNLF_1$. The schematic of the simulation is shown in Figure 6.6. The 160

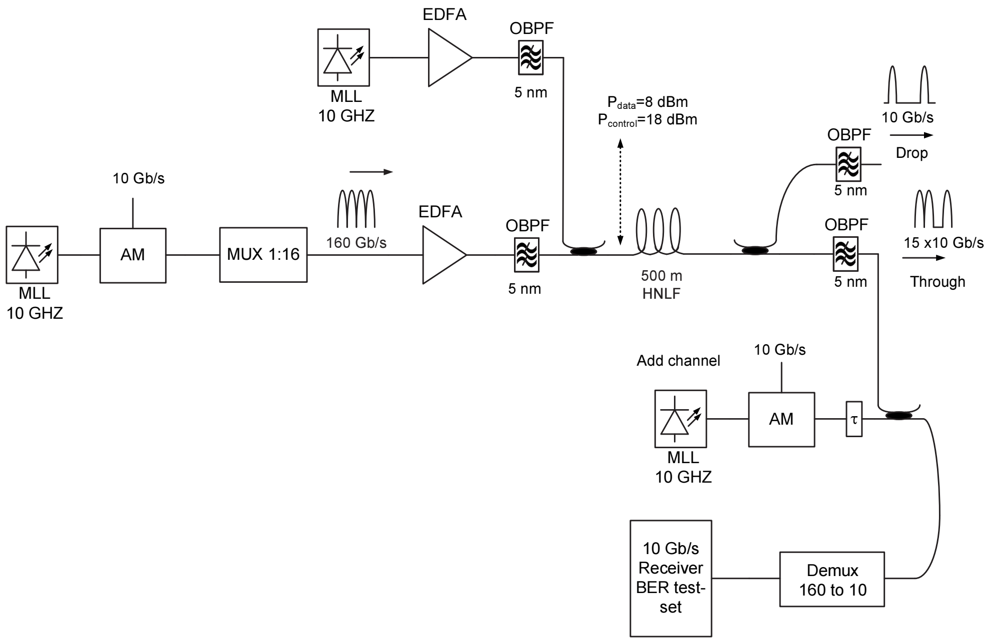

Figure 6.6: Schematic of the simulation setup for an ADM at 160 Gb/s with a 10 Gb/s base rate, based on XPM induced spectral broadening in $HNLF_1$.

Gb/s OTDM signal with a 10 Gb/s base rate is constructed of 1 ps FWHM pulses. The control pulse is a 3 ps FWHM pulse. The wavelength of the data signal is $\lambda_d = 1550$ nm and the wavelength of the control signal is $\lambda_c = 1540$ nm. The OTDM signal was amplified to 8 dBm before entering the HNLF and the control signal was amplified to 18 dBm (1.8 W peak power). The spectrum at the input of the fiber is shown in Figure 6.7 and the spectrum at the output of the fiber is shown in Figure 6.8. By tuning the distance between the peaks of data and control pulses to $\Delta T = 1.5$ ps, it is made sure that the data pulses coincide with the rising edge of the control pulse. This causes a red shift of the targeted demultiplexed channel. This can be seen in the output spectrum depicted in Figure 6.8. The demultiplexed channel, depicted in Figure 6.9 is selected by a 4^{th} order Gaussian OBPF with 5 nm bandwidth with center wavelength 1554.5 nm. At the through port a 4^{th} order Gaussian OBPF with 5 nm bandwidth at $\lambda_d = 1550$ nm is used to select the 15 through channels, depicted in Figure 6.10. The pulse width of the through channels is increased to 1.6 ps. A new channel has been added in the empty time slot. The wavelength of the added channel is $\lambda_d = 1550$ nm and the pulse width is 1 ps FWHM. The eye-diagram of the added channel is shown in Figure 6.11. It is observed that the peak power of the added channel is about 2 mW higher. Pulse broadening of the through channels occurred during the propagation through the 500 m HNLF_1, which results in a reduction of the peak power.

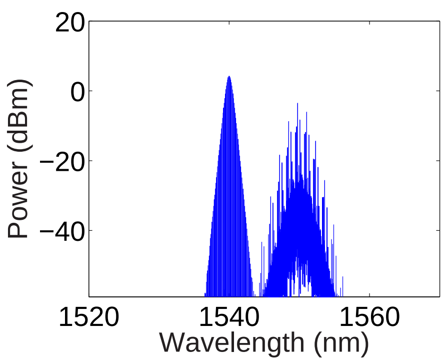

Figure 6.7: Spectrum at the input of the HNLF.

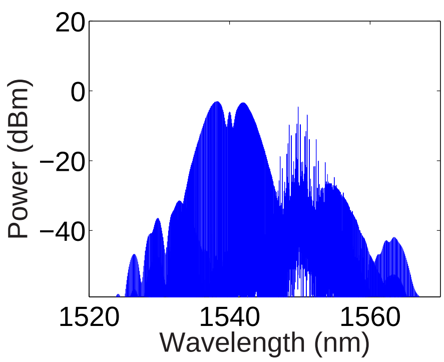

Figure 6.8: Spectrum at the output of the HNLF.

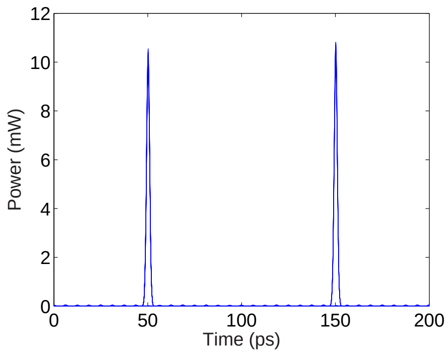

Figure 6.9: Eye diagram of the dropped channel at 10 Gb/s.

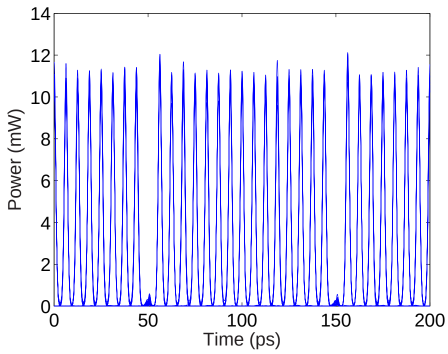

Figure 6.10: Eye diagram of the 15 through channels.

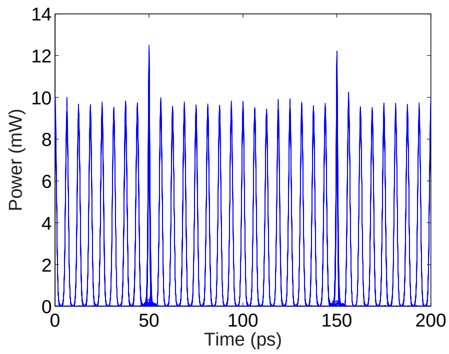

Figure 6.11: Eye diagram of the 15 through channels plus the added channel.

6.3 Experimental Results

Although in [43] the authors show the feasibility is shown of an 160 Gb/s ADM by means of simulations, their experimental work has been limited to 80 Gb/s. In this section, a proof-of-principle experiment will extend the work on time-domain add-drop multiplexing based on XPM spectral broadening to 160 Gb/s. For a time-domain ADM it is important that the targeted demultiplexed channel is completely removed at the through channel output port. To achieve this the complete data pulse needs to be shifted in frequency far enough to be out of the bandwidth of the OBPF that selects the through channels. We have chosen the wavelengths of the control and data signal around the zero-dispersion wavelength of the $HNLF_1$, to minimize the walk-off. The wavelength of the control signal was $\lambda_c = 1535$ nm and the wavelength of the data signal was $\lambda_d = 1553.7$ nm. The walk-off time calculated by using equation (3.31) is $t_w = 0.37$ ps.

In principle it is possible to shift the targeted demultiplexed channel to higher or lower wavelengths, as long as the demultiplexed channel is outside the bandwidth of the OBPF that selects the through channels. Shifting the spectrum of the targeted demultiplexed channel to a higher wavelength is preferable, because no spectral overlap from the broadened spectrum of the control signal is present at the higher wavelength side. The data pulse is therefore aimed to overlap with the rising edge of the control pulse, such that the demultiplexed channel will be shifted to a higher wavelength (in accordance with equation (6.5)). The rising edge of the control pulse should cover the complete data pulse, while the falling edge of the control pulse is short enough so that it does not cover part of the neighboring un-targeted data channel. As a result, asymmetric control pulses are preferred for 160 Gb/s ADMs [43].

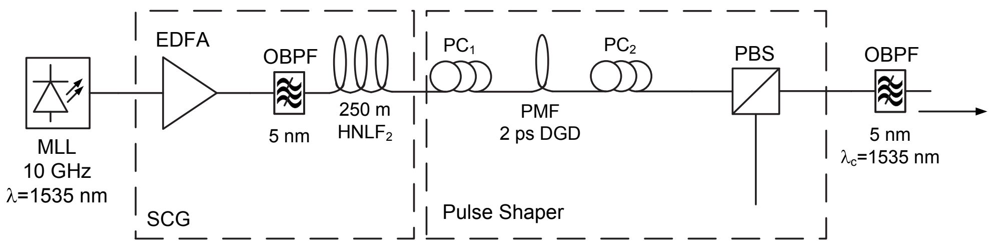

Figure 6.12: The experimental setup for the generation of the control pulse. A super continuum generation (SCG) followed by a pulse shaper and filter.

To achieve an asymmetric pulse, the control pulse is shaped with a pulse shaper before being used in the ADM. The experimental setup of the generation of the control pulse is shown in Figure 6.12. A 10 GHz control pulse at $\lambda_c = 1535$ nm is generated by a commercially available MLL from Pritel. A 1.8 ps control pulse is used as input signal for super continuum generation (SCG) in 250 m $HNLF_2$. The output of the SC is sent to the pulse shaper. The pulse shaper consists of a polarization controller PC_1 followed by a piece of birefringent fiber (= 2 ps DGD PMF), PC_2 and a PBS. During the propagation through the birefringent fiber the different polarization

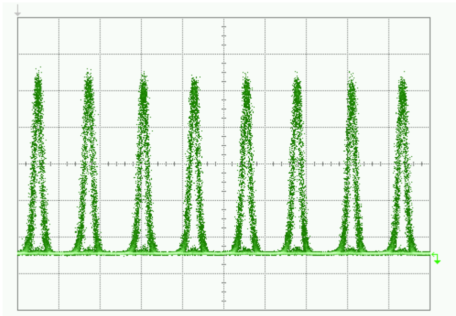

Figure 6.13: 160 Gb/s input signal. Pulse width of the OTDM signal is 1 ps FWHM. X-scale: 5 ps/div, y-scale: a.u.

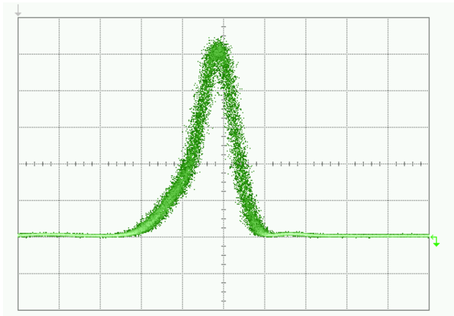

Figure 6.14: Control pulse at $\lambda_c = 1535$ nm, rise time = 1.9 ps and fall time = 800 fs. X-scale: 2 ps/div, y-scale: a.u.

components travel at different speeds, which is determined by the differential group delay (DGD). With the delay being comparable to the pulse width, the pulse shape after the PBS depends on the polarization and the phase difference of the orthogonal pulse components, which can be changed by tuning PC_2 that is placed before the PBS. This pulse shaper can also be used to create rectangular shaped pulses [141].

The control pulse generated for the ADM experiment is shown in Figure 6.14. The rise time from 20% to 80 % is 1.9 ps and the fall time from 80 % to 20 % is 800 fs. The rising edge of the control pulse should cover the complete targeted OTDM channel. To accomplish this the pulse width of the data channel should be smaller than the rising edge of the control pulse minus the walk-off time between control and data. Therefore, the pulse width of the data should be smaller than $1.9 - 0.37 = 1.53$ ps. The 160 Gb/s OTDM signal is shown in Figure 6.13. The pulse width of the data signal is approximately 1 ps FWHM, therefore the complete targeted demultiplexed channel coincides with the rising edge of the control pulse. The targeted demultiplexed 10 Gb/s channel is propagating through $HNLF_1$ together with the rising edge of the control pulse. The experimental setup for the 160 Gb/s ADN based on XPM spectral broadening is shown in Figure 6.15.

The input spectrum is shown in Figure 6.16. The average power of the OTDM and control signal at the input of $HNLF_1$ is 4 and 21.3 dBm, respectively. The spectrum at the output of $HNLF_1$ is shown in Figure 6.17. The control pulse at $\lambda_c = 1535$ nm is considerably broadened by SCG. The power of the control signal is tuned to the maximum power achievable without noticeable spectral overlap between control and data, in order to obtain a maximum XPM induced spectral broadening of the targeted demultiplexed channel. The targeted demultiplexed channel is completely pushed out of the spectral region around the data pulse: $\lambda_d = 1553.7$ nm to a wavelength of 1559.6 nm. The demultiplexed channel is selected by filtering the output with an OBPF with center frequency λ_{demux}=1559.6 nm.

The eye diagram of the through channels is shown in Figure 6.18 and the eye diagram of the added channel is shown in Figure 6.19. The eye diagram of the

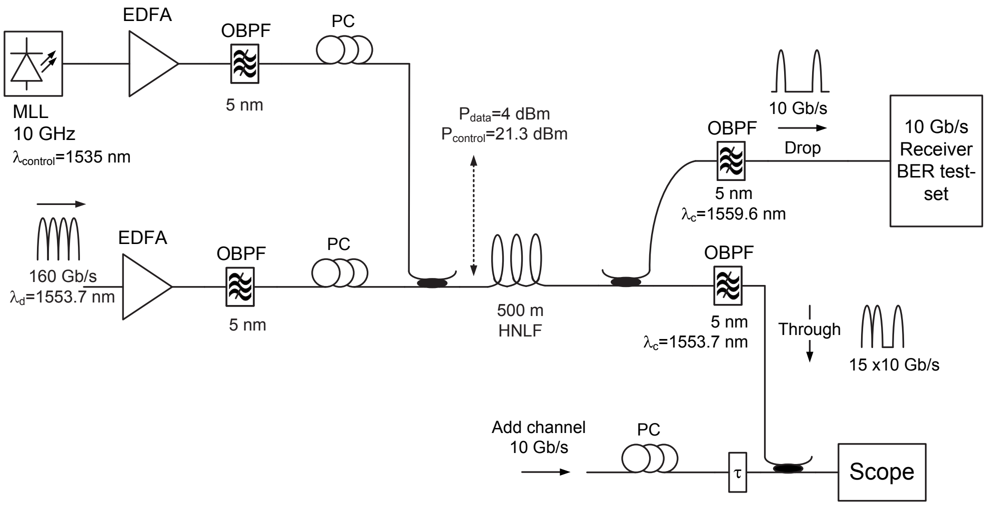

Figure 6.15: The experimental setup of the 160 Gb/s ADN based on XPM spectral broadening.

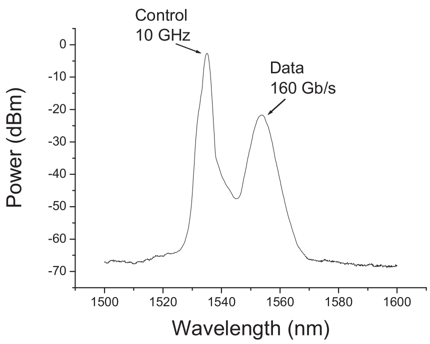

Figure 6.16: The input spectrum before $HNLF_1$ with control wavelength $\lambda_c = 1535$ nm and data wavelength $\lambda_d = 1553.7$ nm.

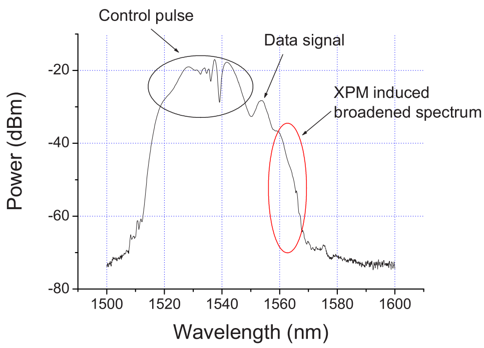

Figure 6.17: Spectrum at the output of the $HNLF_1$. Control pulse spectrum is broadened around $\lambda_c = 1535$ nm. The 15 through channels are at $\lambda_d = 1553.7$ nm and the targeted drop channel is filtered at 1559.6 nm.

demultiplexed channel is shown in Figure 6.20. All eye diagrams show clear and open eyes, which indicates excellent operation. The performance of the ADM is measured by an BER assessment of the demultiplexed channel. The average BER of the 16 demultiplexed channels is shown in Figure 6.21. All the 16 channels show excellent performance and no degradation in receiver sensitivity compared to the B2B signal

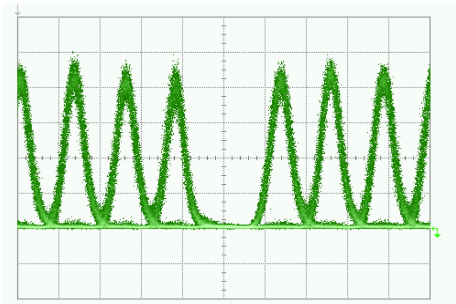

Figure 6.18: Empty time slot of 6.25 ps together with 15 through channels at a 10 Gb/s base rate. X-scale: 5 ps/div, y-scale: a.u.

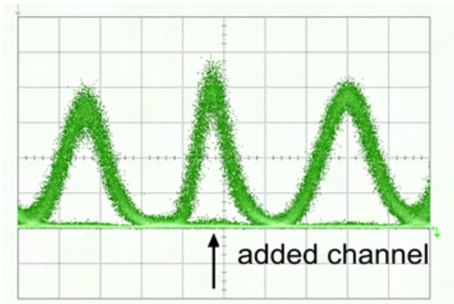

Figure 6.19: 15 through channels plus one add channel at 10 Gb/s. X-scale: 2 ps/div, y-scale: a.u.

at 10 Gb/s is visible. The absence of a sensitivity penalty can be contributed to the 2R regenerative effect introduced by the effect of XPM and SPM in combination with optical filtering used in the demultiplexing method [142]. Unfortunately a second demultiplexing technique to assess the quality of the added channel was not available at the time of the measurements. However, because of the clear and open eye of the added channel (see Figure 6.19), a good performance is to be expected. The difference in pulse width observed in Figure 6.19 between the added channel and the through channels can be explained by the fact that the pulse width of the OTDM signal is broadened from 1 ps to 2.4 ps after propagation through $HNLF_1$.

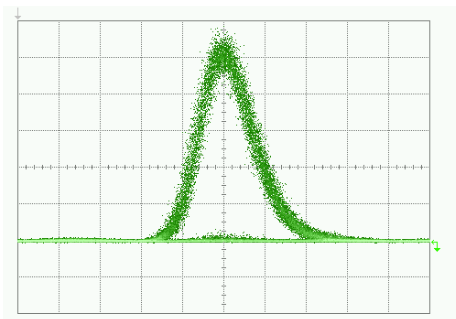

Figure 6.20: Demultiplexed channel at 10 Gb/s. X-scale: 2 ps/div, y-scale: a.u.

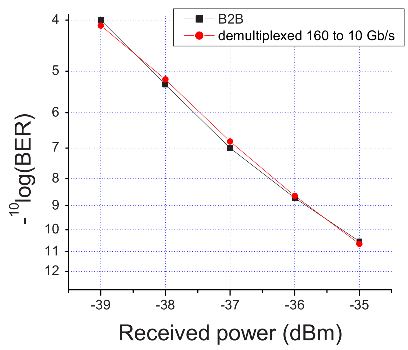

Figure 6.21: BER for demultiplexing from 160 Gb/s to 10 Gb/s.

6.4 Conclusion

XPM spectral broadening can be used for time domain demultiplexing as well as for add-drop multiplexing. The number of components required for ADM based on XPM spectral broadening in HNLF is small. A nonlinear medium, HNLF in our case, and two filters are sufficient (one filter to select the demultiplexed channel and one filter to select the through channels). Simulations and experimental results shows the possibility to use this method for add-drop multiplexing at 160 Gb/s with $HNLF_1$. The demultiplexing of a channel at a 10 Gb/s base rate shows excellent performance and no degradation in receiver sensitivity compared to the B2B signal.

The disadvantage of this method is the pulse width requirement for the data and control pulse. For an ADM it is crucial that the rising edge (or falling edge) of the control pulse covers the total data pulse. The rising edge must therefore be wider than the sum of the width of the control pulse plus the walk-off time between control and data. Increasing the bit rate will lead to an increase in the spectral width and therefore an increase of the walk-off time, which currently limits this method to a 160 Gb/s ADM.

Chapter 7

Kerr Shutter

The use of a Kerr gate has been demonstrated to be a promising tool for optical add-drop multiplexing (ADM) [44–46]. The Kerr gate uses cross-phase modulation (XPM) induced polarization rotation in a highly nonlinear fiber (HNLF). The theory of this concept is described in more detail in [83]. To be able to simultaneously obtain good add and drop operation, the output of the HNLF is split and two separate polarization beam splitters (PBSs) are used to separately optimize for the through and drop function. The outline of this chapter is as follows. In section 7.1 the operation principle of the Kerr switch is explained. In section 7.2 the experimental characterization of the switching window of the Kerr switch is described. Despite the increased interest in differential phase shift keying (DPSK) signals, time domain add-drop multiplexing for DPSK has not been considered so far. In section 7.3 the feasibility to create an ADM for RZ-DPSK OTDM signals based on the Kerr shutter in HNLF is discussed. The results of the RZ-DPSK OTDM ADM have been published in *[47]*. In section 7.4, the 320 Gb/s ADM experiments employing the Kerr switch are described. Finally, in section 7.5 concluding remarks are made.

7.1 Operation Principle

The operation principle of the Kerr shutter is schematically shown in Figure 7.1. A high intensity control pulse (pump) is launched into a HNLF together with a data signal (probe). The changes in refractive indices for the parallel and perpendicular components of the probe with respect to the direction of pump polarization are slightly different owing to the pump-induced birefringence. The phase difference between the two polarization components of the probe at the fiber output leads to a change in the state of polarization (SOP) of the probe signal. If the induced phase difference between the two polarization components of the data signal at the end of the fiber equals π, then the signal at the output is perpendicular in polarization compared to the data signal at the output without influence of the external control pulse. In this case one single PBS can be used to extract the drop channel as well as the through channels. If the nonlinear interaction is too low and consequently the phase shift is

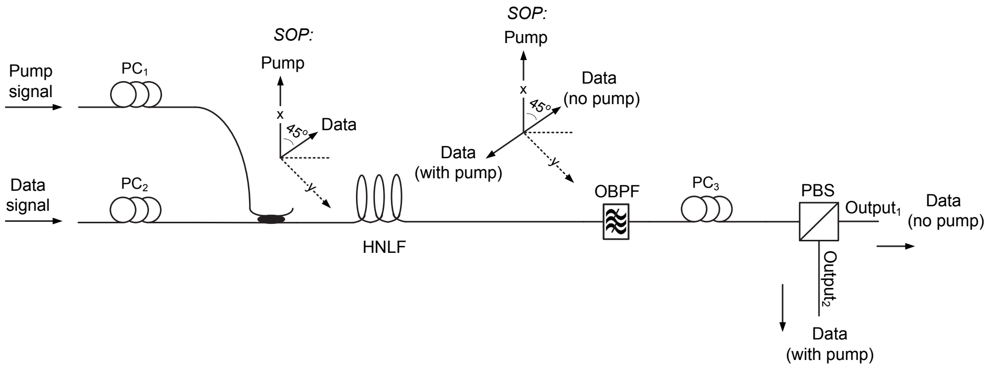

Figure 7.1: Operation principle of the Kerr shutter.

less than π, two separate PBSs are required to separately optimize for drop and for through operation. Optimum operation requires that the pump and the probe are linearly polarized at the fiber input with a 45° angle between their state of polarization [83]. The phase difference between the two polarization components of the probe at the output of the fiber can be written as:

$$\Delta\phi = \frac{2\pi}{\lambda}(\tilde{n}_x - \tilde{n}_y)L_{\text{eff}} \tag{7.1}$$

where λ is the probe wavelength, L_{eff} is the effective length of the HNLF (given by equation (3.38)) and $\tilde{n}_x$, $\tilde{n}_y$ are the refractive indices for the polarization component in the x and y-direction. The coefficients $\tilde{n}_x$ and $\tilde{n}_y$ consist of a linear part (n_x, n_y) and a nonlinear part (Δn_x, Δn_y). The nonlinear parts are different because of the pump-induced birefringence. It is assumed that the power of the data signal is small with respect to the pump signal. Therefore, the self-phase modulation (SPM) is neglected and only the XPM between pump and data is taken into account. Furthermore, the polarization of the pump signal is assumed to be in the x-direction. The nonlinear part of the refractive index is given by:

$$\Delta n_x = 2n_2|E_p|^2 \tag{7.2a}$$

$$\Delta n_y = 2n_2 b|E_p|^2 \tag{7.2b}$$

where n_2 is the nonlinear refractive index, $|E_p|^2$ is the pump intensity and the constant $b = 1/3$, as indicated in section 3.3.2. The total phase change between the x and y component is given by:

$$\Delta\phi = \frac{2\pi L_{\text{eff}}}{\lambda}(\Delta n_L + 2n_2(1-b)|E_p|^2) \tag{7.3}$$

The linear part of the phase change $\Delta\phi_L$ can be compensated at the receiver by optimizing polarization controller 3 (PC_3) before the PBS. The transmissivity of the

PBS is described by:

$$T_{\text{PBS}_1} = \cos^2(\frac{\Delta\phi}{2}) \tag{7.4a}$$

$$T_{\text{PBS}_2} = \sin^2(\frac{\Delta\phi}{2}) \tag{7.4b}$$

Without a pump signal the phase difference is zero ($\Delta\phi = 0$) and the data signal is directed to output port 1 of the PBS, but under the presence of a pump signal the phase difference equals π ($\Delta\phi = \pi$) and the data signal is directed to output port 2 of the PBS.

7.2 Static Characterization

For the static characterization of the ADM based on the Kerr shutter using HNLF as nonlinear element, a measurement of the switching window has been made, described in section 7.2.1. A measurement of the angle of rotation of the data signal and the relation with the pump power is presented in section 7.2.2.

7.2.1 Switching Window

To characterize the Kerr switch for time domain add-drop multiplexing a measurement of the switching window has been performed under static operation. The experimental setup for the Kerr shutter switching window measurement is shown in Figure 7.2. A mode-locked laser (MLL) operating at 10 GHz produces 3 ps full width half maximum (FWHM) pulses at $\lambda = 1555$ nm. This signal is assigned as the pump signal. The CW signal (probe) is generated by a tuneable laser source (TLS) operating at the wavelength $\lambda_{CW} = 1545$ nm. The nonlinear element in the Kerr shutter is HNLF_1, the parameters of this fiber are listed in Table A.1. At the output of HNLF_1 an optical band pass filter (OBPF) is placed to select the probe signal. After the OBPF the signal is split and the SOP is separately optimized in both arms for drop and through operation. The average power of the pump signal at the input of HNLF_1 is 9.2 dBm and the average power of the CW signal at the input of HNLF_1 is 10.6 dBm. The switching windows are shown in Figure 7.3. The window of the drop port is 2.1 ps and the window of the through port is 5.3 ps. Contrast ratios are larger than 15 dB. These switching windows predict good operation at high bit rates, i.e. 160 Gb/s.

7.2.2 State of Polarization Rotation Angle

According to equation (7.4a) and (7.4b), the rotation of the SOP of the data signal defines the transmissivity of the PBS output ports. The required pump power to achieve a rotation of the SOP of the data signal of π radians is an important parameter in the design of the Kerr shutter. Therefore, a static characterization of the SOP rotation angle of the data signal has been performed. The schematic for this experimental setup is shown in Figure 7.4. A 10 Gb/s RZ-DPSK input signal at

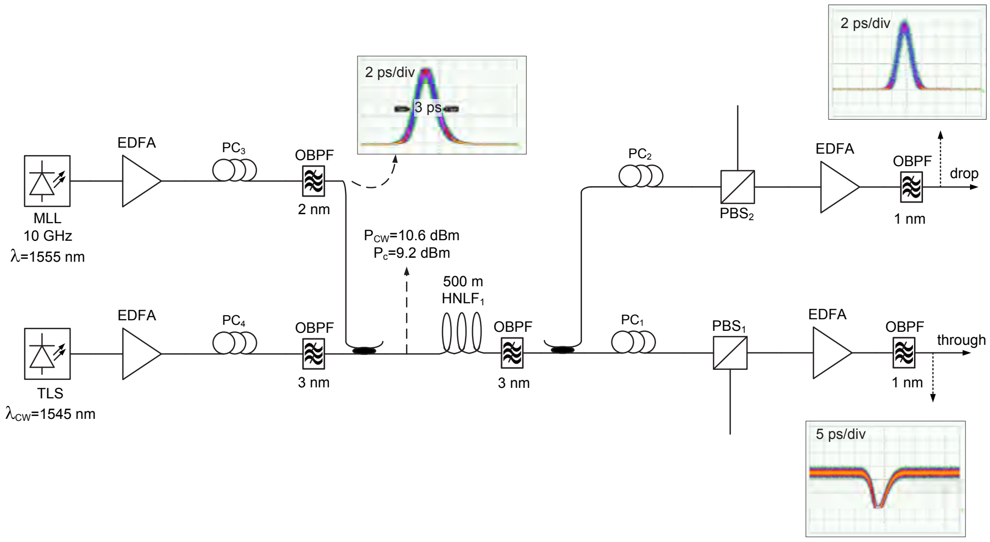

Figure 7.2: Experimental setup for the measurements of the switching windows of the Kerr shutter.

wavelength λ_s = 1557 nm with a 2.4 ps FWHM pulse has been applied. The pump signal is a 10 GHz pulse train of 2.3 ps FWHM pulses at the wavelength λ_c = 1545 nm. The nonlinear element in the Kerr shutter is $HNLF_2$. The parameters of this fiber are listed in Table A.2. The PC at the output of the 375 m $HNLF_2$ is optimized such that the power measured at port 1 (through port) is maximal and the power at port 2 (drop port) is minimal when the control signal is absent. The power at both outputs of the PBS is measured versus the average power of the 10 GHz control signal. This is shown in Figure 7.5. The OBPF after $HNLF_2$ is used to select the data signal at λ_d = 1557 nm and to block the 1545 nm pump signal. The amount of rotation of the data signal can be derived from the power measured at the output ports of the PBS. Figure 7.6 shows that 17 dBm is required for a rotation of 0.8π. Within the experimental context a full π rotation of the SOP could not be achieved, therefore separate optimization of the add and drop ports is required to minimize the receiver sensitivity penalty.

7.3 Add-Drop Multiplexing RZ-DPSK OTDM Signals

In recent years the interest in phase modulated signals, like differential phase shift keying (DPSK), for long haul transmission has increased significantly. The DPSK format has been shown to improve the receiver sensitivity by 3 dB and has an increased tolerance towards fiber nonlinearities with respect to on-off keying (OOK)

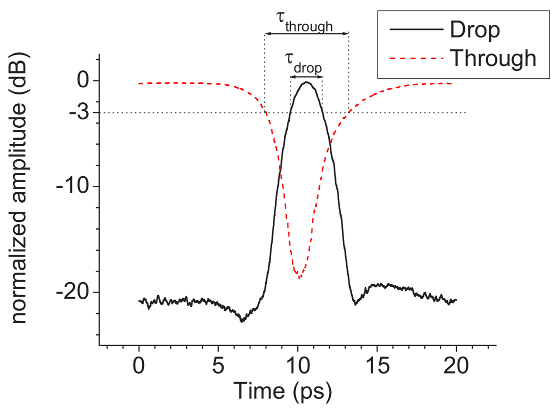

Figure 7.3: Measured switching windows for drop and through operation of the Kerr shutter.

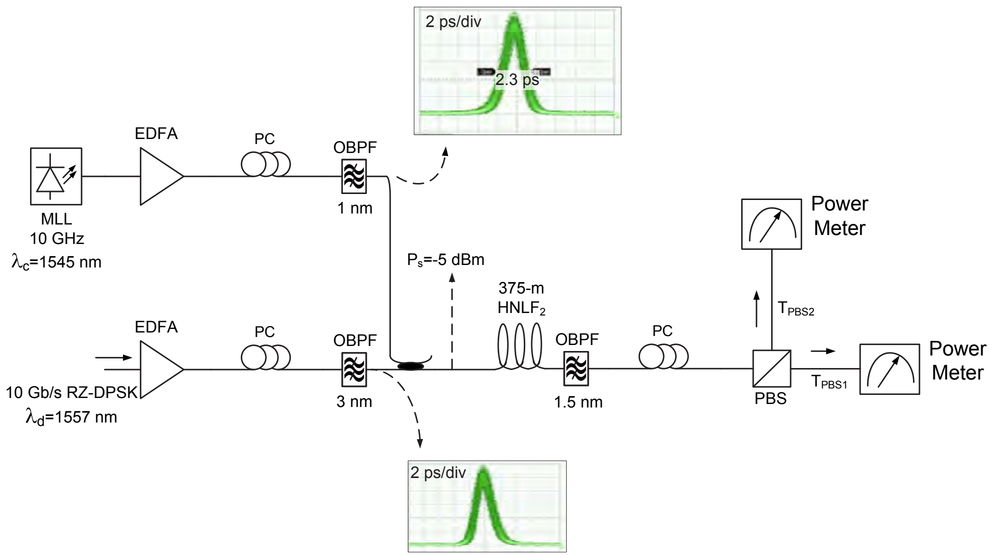

Figure 7.4: Experimental setup to measure the SOP rotation angle at the Kerr shutter output.

[143]. Recent interest in all-optical signal processing of DPSK signals using highly nonlinear fiber (HNLF) has shown the feasibility of phase sensitive amplification in a fiber parametric amplifier to regenerate the phase [144]. Despite the increased interest in DPSK signals, time domain add-drop multiplexing for DPSK has not been

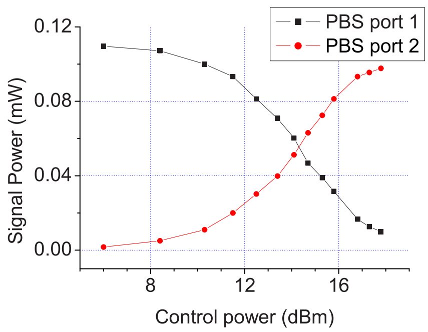

Figure 7.5: Average power out of both output ports of the PBS.

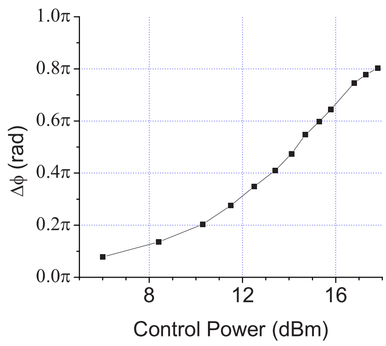

Figure 7.6: Rotation of the signal SOP versus the average control power.

investigated so far. We have therefore looked at the feasibility to create an add-drop multiplexer (ADM) for RZ-DPSK OTDM signals based on the Kerr shutter in HNLF. This ADM has the potential to operate at Tbit/s thanks to the ultrafast fiber nonlinearities. The results of the RZ-DPSK OTDM ADM described in this section have been published in [47].

7.3.1 Experimental Setup

The schematic of the 80 Gb/s RZ-DPSK OTDM transmitter used in the experiments is presented in Figure 7.7. The transmitter requires a pulse train that is stable in phase from pulse to pulse. Our MLL that is operated at $\lambda_c = 1545$ nm does not fulfill this requirement. Therefore, a wavelength conversion scheme based on $HNLF_2$ in a nonlinear optical loop mirror (NOLM) is employed. The parameters of $HNLF_2$ are listed in Table A.2. The NOLM consists of a 125 m long $HNLF_2$. The control pulse is a 2.3 ps FWHM pulse at the repetition rate of 10 GHz and the wavelength $\lambda_c = 1545$ nm. The CW signal is operated at $\lambda_s = 1557$ nm. The walk-off between control and data can be neglected because of the small dispersion slope S=0.029 ps·nm^{-2}·km^{-1} and the short length of the $HNLF_2$. A PC in the NOLM is used to optimize the switching characteristics of the NOLM that contains non polarization maintaining fibers. At the output of the NOLM an OBPF is used to select the converted signal at 1557 nm. The converted 10 GHz pulse is sent to a $LiNbO_3$ phase modulator driven at a 2^7-1 pseudo random bit sequence (PRBS). This signal is then amplified, filtered and multiplexed with passive delay line multiplexers up to 80 Gb/s OTDM single polarization. The multiplexer is a commercial device based on Mach-Zehnder interferometers (MZIs), constructed from polarization maintaining fibers. The bit separation delays were 6.4, 3.2 and 1.6 ns respectively. The relative optical phases between the tributaries are not controlled, since this is not required to prove the principle of add-drop multiplexing. Our OTDM rate was limited to 80 Gb/s due

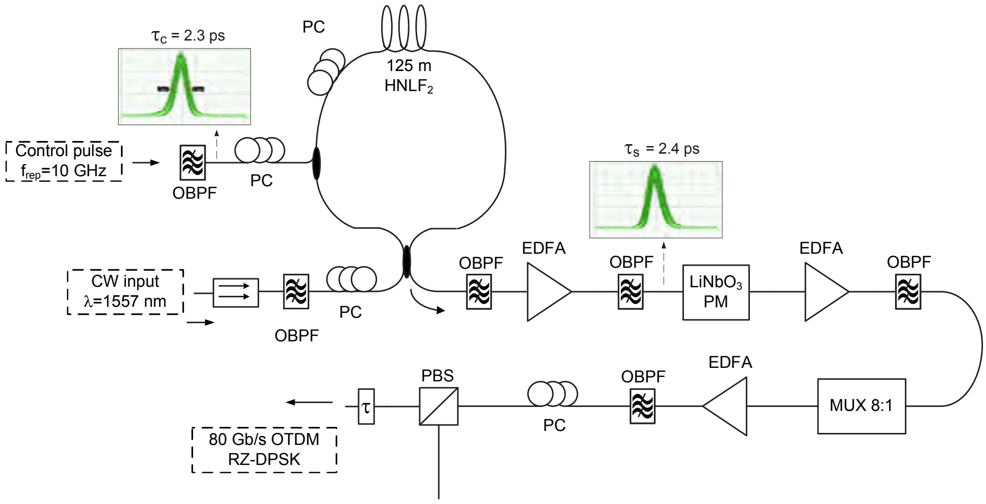

Figure 7.7: Schematic diagram of the 80 Gb/s RZ-DPSK OTDM transmitter. EDFA: Erbium-doped fiber amplifier, PM: phase modulator, MUX: Multiplexer, τ: tuneable optical delay line.

the wavelength conversion in the NOLM, but in a real system with a phase stable pulse source 160 Gb/s can be easily achieved. When the SOP in the NOLM loses the optimal SOP due to small fluctuations in the temperature, the extinction ratio of the wavelength converted pulse is deteriorated. Consequently interferometric noise appears on the pulses of the 80 Gb/s signal after the multiplexing sections. The actual ADM is constructed of a Kerr shutter. The schematic of the experimental setup is shown in Figure 7.8. The control pulse is obtained from the same MLL as the control pulse depicted in Figure 7.7 by splitting the signal with a coupler. The control and data signals are combined and inserted into 375 m of $HNLF_2$. The SOP of control and data signals are aligned in such a way that they are linear and that there is a 45 degrees angle between their SOPs. An OBPF is used at the output of the 375 m long $HNLF_2$ to block the control signal. The PC in front of the polarization beam splitter (PBS) is adjusted in such a way that the signal is sent to the through port without the presence of a control signal. If a control signal is present in the 375 m $HNLF_2$, the data channel that co-propagates with the control signal experiences an extra amount of birefringence. This birefringence induces a rotation of the SOP of the data signal. The rotation results in a transmittance of the data signal to the drop port. The average power of the control signal in the experiments at the input of $HNLF_2$ was $P_c = 17$ dBm. The average power of the data signal was $P_s = -1.7$ dBm.

At the through port a new add-channel, which is a copy of the 10 Gb/s signal obtained from the NOLM, is inserted in the cleared time slot of the data signal. The SOP of the add-channel is aligned to be equal to the SOP of the seven through channels. The synchronization between control signal, data signal and add-channel has been

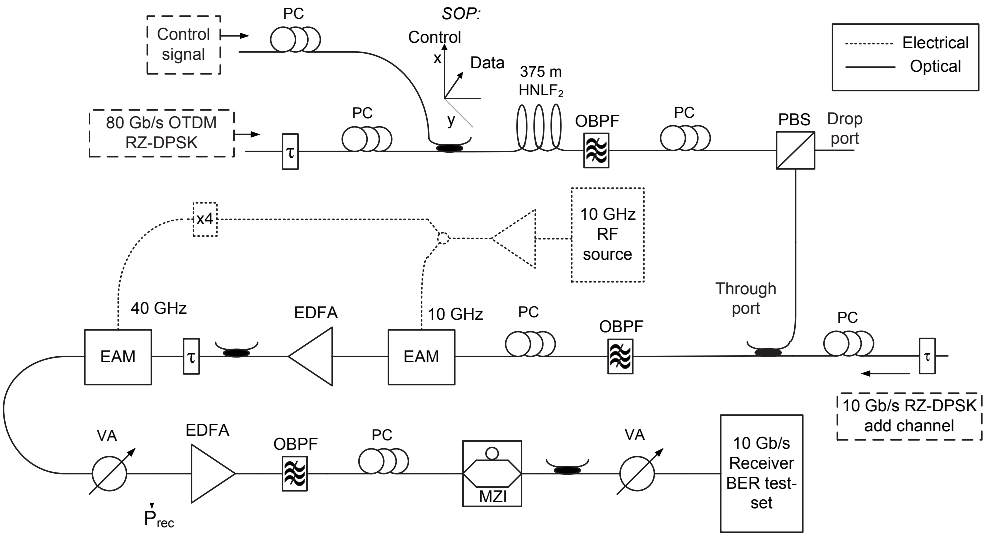

Figure 7.8: Schematic diagram of the 80 Gb/s ADM. MZI: Mach-Zehnder interferometer, EAM: electroabsorption modulator, VA: variable attenuator. The inset show the in- and output spectrum of the $HNLF_2$.

performed manually in this experiment using tuneable optical delay lines. In a real system an automated polarization controller and a clock recovery scheme would be required; moreover, an add-channel would require an independent wavelength matched source. The DPSK receiver consists of an optical pre-amplifier followed by an OBPF to remove amplified spontaneous emission (ASE) noise and an asymmetric one-bit (100 ps) delay MZI composed of spliced standard single mode fiber (SMF) pigtailed components to convert the phase information into an amplitude modulated signal. The DPSK receiver is more thoroughly described in section 5.3.2. At the time of the experiment, the infrastructure to work with balanced photo detectors was not available. Working with balanced photo detectors would have improved the sensitivity of the receiver with at least 3 dB. One problem of the home-made MZI in this setup was a slow drift of the SOP inside the MZI, which changed over time due to temperature fluctuations.

The performance of the add-channel and the seven through channels was measured by assessing the bit error rate (BER). The 80 Gb/s OTDM signal was demultiplexed to 10 Gb/s with two consecutive EAMs. The first EAM was driven at 10 GHz and the second EAM was driven at 40 GHz to obtain a switching window sufficiently small to demultiplex error-free. The EAM switching window is shown in Figure 7.9(a) and is 9.5 ps. The eye diagrams of the demultiplexed channel after the first and second EAM are shown in Figure 7.9(b) and Figure 7.9(c). Residual contributions of other channels are still visible in the eye-diagram, which cause a penalty at the receiver.

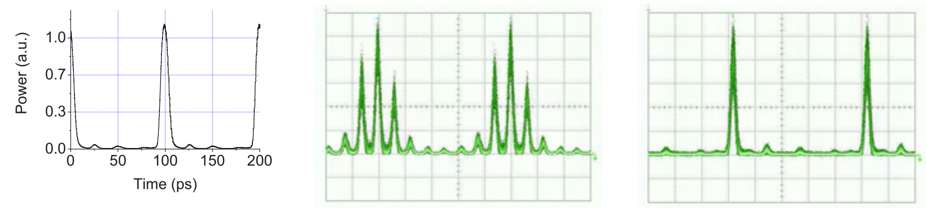

(a) Switching window two consecutive EAM demultiplexer.

(b) Eye diagram after the first EAM. X-scale: 20 ps/div, y-scale: a.u.

(c) Eye diagram after the second EAM. X-scale: 20 ps/div, y-scale: a.u.

Figure 7.9: Two consecutive EAMs serve as demultiplexer from 80 to 10 Gb/s.

7.3.2 Results

The spectra of control and data signal at the input and output of the 375 m $HNLF_2$ are visualized in Figure 7.10. The spectrum of the control pulse is broadened considerably. A further increase in the control power leads to an overlap of the spectrum of the control and the data signal. Eventually this results in crosstalk and degradation of the data signal.

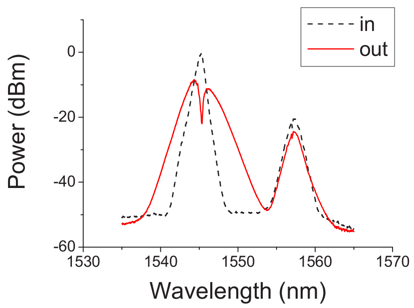

Figure 7.10: Spectra at the input and at the output of 375 m $HNLF_2$.

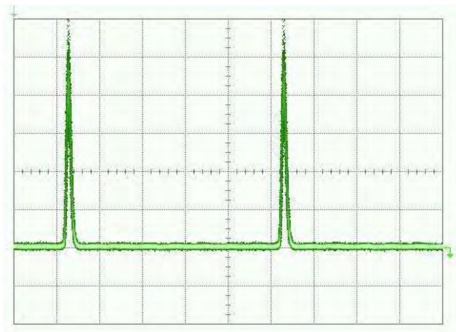

Figure 7.11: Dropped channel. X-scale: 20 ps/div, y-scale: a.u.

The eye diagrams of the 80 Gb/s OTDM RZ-DPSK time domain ADM are presented in Figure 7.11 and 7.12. In Figure 7.11 the eye diagram of the dropped channel can be observed. In Figure 7.12(a) the through channels and one cleared time slot are visualized and in Figure 7.12(b) a new channel is added in the cleared time slot. All eye diagrams show clear and open eyes, which indicates excellent operation. After the time domain add-drop multiplexing the quality of the dropped, added and through channels is assessed by measurement of the BER. The BER of the dropped channels compared to the back-to-back (B2B) signal is shown in Figure 7.13(a). The BER is

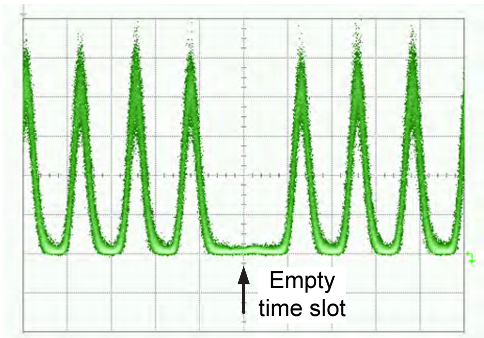

(a) Through channels and one cleared time slot. X-scale: 10 ps/div, y-scale: a.u.

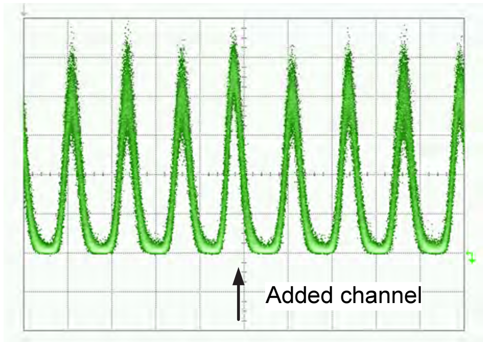

(b) The through channels with in the middle the added channel. X-scale: 10 ps/div, y-scale: a.u.

Figure 7.12: Eye diagrams of the optical add-drop node at 80 Gb/s RZ-DPSK OTDM.

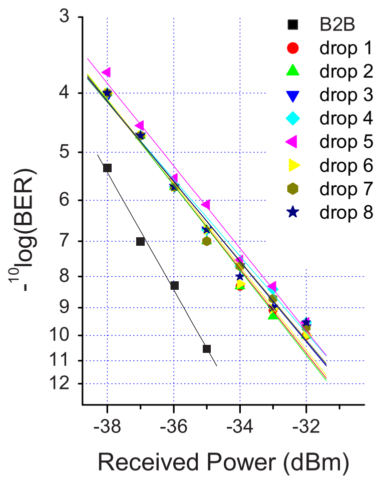

(a) BER of the dropped channels.

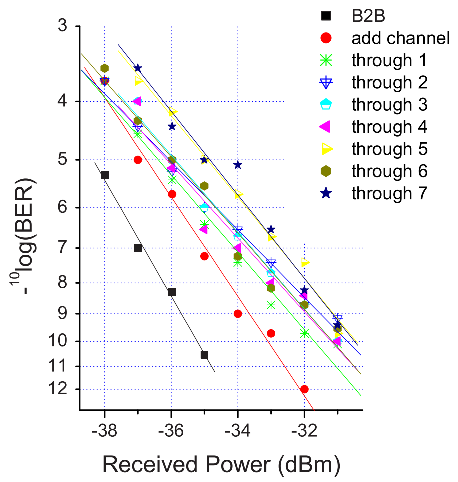

(b) BER of the added and through channels.

Figure 7.13: BER measurement of the 80 Gb/s RZ-DPSK OTDM add-drop node.

measured versus the received power indicated as P_{rec} in Figure 7.8. All channels show error free operation (BER $< 10^{-9}$) and no error-floor is observed, which indicates excellent performance of the ADM. The sensitivity penalty of the dropped channels at BER 10^{-9} is 2.6 dB for the best channel and 3.2 dB for the worst channel. The penalty of the dropped channels can be attributed to the interferometric noise that appears on the 80 Gb/s signal after multiplexing plus the penalty inherent to the Kerr switch. Inherently, the 10 Gb/s add channel suffers far less from interferometric noise (see also Fig. 7.12(b)). It's main penalty contribution should be assigned to the dual stage EAM demultiplexer that is utilized to demultiplex the 80 Gb/s RZ-DPSK OTDM signal after the ADM. The performance of the added and through channels are visualized in Fig. 7.13(b). A 2.1 dB penalty is observed for the add-channel compared to the B2B channel. For the through channels the sensitivity penalty is 3.3 dB for the best channel and 4.6 dB for the worst channel. The better performance of the add-channel can be understood by the fact that we insert the add channel after the multiplexer and Kerr switch. A large contribution to the penalty of the through channels is due the limited extinction ratio of the transmitter, which causes the interferometric noise in the pulses of the 80 Gb/s signal after the multiplexing sections. The variation of the receiver sensitivity in the BER of the through channels is an accumulation of the polarization instability penalties caused by the polarization dependence of the MZI, NOLM and EAMs. The imperfect OTDM receiver, consisting of two EAMs, of which the switching window is depicted in Figure 7.9(a) adds an extra penalty compared to the dropped channels. An optimized input signal and an optimized receiver would significantly reduce the penalty. A summary of the penalty contributions for drop, add and through channels relative to the B2B BER curve is shown in Table 7.1. Our findings on RZ-DPSK OTDM add-drop multiplexing have been published in *[47]*.

Table 7.1: Summary of the penalties with respect to the back-to-back BER configuration.

Channel	Value [dB]	Penalty contributions
drop	2.6-3.2	Interferometric noise after the multiplexer + Kerr switch
add	2	dual EAM demultiplexer + Kerr switch
through	3.3-4.6	Interferometric noise after the multiplexer + Kerr switch + dual EAM demultiplexer

7.4 Add-Drop Multiplexing at 320 Gb/s

In this section the performance of the Kerr shutter as key component in an ADM is assessed for amplitude modulated signals. The bit rate of the transmitter can be increased from 80 Gb/s to 320 Gb/s, if we apply amplitude modulation instead of phase modulation. The multiplexer is no longer influenced by the extinction ratio reduction in the NOLM wavelength converter, because no phase stable pulses are required. Therefore, the NOLM can be bypassed.

7.4.1 Experimental Setup

The schematic of the experimental setup of the 320 Gb/s transmitter is shown in Figure 7.14. The transmitter requires pulses smaller than 1 ps. A MLL that produces a 9.95328-GHz pulse train at $\lambda = 1550$ nm and 1.6 ps FWHM pulses is employed. Pulse compression is applied to reduce the pulse width. The pulse compression is based on super continuum generation (SCG) in 250 m $HNLF_2$. The original pulse train is amplified by an EDFA and filtered by an OBPF to an average power at the input of the 250 m $HNLF_2$ of 21.7 dBm. The parameters of $HNLF_2$ are listed in Table A.2. Super continuum generation-based pulse compression takes place in $HNLF_2$. Pulse compression based on SCG is more thoroughly explained in appendix B.2. The SC is filtered with an OBPF centered at $\lambda_d = 1553.4$ nm. After the pulse

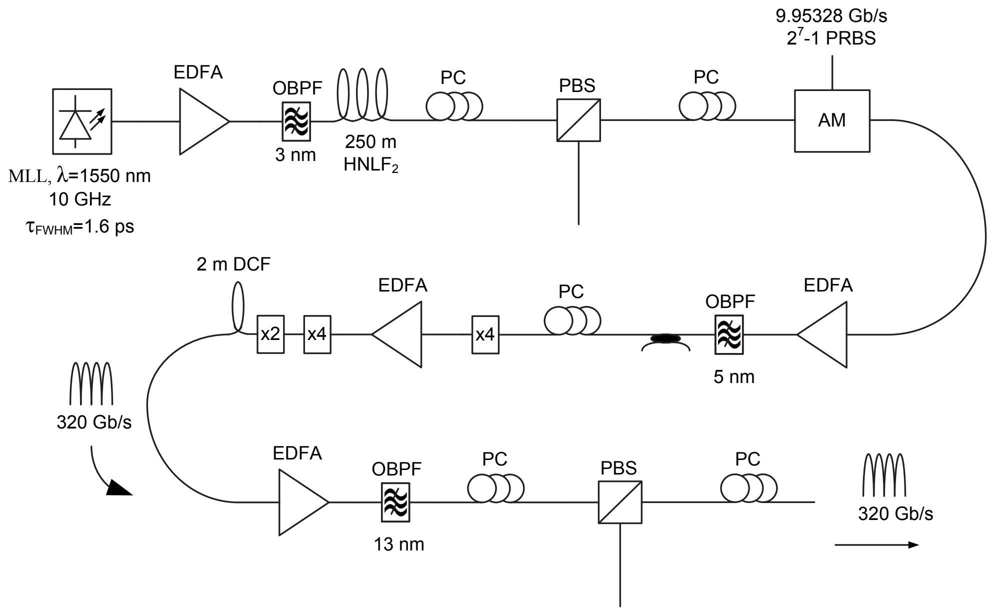

Figure 7.14: Schematic diagram of the 320 Gb/s transmitter.

compression the signal is modulated by a Mach-Zehnder amplitude modulator (AM) with a $2^7 - 1$ PRBS. The signal is then amplified, filtered and multiplexed with passive delay line multiplexers to a 320 Gb/s OTDM signal. The pulses are compressed to 680 fs FWHM. To maintain this pulse width small pieces of several meters of dispersion compensating fiber (DCF) are required to compensate for dispersion in the fiber patch cords. A PC in combination with a PBS is used as polarization filter to ensure a constant polarization at the input of our Kerr switch. A schematic of the experimental setup of the 320 Gb/s ADM based on the Kerr shutter is shown in Figure 7.15. The control pulse employed in the ADM is generated by a different MLL pulse source. This second MLL generates 1.8 ps FWHM pulses at $\lambda_c = 1537$

nm and at 10 GHz. This control pulse is also compressed to 1.6 ps FWHM before combining it with the OTDM signal. The eye diagram of the control pulse before the ADM is depicted in Figure 7.16. The 10 GHz control and the 320 Gb/s data signal are combined by a passive coupler, before entering the Kerr shutter. The Kerr shutter consits of a 500 m $HNLF_1$, followed by a 5 nm OBPF, a PC and a PBS.

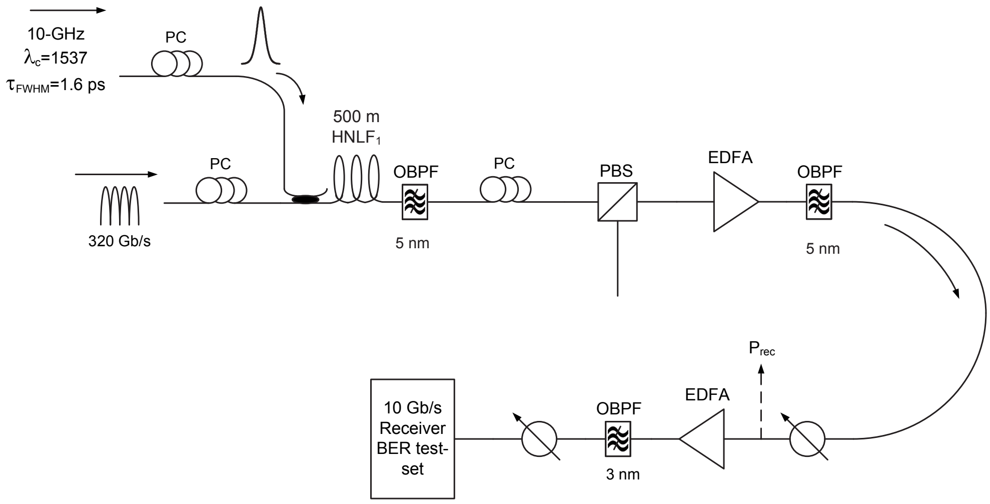

Figure 7.15: Experimental setup of the 320 Gb/s ADM based on the Kerr shutter.

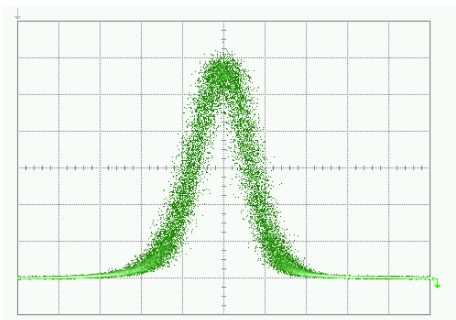

Figure 7.16: Control pulse before $HNLF_1$. X-scale: 1 ps/div, y-scale: a.u.

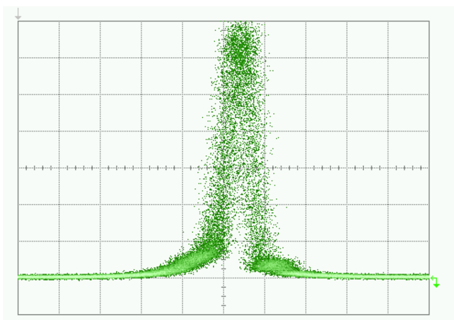

Figure 7.17: Control pulse after $HNLF_1$. X-scale: 1 ps/div, y-scale: a.u.

7.4.2 Results

In $HNLF_1$ the polarization of the data signal is rotated according to the operation principle described in section 7.1. The average power of the control pulse coupled into the $HNLF_1$ is 12.1 dBm, and the average power of the OTDM signal power coupled into $HNLF_1$ is P_d = +5.7 dBm. In the $HNLF_1$ the control pulse is compressed. The control pulse after propagation through $HNLF_1$ is shown in Figure 7.17. The control pulse width, measured on the autocorrelator, is compressed to 800 fs FWHM. The spectra at the input and output of the 500 m long $HNLF_1$ are shown in Figure 7.18 and 7.19, respectively. The FWHM spectral width of the control pulse (τ_c) is broadened from 2.9 nm to 8.3 nm. Increasing the control power beyond 12.1 dBm would introduce crosstalk because of spectral overlapping.

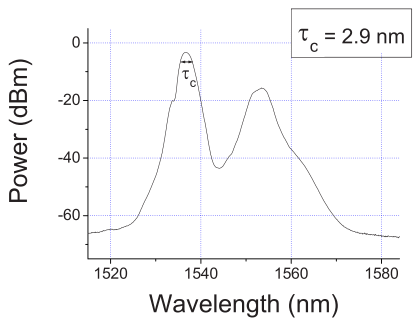

Figure 7.18: Spectrum at the input of 500 m $HNLF_1$ with 320 Gb/s input signal at $\lambda_d = 1553$ nm and control signal at $\lambda_c =$ 1537 nm (res. bw. = 1 nm).

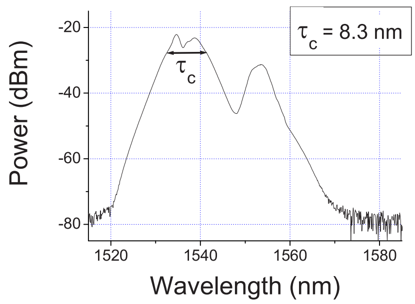

Figure 7.19: Spectrum at the output of 500 m $HNLF_1$ with 320 Gb/s input signal at $\lambda_d = 1553$ nm and control signal at $\lambda_c =$ 1537 nm (res. bw. = 1 nm).

The eye diagrams of the 320 Gb/s ADM are shown in Figures 7.20 to 7.23. The input 320 Gb/s signal is shown in Figure 7.20. When taking a careful look at the through channels in Figure 7.22 a small broadening of the data pulses is observed. Careful tuning of the dispersion is required for these short optical pulses. Short pieces of DCF are used to optimize the dispersion compensation for the accumulated dispersion in the patch cords and EDFAs. All eye diagrams show clear and open eyes, which indicates excellent operation.

After the ADM the quality of the dropped channel is assessed by a BER-measurement. The BER of the 320 Gb/s to 10 Gb/s demultiplexed channel is compared to a 10 Gb/s RZ B2B signal and to a 160 Gb/s to 10 Gb/s demultiplexed signal. These BER curves are shown in Figure 7.24. The BER is measured versus the received power as indicated in the schematic of the experimental setup, depicted in Figure 7.15. A BER measurement of the added and through channels could unfortunately not be performed because of the unavailability of a second drop mechanism, however the eye diagrams in Figure 7.22 and 7.23 predict good performance. The sensitivity penalty of the dropped channel from 160 Gb/s to 10 Gb/s at BER=10^{-9} is 1.7 dB for the best channel and 2.7 dB for the worst channel. The sensitivity penalty for the 320 Gb/s to 10 Gb/s demultiplexed channels is 3.9 dB for the best channel and 5.1 dB for the worst channel.

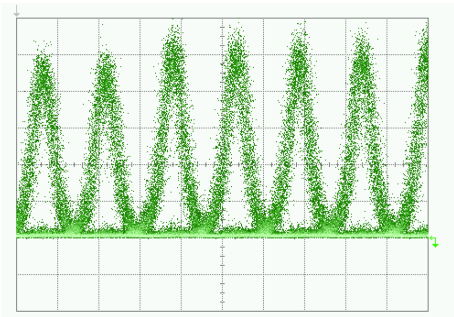

Figure 7.20: 320 Gb/s input signal. X-scale: 2 ps/div, y-scale: a.u.

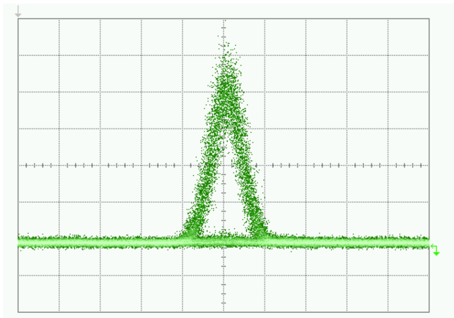

Figure 7.21: Demultiplexed channel from 320 Gb/s to 10 Gb/s. X-scale: 2 ps/div, y-scale: a.u.

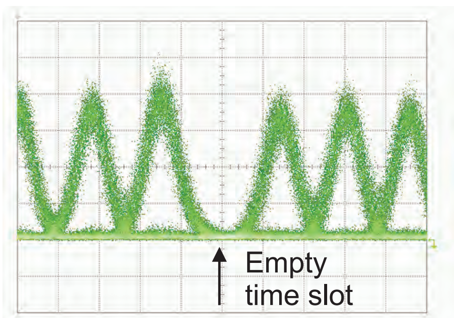

Figure 7.22: Through channels 31 × 10 Gb/s. X-scale: 2 ps/div, y-scale: a.u.

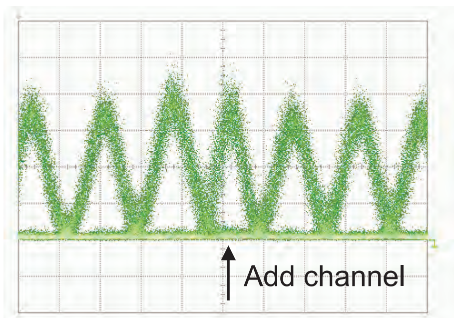

Figure 7.23: Through channels plus add channel. X-scale: 2 ps/div, y-scale: a.u.

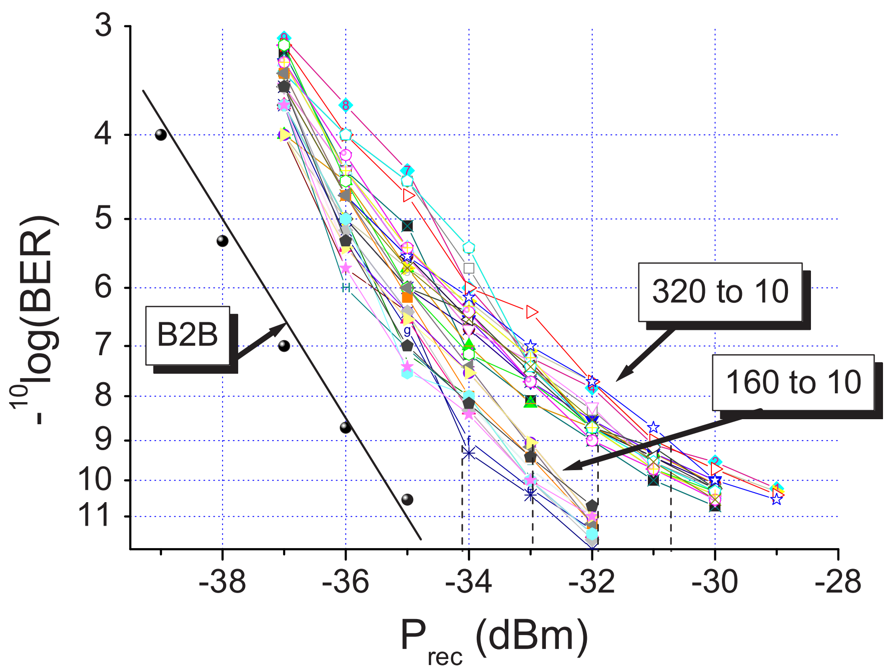

Figure 7.24: BER of demultiplexing from 160 Gb/s to 10 Gb/s and from 320 Gb/s to 10 Gb/s compared with a B2B signal.

7.5 Conclusion

The Kerr shutter is a promising tool to establish an optical add-drop multiplexer (ADM) with the potential to operate at Tbit/s owing to the ultrafast fiber nonlinearities. It uses the nonlinear birefringence of a highly nonlinear fiber (HNLF). Measurement of the switching window shows contrast ratios larger than 15 dB. The measurement of the angle of rotation of the state of polarization (SOP) shows that 17 dBm average power for a 2.3 ps FWHM 10 GHz control pulse results in a 0.8 π radian rotation. Within the experimental context, a full π rotation of the SOP has not been achieved, therefore separate optimization of the add and drop ports is required to minimize the receiver sensitivity penalty. Unfortunately, separate optimization of the drop and through function requires more components, making the setup more complex.

A feasibility study to create an add-drop multiplexer (ADM) for RZ-DPSK OTDM signals based on the Kerr shutter in HNLF has been performed. All-optical time domain add-drop multiplexing for a 80 Gb/s RZ-DPSK OTDM signal based on a Kerr shutter consisting of 375 m $HNLF_2$ has been shown to be feasible. The phase information in the signal is preserved in the complete add-drop node and the demultiplexer of the OTDM receiver, including a highly nonlinear fiber, a polarization beam splitter and two EAMs. In this experiment we were limited to 80 Gb/s because of the limited extinction ratio at the transmitter side, but in principle the ultrafast fiber nonlinearities ensure the possibility to upgrade the system to 160 Gb/s and higher.

An experimental proof-of-principle experiment shows the feasibility of operating the Kerr shutter as ADM for amplitude modulated signals at 160 Gb/s and 320 Gb/s. Error free demultiplexing from 160 Gb/s and 320 Gb/s is achieved and eye diagrams show good functioning of the through and add operation. The Kerr shutter is a good alternative for the NOLM as all-optical ADM at 320 Gb/s.

Chapter 8

Towards 640 Gb/s

The next step after a successful demonstration of a 320 Gb/s add-drop multiplexer (ADM) is to increase the line rate of the optical time division multiplexed (OTDM) signal to 640 Gb/s. Further enhancement of high-speed OTDM networks to 640 Gb/s requires knowledge about special requirements for the transmitter, the transmission line and the receiver. In a 640 Gb/s OTDM system the spacing between consecutive pulses is only 1.56 ps and hence it is required to operate with femtosecond pulse sources. The generation of stable, low jitter femtosecond pulses is the first challenge that has to be overcome. The second challenge appears in the transmission line. Careful compensation for second order dispersion (SOD), third order dispersion (TOD) and fourth order dispersion (FOD) is required. The third challenge arises at the receiver. The incoming OTDM signal needs to be demultiplexed to the base rate before it can be processed in the electrical domain.

This chapter starts with a short description of the transmitter in section 8.1. The transmission line and the influence of FOD is presented in section 8.2. In section 8.3 the receiver is described and the experimental results of demultiplexing at 640 Gb/s are presented. Finally, this chapter ends with conclusions in section 8.4.

8.1 Transmitter

To create an OTDM signal, which exceeds a line rate of 320 Gb/s, the availability of a femtosecond pulse source is required. A mode-locked laser (MLL) appears to be a good option. Since it is difficult to generate a femtosecond pulse train directly from an MLL, external pulse compression is commonly used [15, 145, 146]. The electrical modulation speed of digital signals is currently limited to 100 Gb/s, so it is not yet possible to prepare an optical source with repetition rates exceeding 100 Gb/s. Hence, it is important to generate a pulse train at 10, 40 or 100 GHz with full width half maximum (FWHM) pulse widths of less or equal to 500 fs. Moreover, a low timing jitter (< 75 fs) on the pulse train is desired. The schematic diagram of the transmitter utilized in our experimental work is shown in Figure 8.1. A commercial available MLL from Pritel has been used as pulse source. The MLL produces a 9.95328-GHz pulse

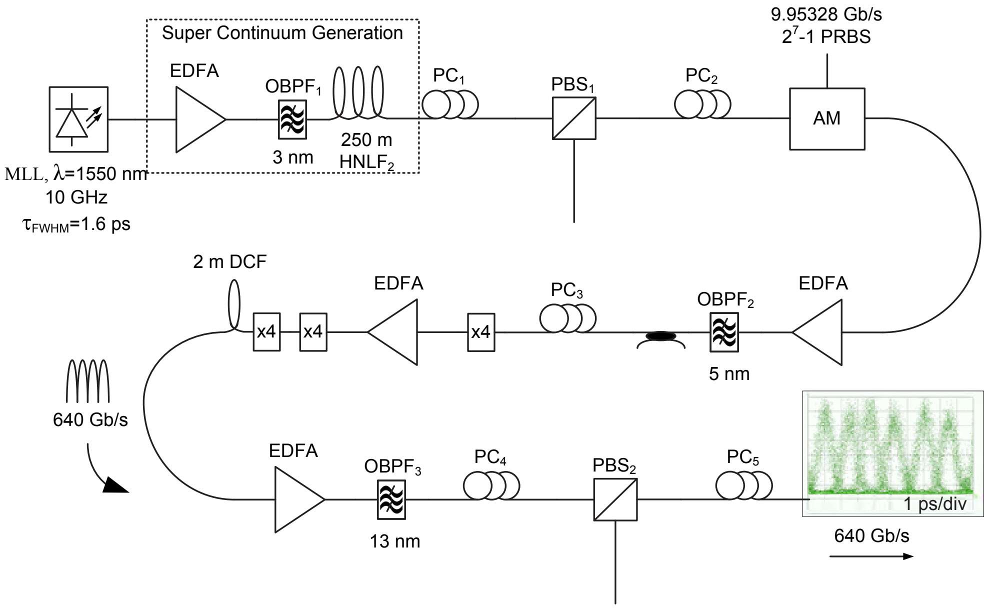

Figure 8.1: Schematic diagram of the 640 Gb/s transmitter.

train at $\lambda = 1550$ nm with 1.6 ps FWHM pulses. This pulse train is amplified by an Erbium-doped fiber amplifier (EDFA) and filtered by optical band pass filter 1 ($OBPF_1$). Pulse compression takes place in highly nonlinear $fiber_2$ ($HNLF_2$), based on super continuum generation (SCG). The parameters of $HNLF_2$ are listed in Table A.2. The average power at the input of the 250 m long $HNLF_2$ is 21.7 dBm. Pulse compression based on SCG is more thoroughly explained in appendix B.2. The super continuum spectrum is filtered with an $OBPF_2$ centered at $\lambda_d = 1553.4$ nm. After the pulse compression the signal is modulated by an Mach-Zehnder amplitude modulator (AM) with a 2^7-1 pseudo random bit sequence (PRBS) data signal. The signal is then amplified, filtered and 64 times multiplexed with passive delay line multiplexers to a 640 Gb/s OTDM signal. The pulses are 680 fs FWHM after the pulse compression. To maintain this pulse width small pieces of several meters of dispersion compensating fiber (DCF) are required to compensate for dispersion in the fiber patch cords and EDFAs. The rule of thumb states that the pulse width has to be 15%-30% of the bit slot. Our input pulse of 680 fs is therefore too large and consequently an extra penalty at the receiver is expected. A polarization controller (PC_4) in combination with a polarization beam splitter (PBS_2) is used as polarization filter to ensure a constant polarization.

8.2 Transmission

Previously reported experiments have shown a 640 Gb/s OTDM signal to be transmitted over 100 km by using a 300 fs pulse train [145]. 1.28 Tbit/s OTDM transmission has been shown with pulses of 200-400 fs, by adopting alternating polarization [146]. To realize 640 Gb/s (or higher) bit rates with OTDM using femtosecond pulses, it is very important to find a way to compensate for the dispersion of the transmission lines. Second and third order dispersion can be compensated for by a combination of different fibers (dispersion plus dispersion slope compensation). Since the spectral width of the transmitted pulse is very high the higher-order dispersion of transmission lines [147] have to be taken into account as well. The first step is to look at the fourth order dispersion (FOD).

8.2.1 Simulation of Fourth Order Dispersion Effects

To gain more knowledge about the influence of the FOD coefficient, a simulation has been conducted. A 640 Gb/s signal is transmitted over five spans of 100 km true wave reduced slope (TWRS) fiber. The propagation through the TWRS fiber is solved, based on a numerical calculation of the nonlinear Schrödinger equation (NLSE) of linearly-polarized optical signals by using the split-step Fourier method. More information on the split-step Fourier method can be found in Appendix D.1.1. The 640 Gb/s signal is constructed from a 300 fs FWHM secant-shaped pulse train. The signal is transmitted over 100 km TWRS fiber, with dispersion $D = 4.29$ ps·nm^{-1}·km^{-1} and dispersion slope $S = 0.047$ ps·nm^{-2}·km^{-1}. After each span of 100 km, a 8.58 km long dispersion compensating fiber (DCF) is used to compensate for the second order dispersion (SOD) and the third order dispersion (TOD). The dispersion and dispersion slope of the DCF are chosen such that SOD and TOD are 100% compensated. To study the influence of the FOD coefficient (β_4), in the first run the FOD coefficient is set to zero, while in the second run $\beta_4 = 8.6 \cdot 10^{-4}$ ps^4/km [148, 149]. A simplified schematic diagram of the simulation is shown in Figure 8.2. Before each fiber span,

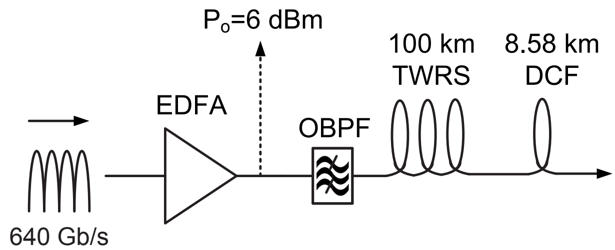

Figure 8.2: Schematic diagram of one fiber span of 640 Gb/s transmission simulation, in order to test the influence of the fourth order dispersion coefficient (β_4).

an idealized EDFA without dispersion and with noise figure of 5 dB is employed to boost the signal to an average power of 6 dBm. At the output of the EDFA a 3rd order 2560 GHz Bessel band pass filter is inserted to filter out part of the ASE noise.

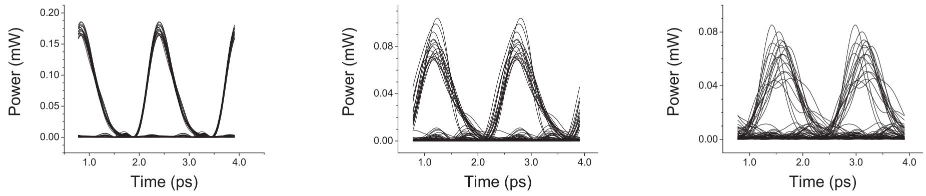

(a) 100 km (b) 300 km (c) 500 km

Figure 8.3: 640 Gb/s eye-diagram. 100% compensation for dispersion and dispersion slope, no FOD is included. Transmission of 100 km (a), 300 km (b) and 500 km (c).

The eye diagrams of the 640 Gb/s OTDM signal, without FOD included ($\beta_4 = 0$) are shown in Figure 8.3 for transmission through 100, 300 and 500 km. The eye-opening is gradually reduced with increasing transmission distance. After 500 km, the eye diagram is still open, but the quality is reduced. The eye-opening reduction of the 640 Gb/s signal is due to the nonlinear impairments during the transmission, induced by the Kerr effect in the fiber. Several examples of the Kerr effect induced impairments are self-phase modulation (SPM), intra-channel cross phase mixing (IXPM) and intra-channel four-wave mixing (IFWM), which are limiting effects for high bit rate OTDM systems [150, 151]. Intra-channel nonlinear effects appear because in the first few meters of fiber the power of the pulse is spread out over several bit slots as a result of dispersion.

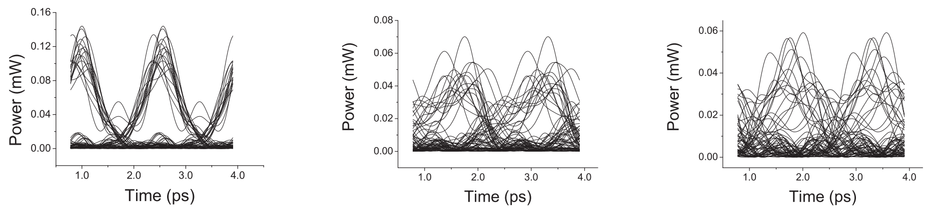

(a) 100 km (b) 300 km (c) 500 km

Figure 8.4: 640 Gb/s eye-diagram. 100% compensation for dispersion and dispersion slope. FOD is included in the transmission line. Transmission of 100 km (a), 300 km (b) and 500 km (c).

The eye diagrams of the 640 Gb/s OTDM signal, with FOD included ($\beta_4 = 8.6 \cdot 10^{-4}$ ps^4/km) are shown in Figure 8.4, for 100, 300 and 500 km transmission. The eye diagram after 100 km still shows an open eye, but when the transmission distance is increased to 300 km and beyond, the eye is completely closed. We can conclude that when no compensation for the FOD is included, the distortion of the 640 Gb/s signal due to FOD is larger than the distortion due to the nonlinear impairments SPM, IXPM and IFWM.

For the implementation of a successful 640 Gb/s OTDM transmission system, it is important to realize some form of FOD compensation. There are two existing techniques for FOD compensation. The first technique applies a frequency-resolved programmable dispersion compensator [152] and the second technique utilizes the combination of the excess SOD of the fiber link in combination with a cosine phase modulation [148, 153].

8.3 Receiver

The difficulty at the receiver is to extract the 10 or 40 Gb/s base rate channel from the 640 Gb/s line rate. In [15, 16, 102], error-free demultiplexing with a nonlinear optical loop mirror (NOLM) is presented. In this section an alternative method, based on combining XPM spectral broadening and the Kerr shutter, is examined for all-optical demultiplexing from 640 Gb/s to 10 Gb/s, which comprises less components than the NOLM-based demultiplexer.

8.3.1 Experimental Results at 640 Gb/s

The most suitable fiber in our lab to conduct a 640 Gb/s experiment is $HNLF_1$, whose parameters are listed in Table A.1. $HNLF_1$ is the most suitable fiber because its zero dispersion wavelength is located at $\lambda_0 = 1545$ nm and the control and data signal can be placed symmetrically around λ_0 to minimize the walk-off time. An experimental assessment of the demultiplexing performance with $HNLF_1$ has been performed first, before considering any ADM configurations. The experimental setup is shown in Figure 8.5. A 10 GHz control signal with 1 ps FWHM control pulses at $\lambda_c = 1535$

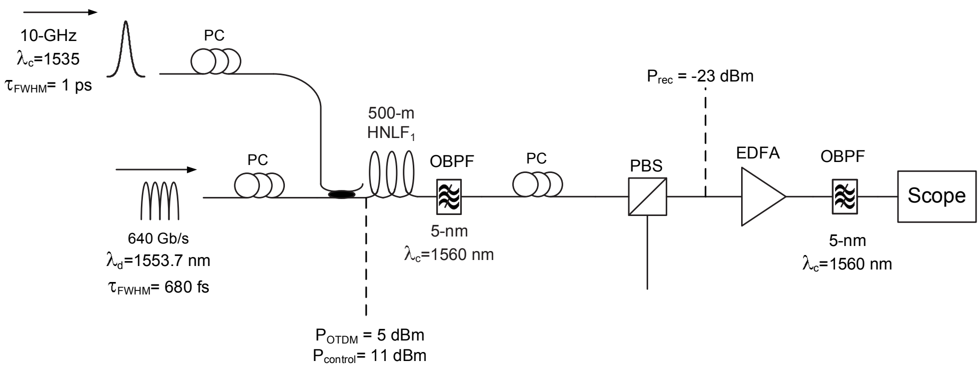

Figure 8.5: Schematic diagram of a 640 Gb/s demultiplexer.

nm is combined with a 640 Gb/s (64 × 10 Gb/s) OTDM signal with 680 fs FWHM data pulses. The spectrum of the generated 640 Gb/s signal at $\lambda_d = 1553.4$ nm is shown in Figure 8.6. The -3 dB spectral width of the 640 Gb/s input signal is 2.9 nm and the eye diagram is shown in the inset of Figure 8.1.

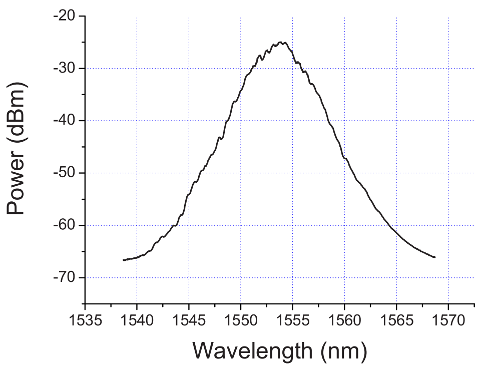

Figure 8.6: Spectrum of the 640 Gb/s OTDM signal, spectral width is 2.9 nm (res. bw. = 0.5 nm).

The walk-off time is minimized by placing the wavelengths of control and data almost symmetrically around the zero dispersion wavelength $\lambda_0 = 1545$ nm. The walk-off between the $\lambda_c = 1535$ nm control signal and the $\lambda_d = 1553.4$ nm data signal is governed by equation (3.31), and is $t_w = 370$ fs. The OTDM signal is broadened by control pulse induced XPM spectral broadening. The demultiplexed channel is selected by filtering at $\lambda_{\text{demux}} = 1560$ nm. Moreover, the polarization of the targeted demultiplexed channel is also rotated. Therefore, it can be stated that this method is a combination of the techniques described in Chapter 6 and 7. The power at the input of HNLF_1 is $\text{P}_{\text{control}} = 11$ dBm and $\text{P}_{\text{OTDM}} = 5$ dBm.

The broadening of the spectrum of the control pulse has a strong influence on the walk-off time between the spectral broadened parts of the control pulse spectrum and the data signal. The -3 dB spectral width of the control pulse is increased from 2.9 nm to 10 nm. The walk-off time of a 1553.4 nm data signal and the control signal is shown in Figure 8.7. Projecting the broadened spectrum of the control pulse on the walk-off time graph, it can be noted that the walk-off between the most red-shifted and the most blue-shifted components of the control pulse is 1.5 ps.

A second detrimental effect, similar to the walk-off also caused by dispersion, is pulse broadening. The dispersion at $\lambda_d = 1553.4$ nm can be calculated by using equation (3.29): $D = 0.241$ ps·nm^{-1}·km^{-1}. The spectral width of the input 640 Gb/s OTDM signal is $\Delta\lambda_{sw} = 2.9$ nm. Broadening of the pulse in the time domain after transmission through the 500 m long HNLF_1 is estimated by: $D \cdot L \cdot \Delta\lambda_{sw} \approx 300$ fs.

The bit time slot of a 640 Gb/s OTDM signal is 1.56 ps. The required pulse width to avoid intra channel crosstalk ($\leq 30\%$ of the bit slot) is about 500 fs. The combination of the walk-off, the dispersion and unwanted nonlinear impairments like SPM, IXPM, IFWM on the OTDM and control signal limits the performance of our all-optical demultiplexer in this experiment.

Under these conditions a 640 Gb/s demultiplexing experiment can not be carried

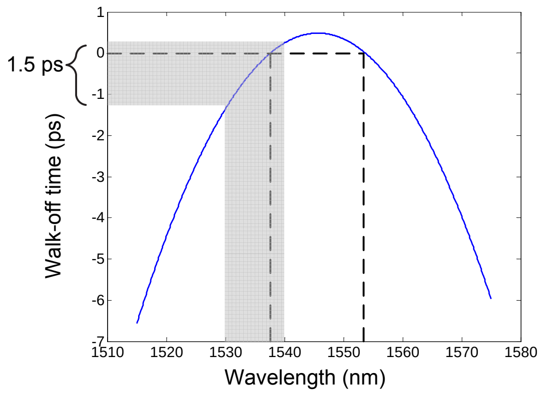

Figure 8.7: Walk-off time between a 1553.4 nm data signal and a control signal versus the wavelength of the control signal.

out successfully. The eye diagram of the 640 to 10 demultiplexed signal (see Figure 8.9) is closed, which indicates an error rate floor (error floor at at BER=10^{-4}).

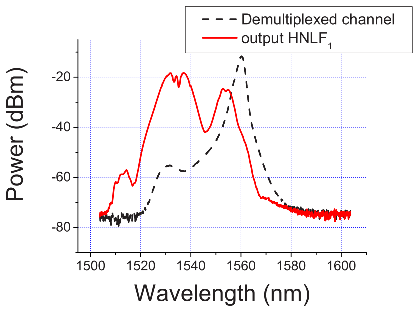

Figure 8.8: Spectrum of the 640 Gb/s OTDM signal and the control pulse at the output of HNLF$_1$ and the filtering of the demultiplexed channel at λ_{demux} = 1560 nm.

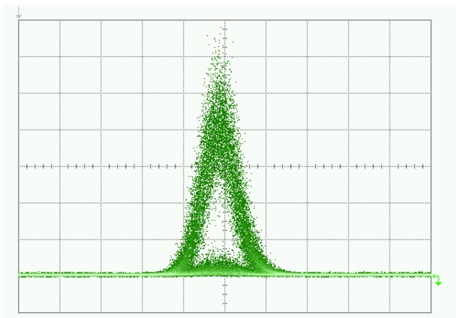

Figure 8.9: Eye diagram of the 640 Gb/s to 10 Gb/s demultiplexed channel based on the combined effect of XPM spectral broadening and the Kerr shutter.

To improve the performance of the 640 Gb/s all-optical demultiplexer, shorter lengths of 50 or 100 m HNLF are preferable [154]. With an increasing length of the HNLF, the spectral overlap of control and data at the output of the HNLF also increases, causing a degradation of the switching window and consequently of the quality of the dropped channel.

8.4 Conclusion

A 640 Gb/s transmitter is realized by applying pulse compression to a 1.6 ps, 10 GHz pulse train that was originated from a mode-locked laser (MLL). When second order dispersion (SOD) and third order dispersion (TOD) are compensated in the transmission line, then the fourth order dispersion (FOD) has to be taken into account. The influence of FOD is characterized by simulations and limits the transmission distance to 100 km, without applying any form of FOD compensation.

The ultrafast fiber nonlinearities (in the order of a few femtoseconds) are in principle fast enough for creating a 640 Gb/s all-optical demultiplexer and an add-drop multiplexer (ADM). However, difficulties arise in controlling the walk-off and the dispersion effect. Control pulses in the order of ≤ 1 ps, and equally short pulses for the OTDM signal have in general a small walk-off length (equation (3.27)). Walk-off between control and data signals limits the interaction time. The interaction only takes place, when control and data pulses overlap in time. The walk-off is caused by the combination of SOD and TOD. A second detrimental effect caused by dispersion is pulse broadening. When the pulses are short, they exhibit a large spectral width. This results in pulse broadening even in short lengths of fiber.

An experiment that combines two demultiplexing methods has been presented. The first method is based on control pulse induced cross-phase modulation (XPM) spectral broadening of the data signal, which is more thoroughly described in Chapter 6. The second method is based on control pulse induced polarization rotation of the data signal (Kerr shutter), which is studied in Chapter 7. The length of the highly nonlinear fiber (HNLF) in the 640 Gb/s demultiplexing experiment is 500 m, which is too long. Increasing the nonlinear coefficient, which enables the possibility to employ shorter lengths, with the combination of a smaller dispersion and dispersion slope of the fiber will lead to a successful all-optical demultiplexer and subsequently the development of a 640 Gb/s ADM.

Chapter 9

Conclusions and Recommendations

In this work we have studied all-optical add-drop multiplexing techniques for optical time division multiplexed (OTDM) networks. The objective was to investigate high-speed switching technologies at 160 Gb/s and beyond, for all-optical demultiplexing and add-drop multiplexing in an OTDM based network.

Optical add-drop multiplexers (ADMs) can be subdivided into two categories. Semiconductor-based solutions and solutions based on the third order nonlinear susceptibility (Kerr effect) in a highly nonlinear fiber (HNLF). Semiconductor-based solutions have the advantage that they can be integrated on a photonic chip. However, their disadvantage is the limited recovery time of the semiconductor optical amplifiers and electroabsorption modulators, providing in general an upper boundary for the maximum obtainable bit rate. On the other hand, fiber-based solutions apply the nonlinear Kerr effect, which has a response in the order of a few femtoseconds which basically allows operation at Tb/s speeds. In this chapter we will try to give an answer to the research questions that have been raised in section 1.6 of the introduction, building on the research results of this thesis work.

- *Is it possible to develop an add-drop multiplexer based on electroabsorption modulators (EAMs) in an optically pumped configuration? Moreover, is it possible to integrate this solution with an all-optical mode-locked laser clock recovery device?*

  Integration of an EAM with a laser has already been shown [155]. Therefore, it most likely is possible to integrate an EAM together with an MLL clock recovery and to design a fully integrated time domain ADM. An ADM based on optically controlled EAMs, employing the cross-absorption modulation (XAM) effect, is limited by the carrier recovery time of the EAM. The maximum obtained operation speed with an EAM that is not optimized for XAM and without exceeding the maximum non-destructive input power is 80 Gb/s. Increasing the reverse bias voltage decreases the recovery time. However, this leads to an increase in absorption, which requires a higher input power to saturate the absorption, otherwise degradation of the signal-to-noise ratio (SNR) is unavoidable. This requirement for high input power is confirmed by our simulation model; however, in the experimental work we were severely limited by the maximum non-destructive input power of the commercially available EAM. Designing an EAM optimized for XAM will reduce the required optical power to bleach the absorption. In [57, 58] an XAM optimized design reduces the switching energy to 500 fJ per data pulse. If we compare this with the 5 pJ obtained from our simulation, the required power is reduced with a factor of 10. Ongoing research on overcoming the limit of the carrier recovery time, by looking at ultrafast phenomena, like carrier heating and spectral hole burning and two photon absorption in semiconductor devices [156, 157] looks promising.

- *What is the most suitable add-drop multiplexing technique based on the Kerr effect in a highly nonlinear fiber?*

  All-optical signal processing using the Kerr effect in a highly nonlinear fiber (HNLF) and its potential applications for OTDM add-drop multiplexing are promising. Fiber based interferometric gates are independent of the control pulse rate and can operate at ultrafast speed, because of the ultrafast nonlinearities in the order of several femtoseconds. This makes them suitable as ADM and a good alternative to semiconductor-based solutions.

  In this thesis, experimental proof of the feasibility of generating an ADM at 160 Gb/s and 320 Gb/s, with the NOLM in Chapter 4 and the Kerr shutter in Chapter 7, is given. An ADM based on FWM in HNLF appears to be less promising. In spite of the ultrafast FWM mechanism, the low conversion efficiency for larger spectral widths of the ultra short optical pulses limits the performance. Control pulse induced cross-phase modulation (XPM) spectral broadening has strict requirements on the control pulse shape, but a 160 Gb/s ADM can still be achieved. For an ADM based on XPM spectral broadening it is crucial that the rising edge (or falling edge) of the control pulse covers the complete data pulse. If this is not the case, crosstalk in the through channel will appear. The difference in performance between the two most promising solutions, the NOLM and the Kerr shutter, is considered to be small according to the results presented in this work. The penalty for demultiplexing from 320 Gb/s to 10 Gb/s for the Kerr shutter is 3.9 dB for the best channel and 5.1 dB for the worst channel, and for demultiplexing from 320 Gb/s to 10 Gb/s with the NOLM a penalty of 6 dB is observed. The differences can be attributed to several limiting and "on the edge" factors for operating at 320 Gb/s. The critical parameters are: data pulse width, control pulse width and shape, dispersion, walk-off time and unwanted nonlinear effects like for example self-phase modulation (SPM), intra-channel cross-phase mixing (IXPM) and intra-channel four-wave mixing (IFWM). To conclude, the choice between NOLM and Kerr shutter as the most suitable ADM will be based on requirements of complexity, robustness and efficiency. A series of experiments under exactly the same conditions to determine the difference in efficiency for the NOLM and Kerr shutter are required. Careful optimization of the control pulse shape and width, as well as a detailed study on the optimal wavelength allocation is desired. In particular, the tolerance towards dispersion, and walk-off time needs to be addressed. Moreover, the polarization dependence of the add-drop multiplexing techniques have to be solved by working towards polarization maintaining HNLF solutions and/or polarization diversity solutions.

- *Can we combine transmultiplexing from OTDM-to-WDM and WDM-to-OTDM to make a more flexible network node?*

  Transmultiplexing based on FWM in a HNLF has been studied. Conversion from OTDM-to-WDM is feasible for 160 (4×40) Gb/s. Conversion back from 4×40 Gb/s WDM-to-OTDM has been studied based on FWM in a HNLF, similar to the OTDM-to-WDM conversion concept. Several advantages of employing FWM as transmultiplexing mechanism are the format transparency of FWM and that no extra conversion step from NRZ-to-RZ is required before the transmultiplexing. However, achieving good performance is more challenging, due to the low conversion efficiency of the FWM process when many unwanted FWM processes diminish the efficiency of the targeted FWM product. This WDM-to-OTDM conversion technique based on FWM in HNLF is limited to two WDM channels of 40 or 80 Gb/s. An increase of the number of channels requires a different transmultiplexing concept with an extra NRZ-to-RZ conversion step.

- *Despite the increased interest in differential phase shift keying (DPSK) systems, add-drop multiplexing has not been investigated for DPSK so far. Therefore, we want to know if it is possible to create an all-optical time domain add-drop multiplexer for phase modulated signals?*

  A feasibility study to create an add-drop multiplexer (ADM) for RZ-DPSK OTDM signals based on the Kerr shutter in HNLF has been performed. All-optical time domain add-drop multiplexing for a 80 Gb/s RZ-DPSK OTDM signal based on a Kerr shutter consisting of 375 m $HNLF_2$ has been shown to be feasible. The phase information in the signal is preserved in the complete add-drop node and the demultiplexer of the OTDM receiver, including a highly nonlinear fiber, a polarization beam splitter and two EAMs. In the experimental work we were limited to 80 Gb/s because of the limited extinction ratio at the transmitter side, but in principle the ultrafast fiber nonlinearities ensures the possibility to upgrade the system to higher bit rates. Operating the Kerr shutter with an amplitude modulated OTDM signal, an ADM with a bit rate of up to 320 Gb/s can be generated and has been presented in this work. An interesting point for further research is to study RZ-DPSK ADMs at such ultra high bit rates, based on the Kerr shutter. To complete this task, a femtosecond pulse source with stable phase from pulse to pulse is a necessity. Also a study on alternative techniques for RZ-DPSK add-drop multiplexing is an interesting topic for further research.

Future OTDM systems with ultra high bit rates (≥ 640 Gb/s) will require research on femtosecond pulse generation and propagation. A high bit rate OTDM system requires a stable short pulse source, to improve the performance of all-optical time domain add-drop multiplexers. The first challenges in creating a successful 640 Gb/s ADM is to be able to create a good control pulse and a good 640 Gb/s input signal. Control pulses in the order of ≤ 1 ps, and equally short pulses for the OTDM signal have in general a small walk-off length (equation (3.27)). Walk-off between control and data pulses limits the interaction time. Interaction only takes place, when they overlap in time. The walk-off is caused by the fiber dispersion. A second detrimental effect caused by dispersion is pulse broadening. When the pulses are short, they exhibit a large spectral width. This results in pulse broadening, even in short lengths of fiber. The ultrafast fiber nonlinearities (in the order of a few femtoseconds) are in principle fast enough for creating a 640 Gb/s ADM. However, with a HNLF that has a nonlinear coefficient of 15 or 20, lengths in the order of several hundreds of meters are necessary, to achieve the amount of nonlinear interaction with a reasonable pump power, required to switch on the basis of the Kerr shutter (Chapter 7) or the NOLM (Chapter 4). An demultiplexing experiment at 640 Gb/s with HNLF_1, presented in Chapter 8, clearly shows our current practical limitations. The area of 640 Gb/s OTDM signal processing, and in particular add-drop multiplexing, is largely unexplored. The interplay between the different nonlinear effects is not covered as well as it should be. An estimate of the required power to achieve ADM at 640 Gb/s needs to be studied, because the current formulas described in the theoretical Chapter 3 for XPM, SPM and FWM do not include the increase of the spectral width and the corresponding lowering of the peak power. Also, the effects of dispersion on these nonlinear effects can not be neglected. Up to date, only numerical solutions for these issues exist.

With the development of improved types of HNLF, with an increased nonlinear coefficient of 1360 $\mathrm{W}^{-1}\mathrm{km}^{-1}$ [158] shorter lengths are required to achieve the same amount of nonlinear interaction, and at the same time the influence of dispersion is reduced. In short, a HNLF is a versatile component. It can be used for a number of all-optical signal processing techniques. Besides the functionalities described in this thesis (demultiplexing and add-drop multiplexing), also other functionalities like pulse compression, regeneration, wavelength conversion, parametric amplification, optical cross connecting and packet routing are achievable at high bit rates.

Future optical networks employing 160 Gb/s or even higher bit rates of 640 Gb/s are opposed by many challenges. Ultra-high bit rate signals at one single wavelength compared to lower bit rate signals are less tolerant towards impairments like chromatic dispersion, polarization mode dispersion and the influence of nonlinear effects. These issues need to be solved in order to be able to increase the optical reach. Also the cascadability of ADMs in an optical network is an issue of concern. An extensive study on the influence of the extinction ratio and the shape of the switching window for the cascadability of various add-drop multiplexing methods are a topic for further research. To conclude, the technology of transmitter, regenerator and receiver for high-speed OTDM systems needs to mature considerably such that the cost of these components drop drastically, before cost-effective realization of OTDM systems is possible.

Appendix A

HNLF and DSF Parameters

The parameters of the fibers used in the experiments are described in this appendix. Two different samples of highly nonlinear fiber (HNLF), accommodating an increased nonlinear coefficient, are available for our experimental work. The parameters of these fibers are listed in the Table A.1 and Table A.2. These fibers are commercially available products from Sumitomo Electric Industries. Besides fibers with an increased nonlinear coefficient, also a normal dispersion shifted fiber (DSF) is employed for super continuum generation (SCG). The SCG process is described in Appendix B. This fiber is originating from Corning. The parameters of the DSF are listed in Table A.3.

Table A.1: Parameters of $HNLF_1$.

Parameter	Value
Length [m]	500
Effective length [m]	484
PMD [ps/$\sqrt{\text{km}}$]	0.14
Loss at 1550 nm [dB/km]	0.57
Zero dispersion wavelength λ_0 [nm]	1545
Dispersion at 1550 nm [ps·nm^{-1}·km^{-1}]	0.13
Dispersion Slope at 1550 nm [ps·nm^{-2}·km^{-1}]	0.03
Cut-off wavelength λ_c [nm]	1470
Effective cross-sectional area: A_{eff} [μm^2]	10.3
Mode field diameter [μm]	3.7
Nonlinear coefficient γ [W^{-1}·km^{-1}]	15

Table A.2: Parameters of $HNLF_2$.

Parameter	450-7381-01	450-7381-02	450-7381-03
Length [m]	250	125	125
Effective length [m]	245.7	123.9	123.9
Coil insertion loss [dB]	0.71	0.82	0.75
Polarization mode dispersion at 1550 [ps/$\sqrt{\text{km}}$]	0.02	0.03	0.06
Loss at 1550 nm [dB/km]		0.6	
Zero dispersion wavelength λ_0 [nm]		1590	
Dispersion at 1550 nm [ps·nm^{-1}·km^{-1}]		-1.1	
Dispersion Slope at 1550 nm [ps·nm^{-2}·km^{-1}]		+0.029	
Cut-off wavelength λ_c [nm]		1440	
Effective cross-sectional area: A_{eff} [μm^2]		11	
Mode field diameter at 1550 nm [μm]		3.8	
Nonlinear coefficient γ [W^{-1}·km^{-1}]		20	

Table A.3: Parameters of the DSF.

Parameter	Value
Length [km]	2.25
Effective length [km]	2.11
Loss at 1550 nm [dB/km]	0.25
Zero dispersion wavelength λ_0 [nm]	1550
Dispersion at 1550 nm [ps·nm^{-1}·km^{-1}]	0.0
Dispersion Slope at 1550 nm [ps·nm^{-2}·km^{-1}]	0.075
Effective cross-sectional area: A_{eff} [μm^2]	50
Nonlinear coefficient γ [W^{-1}·km^{-1}]	2.6

Appendix B

Super Continuum Generation

A super continuum (SC) spectrum refers to a generated optical spectrum that is continuous over a broad range of frequencies. A SC is generated by sending a picosecond pulse train (or shorter) through a nonlinear medium, like a fiber. Super continuum generation (SCG) in a fiber stems from the third order nonlinear susceptibility. The input spectrum broadens as a result of the combination of self-phase modulation (SPM), cross-phase modulation (XPM), four-wave mixing (FWM) and stimulated Raman scattering (SRS). A SC spectrum originating from a mode-locked laser (MLL) source does not only have a broad spectral range, but also has high coherency, high stability and a small amount of timing jitter. Recently SC has been demonstrated for a versatile number of functions in optical communications networks. SC generation (SCG) in optical fibers has been utilized in wavelength conversion [159], multiple-wavelength signal generation for dense WDM [3, 160] and *[132]*, ultra-short optical pulse generation for optical time division multiplexing [161], optical pulse shaping and all-optical data regeneration [162], multicasting and optical switching in packet-based optical networks [163]. In the work presented in this thesis SCG is utilized as wavelength conversion mechanism and as pulse compression mechanism. In section B.1 the generation of a control pulse based on super continuum generation in 2.25 km DSF is explained.

B.1 Control Pulse Generation

In our all-optical time domain add-drop multiplexers (ADMs) it is important to have a control signal that is synchronized, stable, has a low jitter and a pulse width smaller than the inverse of the aggregate bit rate. In our Freeband Impulse project: "Key components for 160 to 640 Gb/s Optical Time Domain Multiplexed (OTDM) Networking" a mode-locked laser (MLL) is under development that fulfills the control pulse requirements. At the time of the experiments this MLL was not yet available, therefore an alternative solution for the generation of the control pulse is required. In section B.1.1 the generation of the 40 GHz control pulse utilized for the 160 Gb/s ADM based on the NOLM is described. For the 320 Gb/s ADM operation a 10 GHz control pulse is required. The generation of this control pulse is described in section B.1.2.

B.1.1 40 GHz Control Pulse for 160 Gb/s Add-Drop Multiplexer

The schematic of the 40 GHz control pulse generation is shown in Figure B.1. A commercially available MLL from Calmar (type: PSL-40) is used to generate a 40 GHz 1.5 full width half maximum (FWHM) ps pulse train at $\lambda = 1549$ nm. The 40 GHz signal is then amplified by an Erbium-doped fiber amplifier (EDFA). The average power at the input of the 2.25 km DSF is 18 dBm. The parameters of the DSF are listed in Table A.3. The schematic of the experimental setup for this control pulse generation is shown in Figure B.1. The broadened spectrum at the output of the DSF is shown in Figure B.2. The 40 GHz control signal is obtained by spectrally slicing the fiber output signal at $\lambda = 1555.78$ nm with a 0.92 nm optical band pass filter (OBPF). The eye diagram of the wavelength converted pulse is shown in Figure B.3.

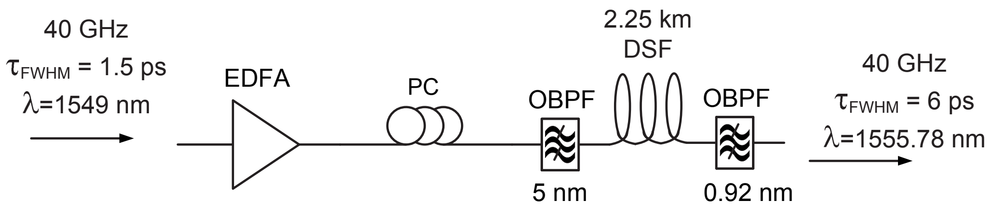

Figure B.1: Schematic of the setup for the control pulse generation at 40 GHz for the 160 Gb/s ADM.

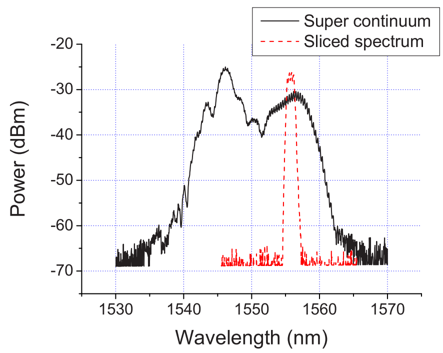

Figure B.2: SCG spectrum after the 2.25-km DSF. Input signal is at $\lambda = 1549$ nm and $\tau = 1.5$ ps.

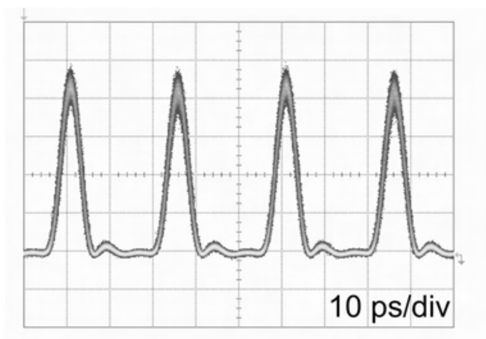

Figure B.3: Sliced spectrum of the control pulse at $\lambda = 1555.78$ nm.

B.1.2 Control Pulse for 320 Gb/s Add-Drop Multiplexer

For our 320 Gb/s ADM based on the NOLM (section 4.3.3), a low jitter, narrow control pulse is required. The input pulse is compressed in 1 km dispersion decreasing fiber (DDF) to create a pulse width of 800 fs FWHM. Higher compression can be achieved when careful tuning of power to the pulse compressor and dispersion is optimized, but for 320 Gb/s add-drop multiplexing 800 fs FWHM pulses are satisfactory. The schematic of the experimental setup for the generation of the control signal is shown in Figure B.4. The compressed pulse is amplified with an EDFA operating at constant output power $P_o = 24$ dBm. The amplified signal is filtered with a 13 nm OBPF to remove part of the ASE noise. The signal is transmitted through a 2.25 km long DSF and the spectrum at the output is broadened because of SCG, as can be seen in Figure B.5. The parameters of the DSF are listed in Table A.3. A 5 nm OBPF is used to select the wavelength of the converted control pulse.

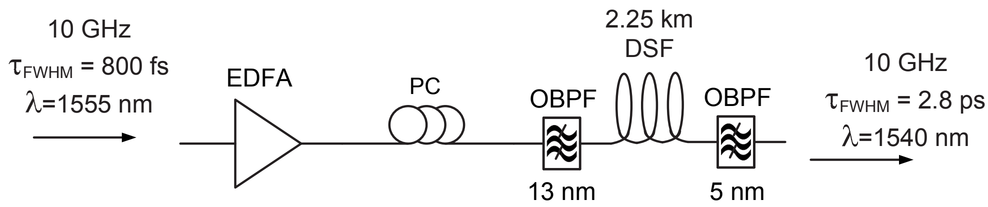

Figure B.4: Schematic of the setup for the control pulse generation

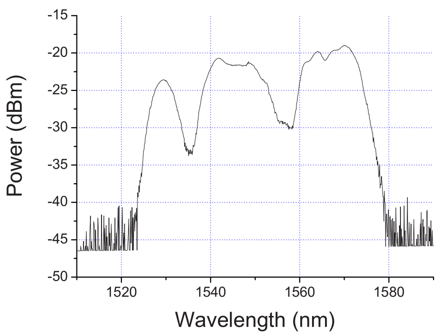

Figure B.5: SCG spectrum after the 2.25-km DSF. Input signal is at $\lambda = 1555$ nm and $\tau = 800$ fs.

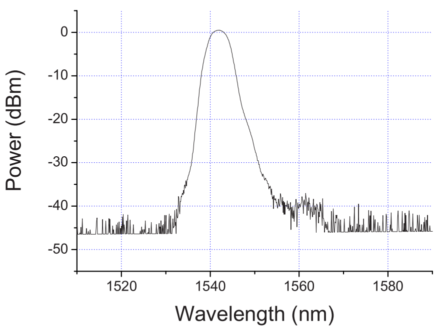

Figure B.6: Sliced spectrum of the control pulse at $\lambda = 1540$ nm.

B.2 Pulse Compression

SCG is utilized as pulse compression mechanism in $HNLF_2$. The parameters of $HNLF_2$ are listed in Table A.2. The compressed optical pulse train is used for optical time division multiplexing to a line rate of 320 or 640 Gb/s. The experimental setup of the 320 Gb/s transmitter is shown in Figure B.7. A MLL produces a 9.95328-GHz pulse train at $\lambda = 1550$ nm, with 1.6 ps FWHM pulses. The signal is amplified by and EDFA to an average power of 21.7 dBm at the input of the 250 m $HNLF_2$. Super continuum generation (SCG) takes place in $HNLF_2$. The zero-dispersion wavelength of $HNLF_2$ is $\lambda_0 = 1590$ nm. The generated SC is in the normal dispersion region and ahs a rather flat spectrum compared to a SC in an anomalous dispersion region. The SC generated spectrum at the output of $HNLF_2$ is shown in Figure B.8. The spectrum is linearly chirped. This SCG spectrum is filtered with an OBPF centered at $\lambda_d = 1553.4$ nm. By dispersive compression the pulse width is reduced to 680 fs. This signal is modulated and multiplexed to 320 Gb/s. The eye diagram of the 320 Gb/s signal is shown in figure B.9.

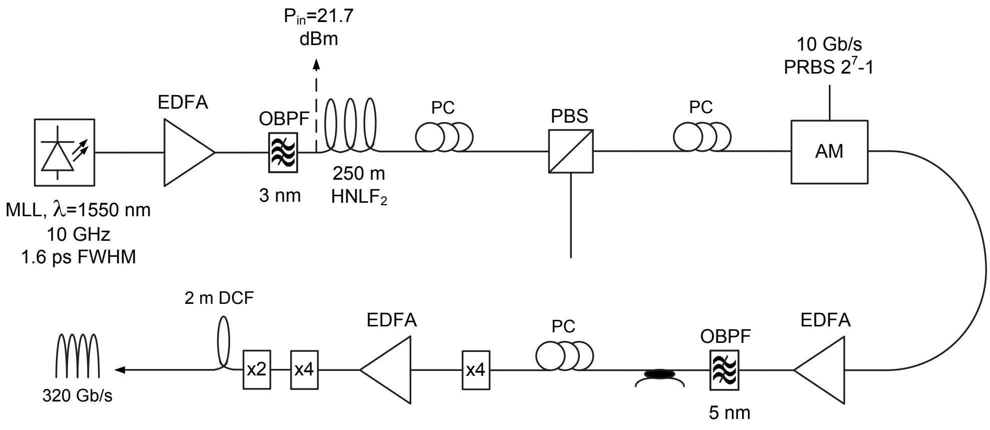

Figure B.7: Experimental setup of the 320 Gb/s transmitter.

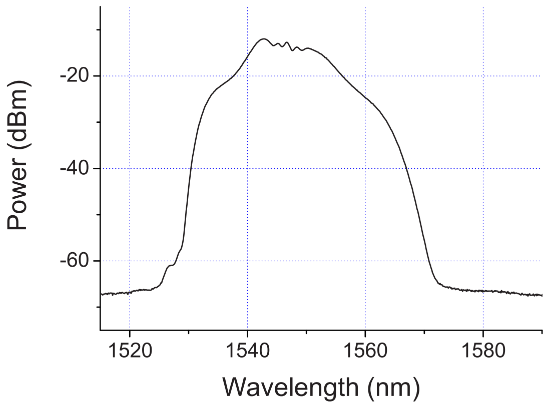

Figure B.8: Spectrum at the output of 250-m $HNLF_2$. The 10-GHz input pulse is at $\lambda = 1550$ nm, 1.6 ps FWHM and 21.7 dBm average power (res. bw.=1 nm).

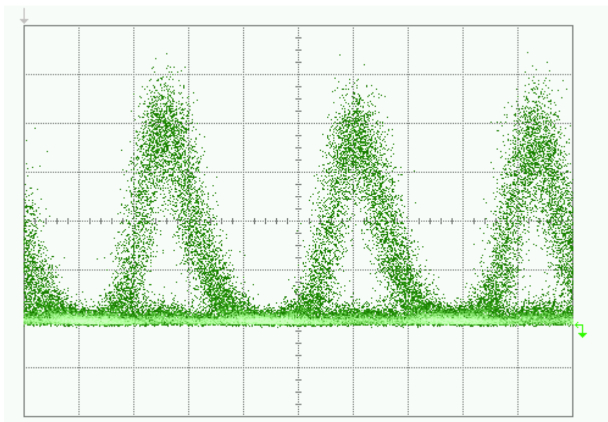

Figure B.9: Eye diagram of the 320 Gb/s OTDM signal. X-scale: 2 ps/div, Y-scale: a.u.

Appendix C

Simulation Parameters Electroabsorption Modulator Model

The parameters and constants used in the simulations with the electroabsorption modulator (EAM) model are given in Table C.1.

Table C.1: Simulation parameters EAM model.

parameter	value	description
N_{tr}	$1 \cdot 10^{24}$	Carrier density at transparency [m^{-3}]
α_{int}	$40 \cdot 10^{2}$	Internal losses [m^{-1}]
Γ	0.285	Confinement factor
c	$3 \cdot 10^{8}$	Speed of light in vacuum [m/s]
n_g	3	Group refractive index
τ_0	$8 \cdot 10^{-12}$	Sweep out time at zero carrier density [s]
τ_{tr}	$25 \cdot 10^{-12}$	Sweep out time at transparency density [s]
h	$6.625 \cdot 10^{-34}$	Planck's constant [J·sec]
A_{eff}	$3.6 \cdot 10^{-13}$	Effective Area of active region [m^2]
k_B	$1.38 \cdot 10^{-23}$	Boltzmann constant [J/K]
ϵ_{sup}	$2 \cdot 10^{-24}$	Absorption suppression [m^{-3}]
α_0	$1.3 \cdot 10^{5}$	Unsaturated absorption [m^{-1}]
τ_{uc}, τ_{uv}	$1 \cdot 10^{-12}$	Carrier energy relaxation time [s]
$T_{c_{eq}}$, $T_{v_{eq}}$	300	Temperature of the carriers at equilibrium [K]
E_{gap}	0.7992	Bandgap energy of InGaAsP-material [eV]
m_e	$9.11 \cdot 10^{-31}$	Electron mass [kg]
m_v	$0.45 \cdot m_e$	Mass of holes in the valence band
m_c	$0.046 \cdot m_e$	Mass of electrons in the conduction band

Appendix D

VPI Modules

The simulations described in Chapter 4, 5 and 6 are performed with the simulation tool VPI: Virtual Photonics Incorporated™. The fiber model and the bit error rate (BER) model are explained in this appendix very briefly. For more detailed information we would like to refer to the manual of VPI TransmissionMaker 7.0.

D.1 Fiber Model

The fiber model in VPI uses the nonlinear Schrödinger equation (NLSE) describing the propagation of linearly-polarized optical waves using the split-step Fourier method. The model takes into account stimulated Raman scattering (SRS), four-wave mixing (FWM), self-phase modulation (SPM), cross-phase modulation (XPM), first order group-velocity dispersion (GVD), second order GVD and attenuation of the fiber. The NLSE is solved by using the split-step Fourier method. This method is described in more detail in section D.1.1.

D.1.1 Split-Step Fourier Method

To understand the split-step Fourier method it is useful to write the NLSE in the form

$$\frac{\partial E_{SV}(z,t)}{\partial z} = [\hat{D} + \hat{N}] \cdot E_{SV}(z,t) \tag{D.1}$$

where E_{SV} is the slowly varying envelope of the electric field and $\hat{N}$ is the nonlinearity operator and $\hat{D}$ is the dispersion operator accounting for dispersion and absorption. These operators can be written as:

$$\hat{D} = -\frac{i\beta_2}{2}\frac{\partial^2}{\partial T^2} + \frac{\beta_3}{6}\frac{\partial^3}{\partial T^3} - \frac{\alpha}{2} \tag{D.2}$$

and by neglecting the stimulated Raman effect and higher order time derivatives of the nonlinear polarization (P_{NL}) the nonlinear operator can be written as:

$$\hat{N} = i\gamma |E_{SV}(z,t)| \tag{D.3}$$

In general dispersion and nonlinearities act simultaneously in the fiber. In the split-step Fourier method we assume that in a short piece of fiber we can pretend the nonlinear effect and the dispersion to operate independently. The fiber is divided into alternate sections of two types. The first section presents the dispersion in the frequency domain and the second section represents the nonlinearity in the time domain. The choice of step size is now a balance between computation time and accuracy. The mathematical expression of the slowly varying envelope of the electric field at Δz is:

$$E_{SV}(z + \Delta z_0, t) = [\exp(\Delta z \hat{N}) E_{SV}(z_0, t)] \exp(\Delta z \hat{D}) \tag{D.4}$$

Here the exponential operator $\exp(\Delta z \hat{D})$ is evaluated in the Fourier domain, because equation (D.2) with replacing $\partial/\partial T$ by $i\omega$ leads to an expression for $\hat{D}(i\omega)$. By the use of the FFT algorithm the numerical evaluation is relatively fast. The slowly varying envelop is now calculated by:

$$E_{SV}(z + \Delta z_0, t) = F_T^{-1} \exp(\Delta z \hat{D}(i\omega)) F_T[\exp(\Delta z \hat{N}) E_{SV}(z_0, t)] \tag{D.5}$$

where F_T denotes the Fourier-transform and F_T^{-1} denotes the inverse Fourier-transform.

D.2 BER Analysis

A deterministic approach is used to calculate the BER. The deterministic approach implies that all fluctuations of the signal shape are imposed by crosstalk, intersymbol interference, fiber dispersion, and nonlinearities. This makes the variations in the received signal not statistical and can therefore not be added to the total noise variance. The error probability of a bit is calculated by combining the distorted waveform analysis with the noise power calculated from separate optical noise bins, and the expected electrical noise contributions.

The variance of each bit is determined from the statistical distribution of the noise accumulated along the optical path, together with the photodiode noise, and can for an arbitrary bit be written as

$$\sigma^2 = \sigma^2_{ASE,signal} + \sigma^2_{ASE,ASE} + \sigma^2_{th} + \sigma^2_{sh} \tag{D.6}$$

where the noise contributions from left to right are the signal-ASE beat noise, the ASE-ASE beat noise, the thermal noise and the shot noise. More information on the BER calculation can be found in the manual of VPI.

References

[1] A.M.J. Koonen, “Fiber to the home/fiber to the premises: What, where, and when?” *Proceedings of the IEEE*, vol. 94, no. 5, pp. 911–934, May 2006.

[2] S. Bigo, Y. Frignac, G. Charlet, W. Idler, S. Borne, H. Gross, R. Dischler, W. Poehlmann, P. Tran, C. Simonneau, D. Bayart, G. Veith, A. Jourdan, and J.-P. Hamaide, “10.2Tbit/s (256x42.7Gbit/s PDM/WDM) transmission over 100km teralight fiber with 1.28bit/s/Hz spectral efficiency,” in *OFC 2001 Proceedings*, vol. 4, 2001, paper PD25-1 - PD25-3.

[3] S. Kawanishi, H. Takara, K. Uchiyama, I. Shake, and K. Mori, “3 Tbit/s (160 Gbit/s $\times$ 19 channel) optical TDM and WDM transmission experiment,” *Electronics Letters*, vol. 35, no. 10, pp. 826–827, 1999.

[4] M.J. O’Mahony, “Optical multiplexing in fiber networks: progress in WDM and OTDM,” *IEEE Communications Magazine*, vol. 33, no. 12, pp. 82–88, December 1995.

[5] B. Mikkelsen, G. Raybon, and R.-J. Essiambre, “160 Gb/s TDM transmission systems,” in *ECOC 2000 Proceedings*, vol. 2, Munich, Germany, September 2000, pp. 125–128.

[6] K. Murata, K. Sano, H. Kitabayashi, S. Sugitani, H. Sugahara, and T. Enoki, “100-Gb/s multiplexing and demultiplexing IC operations in InP HEMT technology,” *IEEE Journal of Solid-State Circuits*, vol. 39, no. 1, pp. 207–213, January 2004.

[7] H. Toyoda, S. Nishimura, M. Okuno, R. Yamaoka, and H. Nishi, “A 100-Gb-Ehternet subsystem for next-generation metro-area network,” in *ICC 2005 Proceedings*, vol. 2, Seoul Korea, May 2005, pp. 1036–1042.

[8] A.A.M. Saleh and J.M. Simmons, “Evolution toward the next-generation core optical network,” *Journal of Lightwave Technology*, vol. 24, no. 9, pp. 3303–3321, September 2006.

[9] M. Eiselt, W. Pieper, and H.G. Weber, “All-optical high speed demultiplexing with a semiconductor laser amplifier in a loop mirror configuration,” *Electronics Letters*, vol. 29, no. 13, pp. 1167–1168, June 1993.

[10] S. Diez, R. Ludwig, and H.G. Weber, “All-optical switch for TDM and WDM/TDM systems demonstrated in a 640 Gbit/s demultiplexing experiment,” *Electronics Letters*, vol. 34, no. 8, pp. 803–805, April 1998.

[11] G. Toptchiyski, S. Randel, K. Petermann, S. Diez, C. Schmidt, C. Schubert, R. Ludwig, and H.G. Weber, “Analysis of switching windows in a gain-transparent-SLALOM configuration,” *Journal of Lightwave Technology*, vol. 18, no. 12, pp. 2188–2195, December 2000.

[12] C. Schubert, J. Berger, S. Diez, H.J. Ehrke, R. Ludwig, U. Feiste, C. Schmidt, H.G. Weber, G. Toptchiyski, S. Randel, and K. Petermann, “Comparison of interferometric all-optical switches for demultiplexing applications in high-speed OTDM systems,” *Journal of Lightwave Technology*, vol. 20, no. 4, pp. 618–624, April 2002.

[13] J.P. Sokoloff, P.R. Pruncnal, I. Glesk, and M. Kane, “A terahertz optical asymmetric demultiplexer (TOAD),” *IEEE Photonics Technology Letters*, vol. 5, no. 7, pp. 787–790, July 1993.

[14] N.J. Doran and D. Wood, “Nonlinear-optical loop mirror,” *Optics Letters*, vol. 13, no. 1, pp. 56–58, January 1988.

[15] M. Nakazawa, E. Yoshida, T. Yamamoto, E. Yamada, and A. Sahara, “TDM single channel 640 Gbit/s transmission experiment over 60 km using 400 fs pulse train and walk-off free, dispersion flattened nonlinear optical loop mirror,” *Electronics Letters*, vol. 34, no. 9, pp. 907–908, April 1998.

[16] H. Sotobayashi and W. Chujo, “Inter-wavelength-band conversions and demultiplexings of 640 Gbit/s OTDM signals,” in *OFC 2002 Proceedings*, Anaheim, CA, USA, March 2002, pp. 261–262, paper WM2.

[17] S. Nakamura, Y. Ueno, and K. Tajima, “Error-free all-optical demultiplexing at 336 Gb/s with a hybrid-integrated symmetric-Mach-Zehnder switch,” in *OFC 2002 Proceedings*, Anaheim, CA, USA, March 2002, pp. FD3–1–FD3–3.

[18] C. Schubert, S. Diez, J. Berger, R. Ludwig, U. Feiste, H. G. Weber, G. Toptchiyski, K. Petermann, and V. Krajinovic, “160-Gb/s all-optical demultiplexing using a gain-transparent ultrafast-nonlinear interferometer (GT-UNI),” *IEEE Photonics Technology Letters*, vol. 13, no. 5, pp. 475–477, May 2001.

[19] I.D. Philips, A. Gloag, D.G. Moodie, N.J. Doran, I. Bennion, and A.D. Ellis, “Drop and insert multiplexing with simultaneous clock reecovery using an electroabsorption modulator,” *IEEE Photonics Technology Letters*, vol. 10, no. 2, pp. 291–293, February 1998.

[20] E.S. Awad, P.S. Cho, N. Mouton, and J. Goldhar, “All-optical timing extraction with simultaneous optical demultiplexing from 40 Gb/s using a single electroabsorption modulator,” *IEEE Photonics Technology Letters*, vol. 15, no. 1, pp. 126–128, January 2003.

[21] S. Kodama, T. Yoshimatsu, and H. Ito, "500-Gbit/s demultiplexing operation of monolithic PD-EAM optical gate," in *ECOC 2003 Proceedings*, vol. 6, Rimini, Italy, September 2003, pp. 58–59, paper Th 4.2.8.

[22] M.F.C. Stephens, A.E. Kelly, D. Nesset, A. Wonfor, and R.V. Penty, "Demonstration of time division demultiplexing from 40 Gb/s to 10 Gb/s via polarisation switching in a semiconductor optical amplifier," in *CLEO/Europe '98 Proceedings*, Glasgow, UK, September 1998, pp. 383–383, paper CFG8.

[23] S.L. Jansen, M. Heid, S. Spälter, E. Meissner, C.-J. Weiske, A. Schopflin, G.D. Khoe, and H. de Waardt, "Demultiplexing 160 Gbit/s OTDM signal to 40 Gbit/s by FWM in SOA," *Electronics Letters*, vol. 38, no. 17, pp. 978–980, August 2002.

[24] T. Morioka, H. Takara, S. Kawanishi, T. Kitoh, and M. Saruwatari, "Error-free 500Gbit/s all-optical demultiplexing using low-noise, low-jitter supercontinuum short pulses," *Electronics Letters*, vol. 32, no. 9, pp. 833–834, April 1996.

[25] Y. Fuckuchi, T. Sakamoto, K. Taira, and K. Kikuchi, "Cascaded second-order nonlinear effect in quasi-phase matched $LiNbO_3$ waveguide device," *Electronics Letters*, vol. 39, no. 10, pp. 789–790, May 2003.

[26] B.-E. Olsson and D.J. Blumenthal, "All-optical demultiplexing using fiber cross-phase modulation (XPM) and optical filtering," *IEEE Photonics Technology Letters*, vol. 13, no. 8, pp. 875–877, August 2001.

[27] J. Li, B.-E. Olsson, M. Karlsson, and P.A. Andrekson, "OTDM demultiplexer based on XPM-induced wavelength shifting in highly nonlinear fiber," *IEEE Photonics Technology Letters*, vol. 15, no. 12, pp. 1770–1772, December 2003.

[28] E. Tangdiongga, Y. Liu, H. de Waardt, G.D. Khoe, and H.J.S. Dorren, "320-to-40-Gb/s demultiplexing using a single SOA assisted by an optical filter," *Photonics Technology Letters*, vol. 18, no. 8, pp. 908–910, April 2006.

[29] A. Buxens, H.N. Poulsen, A.T. Clausen, and P. Jeppesen, "All-optical OTDM-to-WDM signal-format translation and OTDM add-drop functionality using bidirectional four wave mixing in semiconductor optical amplifier," *Electronics Letters*, vol. 36, no. 2, pp. 156–158, January 2000.

[30] L. Rau, S. Rangarajan, W. Wei, and D.J. Blumenthal, "All-optical add-drop of an OTDM channel using an ultra-fast fiber based wavelength converter," in *OFC 2002 Proceedings*, vol. 1, Anaheim, CA, USA, March 2002, pp. 259–261, paper WM1.

[31] J.P. Turkiewicz, E. Tangdiongga, H. Rohde, W. Schairer, G. Lehmann, G.D. Khoe, and H. de Waardt, "Simultaneous high speed OTDM add-drop multiplexing using GT-UNI switch," *Electronics Letters*, vol. 39, no. 10, pp. 795–796, May 2003.

[32] C. Schubert, C. Schmidt, S. Ferber, R. Ludwig, and H.G. Weber, "Error-free all-optical add-drop multiplexing at 160 Gbit/s," *Electronics Letters*, vol. 39, no. 14, pp. 1074–1076, July 2003.

[33] J.P. Turkiewicz, E. Tangdiongga, H. Rohde, W. Schairer, G. Lehmann, G.D. Khoe, and H. de Waardt, "All optical add-drop node at 16 x 10 Gb/s in between two fibre links of 150 km," in *ECOC 2003 Proceedings*, Rimini, Italy, 2003, paper Th 4.4.5.

[34] S. Diez, R. Ludwig, and H.G. Weber, "Gain-transparent SOA-switch for high-bitrate OTDM add/drop multiplexing," *IEEE Photonics Technology Letters*, vol. 11, no. 1, pp. 60–62, January 1999.

[35] H.-F. Chou, J.E. Bowers, and D.J. Blumenthal, "Compact 160-Gb/s add-drop multiplexer with a 40 Gb/s base rate using electroabsorption modulators," *IEEE Photonics Technology Letters*, vol. 16, no. 6, pp. 1564–1566, June 2004.

[36] R. Hess, M. Duelk, W. Vogt, E. Gamper, E. Gini, P.A. Besse, H. Melchior, K. S. Jepsen, B. Mikkelsen, M. Vaa, H.N. Poulsen, A.T. Clausen, K.E. Stubkjaer, S. Bouchoule, and F. Devaux, "Simultaneous all-optical add and drop multiplexing of 40 Gbit/s OTDM signals using monolithically integrated Mach-Zehnder interferometer," *Electronics Letters*, vol. 34, no. 6, pp. 579–580, October 1998.

[37] S. Fischer, M. Dulk, E. Gamper, W. Vogt, W. Hunziker, E. Gini, H. Melchior, A. Buxens, H.N. Poulsen, and A.T. Clausen, "All-optical regenerative OTDM add-drop multiplexing at 40 Gb/s using monolithic InP Mach-Zehnder interferometer," *Photonics Technology Letters, IEEE*, vol. 12, no. 3, pp. 335–337, March 2000.

[38] E.J.M. Verdurmen, Y. Zhao, E. Tangdiongga, J.P. Turkiewicz, G.D. Khoe, and H. de Waardt, "Error-free all-optical add-drop multiplexing using HNLF in a NOLM at 160 Gbit/s," *Electronics Letters*, vol. 41, no. 6, pp. 349–350, March 2005.

[39] E.J.M. Verdurmen, J.P. Turkiewicz, E. Tangdiongga, G.D. Khoe, and H. de Waardt, "Towards all-optical 320 Gb/s add-drop multiplexing using a nonlinear optical loop mirror," in *ECOC 2005 Proceedings*, Glasgow, UK, September 2005, paper Th 3.1.7.

[40] P.J. Almeida, P. Petropoulos, M. Ibsen, M.R. Mokhtar, B.C. Thomsen, and D.J. Richardson, "All-optical TDM add-drop multiplexer based on time to wavelength conversion," in *ECOC 2004 Proceedings*, Stockholm, Sweden, September 2004, pp. 438–439, paper We 3.5.5.

[41] P.J. Almeida, P. Petropoulos, F. Parigiani, M. Ibsen, and D.J. Richardson, "OTDM add-drop multiplexer based on time-frequency signal processing," *Journal of Lightwave Technology*, vol. 24, no. 7, pp. 2720–2732, July 2006.

[42] J. Li, B.E. Olsson, M. Karlsson, and P.A. Andrekson, “OTDM add-drop multiplexer based on XPM-induced wavelength shifting in highly nonlinear fiber,” in *OFC 2004 Proceedings*, vol. 2, February 2004, paper ThN4.

[43] J. Li, B.-E. Olsson, M. Karlsson, and P.A. Andrekson, “OTDM add-drop multiplexer based XPM-induced wavelength shifting in highly nonlinear fiber,” *Journal of Lightwave Technology*, vol. 23, no. 9, pp. 2654–2661, September 2005.

[44] J.H. Lee, K. Kikuchi, T. Nagashima, T. Hasegawa, S. Ohara, and N. Sugimoto, “All fiber-based 160-Gbit/s add/drop multiplexer incorporating a 1-m-long Bismuth Oxide-based ultra-high nonlinearity fiber,” *Optics Express*, vol. 13, no. 18, pp. 6864–6869, August 2005.

[45] J. Suzuki, K. Taira, Y. Fukuchi, Y. Ozeki, T. Tanemura, and K. Kikuchi, “All-optical time-division add-drop multiplexer using optical fibre kerr shutter,” *Electronics Letters*, vol. 40, no. 7, pp. 445–446, April 2004.

[46] C. Schubert, C. Schmidt-Langhorst, K. Schulze, V. Marembert, and H.G. Weber, “Time division add-drop multiplexing up to 320 Gbit/s,” in *OFC 2005 Proceedings*, vol. 4, Anaheim, CA, USA, 2005, paper OThN2.

[47] E.J.M. Verdurmen, A.M.J. Koonen, and H. de Waardt, “Time domain add-drop multiplexing for RZ-DPSK OTDM signals,” *Optics Express*, vol. 14, no. 12, pp. 5514–5120, June 2006.

[48] M. Takahashi, Y. Mimura, J. Hiroishi, R. Sugizaki, M. Sakano, and T. Yagi, “Study of down-sized silica highly non-linear fiber,” in *ECOC 2005 Proceedings*, Glasgow, UK, September 2005, paper We 3.4.2.

[49] Y. Barbarin, E.A.J.M. Bente, M.J.R. Heck, Y.S. Oei, R. Notzel, and M.K. Smit, “Passively modelocked 20 and 40 GHz bulk InGaAsP lasers,” in *ECOC 2005 Proceedings*, vol. 3, Glasgow, UK, September 2005, pp. 673–674, paper We 4.P.086.

[50] Y. Barbarin, E.A.J.M. Bente, M.J.R. Heck, J.H. den Besten, G. Guidi, Y.S. Oei, J.J.M. Binsma, and M.K. Smit, “Realization and modeling of a 27-GHz integrated passively mode-locked ring laser,” *Photonics Technology Letters*, vol. 17, no. 11, pp. 2277–2279, November 2005.

[51] V. Kaman and J.E. Bowers, “120 Gbit/s OTDM system using electroabsoprion transmitter and demultiplexer operating at 30 GHz,” *Electronics Letters*, vol. 36, pp. 1477–1479, August 2000.

[52] H.-F. Chou, Y.-J. Chiu, and J.E. Bowers, “Standing-wave enhanced electroabsoption modulator for 40-GHz optical pulse generation,” *IEEE Photonics Technology Letters*, vol. 15, pp. 215–217, February 2003.

[53] H. Kawanishi, Y. Yamauchi, N. Mineo, Y. Shibuya, H. Murai, K. Yamada, and H. Wada, “EAM-integrated DFB laser modules with more than 40-GHz bandwidth,” *IEEE Photonics Technology Letters*, vol. 13, no. 9, pp. 954–956, September 2001.

[54] K. Nishimura, R. Inohara, M. Tsurusawa, and M. Usami, “80 Gbit/s wavelength conversion using MQW electroabsorption modulator in delayed-interferometric configuration,” *Electronics Letters*, vol. 39, no. 10, pp. 792–794, May 2003.

[55] K. Nishimura, R. Inohara, M. Tsurusawa, and M. Usami, “Patterning effect at 40 Gbit/s of wavelength converter utilizing cross-phase modulation in InGaAsP/InP electroabsorption modulator,” in *Indium Phoshpide and related materials*, May 2003, pp. 198–201, paper TuP27.

[56] K. Nishimura, R. Inohara, M. Usami, and S. Akiba, “All-optical wavelength conversion by electroabsorption modulator,” *IEEE Journal of Selected Topics in Quantum Electronics*, vol. 11, no. 1, pp. 278–280, January/February 2005.

[57] N. El Dahdah, J. Decobert, A. Shen, S. Bouchoule, C. Kazmierski, G. Aubin, B.-E. Benkelfat, and A. Ramdane, “New design of InGaAs-InGaAlAs MQW electroabsorption modulator for high-speed all-optical wavelength conversion,” *IEEE Photonics Technology Letters*, vol. 16, no. 10, pp. 2302–2304, October 2004.

[58] N. El Dahdah, R. Coquillé, B. Charbonnier, E. Pincemin, C. Kazmierski, J. Decobert, A. Vedadi, G. Aubin, and A. Ramdane, “All-optical wavelength conversion by EAM with shifted bandpass filter for high bit-rate networks,” *IEEE Photonics Technology Letters*, vol. 18, no. 1, pp. 61–63, January 2006.

[59] E.S. Awad, P.S. Cho, and J. Goldhar, “Simultaneous four-wave mixing and cross-absorption modulation inside a single EAM for high-speed optical demultiplexing and clock recovery,” *IEEE Photonics Technology Letters*, vol. 17, no. 7, pp. 1534–1536, July 2005.

[60] C. Boerner, C. Schubert, C. Schmidt, E. Hilliger, V. Marembert, J. Berger, S. Ferber, E. Dietrich, R. Ludwig, B. Schmauss, and H. G. Weber, “160 Gbit/s clock recovery with electro-optical PLL using bidirectionally operated electroabsorption modulator as phase comparator,” *Electronics Letters*, vol. 39, no. 14, pp. 1071—1073, July 2003.

[61] E.S. Awad, P.S. Cho, N. Mouton, and J. Goldhar, “Subharmonic optical clock recovery from 160 Gb/s using time-dependent loss saturation inside a single electroabsorption modulator,” *IEEE Photonics Technology Letters*, vol. 15, no. 12, pp. 1764–1766, December 2003.

[62] J.P. Turkiewicz, E. Tangdiongga, G.D. Khoe, and H. de Waardt, “Clock recovery and demultiplexing performance of 160-Gb/s OTDM field experiments,” *Photonics Technology Letters*, vol. 16, no. 6, pp. 1555–1557, June 2004.

[63] E.S. Awad, P.S. Cho, C. Richardson, N. Moulton, and J. Goldhar, “Optical 3R regeneration using a single EAM for all-optical timing extraction with simultaneous reshaping and wavelength conversion,” *Photonics Technology Letters, IEEE*, vol. 14, no. 9, pp. 1378–1380, 2002.

[64] E.S. Awad, P.S. Cho, N. Moulton, and J. Goldhar, “3R optical regeneration with simultaneous optical clock recovery and all-optical wavelength conversion using a single electro-absorption modulator,” in *CLEO 2002 Proceedings*, vol. 1, May 2002, pp. 611–612, paper CThAA4.

[65] K. Nishimura, M. Tsurusawa, and M. Usami, “Optical 3R regeneration with single InGaAsP/InP electroabsorption modulator,” in *IPRM 2002 Proceedings*, Stockholm, Sweden, May 2002, pp. 677–680.

[66] S. Kodama, T. Yoshimatsu, and H. Ito, “320 Gbit/s optical gate monolithically integrating photodiode and electroabsorption modulator,” *Electronics Letters*, vol. 39, no. 4, pp. 383–385, February 2003.

[67] S. Kodama, T. Ito, N. Watanabe, S. Kondo, H. Takeuchi, H. Ito, and T. Ishibashi, “2.3 picoseconds optical gate monolithically integrating photodiode and electroabsorption modulator,” *Electronics Letters*, vol. 37, no. 19, pp. 1185–1186, September 2001.

[68] L. Xu, N. Chi, L.J. Christiansen, K. Yvind, L.K. Oxenløwe, J. Mørk, and P. Jeppesen, “160 to 10 Gb/s all-optical demultiplexing using a single electroabsorption modulator,” in *ECOC 2004 Proceedings*, Stockholm, Sweden, September 2004, paper We 1.5.3.

[69] K. Schuh, M. Schmidt, E. Lach, B. Junginger, A. Klekamp, G. Veith, and P. Sillard, “4 x 160 Gbit/s DWMD/OTDM transmission over 3 x 80km teralight^{TM}-reverse teralight^{TM} fibre,” in *ECOC 2002 Proceedings*, Copenhagen, Denmark, 2002, paper 2.1.2.

[70] T. Ohno, R. Iga, Y. Kondo, T. Ito, T. Furuta, K. Yoshino, H. Ito, and K. Sato, “Wide-locking-range 160 GHz optical clock recovery from 160-Gbit/s signal using a mode-locked laser diode,” in *OFC 2004 Proceedings*, Los Angeles, CA, USA, February 2004, paper WD-5.

[71] E.J.M. Verdurmen, M. Heck, G.D. Khoe, and H. de Waardt, “Modelling and study of all-optical demultiplexing of a 160 Gb/s OTDM signal using QW-EAM,” in *Proceedings IEEE/LEOS Benelux Chapter 2003*, Enschede, The Netherlands, November 2003, pp. 161–164.

[72] E.J.M. Verdurmen, Y. Liu, G.D. Khoe, and H. de Waardt, “Study on the limits of all-optical time-domain demultiplexing using cross-absorption modulation in an electroabsorption modulator,” *IEE Proceedings-Optoelectronics*, vol. 153, no. 2, pp. 75–83, April 2006.

[73] D.A.B. Miller, D.S. Chemla, T.C. Damen, A. Gossard, W. Wiegmann, and T. Wood, “Electric field dependence of optical aborption near the bandgap of quantum-well structures,” *Phys. Rev. B*, vol. 32, no. 2, pp. 1043–1060, 1985.

[74] L. Xu, L.K. Oxenløwe, N. Chi, J. Mørk, P. Jeppesen, K. Hoppe, and J. Hanberg, “Experimental characterisation of wavelength conversion at 40 Gb/s based on

electroabsorption modulators," in *LEOS 2002 Proceedings*, vol. 1, November 2002, pp. 111–112.

[75] Y. Liu, J.P. Turkiewicz, E.J.M. Verdurmen, H. de Waardt, G.D. Khoe, and H.J.S. Dorren, "All-optical wavelength conversion by utilizing cross-polarization modulation in an electro-absorption modulator," in *ECOC 2003 Proceedings*, Rimini, Italy, September 2003, paper We 4.P78.

[76] A.V. Uskov, J.R. Karin, J.E. Bowers, J.G. McInerney, and J.L. Bihan, "Effects of carrier cooling and carrier heating in saturation dynamics and pulse propagation through bulk semiconductor absorbers," *IEEE Journal of Quantum Electronics*, vol. 34, no. 11, pp. 2162–2171, November 1998.

[77] S. Højfeldt, "Modeling of carrier dynamics in electroabsorption modulators," Ph.D. dissertation, COM Technical University of Denmark, May 2002.

[78] F. Koyama, K.-Y. Liou, A.G. Dentai, G. Raybon, and C.A. Burrus, "Measurment of chirp parameter in GaInAs/GaInAsP quantum well electroabsorption modulators by using intracavity modulation," *IEEE Photonics Technology Letters*, vol. 5, no. 12, pp. 1389–1391, December 1993.

[79] J. Piprek, Y.-J. Chiu, and J.E. Bowers, "Analysis of multi-quantum well electroabsorption modulators," in *Proceedings of SPIE*, vol. 4646 - Physics and simulation of optoelectronic devices X, San Jose, CA, USA, January 2002, pp. 609–617.

[80] P.I. Kuindersma, M.W. Snikkers, G.P.J.M. Cuypers, J.J.M. Binsma, E. Jansen, A. van Geelen, and T. van Dongen, "Universality of the chirp-parameter of bulk active electro absorption modulators," in *ECOC 1998 Proceedings*, vol. 1, Madrid, Spain, September 1998, pp. 473–474.

[81] Y. Du, T. Tekin, R.G. Broeke, N. Chubun, C. Ji, J. Cao, S.J.B. Yoo, K.Y. Liou, J.R. Lothian, S. Vatanapradit, S.N.G. Chu, B. Patel, W.S. Hobson, D.V. Tishinin, and W.T. Tsang, "A novel monolithically integrated Mach-Zehnder wavelength converter using cross modulation in electro-absorber," in *ECOC 2005 Proceedings*, Glasgow, Scotland, September 2005, paper We 1.5.1.

[82] G. Meloni, M. Scaffardi, P. Ghelfi, A. Bogoni, L. Poti, and N. Calabretta, "Ultrafast all-optical add-drop multiplexer based on 1-m-long Bismuth Oxide-based highly nonlinear fiber," *Photonics Technology Letters*, vol. 17, no. 12, pp. 2661–2663, December 2005.

[83] G.P. Agrawal, *Nonlinear Fiber Optics*, 3rd ed. Academic Press, 2001.

[84] J.A. Buck, *Fundamentals of Optical Fibers*, 2nd ed., Bahaa E.A. Saleh, Ed. Wiley-Interscience, 2004.

[85] J. Capmany, D. Pastor, S. Sales, and B. Ortega, "Effects of fourth-order dispersion in very high-speed optical time-division multiplexed transmission," *Optics Letters*, vol. 27, no. 11, pp. 960–962, June 2002.

[86] M. Karlsson, P.A. Andrekson, and H. Sunnerud, "High-speed OTDM and impact of PMD," in *Proceedings LEOS 1999*, vol. 1, November 1999, pp. 343–344, paper TuZ2.

[87] F. Curti, B. Daino, G. de Marchis, and F. Matera, "Statistical treatment of the evolution of the principal states of polarization in single-mode fibers," *Journal of Lightwave Technology*, vol. 8, no. 8, pp. 1162–1166, August 1990.

[88] H. Sunnerud, M. Karlsson, and P.A. Andrekson, "A comparison between NRZ and RZ data formats with respect to PMD-induced system degradation," *IEEE Photonics Technology Letters*, vol. 13, no. 5, pp. 448–450, May 2001.

[89] C. Xie, L. Möller, H. Haunstein, and S. Hunsche, "Comparison of system tolerance to polarization-mode dispersion between different modulation formats," *IEEE Photonics Technology Letters*, vol. 15, no. 8, pp. 1168–1170, August 2003.

[90] G. Charlet, P. Tran, H. Mardoyan, M. Lefrançois, T. Fauconnier, F. Jorge, and S. Bigo, "151x43Gb/s transmission over 4,080km based on return-to-zero differential quadrature phase-shift keying," in *ECOC 2005 Proceedings*, vol. 6, Glasgow, UK, September 2005, pp. 5–6, paper Th 4.1.3.

[91] H.G. Weber, S. Ferber, M. Kroh, C. Schmidt-Langhorst, R. Ludwig, V. Marembert, C. Boerner, F. Futami, S. Watanabe, and C. Schubert, "Single channel 1.28 Tbit/s and 2.56 Tbit/s DQPSK transmission," in *ECOC 2005 Proceedings*, vol. 6, Glasgow, UK, September 2005, pp. 3–4, paper Th 4.1.2.

[92] C. Xie, "Polarization mode dispersion and its mitigation techniques in high speed fiber optical communication systems," in *Proceedings WOCC 2005*, April 2005, pp. 34–35.

[93] H. Bulow, F. Buchali, W. Baumert, R. Ballentin, and T. Wehren, "PMD mitigation at 10 Gbit/s using linear and nonlinear integrated electronic equalizer circuits," *Electronics Letters*, vol. 36, no. 2, pp. 163–164, January 2000.

[94] H. Sunnerud, M. Karlsson, C. Xie, and P.A. Andrekson, "Polarization-mode dispersion in high-speed fiber-optic transmission systems," *Journal of Lightwave Technology*, vol. 20, no. 12, pp. 2204–2219, December 2002.

[95] A. Hasegawa and Y. Kodama, *Solitons in Optical Communications*. Oxford University Press, 1995.

[96] W. Wang, H.N. Poulsen, H.-F. Chou, J.E. Bowers, and D.J. Blumenthal, "Raman-enhanced regenerative ultrafast all-optical fiber XPM wavelength converter," *Journal of Lightwave Technology*, vol. 23, no. 3, pp. 1105–1115, March 2005.

[97] P.O. Hedekvist, M. Karlsson, and P.A. Andrekson, "Fiber four-wave mixing demultiplexing with inherent parametric amplification," *Journal of Lightwave Technology*, vol. 15, no. 11, pp. 2051–2058, November 1997.

[98] J. Yu, P. Jeppesen, and S.N. Knudsen, "80 Gbit/s pulsewidth-maintained wavelength conversion based on HNL DSF-NOLM including transmission over 80 km of conventional SMF," *Electronics Letters*, vol. 37, no. 9, pp. 577–579, April 2001.

[99] T. Sakamoto, H.C. Lim, and K. Kikuchi, "All-optical polarization-insensitive time-division demultiplexer using a nonlinear optical loop mirror with a pair of short polarization-maintaining fibers," *IEEE Photonics Technology Letters*, vol. 14, no. 12, pp. 1737–1739, December 2002.

[100] A. Bogoni, P. Ghelfi, M. Scaffardi, and L. Poti, "All-optical regeneration and demultiplexing for 160 Gb/s transmission systems using a NOLM-based three-stage scheme," *IEEE Journal of Selected Topics in Quantum Electronics*, vol. 10, no. 1, pp. 192–196, Jan-Feb 2004.

[101] H. Sotobayashi, C. Sawaguchi, Y. Koyamada, and W. Chujo, "Ultrafast walk-off-free nonlinear optical loop mirror by a simplified configuration for 320-Gbit/s timedivision multiplexing signal demultiplexing," *Optics Letters*, vol. 27, no. 17, pp. 1555–1557, September 2002.

[102] T. Yamamoto, E. Yoshida, and M. Nakazawa, "Ultrafast nonlinear optical loop mirror for demultiplexing 640 Gbit/s TDM signal," *Electronic Letters*, vol. 34, pp. 1013–1014, 1998.

[103] J. Seoane, A.I. Siahlo, A.T. Clausen, L.K. Oxenløwe, P. Jeppesen, M. Schmidt, M. Schilling, and E. Lach, "Ultra high-speed demultiplexing using a NOLM based on commercially available highly non-linear fibre," in *ECOC 2004 Proceedings*, Stockholm, Sweden, 2004, paper We 1.5.4.

[104] A.T. Clausen, A.I. Siahlo, J. Seoane, L.K. Oxenløwe, and P. Jeppesen, "320 to 10 Gbit/s demultiplexing using a NOLM based on commercially available components," *Electronics Letters*, vol. 41, no. 5, pp. 265–266, March 2005.

[105] A.I. Siahlo, L.K. Oxenløwe, K.S. Berg, A.T. Cluasen, P.A. Andersen, C. Peucheret, A. Tersigni, P. Jeppesen, K.P. Hansen, and J.R. Folkenberg, "A high-speed demultiplexer based on a nonlinear optical loop mirror with a photonic crystal fiber," *IEEE Photonics Technology Letters*, vol. 15, no. 8, pp. 1147–1149, August 2003.

[106] S. Arahira and Y. Ogawa, "160-Gb/s OTDM signal source with 3R function utilizing ultrafast mode-locked laser diodes and modified NOLM," *IEEE Photonics Technology Letters*, vol. 17, no. 5, pp. 992–994, May 2005.

[107] M. Meissner, K. Sponsel, K. Cvecek, A. Benz, S. Weisser, B. Schmauss, and G. Leuchs, "3.9-dB OSNR gain by an NOLM-based 2-R regenerator," *IEEE Photonics Technology Letters*, vol. 16, no. 9, pp. 2105–2107, September 2004.

[108] E.J.M. Verdurmen, G.D. Khoe, A.M.J. Koonen, and H. de Waardt, "Comparison of demultiplexing techniques using XPM and FWM in HNLF," in *Proceedings IEEE/LEOS Benelux Chapter 2005*, Mons, Belgium, December 2005, pp. 185–188.

[109] E.J.M. Verdurmen, Y. Zhao, G.D. Khoe, and H. de Waardt, "OTDM demultiplexing using HNLF in a NOLM at 160 Gb/s," in *Proceedings IEEE/LEOS Benelux Chapter 2004*, Ghent, Belgium, December 2004, pp. 239–242.

[110] D.B. Mortimore, "Fiber loop reflectors," *Journal of Lightwave Technology*, vol. 6, no. 7, pp. 1217–1224, July 1988.

[111] D.L. Butler, P.S. Cho, M.W. Chbat, J. Goldhar, F.-S. Choa, and G.L. Burdge, "Operation of a nonlinear optical loop mirror with orthogonally polarized waves in nonpolarization-preserving, single-mode fiber," *IEEE Photonics Technology Letters*, vol. 8, no. 6, pp. 779–781, June 1996.

[112] D. Wang, E.A. Golovchenko, A.N. Pilipetskii, C.R. Menyuk, and M.F. Arend, "Nonlinear optical loop mirror based on standard communication fiber," *Journal of Lightwave Technology*, vol. 15, no. 4, pp. 642–646, April 1997.

[113] K. Uchiyama, T. Morioka, S. Kawanishi, H. Takara, and M. Saruwatari, "Signal-to-noise ratio analysis of 100Gb/s demultiplexing using nonlinear optical loop mirror," *Journal of Lightwave Technology*, vol. 15, no. 2, pp. 194–201, February 1997.

[114] M. Jinno, "Effects of crosstalk and timing jitter on all-optical time-division demultiplexing using a nonlinear fiber sagnac interferometer switch," *IEEE Journal of Quantum Electronics*, vol. 30, no. 12, pp. 2842–2853, December 1994.

[115] F. Zhang and P. Ye, "Theory and numerical analysis of higher order dispersion effects on ultra-high-speed nonlinear optical loop mirror demultiplexer," *Microwave and Optical Technology Letters*, vol. 30, no. 2, pp. 124–127, July 2001.

[116] T. Sakamoto and K. Kikuchi, "Nonlinear optical loop mirror with an optical bias controller for achieving full-swing operation of gate switching," *IEEE Photonics Technology Letters*, vol. 16, no. 2, pp. 545–547, February 2004.

[117] B. Batagelj, "Conversion efficiency of fiber wavelength converter based on degenerate FWM," in *Transparent Optical Networks, 2000 2nd International Conference on*, 2000, pp. 179–182.

[118] M.D. Reid and D.F. Walls, "Squeezing in nondegenerate four-wave mixing," *Physical Review A*, vol. 33, no. 6, pp. 4465–4468, June 1986.

[119] T.T. Ng, J.L. Blows, J.T. Mok, R.W. McKerracher, and B.J. Eggleton, "Cascaded four-wave mixing in fiber optical parametric amplifiers: Application to residual dispersion monitoring," *Journal of Lightwave Technology*, vol. 23, no. 2, pp. 818–826, February 2005.

[120] E.J.M. Verdurmen, G.D. Khoe, A.M.J. Koonen, and H. de Waardt, "All-optical data format conversion from WDM to OTDM based on FWM," *Microwave and Optical Technology Letters*, vol. 48, no. 5, pp. 992–994, May 2006.

[121] T. Morioka, S. Kawanishi, H. Takara, and M. Saruwatari, "Multiple-output, 100 Gbit/s all-optical demultiplexer based on multichannel four-wave mixing pumped by a linearly-chirped square pulse," *Electronics Letters*, vol. 30, no. 23, pp. 1959–1960, 1994.

[122] D. Norte and A.E. Willner, "All-optical data format conversions and reconversions between the wavelength and time domains for dynamically reconfigurable WDM networks," *Journal of Lightwave Technology*, vol. 14, no. 6, pp. 1170–1182, 1996.

[123] B.E. Olsson and D.J. Blumenthal, "WDM to OTDM multiplexing using an ultrafast all-optical wavelength converter," *Photonics Technology Letters, IEEE*, vol. 13, no. 9, pp. 1005–1007, 2001.

[124] L. Rau, W. Wei, B.E. Olsson, C. Yijen, H.-F. Chou, D.J. Blumenthal, and J.E. Bowers, "Simultaneous all-optical demultiplexing of a 40-Gb/s signal to 4/spl times/10 Gb/s WDM channel's using an ultrafast fiber wavelength converter," *Photonics Technology Letters, IEEE*, vol. 14, no. 12, pp. 1725–1727, 2002.

[125] H. Sotobayashi, W. Chujo, and T. Ozeki, "80 Gbit/s simultaneous photonic demultiplexing based on OTDM-to-WDM conversion by four-wave mixing with supercontinuum light source," *Electronics Letters*, vol. 37, no. 10, pp. 640–642, May 2001.

[126] K. Uchiyama, S. Kawanishi, and M. Saruwatari, "100-Gb/s multiple-channel output all-optical OTDM demultiplexing using multichannel four-wave mixing in a semiconductor optical amplifier," *Photonics Technology Letters, IEEE*, vol. 10, no. 6, pp. 890–892, June 1998.

[127] M.R.H. Daza, H.F. Liu, M. Tsuchiya, Y. Ogawa, and T. Kamiya, "All-optical WDM-to-TDM conversion with total capacity of 33 Gb/s for WDM network links," *IEEE Journal of Selected Topics in Quantum Electronics*, vol. 3, no. 5, pp. 1287–1294, 1997.

[128] M. Hayashi, H. Tanaka, K. Ohara, T. Otani, and M. Suzuki, "OTDM transmitter using WDM-TDM conversion with an electroabsorption wavelength converter," *Journal of Lightwave Technology*, vol. 20, no. 2, pp. 236–242, 2002.

[129] J. Yu, K. Keisuke, and N. Chand, "WDM-OTDM transmultiplexing using a nonlinear optical loop mirror," in *OFC 2002 Proceedings*, March 2002, pp. 756–757.

[130] J.P.R. Lacey, M.V. Chan, R.S. Tucker, A.J. Lowery, and M.A. Summerfield, "All-optical WDM to TDM transmultiplexer," *Electronics Letters*, vol. 30, no. 19, pp. 1612–1613, 1994.

[131] Y. Awaji, T. Miyazaki, and F. Kubota, "160/4x40Gb/s OTDM/WDM conversion using FWM fibre," in *ECOC 2004 Proceedings*, vol. 3, Stockholm, Sweden, September 2004, paper We 1.5.6.

[132] Y. Zhao, E.J.M. Verdurmen, G.D. Khoe, and H. de Waardt, "Multiple-wavelength signal generation at 160 Gbit/s using high nonlinear fiber," in *Proceedings IEEE/LEOS Benelux Chapter 2004*, Ghent, Belgium, December 2004, pp. 243–246.

[133] A.H. Gnauck, X. Liu, X. Wei, C.M. Gill, and E.C. Burrows, "Comparison of modulation formats for 42.7 Gb/s single-channel transmission through 1980 km of SSMF," *Photonics Technology Letters*, vol. 16, no. 3, pp. 909–911, March 2004.

[134] T. Morioka, S. Kawanishi, K. Uchiyama, H. Takara, and M. Saruwatari, "Polarisation-independent 100 Gbit/s all-optical demultiplexer using four-wave mixing in a polarisation-maintaining fibre loop," *Electronics Letters*, vol. 30, no. 7, pp. 591–592, 1994.

[135] Y. Liu, E. Tangdiongga, Z. Li, S. Zhang, H. de Waardt, G.D. Khoe, and H.J.S. Dorren, "160 Gb/s SOA-based wavelength converter assisted by an optical bandpass filter," in *OFC 2005 Proceedings*, Anaheim, CA, USA, 2005, paper PDP17.

[136] G. Keiser, *Optical Fiber Communications*, 3rd ed. McGraw-Hill Higher Education, 2000.

[137] W. Wang, L. Rau, H.N. Poulsena, and D.J. Blumenthal, "Raman gain enhanced fwm 160 Gb/s OTDM demultiplexer with highly-nonlinear-fiber," in *OFC 2004 Proceedings*, vol. 2, Los Angeles, CA, USA, February 2004, paper ThN3.

[138] W. Wang, H.N. Poulsen, L. Rau, H.-F. Chou, J.E. Bowers, and D.J. Blumenthal, "Regenerative 80-Gb/s fiber XPM wavelength converter using a hybrid Raman/EDFA gain-enhanced configuration," *IEEE Photonics Technology Letters*, vol. 15, no. 10, pp. 1416–1418, October 2003.

[139] C. Schubert, R. Ludwig, S. Watanabe, F. Futami, C. Schmidt, J. Berger, C. Boerner, S. Ferber, and H.G. Weber, "160 Gbit/s wavelength converter with 3R-regenerating capability," *Electronics Letters*, vol. 38, no. 16, pp. 903–904, August 2002.

[140] S. Watanabe, F. Futami, R. Okabe, Y. Takita, S. Ferber, R. Ludwig, C. Schubert, C. Schmidt, and H.G. Weber, "160 Gbit/s optical 3R-regenerator in a fiber transmission experiment," in *OFC 2003 Proceedings*, paper PD16-1.

[141] C. Schubert, R. Ludwig, S. Watanabe, F. Futami, S. Ferber, J. Berger, C. Schmidt, and H.G. Weber, "Improved performance of a 160 Gb/s fibre based all-optical switch using rectangular gating pulses," in *ECOC 2002 Proceedings*, Copenhagen, Denmark, September 2002, paper 8.3.7.

[142] J. Yu and P. Jeppesen, "Simultaneous all-optical demultiplexing and regeneration of channel from 40 Gbit/s OTDM signals based on SPM and XPM in dispersion-shifted fibre," *Electronics Letters*, vol. 36, no. 21, pp. 1798–1800, October 2000.

[143] A.H. Gnauck and P.J. Winzer, "Optical phase-shift-keyed transmission," *Journal of Lightwave Technology*, vol. 23, no. 1, pp. 115–130, January 2005.

[144] K. Croussore, I. Kim, Y. Han, C. Kim, and G. Li, "Demonstration of phase-regeneration of DPSK signals based on phase-sensitive amplification," *Optics Express*, vol. 13, no. 11, pp. 3945–3950, March 2005.

[145] T. Yamamoto, E. Yoshida, K.R. Tamura, K. Yonenaga, and M. Nakazawa, "640-Gbit/s optical TDM transmission over 92 km through a dispersion-managed fiber consisting of single-mode fiber and "reverse dispersion fiber"," *IEEE Photonics Technology Letters*, vol. 12, no. 3, pp. 353–355, March 2000.

[146] M. Nakazawa, T. Yamamoto, and K.R. Tamura, "1.28 Tbit/s-70km OTDM transmission using third-and fourth-order simultaneous dispersion compensation with a phase modulator," *Electronics Letters*, vol. 36, no. 24, pp. 2027–2029, November 2000.

[147] M. Amemiya, "Pulse broadening due to higher order dispersion and its transmission limit," *Journal of Lightwave Technology*, vol. 20, no. 4, pp. 591–597, April 2002.

[148] T. Yamamoto and M. Nakazawa, "Third- and fourth-order active dispersion compensation with a phase modulator in a terabit-per-second optical time-division multiplexed transmission," *Optics Letters*, vol. 26, no. 9, pp. 647–649, May 2001.

[149] M. Nakazawa, "Solitons for breaking barriers to terabit/second WDM and OTDM transmission in the next millennium," *IEEE Journal on Selected Topics in Quantum Electronics*, vol. 6, no. 6, pp. 1332–1343, November/December 2000.

[150] I. Shake, H. Takara, K. Mori, S. Kawanishi, and Y. Yamabayashi, "Influence of inter-bit four-wave mixing in optical TDM transmission," *Electronics Letters*, vol. 34, no. 16, pp. 1600–1601, August 1998.

[151] R.-J. Essiambre, B. Mikkelsen, and G. Raybon, "Intra-channel cross phase modulation and four wave mixing in high-speed TDM systems," *Electronics Letters*, vol. 35, no. 18, pp. 1576–1578, September 1999.

[152] F. Futami, K. Taira, K. Kikuchi, and A. Suzuki, "Wideband fibre dispersion equalisation up to fourth-order for long-distance subpicosecond optical pulse transmission," *Electronics Letters*, vol. 35, no. 25, pp. 2221–2223, December 1999.

[153] M.D. Pelusi, Y. Matsui, and A. Suzuki, "Fourth-order dispersion suppression of ultrashort optical pulses by second-order dispersion and cosine phase modulaiton," *Optics Letters*, vol. 25, no. 5, pp. 296–298, March 2000.

[154] A.M. Melo, V. Marembert, C. Schmidt-Langhorst C. Schubert, and K. Petermann, "Design optimization of ultra-high bit-rate NOLM-based OTDM demultiplexers," in *LEOS 2005 Proceedings*, Sydney, Australia, October 2005, pp. 920–921, paper ThV4.

[155] Y. Miyazaki, T. Yamatoya, K. Matsumoto, K. Kuramoto, K. Shibata, T. Aoyagi, and T. Ishikawa, "High-power ultralow-chirp 10-Gb/s electroabsorption modulator integrated laser with ultrashort photocarrier lifetime," *IEEE Journal of Quantum Electronics*, vol. 42, no. 4, pp. 357–362, April 2006.

[156] R.P. Schreieck, M.H. Kwakernaak, H. Jäckel, and H. Melchior, "All-optical switching at multi-100-gb/s data rates with Mach-Zehnder interferometer switches," *IEEE Journal of Quantum Electronics*, vol. 38, no. 8, pp. 1053–1061, August 2002.

[157] H.J.S. Dorren, X. Yang, A.K. Mishra, Z. Li, H. Ju, H. de Waardt, G.D. Khoe, T. Simoyama, H. Ishikawa, H. Kawashima, and T. Hasama, "All-optical logic based on ultrafast gain and index dynamics in a semiconductor optical amplifier," *IEEE Journal of Selected Topics in Quantum Electronics*, vol. 10, no. 5, pp. 1079–1092, September-October 2004.

[158] N. Sugimoto, T. Nagashima, T. Hasegawa, S. Ohara, K. Taira, and K. Kikuchi, "Bismuth-based optical fiber with nonlinear coefficient of 1360 $W^{-1}km^{-1}$," in *OFC 2004 Proceedings*, Los Angeles, CA, USA, February 2004, paper PDP26.

[159] S. Watanabe and F. Futami, "All-optical wavelength conversion using ultrafast nonlinearities in optical fibers," *IEICE Transactions on Electronics*, vol. E85-C, no. 4, pp. 889–895, 2002.

[160] L. Boivin, S. Taccheo, C.R. Doerr, P. Schiffer, L.W. Stulz, R. Monnard, and W. Lin, "400 Gbit/s transmission over 544 km from spectrum-sliced supercontinuum source," *Electronics Letters*, vol. 36, no. 4, pp. 335–336, 2000.

[161] B. Mikkelsen, G. Raybon, R.J. Essiambre, J.E. Johnson, K. Dreyer, and L.F. Nelson, "Unrepeatered transmission over 150 km of nonzero-dispersion fibre at 100 Gbit/s with semiconductor based pulse source, demultiplexer and clock recovery," *Electronics Letters*, vol. 35, no. 21, pp. 1866–1868, 1999.

[162] S. Watanabe and F. Futami, "All-optical signal processing using highly-nonlinear optical fibers," *IEICE Transactions on Communications*, vol. E84-B, pp. 1179–1189, 2001.

[163] M. Murata and K. Kitayama, "Ultrafast photonic label switch for asynchronous packets of variable length," in *Proceedings of INFOCOM*, vol. 1, 2002, pp. 371–380.

List of Publications

Journal papers

- E.J.M. Verdurmen, A.M.J. Koonen and H. de Waardt, "Time domain add-drop multiplexing for RZ-DPSK OTDM signals," *Optics Express*, vol. 14, no. 12, pp. 5514–5120, June 2006.

- E.J.M. Verdurmen, G.D. Khoe, A.M.J. Koonen and H. de Waardt, "All-optical data format conversion from WDM to OTDM based on FWM," *Microwave and Optical Technology Letters*, vol. 48, no. 5, pp. 992–994, May 2006.

- E.J.M. Verdurmen, Y. Liu, G.D. Khoe and H. de Waardt, "Study on the limits of all-optical time-domain demultiplexing using cross-absorption modulation in an electroabsorption modulator," IEE *Proceedings-Opto-electronics*, vol. 153, no. 2, pp. 75–83, April 2006.

- E.J.M. Verdurmen, Y. Zhao, E. Tangdiongga, J.P. Turkiewicz, G.D. Khoe and H. de Waardt, "Error-free all-optical add-drop multiplexing using HNLF in a NOLM at 160 Gbit/s," *Electronics Letters*, vol. 41, no. 6, pp. 349–350, March 2005.

- J.J. Vegas Olmos, I. Tafur Monroy, J.P.A. van Berkel, E.J.M. Verdurmen, J.G.L. Jennen and A.M.J. Koonen, "On intranode impairments and engineering rules for an optical label switching router supporting an FSK/IM labeling scheme," *Journal of Lightwave Technology*, vol. 24, no. 9, pp. 3322–3333, September 2006.

- M. García Larrodé, A.M.J. Koonen, J.J. Vegas Olmos, E.J.M. Verdurmen and J.P. Turkiewicz, "Dispersion tolerant radio-over-fibre transmission of 16 and 64 QAM radio signals at 40 GHz," *Electronic Letters*, vol. 42, no. 15, pp. 872–874, July 2006.

- I. Tafur Monroy, E.J.M. Verdurmen, S. Sulur, A.M.J. Koonen, H. de Waardt, G.D. Khoe, N. Chi, P.V. Holm-Nielsen, J. Zhang and C. Peucheret, "Performance of a SOA-MZI wavelength converter for label swapping using combined FSK/IM modulation format," *Optical Fiber Technology*, vol. 10, no. 1, pp. 31–49, January 2004 (invited).

International Conferences

- E.J.M. Verdurmen, J.P. Turkiewicz, E. Tangdiongga, G.D. Khoe and H. de Waardt, "Towards all-optical 320 Gb/s add-drop multiplexing using a nonlinear optical loop mirror," in ECOC 2005 Proceedings, Glasgow, UK, Th 3.1.7, September 2005.

- E.J.M. Verdurmen, Y. Liu, A.M.J. Koonen, H. de Waardt and I. Tafur Monroy, "Chirp properties of SOA-based wavelength converters for FSK/IM combined modulation format," in Proceedings ECOC 2003, Rimini, Italy, Tu 4.4.5, September 2003.

- Y. Liu, J.P. Turkiewicz, E.J.M. Verdurmen, H. de Waardt, G.D. Khoe and H.J.S. Dorren, "All-optical wavelength conversion by utilizing cross-polarization modulation in an electro-absorption modulator," in *ECOC 2003 Proceedings*, Rimini, Italy, We 4.P78, September 2003.

Regional Conferences

- E.J.M. Verdurmen, G.D. Khoe, A.M.J. Koonen and H. de Waardt, "Comparison of demultiplexing techniques using XPM and FWM in HNLF," in *Proceedings IEEE/LEOS Benelux Chapter 2005*, Mons, Belgium, pp. 185–188, December 2005.

- J.J. Vegas Olmos, E.J.M. Verdurmen, I. Tafur Monroy, J.P. Turkiewicz, N. Yan, H. de Waardt and A.M.J. Koonen, "Wavelength conversion with multicasting capabilities deploying highly nonlinear fiber for time-serial labeled networks," in *Proceedings IEEE/LEOS Benelux Chapter 2005*, Mons, Belgium, pp. 181–184, December 2005.

- E.J.M. Verdurmen, Y. Zhao, G.D. Khoe and H. de Waardt, "OTDM Demultiplexing using HNLF in a NOLM at 160 Gb/s," in *Proceedings IEEE/LEOS Benelux Chapter 2004*, Ghent, Belgium, pp. 239–242, December 2004.

- Y. Zhao, E.J.M. Verdurmen, G.D. Khoe and H. de Waardt, "Multiple-wavelength signal generation at 160 Gbit/s using high nonlinear fiber," in *Proceedings IEEE/LEOS Benelux Chapter 2004*, Ghent, Belgium, pp. 243–246, December 2004.

- Y. Liu, J.P. Turkiewicz, S. Zhang, E. Tangdiongga, E.J.M. Verdurmen, H. de Waardt, Z. Li, D. Lenstra, G.D. Khoe and H.J.S. Dorren, "40 Gbit/s SOA-based wavelength conversion assisted by a narrow optical bandpass filter," in *Proceedings IEEE/LEOS Benelux Chapter 2004*, Ghent, Belgium, pp. 251–254, December 2004.

- E.J.M. Verdurmen, M. Heck, G.D. Khoe and H. de Waardt, "Modelling and study of all-optical demultiplexing of a 160 Gb/s OTDM signal using QW-EAM," in *Proceedings IEEE/LEOS Benelux Chapter 2003*, Enschede, The Netherlands, pp. 161–164, November 2003.
- E.J.M. Verdurmen, F.M. Huijskens, H. de Waardt, A.M.J. Koonen and I. Tafur Monroy, "Characterization of an all optical label swapping node for IP over WDM", in *Proceedings IEEE/LEOS Benelux Chapter 2002*, Amsterdam, The Netherlands, pp. 286–289, December 2002.
- R.G. Broeke, J.J.M. Binsma, M. van Geemert, F. Heinrichsdorff, T. van Dongen, J. van Zantvoort, E. Verdurmen, E. Tangdiongga, X.J.M. Leijtens, M.K. Smit, "Measurements and analysis of a monolithical integrated all-optical wavelength converter and a 4-channel digitally tunable laser," in *Proceedings IEEE/LEOS Benelux Chapter 2002*, Amsterdam, The Netherlands, pp. 95–98, December 2002.

Samenvatting

Het in dit proefschrift beschreven onderzoek richt zich op het ontrafelen van in het tijdsdomein gestapelde optische signalen, ook wel optical time division multiplexing (OTDM) genoemd, en de bijbehorende technologische uitdagingen. Dit werk richt zich in het bijzonder op het toevoegen en extraheren van een specifieke datastroom uit een OTDM signaal. De component die deze functie uitvoert kan worden aangeduid als een add-drop multiplexer (ADM). Deze ADMs kunnen worden onderverdeeld in twee categorieën. De eerste categorie is gebaseerd op oplossingen die gebruik maken van halfgeleider materiaal en de tweede categorie benut de niet-lineariteit van een glasvezel.

Een onderzochte halfgeleider materiaal ADM techniek is gebaseerd op het cross-absorption modulation (XAM) effect in een electro-absorptie modulator (EAM). Een model, gebaseerd op propagatie-vergelijkingen in halfgeleider materiaal, is ontwikkeld om de invloed van het XAM effect te kunnen simuleren. Resultaten verkregen met dit model komen goed overeen met experimenteel verkregen resultaten. Foutvrij extraheren (demultiplexen) van een 10 Gb/s datakanaal uit een 80 Gb/s OTDM signaal, met behulp van XAM in een EAM is experimenteel aangetoond. Een nieuw concept genaamd cross-polarisatie rotatie (XPR) is geïntroduceerd om het contrast ratio van de EAM demultiplexer te verbeteren. Ondanks verbetering van het contrast ratio van de demultiplexer is er geen significante verbetering van de prestatie waarneembaar. Mogelijkheden om de EAM in een 160 Gb/s demultiplexer configuratie te gebruiken zijn onderzocht. De kwaliteit van de EAM als optische schakelaar is sterk afhankelijk van het maximaal toegestane ingangsvermogen. Een hoger vermogen van het optische kloksignaal leidt tot een sterker absorptie verzadigingseffect. De snelheid van de EAM als optische schakelaar is begrensd door de hersteltijd van de vrije elektronen en gaten in de halfgeleider, gezamenlijk de carriers genoemd. Een verhoging van de negatieve biasspanning leidt tot een verkorting van de carrier hersteltijd. Een nadeel van het gebruik van een hogere biasspanning is de bijkomende hogere absorptie wat resulteert in een hoger vereist ingangsvermogen om de absorptie te verzadigen, omdat anders een verslechtering van de signaal-ruis verhouding onvermijdelijk is.

Een belangrijk deel van het proefschrift richt zich op ADMs die de niet-lineariteit van een glasvezel benutten. Een van de meest veelbelovende oplossingen is gebaseerd op de nonlinear optical loop mirror (NOLM). Een geheel optische tijdsdomein ADM gebaseerd op een NOLM structuur is voor het eerst gedemonstreerd op datasnelheden boven de 80 Gb/s. Simulaties en experimenteel onderzoek zijn uitgevoerd op

160 Gb/s en 320 Gb/s. De prestatie limiterende factoren in de NOLM gebaseerde ADM zijn overspraak van naburige kanalen voor het extraheren van een kanaal en incomplete verwijdering van het geëxtraheerde kanaal voor het toevoegen van een nieuw kanaal. De jitter op het controle- en datasignaal en een niet geoptimaliseerde NOLM ingangskoppelaar verslechteren de kwaliteit van de ADM. De behaalde resultaten openen mogelijkheden om in de toekomst het systeem op te waarderen naar 640 Gb/s.

De conversie van twee 10 Gb/s non-return to zero (NRZ) golflengte gestapelde kanalen (WDM) naar één 20 Gbs return-to-zero (RZ) OTDM signaal is experimenteel gekarakteriseerd. Het conversie principe is gebaseerd op four-wave mixing (FWM) in een sterk niet-lineare vezel (HNLF). Een voordeel van deze conversie techniek is dat er geen extra NRZ naar RZ conversiestap vereist is. Een tweede voordeel is de transparantie van FWM ten opzichte van de gebruikte modulatie techniek. Zo is deze techniek bijvoorbeeld ook geschikt voor fasegemoduleerde datasignalen. De beperkingen van deze conversie techniek zijn onderzocht. Conversie van 2x10 Gb/s WDM naar 20 Gb/s OTDM is experimenteel aangetoond, maar simulaties wijzen uit dat deze techniek niet geschikt is voor conversie van 4x40 Gb/s WDM naar 160 Gb/s OTDM, omdat het optische vermogen van het geconverteerde signaal erg laag is als gevolg van de lage efficiëntie van het FWM proces.

Een alternatieve ADM techniek die ook bestudeerd is, is gebaseerd op cross-phase modulatie (XPM) spectrale verbreding in combinatie met filtering. Het voordeel van deze techniek is het geringere aantal benodigde componenten voor de constructie van een complete ADM in vergelijking met een ADM gebaseerd op een NOLM of een Kerr shutter. Simulaties en experimenteel werk demonstreren de mogelijkheden van deze techniek.

Een geheel optische tijddomein ADM voor fasegemoduleerde signalen is voor de eerste maal aangetoond. Add-drop multiplexing van een 80 Gb/s RZ-DPSK OTDM signaal gebaseerd op de Kerr shutter met 375 meter HNLF is experimenteel gedemonstreerd. De fase-informatie in het signaal is behouden in de complete ADM. Praktische beperkingen in de experimentele set-up begrensden de datasnelheid tot 80 Gb/s. Een ADM experiment op 320 Gb/s met amplitude gemoduleerde signalen geeft een indicatie van de mogelijkheden van de Kerr shutter als ultrasnelle schakelaar.

Acknowledgements

Obtaining a Ph.D. degree is a long and difficult task. It could not have been possible without the help and support of many people. Therefore, I would like to thank everybody who contributed in any possible way to the completion of this thesis. Hereby I want to mention a few persons specifically.

First of all I am thankful for the great time I have had at the Electro-Optical Communications (ECO) Group at the electrical engineering department of the Eindhoven University of Technology over the last 4 years. In particular, I would like to thank Huug de Waardt for his enthusiasm and encouragement throughout the continuous search for innovative solutions, which is a task every Ph.D. student has to fulfill. I am also thankful to my first and second promotor Ton Koonen and Djan Khoe who gave me the opportunity to conduct my research. I am indebted to Yongpeng Zhao, who introduced me into the phenomenon of supercontinuum generation and conducted several experiments together with me. Furthermore, I would like to thank Eduward Tangdiongga, Yong Liu and Jarek Turkiewicz for the great support in the laboratory. Their knowledge about the equipment is truly large. I am also indebted to Frans Huijskens, who fabricated the home-made Mach-Zehnder interferometer and was always willing to help me in the atelier.

I am also very grateful towards Bas Huiszoon and María García Larrodé for reading large parts of my thesis. They are superb reviewers, and I am very confident they will produce a nice thesis in the future themselves. During my stay at the university I have shared an office at the 11^{th} floor with several people. I would like to thank Ewart, Sulur, JJ, Robert, Raymond and Maria for the interesting discussions related to our work and everyday things.

I would like to express my gratitude to Sander Jansen for his interest in my work and his continuing effort in sending valuable equipment from Münich to Eindhoven. I would like to acknowledge Siemens for kindly providing two mode-locked laser sources, which helped me conduct several crucial experiments. I would also like to acknowledge Calmar for kindly providing their 40 GHz mode-locked laser for two weeks. The experiments with the 160 Gb/s add-drop multiplexing based on the NOLM, would not have succeeded without.

I am equally thankful to all the other ECO-staff. To name a few specifically Johan van Zantvoort for helping me with my computer and his great interest in social events like Beugelen, Peter van Bennekom for giving me packages with expensive equipment, René Kramer the friendly neighbor, Els and Susan for counting my free days, Hyun-Do Jung good luck cycling around Eindhoven and Idelfonso Tafur Monroy, who was always interested in my work ever since he was my supervisor during my final master project. Also thanks to Henrie van den Boom, Harm Dorren, Martin Hill, Anthony Ng'Oma, Javier Molina Vazquez, Gert-Jan Rijckenberg for providing a pleasant working environment. I am also thankful to have been surrounded by motivated Ph.D. students from all around the world: Dirk van de Borne, Ronelle Geldenhuys, Christos Tsekrekos, Ni Yan, Zhonggui Li, Archi Delphinanto, Saoxian Zhang, Jianming Zheng, Georgi Petkov, and Patrick Urban. I want to wish them success with the completion of their research and their future plans.

I have learnt that most of the biggest problems in the world can be solved over a cup of coffee. I wish to thank all the people from the ECR group, Maurice, Matti, Tim, Haibing, Iwan, Peter and Jaap. Special thanks to Tim Schenk for being an example of a motivated Ph.D. researcher and his help on a diversity of small problems.

It has always been pleasant to work in the "Freeband OTDM team"with Erwin Bente, Huug de Waardt and Yohan Barbarin, with whom I worked together on several occasions. Furthermore I want to express my gratitude to the user committee, who always showed great interest in my work. Moreover, special thanks goes out to some poeple from the OED group, Martijn van Heck for helping me getting started with my EAM model and Yevgeni Patent and Jan Hendrik den Besten for putting effort in small inter-group projects.

Prof. Andrekson, prof. Mégret and prof. van Leeuwen are kindly acknowledged for their time and effort to help me improve this thesis.

While not related to this thesis, but which helped me in developing creativity, many thanks goes out to my friends from the Taveres club bulletin committee Dennis, Ben, Teun en Karin for their creativity under the pleasant atmosphere of a glass of white wine.

I would like to thank all my friends and family for their support: Bart, Annemieke, Rolf, Mies, Hans en Hans jr. I also am very grateful towards my father and my mother, who is amazed I can write so many pages in English, for raising me. Also I would like to thank my brothers Dennis, Noël, I am sure I can make some time available to be at your wedding with Karin, and Wouter and Sascha. Family is one of the most important things in life, and last but not least I would like to thank my girlfriend Andrea for her unlimited believe in me successfully finishing this task.

Curriculum Vitae

Erwin Verdurmen was born in Breda, The Netherlands, on May 23, 1978. After attending the secondary school at the Reynaert college in Hulst, he started his studies in Electrical Engineering at the Eindhoven University of Technology in September 1996. From April till August 2001 he was at an internship at Research Center COM at the Technical University of Denmark in Copenhagen on propagation properties of the orthogonal modulation formats IM and PM. After that he conducted his master thesis at the faculty of Electrical Engineering in the Electro-optical communications (ECO) group under the scope of the European funded IST project STOLAS. For this project he worked on the characterization of an all-optical label swapping node. He received his Master of Science degree in October 2002. In November 2002 he continued his work within the ECO group and started working towards his Ph.D. degree. Main research topics are cross-absorption modulation in electroabsorption modulators, fiber-based time domain add-drop multiplexing and transmultiplexing between OTDM and WDM. This research was performed as part of the project: "Key components for 160 to 640 Gb/s optical time domain multiplexed (OTDM) networking"within the Freeband Knowledge Impulse program.